Studies of supersymmetry models for the ATLAS experiment at the Large Hadron Collider

Alan James Barr

Churchill College

A dissertation submitted to the University of Cambridge
for the degree of Doctor of Philosophy
November 2002

Studies of supersymmetry models for the ATLAS experiment at the Large Hadron Collider

Alan James Barr

Abstract

This thesis demonstrates that supersymmetry can be discovered with the ATLAS experiment even if nature conspires to choose one of two rather difficult cases.

In the first case where baryon-number is weakly violated, the lightest supersymmetric particle decays into three quarks. This leads to events with a very large multiplicity of jets which presents a difficult combinatorical problem at a hadronic collider. The distinctive property of the second class of model – anomaly-mediation – is the near degeneracy of the super-partners of the SU(2) weak bosons. The heavier charged wino decays producing its invisible neutral partner, the presence of which must be inferred from the apparent non-conservation of transverse momentum, as well as secondary particle(s) with low transverse momentum which must be extracted from a large background.

Monte-Carlo simulations are employed to show that for the models examined not only can the distinctive signature of the model can be extracted, but that a variety of measurements (such as of sparticle masses) can also be made.

The final two chapters present an investigation into part of the experimental hardware which will be vital for these analyses. Beam tests of ATLAS semiconductor tracker modules demonstrate that this sub-detector can be expected to perform to its specification, providing the good spatial resolution and efficiency with low noise, even after the equivalent of ten years of irradiation.

Declaration

This dissertation is the result of my own work, except where explicit reference is made to the work of others, and has not been submitted for another qualification to this or any other university.

Alan Barr

Acknowledgements

I would like to thank the Particle Physics and Astronomy Research Council for providing financial support during this degree (under PPARC student grant number PPA/S/S/1999/02797).

For various parts of the analyses, I have made use of the ATLAS physics analysis framework and tools which are the result of collaboration-wide efforts.

I take this opportunity to thank collaborators and others who have given direction and technical help during the work on this thesis; in particular Ben Allanach, Janet Carter, Lars Eklund, Jose Enrique Garcia, James Hetherington, John Hill, Christopher Lester, Gareth Moorhead, Peter Richardson, David Robinson, Marcel Vos, Bryan Webber, Steve Wotton and especially my supervisor, Andy Parker, have all made very valuable contributions. I owe a special thanks to Claire for her constructive criticism and artistic consultancy.

This thesis is dedicated to my parents.

Publications

Much of the work in this thesis has already been published. The work on R-Partity violating supersymmetry signatures (chapter 4) was published in two JHEP papers [1,2]. The study of anomaly mediated supersymmetry breaking (chapter 3) is available as [3,4].

Much of the testbeam analysis, described in chapter 6 has been made available in [5–7], or will be published in future ATLAS notes.

Happy is the man that findeth wisdom,
and the man that getteth understanding.

For the merchandise of it is better
than the merchandise of silver,
and the gain thereof than fine gold.

Proverbs 3:13-14

Contents

List of Figures

Figures

Figures

List of Tables

Part I

Introduction

Chapter 1

Theory and motivation

> *Something yet of doubt remains ...*
> *How Nature, wise and frugal, could commit*
> *Such disproportions*

The goal of particle physicists is to describe the most fundamental constituents of the universe and the way in which they interact with one another. The standard model (SM) is the name given to the best current mathematical description of these subatomic particles and of the forces between them. The result of decades of theoretical and experimental research, it has been extremely successful at explaining and predicting the results a wide range of experiments, in some cases with extraordinary precision.

There are, however, good reasons to suppose that the SM is not the last word in our understanding of matter and forces. One notable shortcoming is that it does not include the gravitational force. This precludes it from describing interactions at arbitrarily high energies, far beyond the reach of our current particle accelerators.

The huge difference in the strengths of the electroweak and gravitational forces leads to two vastly different length scales in the universe – the scale of the atoms and that of the stars. The disparity in scales which baffled and inspired Milton hundreds of years ago continues to cause anxiety to many theorists today[a]. The unexpectedly small mass of the Higgs particle is one such problem, and is presented in this chapter as part of the motivation for introducing supersymmetry to the standard model.

1.1 The standard model

1.1.1 Particles and interactions

The SM describes all matter and interactions in terms of fundamental point-like particles. These have no spatial extension but do carry internal angular momentum which is characterised by the spin quantum number, s. The matter component of the theory consists of particles which have $s = \frac{1}{2}$. The forces between the matter particles are mediated by other particles which have integer spin.

The fundamental fermions can be divided into two types, according to whether or not they can interact via the strong nuclear force. Those which respond to the strong force are known as quarks, and are confined by it in more complicated objects known as hadrons. The other basic fermions, the leptons, have only weak-nuclear or electromagnetic charges, and so can exist as free particles.

Each of the three SM forces is associated with the local symmetry operations of a particular Lie group. The quanta of the forces are spin-1 particles known as gauge bosons.

The strong force, which holds the nucleus together, is described by the theory of

---

[a] Participants at the Strings 2000 [8] conference were invited to pose what they thought were the important unsolved problems in fundamental physics. One of the ten questions selected was: *What physics explains the enormous disparity between the gravitational scale and the typical mass scale of the elementary particles?* Another was: *Is Nature supersymmetric, and if so, how is supersymmetry broken?*

families	color$_{L,R}$	T^3_L	Y_L	T^3_R	Y_R	$Q = T^3 + Y$
$\begin{pmatrix} u \\ d \end{pmatrix}, \begin{pmatrix} c \\ s \end{pmatrix}, \begin{pmatrix} t \\ b \end{pmatrix}$	$\mathbf{3}, \bar{\mathbf{3}}$	$\frac{1}{2}$ $-\frac{1}{2}$	$\frac{1}{6}$ $\frac{1}{6}$	0 0	$\frac{2}{3}$ $-\frac{1}{3}$	$\frac{2}{3}$ $-\frac{1}{3}$
$\begin{pmatrix} \nu_e \\ e^- \end{pmatrix}, \begin{pmatrix} \nu_\mu \\ \mu^- \end{pmatrix}, \begin{pmatrix} \nu_\tau \\ \tau^- \end{pmatrix}$	$\mathbf{1}, \mathbf{1}$	$\frac{1}{2}$ $-\frac{1}{2}$	$-\frac{1}{2}$ $-\frac{1}{2}$	0 0	0 -1	0 -1

Table 1.1: Gauge quantum numbers of the standard model fermions. T is the weak isospin, and T^3 its third component. Y is the $SU(1)_Y$ hypercharge, and Q is the electric charge. The subscripts denote left and right handed Weyl spinors.

quantum chromodynamics (QCD). Each quark is a ‘colour’ triplet under the QCD gauge group, $SU(3)_C$. The vector bosons which mediate this force are known as gluons, and form the octet representation. Since $SU(3)$ is a non-Abelian group the gluons themselves have colour charges. The interactions between these force carriers leads to a rich and complex phenomenology.

The other two forces – electromagnetism and the weak force – can be described in terms of the $SU(2)_L$ and $U(1)_Y$ groups of the unbroken weak and electromagnetic forces, and the corresponding charges of the fermions: weak isospin and hypercharge. The various charge quantum numbers of the quarks and leptons are given in table 1.1.

It is notable that there are three families of quarks and leptons, which transform identically under the gauge groups, but which have different masses. Ordinary matter consists only of the lighest two quarks (u and d) and the lighest charged lepton (the electron). The origin of the SM family structure remains mysterious, but clues may be found at the LHC (see sec. 4.7).

1.1.2 The description of mass

Since almost all observed particles are massive (see fig. 1.1), in order to complete the description of the particles and interactions given in sec. 1.1 one must add a mechanism for mass generation. Adding gauge boson mass terms by hand destroys the gauge symmetry of the lagrangian, and results in non-renormalizable theories.

A method of giving mass to vector bosons while maintaining gauge invariance at high energy was described by Higgs [9], Rout and Englert [10]. They considered a pair of real scalar fields, (φ_1, φ_2), with a potential, $V(\varphi_1^2+\varphi_2^2)$, that has a degenerate minimum. These scalar fields are coupled to a real vector field, A_μ. By considering small oscillations about a vacuum solution:

$$\varphi_1 = 0, \quad \varphi_2 = \varphi_0, \quad \text{with} \quad V'(\varphi_0^2) = 0, \quad V''(\phi_0^2) > 0, \tag{1.1}$$

it can be shown[b] that the vector bosons receive an effective mass, $\mu = e\varphi_0$, where e is the coupling constant.

In becoming massive, the vector boson acquires a longitudinal degree of freedom which is taken from the scalar fields. The remaining degree of freedom produces a massive scalar excitation in $\Delta\varphi_2$ which represents the physical Higgs boson, h.

In the SM, it is through the Higgs mechanism that the electroweak bosons ($W^\pm$ and Z^0) obtain their masses. The gauge group $SU(2) \times U(1)$, has gauge bosons W_μ^i, $(i = 1, 2, 3)$, and B_μ, and coupling constants g and g' for the $SU(2)$ and the $U(1)$ parts respectively. The self-interactions of a complex scalar doublet field (the Higgs field), $\Phi \equiv \begin{pmatrix} \phi^+ \\ \phi^0 \end{pmatrix}$, cause spontaneous symmetry breaking, after which the

---

[b] See appendix B for mathematical details.

new mass eigenstates are linear combinations of the original gauge eigenstates:

$$W^{\pm} = (W^1 \mp iW^2)/\sqrt{2}, \quad Z = -B\sin\theta_W + W^3\cos\theta_W \tag{1.2}$$

with $\theta_W \equiv \tan^{-1}(g'/g)$. The masses of the gauge bosons are also linked by $\cos\theta_W = M_W/M_Z$ at tree level.

The masses of the SM fermions are generated from Yukawa couplings to the Higgs doublet field, with the values of each coupling proportional to the mass. Since the mass eigenstates of the quarks are not the same as the weak eigenstates, charged weak interactions can cause transitions between generations. The same mixing matrix introduces a single complex phase which violates the combined symmetry CP, in which particles are exchanged for their anti-particles and the spacial coordinates are inverted.

It is worth noting that there is also now also good experimental evidence [11–13] that neutrinos have small ($\lesssim$ few eV), but non-zero masses, which allow them to oscillate between different flavour eigenstates. However the mechanism by which neutrinos gain mass remains unclear. Neutrino masses can be incorporated into the SM in the same way as the other fermions, but alternative schemes exist[c].

1.1.3 The Higgs mass and the technical hierarchy problem

The Higgs boson is the only particle in the SM which has not yet been experimentally observed[d].

The bare mass of a Higgs boson depends on the curvature of the scalar potential at

---

[c] A particularly interesting example from the point of view of supersymmetry phenomenology is from lepton-number R-parity violating couplings, such as in [14].

[d] Searches at LEP for a Standard Model Higgs boson are not definitive [15].

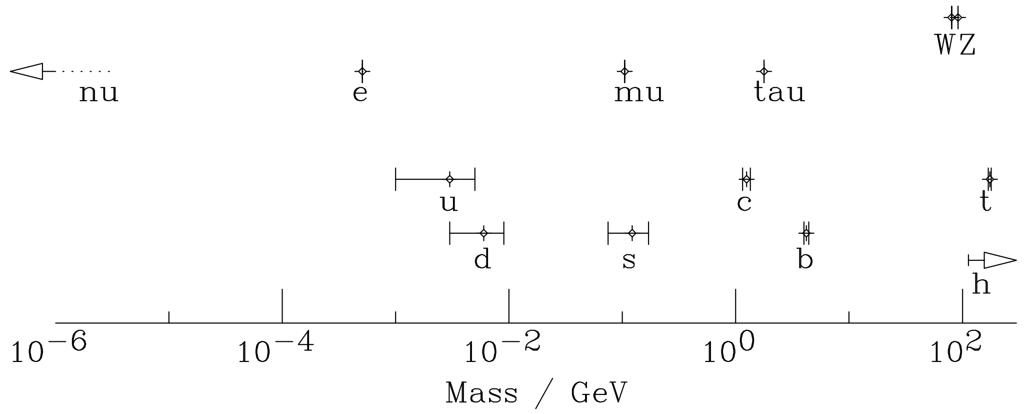

Figure 1.1: Mass values for SM particles, with their uncertainties. A lower limit is shown for the SM Higgs particle. Approximate upper limits on the neutrino masses are shown based on the direct limit on the mass of the electron neutrino. The photon is assumed to be massless.

its vacuum minimum, which is a parameter (rather than a prediction) of the SM.

There are however bounds on the renormalized mass. By imposing the condition that the S-matrix to be unitary for the elastic scattering process $W^+W^- \to W^+W^-$, the renormalized Higgs mass must be less than $(\frac{8\pi\sqrt{2}}{3G_{\mathrm{F}}})^{\frac{1}{2}} \approx 1000$ GeV [17]. Indeed global fits to electroweak data, which are sensitive to the logarithm of the Higgs mass through radiative corrections, tend to favour a light Higgs (see fig. 1.2).

A problem arises because there are large radiative corrections to m_h^{bare}, through loop diagrams, such as those shown in fig. 1.3. These corrections when summed result in divergences which grow quadratically with the cut-off scale, Λ. A fermion with mass m_f and coupling λ_f to the Higgs field gives a contribution,

$$\delta M_{\mathrm{HF}}^2 = \frac{|\lambda_f|^2}{16\pi^2}\left[-2\Lambda^2 + 6m_f^2\ln(\Lambda/m_f) + \cdots\right] \tag{1.3}$$

to the square of the Higgs mass through diagrams such as fig. 1.3a. For a scalar

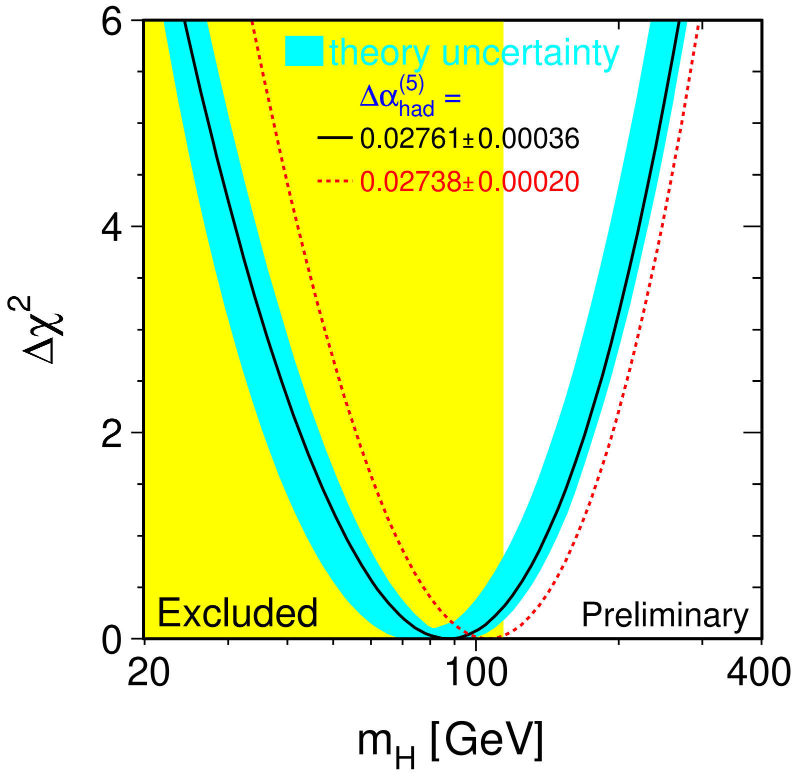

Figure 1.2: The electroweak precision fit $\Delta\chi^2 = \chi^2 - \chi^2_{\text{min}}$ as a function of the SM Higgs mass. The band represents the theoretical uncertainty from missing higher order corrections. The vertical band shows the region excluded by direct searches at 95% confidence. The dashed line was obtained using an alternative calculation of the QED coupling, $\alpha(M_Z)$. From [16].

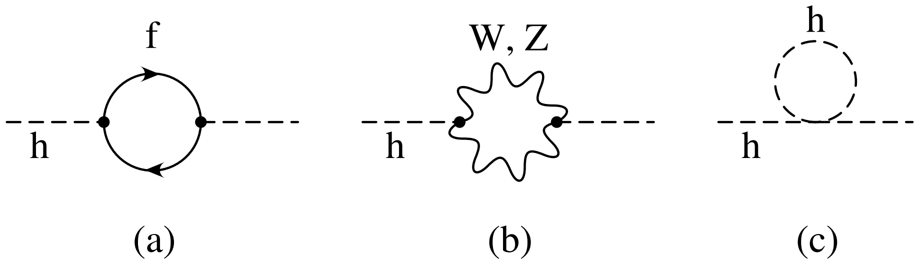

Figure 1.3: 1-loop diagrams contributing to the effective Higgs $(\text{mass})^2$, from (a) fermion loop; (b) gauge boson loop; (c) scalar loop.

loop, such as fig. 1.3(b), there is a similar correction,

$$\delta M_{\mathrm{HS}}^2 = \frac{\lambda_s}{16\pi^2}\left[\Lambda^2 - 2m_s^2 \ln(\Lambda/m_s) + \cdots\right]. \tag{1.4}$$

If the SM is considered to be the ultimate theory of the universe, then this divergence is not necessarily a problem. However there are good reasons to suppose that the SM will not be the last word in our understanding of the fundamental interactions. For example, the omission of gravity from the theory will become important as one approaches the Planck scale $M_{\mathrm{Pl}} = \sqrt{\frac{\hbar c}{G_{\mathrm{N}}}} \sim 10^{19}$ GeV. While the Planck energy regime is far from being realised by any experiment, it places a limit on the validity of the SM, changing its status to that of an effective field theory, valid only below a certain energy level.

Setting the cut-off Λ of the integrals to the Planck scale forces the natural scale of the Higgs mass-squared to huge values around M_{Pl}^2. In order to end up with a physical mass-squared near the electroweak scale, $\sim (100\ \mathrm{GeV})^2$, as demanded by the arguments at the start of this section, one must fix the bare mass extremely precisely to about one part in 10^{16}. Even if Λ, the scale at which new physics enters, is reduced to the unification scale at about 10^{15} GeV (see sec. 1.2.2), a striking cancellation is required over twelve orders of magnitude. This need for extreme fine-tuning is known as the technical hierarchy problem.

It is however possible to avoid such delicate and artificial parameter fixing. Notice that sign of the term quadratic in Λ is opposite in eq. 1.3 as compared to eq. 1.4. This is because the Feynmann rules require a factor of -1 for each fermion loop in the diagram. The cancellation introduces the possibility that the dangerous divergences[e] can be systematically cancelled, provided that each of the SM fermions

---

[e] There are remaining divergences, but they are logarithmic in Λ, and so are much easier to explain in terms of small numerical factors.

are accompanied by two complex scalars with $\lambda_s = |\lambda_f|^2$.

Such companions and couplings are an essential consequence of models which respect a special symmetry principle – *supersymmetry* – which is the subject of sec. 1.2.

1.2 Supersymmetry

The theory of supersymmetry hypothesises a relationship between particles which have integer and half-integer spins. It predicts that particles should come in multiplets containing an equal number of fermionic and bosonic degrees of freedom.

This section promotes the main motivations for extending the Standard Model to include supersymmetry. For a more detailed theoretical description of the supersymetry algebra, and of supersymmetric field theory, the reader is directed towards the pedagogical introductions upon which much of the following discussion is based [18–24].

1.2.1 Overview

Physicists are already familiar with theories which have the same properties after such operations as translation in time or space, or rotations in space. Modern physics also makes use of symmetry under the relativistic Lorentz boosts, and gauge transformations. Supersymmetry is an extension to these existing symmetry principles, and predicts exact relationships between particles with different spins.

To make a stronger statement, it is one of very few extensions available. This was shown by Coleman and Mandula [25,26], who considered the possible symmetries of the scattering matrix. They proved that a theory which describes a finite number of point particles types, which obeys the Lorentz transformations, and in which particles scatter in a physically sensible manner, may only have internal symmetries (like gauge symmetries), and the symmetries of the Poincaré group (*i.e.* Lorentz boosts, translations and rotations). This restriction is known as the Coleman-Mandula 'no-go' theorem.

The only known extension [26] of the allowed symmetries is the possibility of adding operators which relate bosons to fermions – the supersymmetry generating operators, Q. Aficionados favour the argument that since nature has chosen to respect gauge and Lorentz symmetries there is every reason to believe that the supersymmetry should also be physically relevant.

The supersymmetry (SUSY) generating operators change the spin of a single particle state by $\pm\frac{1}{2}$, and in doing so transform bosonic states into fermionic states and *vice versa*. Symmetry under these operations means that for every bosonic degree of freedom in the theory, there must be a corresponding fermionic degree of freedom. Such theories will then naturally provide the companions required to cancel the divergences in the Higgs mass, which were described in sec. 1.1.3.

In the simplest case there is only one distinct copy of the SUSY generators, Q, $Q^\dagger$, and each particle state is accompanied by exactly one other state with spin differing by a half. The more general cases with $N \geq 2$ typically contain super-partners of fermions with opposite chirality, so are difficult to reconcile with the V-A weak couplings in the SM. Hence only simple ($N = 1$) supersymmetry can be physically relevant at low scales.

It is theoretically appealing that if SUSY exists, it is intimately connected with the structure of space-time, as can be seen from the anticommutation equations of the generating operators,

$$\{Q_a, Q_b^\dagger\} = 2(\sigma^\mu)_{ab} P_\mu, \quad \{Q_a, Q_b\} = 0, \tag{1.5}$$

where Q and $Q^\dagger$ are two-component complex spinor operators, P_μ is the four-momentum operator, and the components of $\sigma = (\mathbf{1}, \overrightarrow{\sigma})$ are the identity and the Pauli 2×2 matrices. The SUSY generator, Q_α and its hermitian conjugate $Q_\alpha^\dagger$, commute with the momentum operators,

$$[P^\mu, Q] = [P^\mu, Q^\dagger] = 0 \tag{1.6}$$

while under Lorentz transformations they transforms as Weyl spinors.

The supersymmetry generator Q, can be assumed to commute with the generators of the $SU(3) \times SU(2) \times U(1)$ gauge group[f]. The guage interactions and charges of the superpartners will then precisely cancel the unwanted quadratic Higgs divergences discussed in sec. 1.1.3.

1.2.2 Grand unified theories

There is another piece of circumstantial evidence in favour of SUSY which is related to the hope that all three SM forces might eventually be described in terms of a single grand unified theory (GUT).

The aim of a GUT is to embed the $SU(3) \times SU(2) \times U(1)$ gauge groups in a simple group, which is spontaneously broken at some high scale. Above that scale the couplings will be equal, while below it each will run according to its renormalisation group equation (RGE). These differential equations describe how the value of the gauge couplings change depending on the scale at which they they are observed. From a low-energy perspective a GUT enthusiast would hope to observe all three of the SM gauge couplings tend towards a single point somewhere between the

---

[f] The commutator must be a one-dimensional representation of the gauge group. Since $SU(3)$ and $SU(2)$ have no non-trivial one-dimensional representation, Q must in any case commute with the generators of these groups.

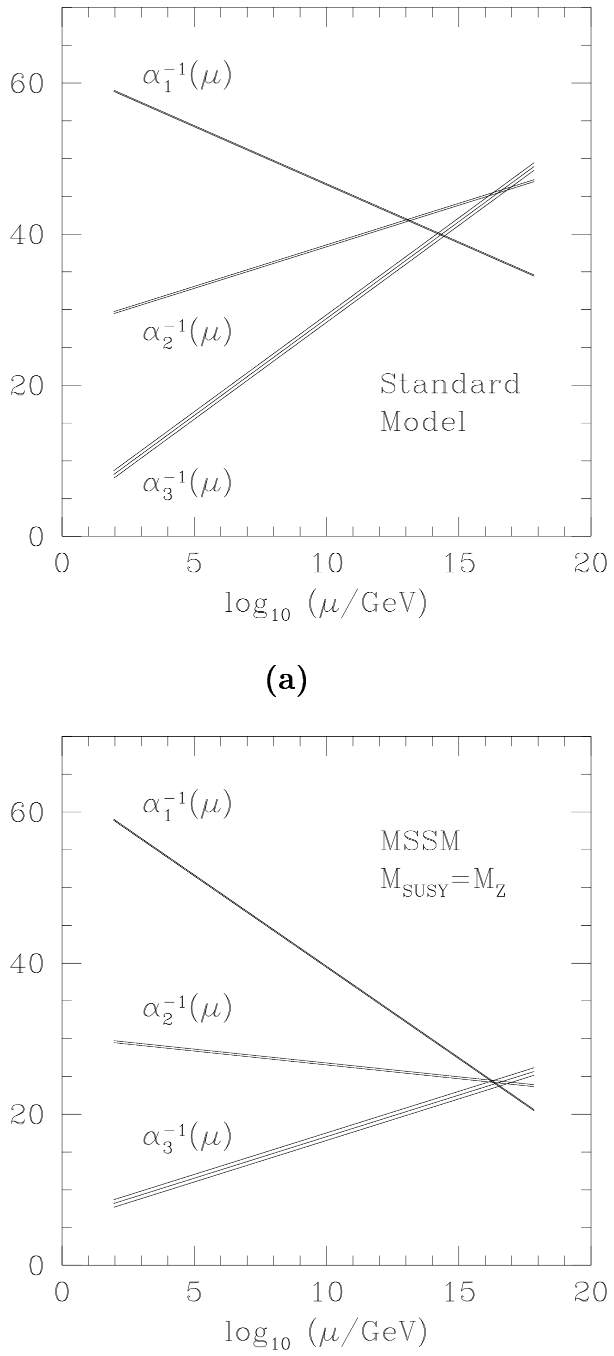

(a)

(b)

Figure 1.4: The running of the $SU(3)$, $SU(2)$ and $U(1)$ gauge couplings **(a)** without and **(b)** with $N = 1$ supersymmetry, according to one loop renormalization group equations. $\alpha_1 \equiv (5/3)\alpha_Y$, where α_Y is the hypercharge coupling in the conventional normalisation. The bands reflect contemporary experimental uncertainties. From [27].

electroweak and Planck scales.

The running of the couplings depends on the particles which are accessable at any particular scale and so will be affected by the addition of new particles. Supporters of supersymmetry therefore consider it a great success that the effect of adding SUSY particles near the electroweak scale is a significant improvement to the unification of the couplings, as shown in fig. 1.4.

1.2.3 The minimal supersymmetric standard model

If supersymmetry is physically relevant then all known particles should have superpartners, known as ‘sparticles’. This section describes the smallest particle content for a supersymmetric theory in which the SM can be embedded, known as the minimal supersymmetric standard model (MSSM).

It is natural to ask if any of the particles of the SM might already be superpartners of one another. The only SM particles with spin differing by a half and with the same gauge quantum numbers are the Higgs boson and the neutrino. However if these were related by a supersymmetry transformation the SUSY equivalent of the SM Yukawa interactions would violate lepton number. So in constructing a supersymmetric extension of the SM each known particle must exist in a multiplet alongside a new ‘sparticle’ partner.

It is most convenient to describe the MSSM in terms of its interaction eigenstates, and at a high energy scale where supersymmetry breaking is small. The particles can be then treated as approximately massless. At low energies, both the SM particles and their SUSY partners will aquire mass through the supersymmetric version of the Higgs mechanism. In sec. 1.2.5 some of the consequences of SUSY breaking are summarised.

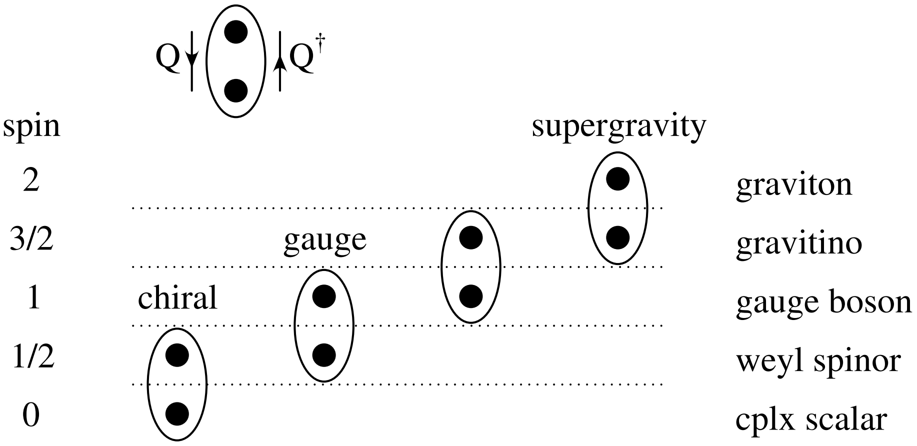

Figure 1.5: The massless $N = 1$ supermultiplets. The blobs represent individual supermultiplets, each of which has two components with spins differing by one half. Supermultiplets can be constructed by the application of the generator operators Q and $Q^\dagger$.

Particles		spin 0	spin $\frac{1}{2}$	$SU(3)$, $SU(2)$, $U(1)$
squarks, quarks	Q	$(\tilde{u}_L\ \tilde{d}_L)$	$(u_L\ d_L)$	$(\mathbf{3},\ \mathbf{2},\ \frac{1}{6})$
(× 3 families)	$\bar{u}$	$\tilde{u}_R^*$	$u_R^\dagger$	$(\bar{\mathbf{3}},\ \mathbf{1},\ \text{-}\frac{2}{3})$
	$\bar{d}$	$\tilde{d}_R^*$	$d_R^\dagger$	$(\bar{\mathbf{3}},\ \mathbf{1},\ \frac{1}{3})$
sleptons, leptons	L	$(\tilde{\nu}\ \tilde{e}_L)$	$(\nu\ e_L)$	$(\mathbf{1},\ \mathbf{2},\ \text{-}\frac{1}{2})$
(× 3 families)	$\bar{e}$	$\tilde{e}_R^*$	$e_R^\dagger$	$(\bar{\mathbf{1}},\ \mathbf{1},\ 1)$
Higgs, Higgsinos	H_u	$(H_u^+\ H_u^0)$	$(\tilde{H}_u^+\ \tilde{H}_u^0)$	$(\mathbf{1},\ \mathbf{2},\ +\frac{1}{2})$
	H_d	$(H_d^0\ H_d^-)$	$(\tilde{H}_d^+\ \tilde{H}_d^0)$	$(\mathbf{1},\ \mathbf{2},\ \text{-}\frac{1}{2})$

Table 1.2: The MSSM chiral supermultiplets, each of which contains both a spin-zero (scalar) and spin-half (Weyl spinor) component. The Higgs fields are given a subscript label depending on whether they give mass to u-type or d-type quarks.

The possible massless multiplets for $N = 1$ SUSY are shown in fig. 1.5. Into this framework must be placed the SM fermions, vector gauge bosons, and a fundamental scalar particle – the Higgs boson. Only two types of such supermultiplet are required to contain all of the standard model particles, these are the chiral and the gauge

Particles	spin $\frac{1}{2}$	spin 1	$SU(3)$, $SU(2)$, $U(1)$
gluino, gluon	$\tilde{g}$	g	$(\mathbf{8}, \mathbf{1}, 0)$
wino, W bosons	$\tilde{W}^{\pm}$, $\tilde{W}^{0}$	$W^{\pm}$, W^{0}	$(\mathbf{1}, \mathbf{3}, 0)$
bino, B bosons	$\tilde{B}^{0}$	B^{0}	$(\mathbf{1}, \mathbf{1}, 0)$

Table 1.3: The MSSM gauge supermultiplets, each of which contains both a spin-half (Weyl spinor) and a spin-one (vector) component.

multiplets.

The SM fermions are placed in chiral multiplets (table 1.2), each of which contains both a spin-zero and a spin-half component. There is another possibility – putting the quarks and leptons in gauge supermultiplets – but this would introduce new vector fields, and therefore additional gauge groups.

Massive quarks and leptons are constructed from pairs of Weyl spinors with opposite chirality. This means that in a supersymmetric theory, every massive quark and lepton must be accompanied by a *pair* of scalar partners, which are known as known as squarks and sleptons respectively. Supersymmetric partners of known particles are denoted by placing a tilde over the corresponding particle, for example $\tilde{e}^{-}$ for a selectron.

Though the scalar partners of the SM fermions are often given the labels 'right' and 'left' they obviously have no 'handedness' themselves. Instead the label refers to the helicity of their respective fermion partners, so for example the 'right up squark' is the scalar partner of the u_R Weyl fermion. The exception to this nomenclature is the third generation of quarks and leptons, which, because of their large Yukawa couplings have larger left-right mixing. Thus the stops, sbottoms and staus are more usually denoted with subscripts 1 and 2 to denote the lighter and heavier state respectively.

The gauge supermultiplets are the SUSY equivalent of the SM gauge bosons – the minimal additional fields necessary to create a theory which is both supersymmetric and gauge invariant. The MSSM gauge multiplets are listed in table 1.3. In addition to a vector boson, each gauge multiplet contains a spin-half partner, known as a gaugino. Those corresponding to unbroken $SU(3) \times SU(2) \times U(1)$ are called the gluinos, winos and bino respectively.

Any Higgs bosons must belong to a chiral supermultiplet, since only they contain scalars. A single Higgs doublet ϕ is sufficient for the SM, as both ϕ and its complex conjugate field ϕ^* can also be used when writing a lagrangian density, to give mass to the quarks of different hypercharge. However a supersymmetric lagrangian densty must not contain terms with both ϕ, and ϕ^*, and so a second Higgs doublet is required, with the opposite hypercharge in order to give mass to both up-type and down-type quarks. Another way of seeing this is that the charged W bosons must have supersymmetric partners after spontaneous electroweak symmetry breaking, which would be impossible with only a single Higgs isodoublet. A more technical discussion of a third reason is given in [19].

The new Higgs doublet leads to additional massive scalar bosons. A pair of complex doublets has eight degrees of freedom. After electroweak symmetry breaking removes three degrees of freedom, there remain five physical Higgs bosons: a charged pair of scalars, $H^{\pm}$, a pair of neutral scalars H, h, and a neutral pseudoscalar A. Their spin-half partners, the Higgsinos, mix with the winos and binos to form mass eigenstates: the charged Higgsinos and winos create two 'charginos' $(\tilde{\chi}^{\pm}_{1,2})$. The two neutral Higgsinos, the neutral wino and the bino also mix, to form four electrically uncharged 'neutralinos' $(\tilde{\chi}^{0}_{1,2,3,4})$.

1.2.4 R-parity

The MSSM as described in the previous section does not distinguish between quark/lepton fields and Higgs fields. As a result baryon- and lepton-number violating interactions are not excluded.

The superpotential, from which the supersymmetric lagrangian density is constructed, can contain the gauge-invariant and renormalizable terms:

$$W_{\mathrm{RPV}} = \frac{1}{2}\lambda^{ijk} L_i L_j \bar{E}_k + \lambda'_{ijk} L_i Q_j \bar{D}_k + \frac{1}{2}\lambda''_{ijk} \bar{U}_i \bar{D}_j \bar{D}_k + \kappa_i L_i H_u \tag{1.7}$$

which is expressed in terms of superfields, each of which contains both partners in the super-multiplet. For example L_2 is the muon isodoublet superfield, containing the left-handed muon, its neutrino, and both of their scalar superpartners. H_u, L and Q are isodoublets while $\bar{U}$ and $\bar{D}$ are isosinglets. Gauge indices have been suppressed and i, j, k are familiy indicies.

The first three terms in eq. 1.7 are Yukawa couplings between the matter superfields. The last term is the mixing term between the Higgs and lepton doublets. When contracted through the appropriate gauge matrices, λ_{ijk} must be antisymmetric under $i \leftrightarrow j$ and λ'' antisymmetric under $j \leftrightarrow k$. W_{RPV} therefore adds $9+27+9+3 = 48$ new parameters.

In the perturbative standard model both bayron number and lepton number are conserved[g]. Baryon number assignments are $+\frac{1}{3}$ for (s)quarks, $-\frac{1}{3}$ for anti-(s)quarks and zero for all other particles. Likewise total lepton number $L = +1$ is given to (s)leptons and -1 for their anti-particles. Non-zero values of the couplings λ, λ', and

---

[g] There does exist within the standard model the possiblity to violate both B and L (but not $B - L$) by quantum mechanical tunneling into a topologically distinct but physically equivalent $SU(2)$ gauge rotated vacuum state [28]. Such processes are non-perturbative and are suppressed by extremely large exponential factors $\sim \exp(-16\pi^2/g^2)$.

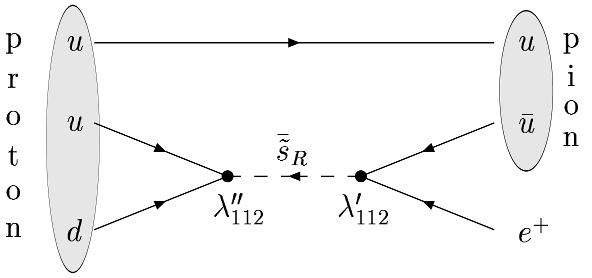

Figure 1.6: Example of a Feynman diagram in which a pair of non-zero R-parity violating couplings leads to squark-mediated proton decay, p → $\pi^0 e^+$.

κ violate total L by one unit, while λ'', violates B by one unit.

Products of baryon- and lepton-violating terms are strongly constrained by experiment. For example, if both λ and λ'' terms were present and of order unity, then proton decay would take place at a rate similar to that of nuclear beta decay. On dimensional grounds, one can estimate that:

$$\Gamma(\text{proton} \to e^+\pi^0) \approx \frac{(\lambda'_{11k})^2(\lambda''_{11k})^2}{m^4_{\tilde{q}}} m^5_{\text{proton}} \tag{1.8}$$

However the proton is remarkably stable – the partial lifetime $\tau/\mathcal{B}(p \to e^+\pi^0)$ for the decay shown in fig. 1.6 is greater than 10^{33} years [29]. Since the squarks are required to be light enough to solve the heirarchy problem, the product of couplings $\lambda'_{11k}\lambda''_{11k}$ must be very small.

The most extreme solution is the imposition of the discrete global multiplicative symmetry:

$$R_P = (-1)^{3B+L+2s} \tag{1.9}$$

where s is the spin of the particle. This combination of quantum numbers ensures that standard model particles have $R_P = +1$ while their superpartners have $R_P = -1$. Such a symmetry excludes the terms in eq. 1.7, and so circumvents fast proton decay problem.

In R-parity conserving (RPC) models, sparticles can only be produced in pairs and must decay to states which also contain an odd number of sparticles, with the result that the lightest supersymmetric particle (LSP) is stable. Each SUSY event must then produce an even number of LSPs which, being weakly-interacting, escape detection and often generate a large missing transverse momentum ($\not{p}_T$). This signature has been exploited by many analyses proposed for the LHC [30], since it provides a clean separation between SUSY events and the SM background. However, the incomplete measurement of the final state makes the reconstruction of the SUSY mass spectrum rather difficult.

A massive particle which is cosmologically stable will have relics from the big bang which contribute to the invisible dark matter of the universe. A discussion of the cosmological relic density of neutralinos is given in sec. 3.5.1.

However the imposition of R-parity conservation is rather *ad hoc*, and is not the only solution. To prevent fast proton decay through the terms in eq. 1.7, it is sufficient that *either* lepton or baryon number are conserved[h]. This can be seen in eq. 1.8, where the strong limit requires only the *product* of B- and L-violating couplings to be small.

If R-Parity (R_P) is violated in nature then the LSP will decay, and the collider signatures can be very different from the R_P conserving case. R-parity violating (RPV) signatures are investigated further in chapter 4.

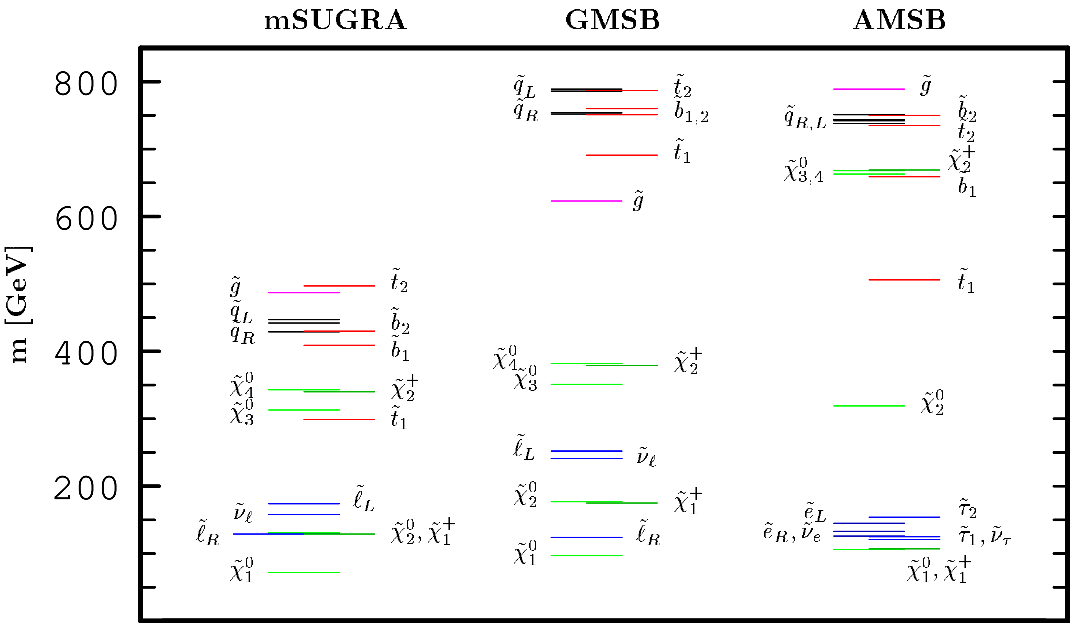

Figure 1.7: Example sparticle spectra for three different examples of high-energy theories with particular choices of parameters. From [31]

1.2.5 Supersymmetry breaking

In a theory in which supersymmetry was exact and unbroken, the properties and interactions of the superpartners would be precisely determined. Therefore most of the differences between supersymmetric models can be traced to the manner in which SUSY becomes broken in the normal vacuum state.

From an experimentalist's viewpoint supersymmetry is only interesting if it can pro-

---

[h] The coupling λ'' effects both $R_P \to -R_P$ and $\Delta B = 1$, so cannot by itself cause decays of the form baryon $\to$ meson + meson.

duce observable experimental effects. Since existing experiments have so far failed to find evidence for supersymmetric partners it is difficult to avoid the conclusion that sparticles (if they do indeed exist) must have large ($\mathcal{O}$ TeV) masses.

A general feature of most realistic models is that SUSY is dynamically (spontaneously) broken by a gauge coupling which becomes strong at some scale M_S. The known quarks and leptons must be neutral under this group otherwise there would be at least one light sparticle [32], so strong supersymmetry breaking must occur in a 'hidden' sector of fields isolated from ordinary particles and interactions.

SUSY breaking must be communicated to the observed particles by some interaction felt by both the visible and hidden sectors. The most commonly discussed methods are through flavour-blind gravitional (mSUGRA), or gauge (GMSB) interactions. A more recent alternative, in which there is no direct contribution from the hidden sector (AMSB), is discussed in chapter 3. Some example sparticle spectra for these models are shown in fig. 1.7.

1.2.6 An experimental perspective on theoretical models

It is extremely difficult to search for new physics without considering what that physics may be. It is therfore instructive for experimentalists to use theoretical models to direct their studies.

Indirect searches for supersymmetry generally measure quantities which are calculable in the SM and can be measured with a very high degree of accuracy. These can be sensitivity to new physics through loop corrections from virtual particles, including those which have not yet been observed directly. Such experiments look for deviations from known physics, so the methods employed are relatively independent of any underlying model.

Precision results which are in agreement with the SM are also very valuable, since they can strongly constrain theory. The measurements can be performed in a model-independant manner, and their values interpreted within the framework of particular models. A brief overview of the constraints on the 'free parameters' of the minimal anomaly mediated supersymmetry breaking (AMSB) scenario are given in sec. 3.5.2 for measurements of the anomalous magnetic moment of the muon and in sec. 3.5.3 for the branching rate for the flavour-changing process $B \rightarrow X_s\gamma$.

The method of analysis and interpretation are rather different at collider experiments such as the LHC, where an enormous number of different measurements can be made. The experimentalist's dilemma is how to chose the variables which might be sensitive to new physics.

The situation is even more complicated because much of the information which could in principle help reconstruct collision events is necessarily lost. The properties of any particles produced have to be deduced from their stable decay products. For example decays which occur sequentially in less than about 10^{-14} of a second cannot be ordered in time. Ambiguities are also introduced from the experimental uncertainty in identifying particles, and most difficult of all, weakly interacting neutral particles do not interact with the experiment at all.

To assist the experimenter in finding discriminatory variables it is therefore valuable to consider the low-energy phenomenology predicted by various well-motivated theoretical models. But which models should be studied?

One possible approach is to parameterise one's ignorance, and to construct a general low-energy effective theory containing *all* physically reasonable terms. It might then be possible to simulate the expected results of collider experiments for each case.

In the case of supersymmetry searches such a strategy is confounded by the large dimensionality of the possible model space. In the MSSM alone there are 105 additional parameters [33] (not including the extra 48 in eq. 1.7) which describe masses, mixing angles and phases after general soft SUSY breaking. A coarse grid of 100 different values of each of these parameters would produce 153^{100} different points in model space. Since individual points require of the order of a day of computing time for even approximate simulation of a minimum number of events, the whole parameter space would require more than 10^{200} computer-days to model – obviously not a viable proposal.

A more pragmatic approach is to choose a subset of 'typical' models which it is hoped will exhibit universal features such as the $\not{p}_T$ signature for RPC supersymmetry. It is the importance of studying a representative set of models that motivates the analyses of R-parity violating and anomaly-mediated supersymmetry presented in part II.

1.3 Summary

There are strong theoretical motivations for suspecting that supersymmetry might be a next step in our understanding of fundamental interactions:

- it provides a solution to the technical hierarchy problem, since cancellations from super-partners prevent the Higgs boson from obtaining a huge mass;
- it improves the prediction of the unification of gauge couplings at high scales and so helps in embedding the SM in a grand unified theory;
- if R-parity is conserved then the lightest of the new supersymmetric particles can provide a cosmologically interesting contribution to the dark matter;
- it may be a stepping stone towards a quantum theory of gravity;

- the Colemann-Mandula theorem severely restricts the choice of other extensions to the standard model.

Despite these theoretical reasons, there is currently no good experimental evidence that SUSY is realized in nature. Yet whether or not one believes in supersymmetry few would argue that it is not important to search for it.

If supersymmetry is indeed the solution to the hierarchy problem, then SUSY partners of known particles must have masses at the TeV scale. This means that the next generation of particle colliders will produce SUSY particles, and the detectors will have the opportunity to uncover a new kind of matter.

Chapter 2

The ATLAS experiment

> *In bulk as huge as whom the Fables name of monstrous size*

2.1 The LHC

The 'large hadron collider' (LHC) is currently under construction in a 27 km circular tunnel at the European particle physics laboratory (CERN) near Geneva. The machine will accelerate protons to energies of 7.0 TeV then collide them head-on to maximise the energy available to create new particles. The LHC has the potential to greatly advance our understanding of fundamental physics, and to constrain the theories which can describe it. Its high energy and luminosity allow exploration of a variety of important questions, such as the origin of mass, the predominance of matter over anti-matter, and the relationship of matter to the forces that act on it.

Some machine parameters of the LHC are shown in table 2.1. In particular the increase of energy and intensity relative to previous pp and $p\bar{p}$ colliders is shown in fig. 2.1. High energy allows the production of heavier particles – for a collider experiment the energy available to produce new particles increases with the beam energy. The luminosity gives a measure of the intensity of the beams, and is proportional to the total number of interactions of a specific type which might be expected.

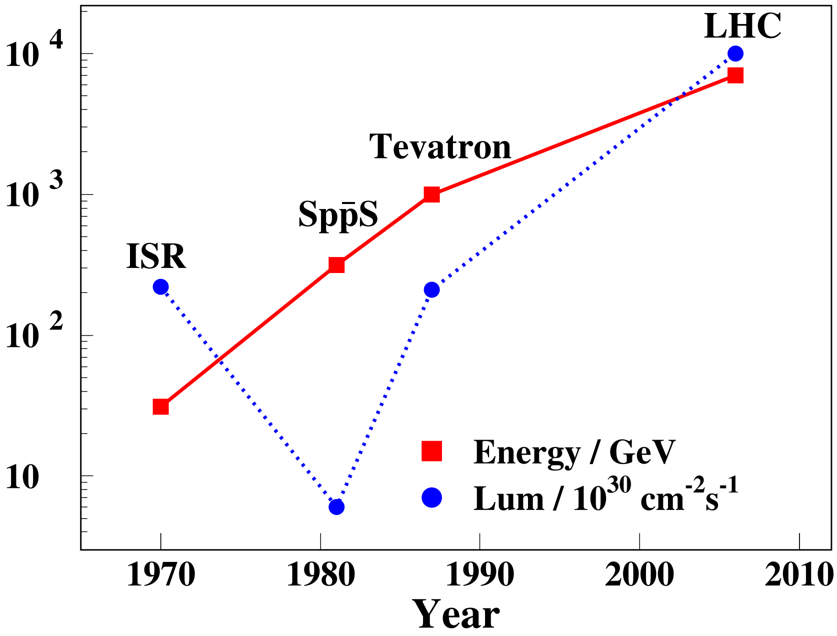

Figure 2.1: The beam energy and luminosity of the various proton–(anti-)proton colliders plotted against their start-up year.

The counter-rotating beams of protons will be made to collide at four points shown in fig. 2.2. Large experiments will measure the properties of the particles produced in the collisions. By studying statistical distributions of large numbers of interactions, insight will be gained into the underlying physical processes.

2.2 Physics goals

In common with many particle physics experiments, ATLAS would be better described as an experimental facility. A wide-ranging physics program includes, but is not limited to:

- **Higgs:** the exploration of the mechanism of electroweak symmetry breaking, incorporating various Higgs boson searches. The Higgs boson is the only par-

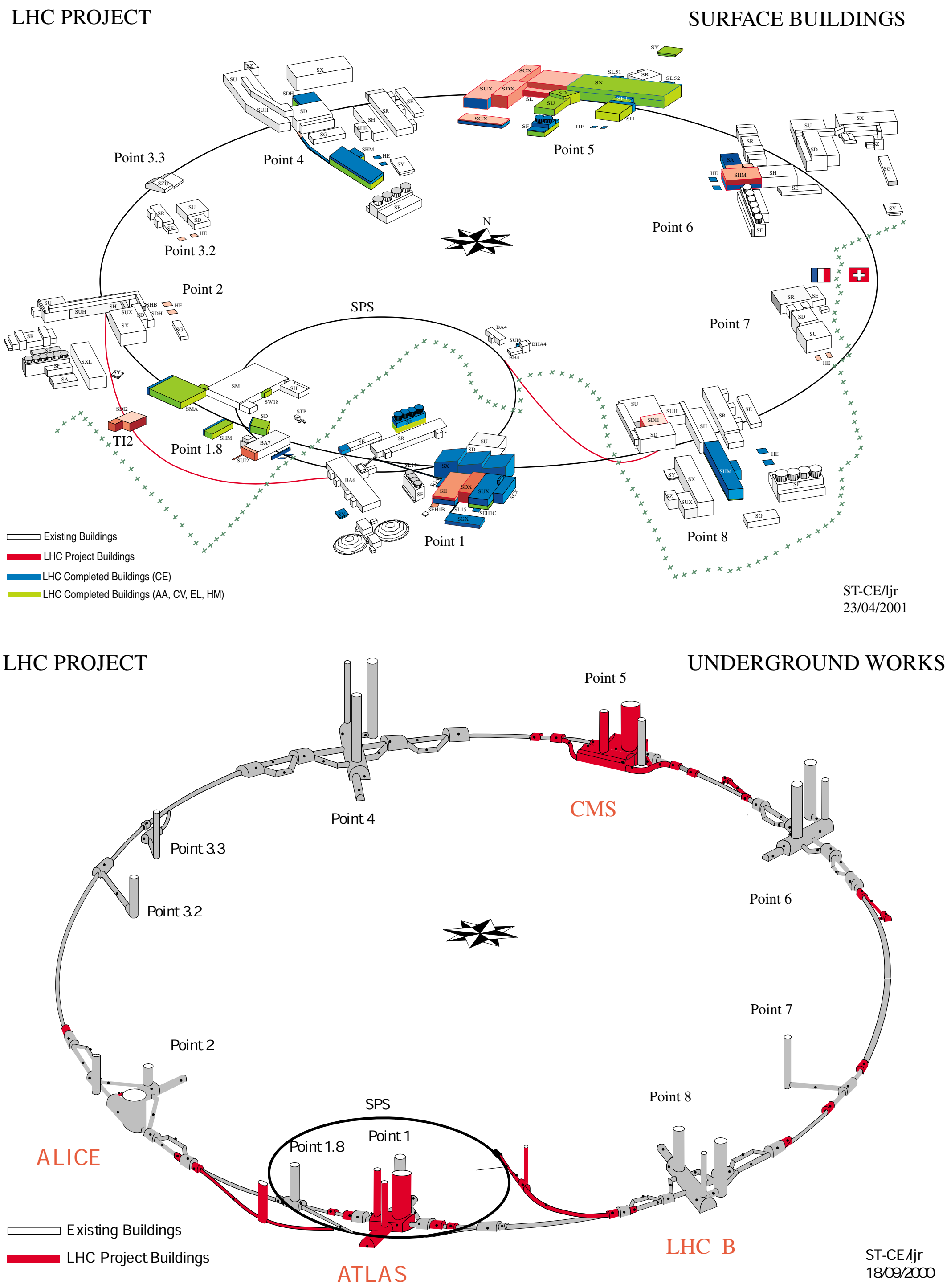

Figure 2.2: The LHC above and below ground. ATLAS and CMS are general purpose detectors, with wide-ranging physics programs. ALICE has been designed to study the products of heavy ion collisions, while LHCb is intended to measure the decay products of hadrons containing b-quarks. Protons will be accelerated progressively in CERN's chain of accelerators, of which only the largest two (the SPS and the LHC) are shown. From [34].

Beam energy	7.0 TeV
Time between collisions	24.95 ns
Luminosity	0.1 to 1.0×10^{34} $\text{cm}^{-2}\text{s}^{-1}$
Circumference	26.659 km
Particles per bunch	10^{11}
Bunch length (σ_z)	7.5 cm
Bunch width (σ_x)	15.9 μm
Bunches per beam	2835
Beam current	0.53 A
Magnetic field strength	8.36 T
Dipole magnet temperature	1.9 K
Cost to completion (approx.)	3080 million CHF

Table 2.1: Some parameters of the LHC (proton–proton mode).

ticle of the SM which has not yet been observed. Extensions to the SM such as supersymmetry often extend the Higgs sector, and so predict multiple Higgs bosons.

- **New physics:** searches for supersymmetry, and for large and small extra dimensions. These extensions to the Standard Model are partly motivated by considerations of the natural scale of the Higgs mass, which was discussed in sec. 1.1.3. They both predict new particles at about the TeV scale, which if they exist should be observable at the LHC.

- **Electroweak:** the precision measurement of the top-quark and the W boson masses, and of the electroweak gauge boson couplings. If and when the Higgs boson is discovered, such measurements will help to over-constrain the parameters of the combined electroweak theory.

- **B-physics:** constraining the flavour sector. Given the very high rate of b-quark production, ATLAS can measure decays of B-hadrons, and help to over-constrain the Cabibbo-Kobayashi-Maskawa mixing matrix parameters, including precise measurements of CP-violation in B-meson decays.
- **Strong interactions:** measurements of the strong coupling constant, α_{S}, and the parton density functions. The basic principles behind the strong nuclear force are well described the gauge theory of QCD. However experimental measurements of QCD parameters are crucial since non-perturbative interactions between particles makes many calculations extremely difficult. The results of these experiments are important both in their own right, and because they are a major part of the background to other processes.

The exploration of each of these topics is achieved by identifying and measuring the properties of those decays products which live long enough to pass through part of the experimental apparatus. From their interactions with that apparatus, one attempts to identify the particles produced, as well as measuring their energy, momentum, and position. Those measurements can then be interpreted with reference to the various theoretical models.

2.3 Detector geometry and terminology

The ATLAS detector has approximate cylindrical symmetry[a]. It is most often described with a coordinate system, $\{R, \phi, z\}$, where the z-axis points parallel to the beam-pipe, R is the transverse distance from it, and the aziuthal angle, ϕ is defined such that the x-axis points from the interaction point to the center of the LHC ring.

---

[a] At the time of writing the various components of the experiment are under construction, with an expected completion date in 2007. The description of the detector is given in the present tense, but it should be noted that the detector may evolve during the intervening period.

The true rapidity $y = \frac{1}{2}\ln[(E+p_z)/(E-p_z)]$ of a Lorentz vector is defined such that the rapidity differences are conserved under a boost along the z axis. It is a useful coordinate in hadrons colliders where the initial z-momenta of the primary partons are not known. However the calculation of the true rapidity requires knowledge of the particle's mass, which is often difficult to determine experimentally. Hence the pseudorapidity $\eta = -\ln[\tan(\theta/2)]$ is defined in terms of the polar angle, θ. This is a good approximation to the true rapidity in the relativistic limit. A highly relativistic particle's 3-momentum vector is often described in terms of the three parameters: transverse momentum (p_T), pseudorapidity (η), and azimuth (ϕ).

In an ideal uniform field, the trajector of a charged particle is described by a helix with five parameters. Three of these describe the velocity vector at the point of closest approach of the helix to the primary vertex. The two additions are the impact parameters: d_0 and z_0, which are the transverse and longitudinal coordinates of that point.

Some particles, such as neutrinos, have a vanishingly small probability of interacting with the detector[b]. The presence of such 'invisible' particles can be inferred from an apparent non-conservation of momentum of the observed particles. To achieve this, the experiment must completely surround the interaction point, so that particles cannot be lost. Electrical, optical and cryogenic services for central subdetectors of the experiment are therefore routed through the outer layers so that they do not create gaps. Two unavoidable gaps are created by the beam-pipes so final state particles in these directions inevitably go undetected. This is one of the reasons for restricting our interest to the missing *transverse* momentum ($\not{p}_T$).

The $\not{p}_T$ signature is important for many physics studies, not least in detecting (R-

---

[b] For example for a muon neutrino the charged current interaction probablility is of the order of 10^{-12} per GeV

Subdetector	Active material	particle	property	B-field	comments
Pixel	depleted silicon	charged	P	CS	3D
SCT	depleted silicon	charged	P	CS	3D (stereo-angle)
TRT	$Xe/CF_4/CO_2$	charged	P	CS	electron ID
LAr ECAL	liquid argon	all	E	-	e,γ ID
LAr HCAL	liquid argon	hadrons	E	-	
Tile HCAL	scintillator	hadrons	E	CS†	
FCAL	liquid argon	all	E	T	
MDT	Ar/CO_2	μ	P	T	
CSC	$Ar/CO_2/CF_4$	μ	P	T	
RPC	$C_2H_2F_4$/iso-C_4H_{10}	μ	P	T	3D
TGC	CO_2/n-C_5H_{12}	μ	P	T	3D

Table 2.2: Summary of the ATLAS sub-detctors. Magnetic fields: CS=central solenoid, T=toroid, †=return flux. Properties: E=energy, P=position (and hence momentum).

parity conserving) supersymmetry, such as in chapter 3 of this thesis.

2.4 Inner detector

The purpose of the ATLAS inner detector (ID) is to reconstruct charged particle tracks and verticies, to measure the momentum and charge sign of the particles, and to contribute to their identification. It should make many precicise measurements of the positions of these particles along their tracks. In order to easily reconstruct tracks from these points, the individual active elements must detect particles with high efficiency, yet with a minimal probability of registering in error. In addition, they must have high granularity with a low average occupancy, so that a particular hit pattern can be efficiently reconstructed into tracks. This is particularly impor-

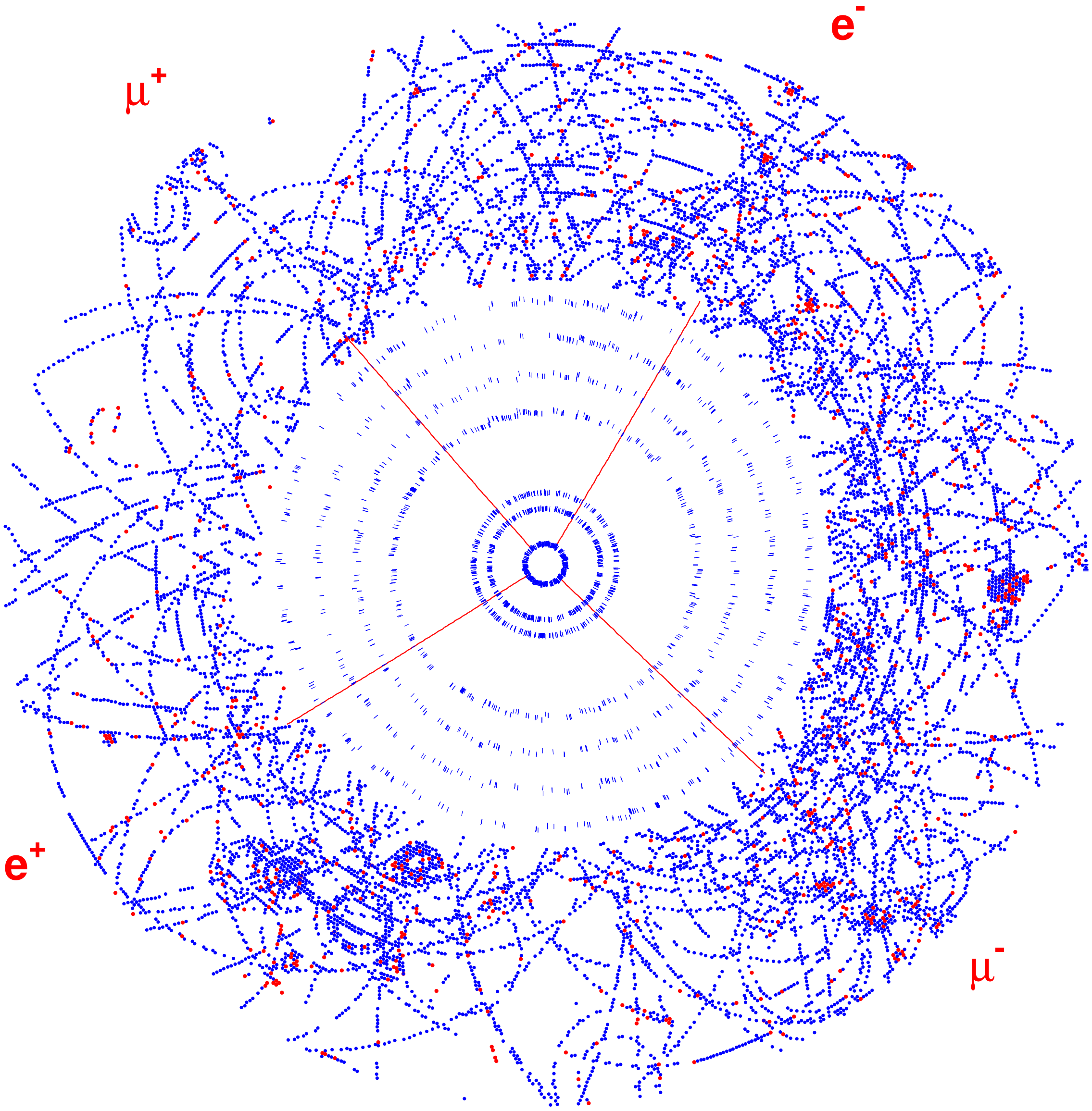

Figure 2.3: Simulated event for the process $h \to ZZ \to \mu^+\mu^-e^+e^-$, showing the large number of tracks in the inner detector. The blue points mark recorded hits in the barrel part of the ID. (This plot is taken from [35], and is based on the layout desribed therein. Modifications since the publication of [35] are referred to in the text.)

tant given the large number of tracks which will be produced in the interactions at the LHC (see fig. 2.3).

The number of precision layers is a compromise between the competing demands of precise track-finding and accurate energy measurement. Each additional layer increases the material between the interaction point and the calorimeter, and so degrades the calorimeter performance. An additional constraint is that the components must be able to tolerate and operate in the high-radiation environment.

The entire tracker is contained within a 2 Tesla solenoidal magnet. Since the B field is directed along the beam-axis, the paths of charged particles will be bent according to the component of their momentum in the transverse direction. The magnet is 2.5 m in diameter, 5.3 m long, and only 45 mm thick, to avoid introducing excess material in front of the calorimeters. Further saving is obtained by the central solenoid and the central electromagnetic calorimeter sharing a common cryostat.

Only a short summary of the ID components can be given in this thesis; for more detailed information the reader is referred to the ATLAS Technical Design Reports for the inner detector [35], the pixel detector [36], and the overall detector and physics performance [30]. Minor changes to the design since the publication of those documents are detailed in various Final Design Reports, with most of the developments summarised in [37].

The ATLAS ID or “tracker” consists of three different elements, as shown in fig. 2.4. These are, from the innermost layer out:

- the pixel detector – high granularity silicon detectors nearest the interaction point;
- the semiconductor tracker (SCT) – precision silicon microstrip detectors;
- and the transition radiation tracker (TRT) – a straw tube tracker with electron identification capability.

Each of these sub-detectors consist of a central cylindrical ‘barrel’ section with two ‘endcaps’ at larger values of $|z|$.

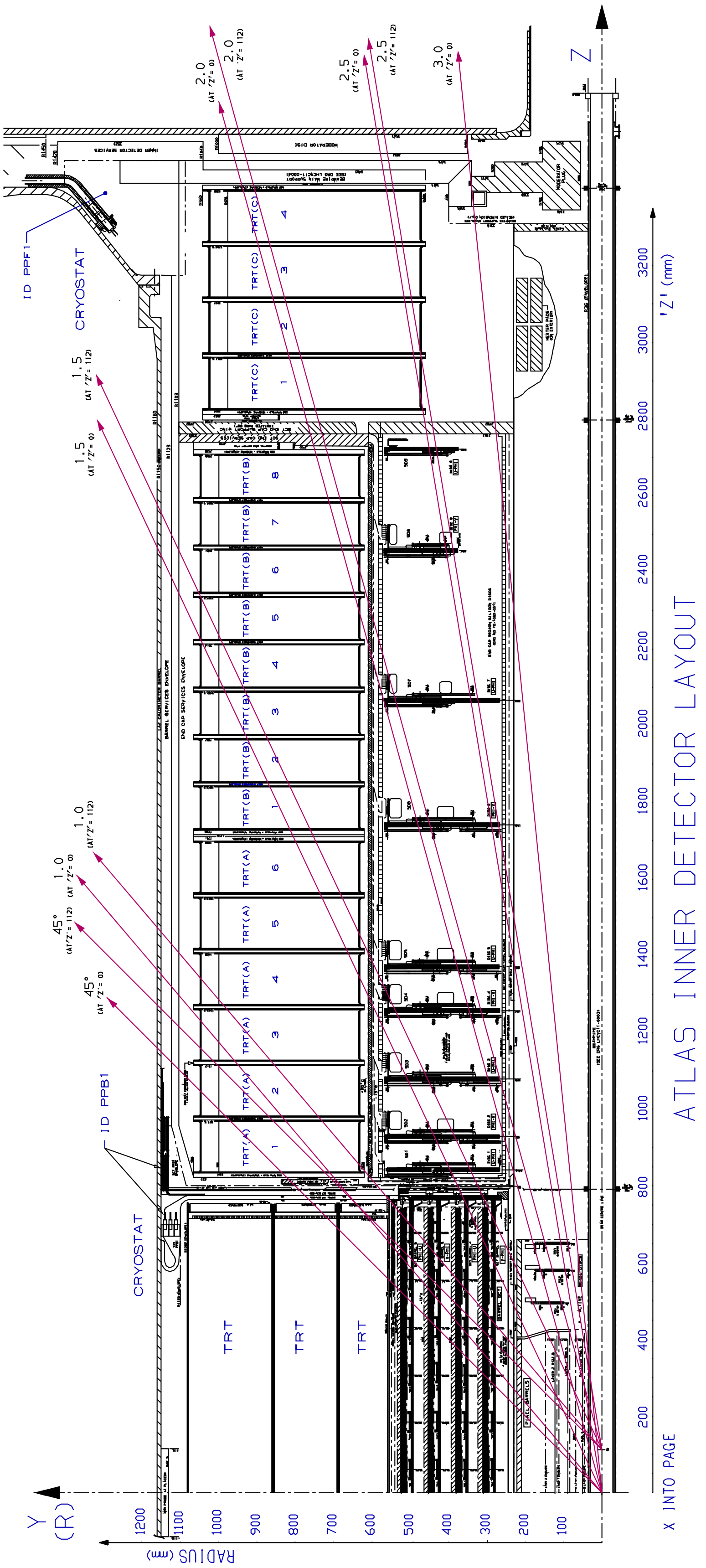

Figure 2.4: Section through one quadrant of the Atlas inner detector. Adapted from [34].

2.4.1 Pixel detector

The main purpose of the pixel layers is to provide precise measurements of charged-particle tracks close to the interaction point. By measuring impact parameters, particles which were produced at secondary vertices can be identified as the daughters of weakly-decaying particles such as b-quarks and τ-leptons.

The barrel has three cylindrical layers, the innermost of which is at an average radius of 43 mm. Each end-cap consists of five discs, which give good spatial resolution out to $|\eta| = 2.5$. Both the disc and barrel regions are instrumented with modular units of size 62.4×21.4mm, with the long side of the module directed parallel to the beam in the barrel and radially in the disks. Barrel modules are tilted in the $R\phi$ plane to reduce the charge spread arising from the Lorentz angle, and to allow overlap.

The pixel detector lies closest to the interaction point where particle tracks are most dense. To achieve the low occupancy required for pattern recognition it must therefore have very a high density of active elements. The sensitive part of the module is a reverse-biased silicon wafer segmented into 46,080 pixels, each 50×400 μm, with finer pitch in $R\phi$ providing a more accurate measurement of the sagitta which is used in the calculation of the particle's momentum. The two dimensional array of diodes is bump-bonded to sixteen flipped front-end readout chips, where the electrical signal is amplified and compared to a threshold to give a binary output.

2.4.2 Semiconductor tracker

Like the pixel layers, the SCT measures particle positions by detecting the electrical charge liberated by a charged particle passing through a reverse-biased silicon diode. While the underlying technology is the same as for the pixel detector, the design is rather different. The decreased track density at larger radii favours silicon microstrip detectors which have fewer read-out channels and less material than pixel detectors, but which can nevertheless provide precise measurements.

There are four barrel layers in the central region, while the end-caps are formed from rings of wedge-shaped modules. In both cases, each module employs four silicon wafers bonded back-to-back in pairs. The $R\phi$ component is accurately measured from the hit strip(s), while the second position coordinate is determined from a 40 mrad stereo angle between the front and back planes.

A study of the performance of SCT modules in beam tests forms a part of this thesis, so more information about this sub-detector can be found in chapter 5.

2.4.3 Transition radiation tracker

The TRT is a drift tube system and forms the bulk of the volume of the ATLAS ID. Its purpose is two-fold – firstly to make a large number of measurements of charged particle position, and secondly to assist in the identification of these particles.

The pseudorapidity coverage of the TRT is $|\eta| < 2.5$, with the barrel region covering $|\eta| < 0.7$. It consists of several hundred thousand “straws”, each of which is a 4 mm diameter cylindrical tube. The inner surface of the straw is covered in aluminium, and acts as a high-voltage cathode. In the middle of the straw is an anode wire made of gold-plated tungsten from which the signal is read out. The straws are filled with a $\mathrm{Xe/CF_4/CO_2}$ gas mixture.

The TRT is read-out by double-threshold binary electronics. The low threshold ($\approx$ 200 eV) setting will detect the charge liberated by the passage of a minimally ionising particle. Averaged over the full pseudorapidity range, 36 low energy hits will be generated per track. This large number of points facilitates track-finding, and provides improved momentum resolution.

A higher threshold level at about 5 keV is designed to detect the transition radiation (TR) photons which give the detector its name. These are soft X-rays produced when ultra-relativistic charged particles cross a boundary between materials with different dielectric constants. The probability of emitting a TR photon at any particular boundary is small so the surrounding materials (polypropylene foils or fibres) are designed to contain many such transitions.

The TR energy radiated increases rapidly with the relativistic γ factor, so particles with $\gamma \gtrsim 1000$ will produce high-threshold hits with reasonable efficiency. For a track of known transverse momentum, γ provides a measure of m, the particle's mass. For an electron identification efficiency of 90%, the resultant pion contamination is expected to be less than 10^{-2}.

2.5 Calorimetry

The basic objective of the calorimetry system is to measure the energy of electrons, photons and jets. Another design requirement is the ability to separate different types of particle based on the shape and structure of the shower.

High energy electrons and photons incident upon matter initiate particle cascades from pair production ($\gamma \rightarrow e^+e^-$) and bremsstrahlung ($e \rightarrow e\gamma$) in the nuclear electric field. Such showers are characterised longitudinally by the radiation length (X_0) and by narrow transverse profiles.

Particle cascades are also produced when high energy hadrons interact with dense material, where multiplication occurs through a succession of inelastic hadron-nuclear interactions. Such showers involve a greater degree of lateral spread than

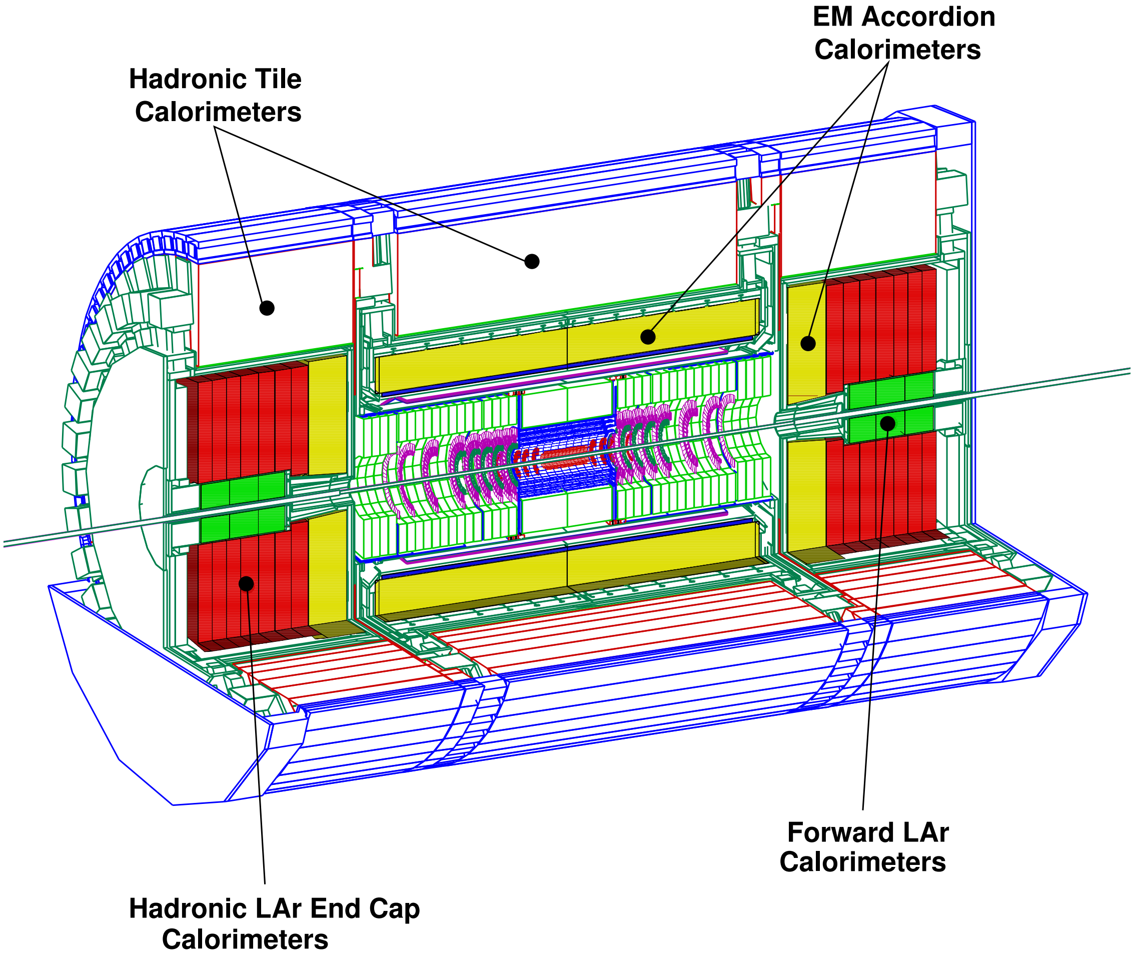

Figure 2.5: Three-dimensional representation of the ATLAS calorimeters. Adapted from [38].

in the purely electromagnetic (EM) case, though they will contain a variable EM component.

Since the nuclear interaction length is about an order of magnitude greater than X_0 (depending on the material), ATLAS like most general-purpose experiments has two different calorimetry systems.

2.5.1 Electromagnetic calorimetry

The electromagnetic calorimeter (ECAL) is a high granularity lead/liquid argon (LAr) sampling calorimeter with accordion geometry [39]. In the barrel region the segmentation is $\Delta\eta\times\Delta\phi = 0.025\times0.025$ (0.003×0.1, 0.05×0.025) in the first (second, third) sampling. The zig-zag shape of the absorbers and electrodes allows continuous azimuthal coverage with minimal density variations. The radiation thickness up to the end of the EM calorimeter is at least $24X_0$ in the barrel and $26X_0$ in the end-caps with an overlap in rapidity through the transition.

Since there are about two radiation lengths (including the solenoid and cryostat) of material in front of the main calorimeter a pre-sampler corrects for upstream energy losses over $|\eta| < 1.8$. The transverse energy profile of the preshower and the first sampling provide good π^0/γ separation. Electrons are identified from both shower shape and inner detector information. The high granularity ECAL and multiple samples can be used to reconstruct the direction in which a shower is pointing, and so one can identify photons which have originated from secondary decays.

Simulations [38] and testbeam data [40] suggest that the EM calorimetry performance will be dominated by sampling fluctuations giving $\sigma_E/E \approx 10\%/\sqrt{(E/\mathrm{GeV})}$. The overall resolution, including contributions from the sampling term, constant term, electronic noise and pile-up when running at high luminosity is expected to be about 1.4% for 50 GeV E_T photons. The ECAL information is expected to provide a rejection of $\sim 10^3$ against jets for an electron efficiency of 90%.

2.5.2 Hadronic calorimetry

In the barrel and 'extended barrel' regions the hadronic calorimeter (HCAL) absorber consists of steel plates which are sampled by plastic scintillator tiles [41].

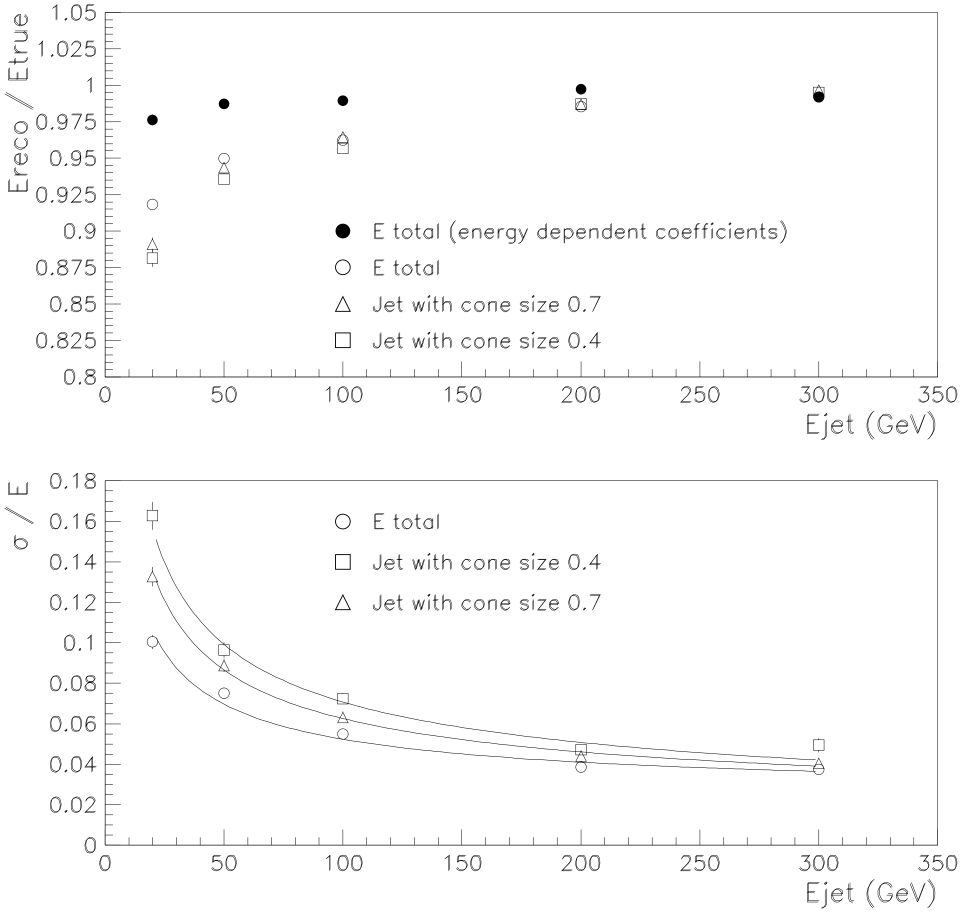

Figure 2.6: Simulated combined calorimeter linearity and resolution for jets at $\eta = 0.6$. The fitted lines are $\sigma_E/E = a/\sqrt{E/\mathrm{GeV}} \oplus b$ where the numerical fit values the statistical term, a, and the constant term b are given in table 2.3 The solid circles were obtained by fitting for the reconstruction efficiency coefficients separately at each energy. From [38].

	a	b
pions	43%	3.6%
jets (total energy)	46%	2%
jet cone size 0.7	60%	2%
jet cone size 0.4	70%	1%

Table 2.3: Jet energy resolution fit parameters for fig. 2.6. a is the statistical term, while b is the constant term.

These are placed perpendicular to the beams, and are grouped into cells at approximately constant η by combining the signal from different wavelength-shifting fibers into a single photomultiplier. The structural material and iron absorber together form the return yoke for the central solenoid.

In the endcap, where radiation damage would severely degrade the scintillator, a parallel-plate copper/LAr hadronic sampling calorimeter provides equivalent energy resolution over $1.5 < |\eta| < 3.2$.

Motivated by missing transverse momentum ($\not{p}_T$) and forward jet detection, a dense Cu/W liquid argon forward calorimeter (FCAL) measures both hadronic and electromagnetic activity at very high-rapidity ($3.2 < |\eta| < 4.9$).

The overall missing energy resolution is estimated from simulations to be $\sigma/\not{p}_T \approx 0.48/\sqrt{\Sigma E_T/\mathrm{GeV}}$ where the sum is over the transverse energy in all of the calorimeters.

2.6 Muon spectrometer

With no strong interactions and a relatively large mass, muons lose energy primarily by ionisation. They can therefore pass through the calorimeters to dedicated detectors which can identify the particle and measure its momentum. The latter becomes especially important at higher energies ($\gtrsim$ 100 GeV) where the relatively small size of the inner detector limits its accuracy in making momentum measurements.

The magnetic field in the muon detectors is provided by superconducting air core toriods. For good track momentum resolution, a large magnetic field is desirable over long distances, so the overall scale of the magnet system is grand – 20 m in diameter and 26 m long, and the average magnetic field strength is 0.6 T. The

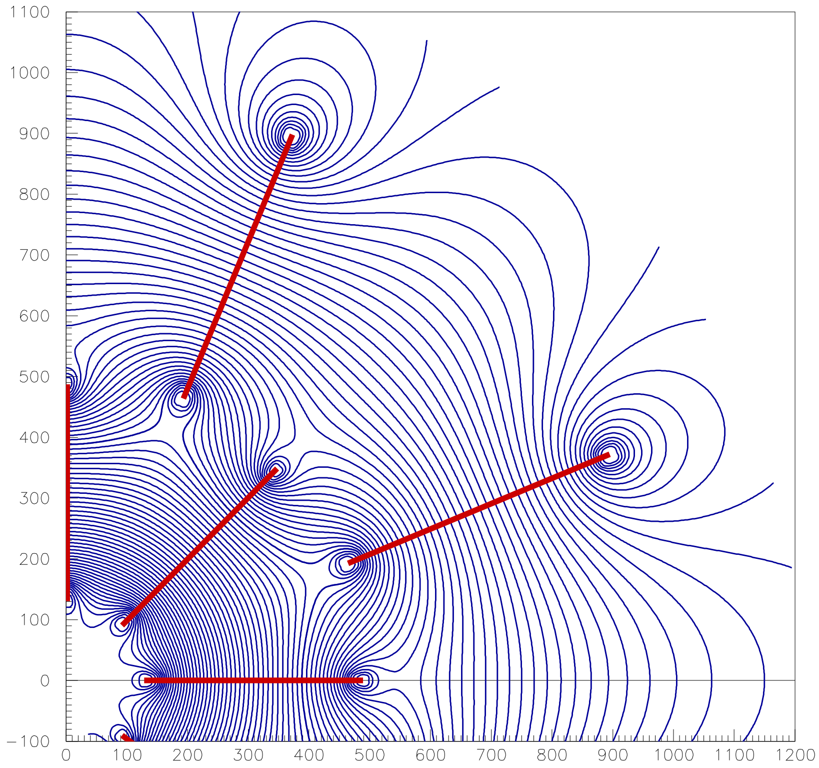

Figure 2.7: Magnetic field map in the barrel–end-cap transition region. Field lines are shown in the R–ϕ plane in the middle of an end-cap toroid. The scales are in centimeters. Adapted from [42].

toroidal geometry keeps the magnetic field direction largely perpendicular to the muon trajectory.

Both the large barrel and smaller end-cap toroids consist of eight flat coils (fig. 2.7) wound in series with flat superconducting NbTi/Cu cable. A liquid helium cryogenic system maintains the coils at the operating temperature of 4.5 K. The quench protection system has both electrical resistors and thermal heaters which can initiate the internal dump of stored energy in all of the coils.

The distribution of the muon precision and trigger chambers is shown in fig. 2.8.

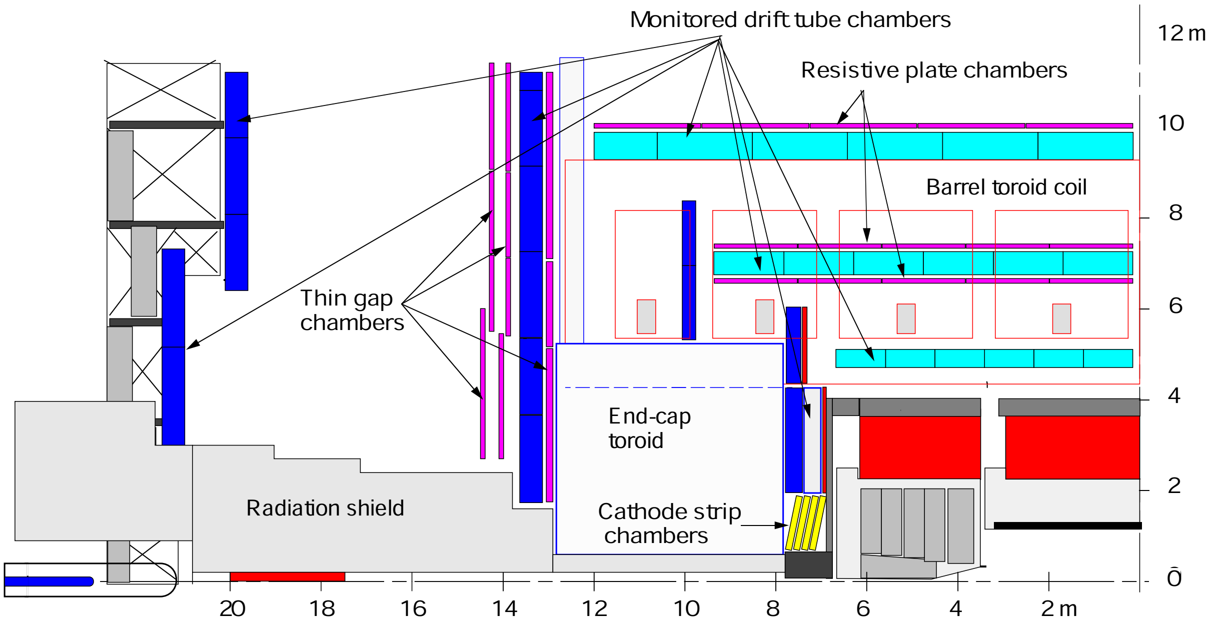

Figure 2.8: Side view of one quadrant of the muon spectrometer, indicating where the different chamber technologies are used. The thin gap and resistive plate chambers are fast trigger chambers, while monitored drift tubes and cathode strip chambers provide the precision sagitta measurements. Adapted from [42].

2.6.1 Precision chambers

The precision measurement in the bending direction will be made by drift-tube chambers. As part of the effort to reduce the uncertainty in the track position, an internal optical survey system will continually monitor any deformations in each chamber to within a few microns.

The highest rates are expected in the innermost forward regions ($2.0 \leq |\eta| \leq 2.7$) where multiwire proportional chambers with cathode-strip readout provide a precision measurement with a smaller occupation time.

Three measurements of position and direction are expected over all η with a reduced acceptance where structural elements and cracks limit coverage. The spectrometer resolution for muons with energies around 20 GeV, a typical energy scale for Higgs boson decays, is expected to be approximately $\Delta p_T/p_T$ of 2%. High energy muons, important in many searches for new physics, will be measured with average $\Delta p_T/p_T$ of approximately 10% at 1 TeV.

2.6.2 Trigger chambers

Dedicated muon detectors with a fast response time (less than two microseconds) will give a rough measurement of p_T which can be used to initiate the read-out of the other sub-detectors. These trigger chambers have two-dimensional segmentation to facilitate pattern recognition and to identify which of the precision hits are related to a particular muon track. The second coordinate is measured with sufficient accuracy to allow corrections for magnetic field inhomegeneities to be applied.

Triggering is be achieved over $0 \leq |\eta| \leq 2.4$ for muons with energy greater than about 6 GeV, with a time resolution of approximately four nanoseconds – comfortably sufficient to identify a single bunch crossing.

2.7 Trigger

In total the ATLAS detector has more than 10^8 electronics channels. Even after zero-suppression the raw event data size is expected to be of the order of 1 Mbyte. If all events were read out (at 40 MHz) this would amount to an output 40 terabytes of data per second, the storage of which would be grossly unachievable[c].

As can be seen in fig. 2.9, the cross-section for producing high p_T physics at the LHC is many orders of magnitude below the total cross-section, so it is clear that

---

[c] The price for a terabyte of disk in 2007 has been estimated by IBM to be about one thousand US dollars. At that rate the cost of disks for storing the first month's data in full would be $2600M (more than the cost of the LHC machine.)

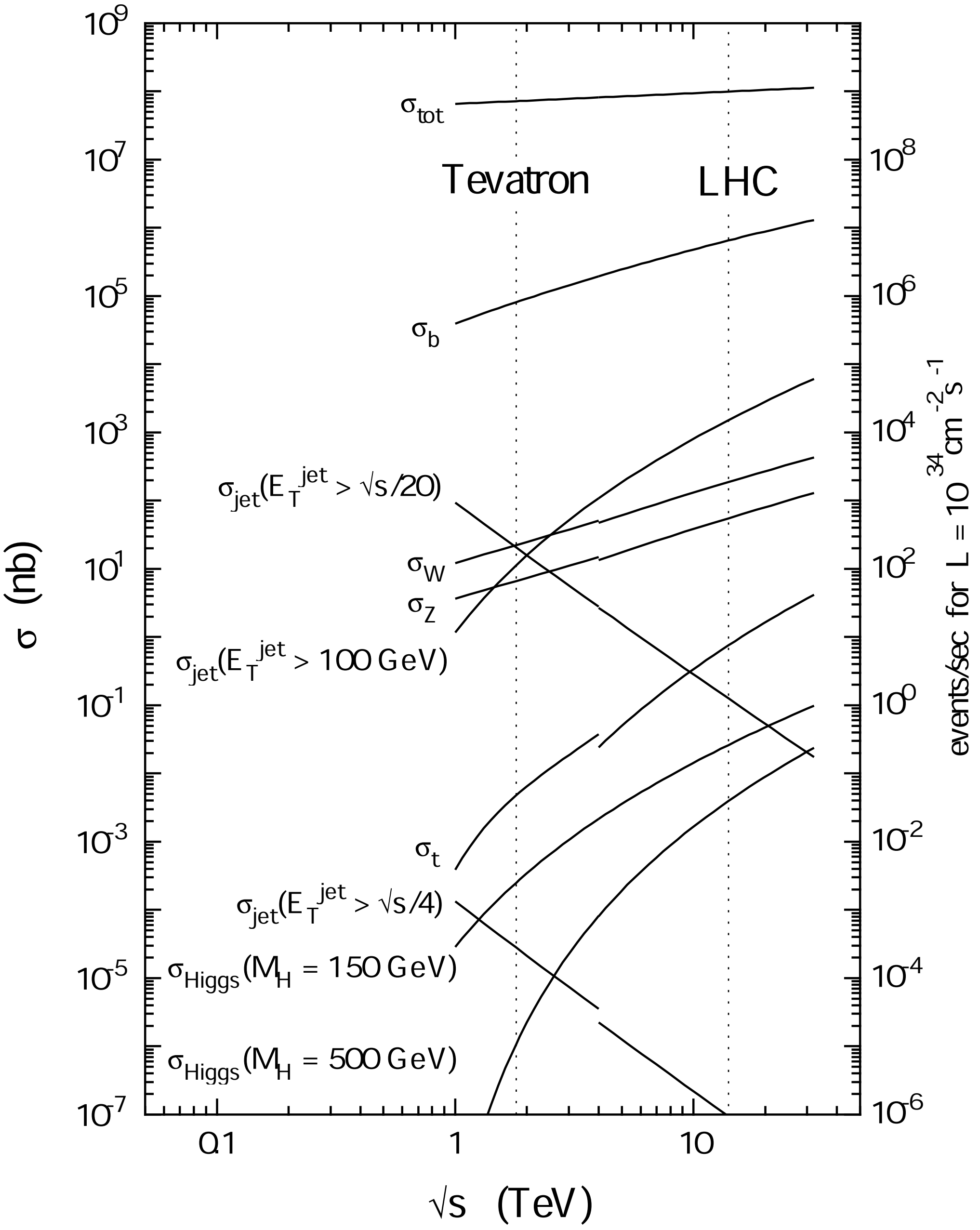

Figure 2.9: Energy dependence of some proton–(anti)proton cross-sections at the LHC and at the Tevatron. The discontinuity at $\sqrt{s}$ = 4 TeV is caused by the transition from $p\bar{p}$ to pp. From [43] after [44].

trigger	accept rate	latency	memory
level 1	75 kHz	$\approx 2.5\mu$s	front-end pipeline
level 2	1 kHz	10 ms	on-crate buffer
event filter	100 Hz	$\mathcal{O}(1\text{ s})$	processor farm

Table 2.4: An overview of the ATLAS trigger system. The final column indicates the physical location of the event temporary storage at each stage.

efficient event selection will be extremely important. An overall rejection factor of nearly 10^7 is required while at the same time maintaining good efficiency for rare new physics.

The ATLAS trigger system is based on three levels of selection (table 2.4). Each subsequent level faces a lower event rate, and so can afford a higher level of sophistication per event. The first level trigger makes a decision based on reduced-granularity calorimeter and muon detector information. Examples of objects which can initiate a first level acceptance are high p_T muons, isolated EM clusters, jets, and missing p_T.

The second level has access to full precision and granularity data, but will concentrate on those regions of interest already selected by level 1. The ID tracking data is considered for the first time at level 2, allowing selection of events with low energy electrons and heavy quark candidates.

At the third and final level the event is fully reconstructed and a decision made as to whether to reject it or pass it to the permanent storage system for later analysis.

2.8 Comment

An enormous investment has been made in the LHC project, both in terms of the decades of research and development and the financial cost of manufacturing the accelerator and the detectors. It is therefore vital that the best possible use is made of the machine. It would be a disappointment to particle physicists if the LHC provided only confirmation of the SM Higgs boson, but no evidence for physics beyond the standard model, but it would be a tragedy if it was later found that the machine was *capable* of making exciting discoveries of new physics, but that the evidence lay undiscovered.

If TeV-scale supersymmetry is accessible then we must ensure that we find it. In part II of this thesis, I present investigations into two supersymmetry scenarios, both of which present severe experimental challenges. In both cases I show that even if nature has chosen one of these ‘difficult’ cases, careful analysis can reveal a great deal about the new particles – rewarding us with fresh insights into the underlying structure of matter and force.

Part II

Simulations of supersymmetry models at ATLAS

Chapter 3

Discovering anomaly-mediated supersymmetry at the LHC

> *How shall I relate To human sense*
> *The secrets of another world?*

The archetypal supersymmetry (SUSY) signature involves leptons or jets which have obtained large transverse momenta from cascade decays, in association with missing transverse momentum from the undetected lightest supersymmetric particle (LSP).

Recently a model was proposed in which the LSP composition is dominated by the neutral wino. Since the mass splitting between the charged and the neutral winos is small, this means that the next-to-lightest supersymmetric particle (NLSP) is only slightly heavier than the $\tilde{\chi}_1^0$, and dominantly decays to the invisible $\tilde{\chi}_1^0$ together with one or more low-momentum charged particles, such as π^+ or $e^+\ \nu_e$.

Thus the 'smoking gun' signature for this type of model is large missing transverse energy along with *soft* tracks from $\tilde{\chi}_1^+$ decay. This chapter investigates the discovery potential of such models, in particular the observability of these soft particles.

In this chapter the AMSB discovery potential of the LHC is investigated for general-purpose detectors from several points of view. I concentrate on the ATLAS detector but similar considerations will also apply to CMS. The anomaly-mediated model is introduced in sec. 3.1. In the next section the properties of the recently proposed benchmark points for minimal anomaly mediation are reviewed. The potential reach of generic SUSY search techniques in detecting minimal anomaly mediated supersymmetry is investigated in sec. 3.3. While the generic search reach is dependent on the mAMSB spectrum, the same is not true for the classic anomaly-mediated signature – the wino-like LSP – which will apply beyond the minimal model. The signatures for identifying wino-like LSPs at the LHC are explored in sec. 3.4. Finally in sec. 3.5 constraints on mAMSB from measurements of the cosmological relic density, the muon anomalous magnetic moment, and the branching ratio $B \to X_s\gamma$ are examimed.

3.1 Anomaly mediated supersymmetry

A mechanism of supersymmetry breaking known as anomaly-mediation (AMSB) was proposed in [45, 46] in which a conformal (re-scaling) anomaly in the auxiliary field of the supergravity multiplet transmits SUSY-breaking to the observable sector. There is always an anomaly-mediated contribution to the gaugino masses in any hidden-sector model, but where no other direct contribution is present, AMSB will be the leading effect.

Anomaly mediation provides a potential solution to the SUSY flavour problem, in a highly predictive model. One undesirable feature of pure anomaly-mediation is that the slepton has a negative mass-squared. There are various ways to solve this problem [45, 47–58], the simplest of which is the addition of a universal scalar mass at the GUT scale. The unmeasured parameters of the minimal model (mAMSB) are then $m_{3/2}$ – the gravitino mass; m_0 – the universal scalar mass; $\tan\beta$ – the ratio of the vacuum expectation value of the Higgs fields; and the sign of the μ parameter multiplying $H_u H_d$ in the superpotential, the magnitude of which is fixed from the condition of correct electroweak symmetry breaking.

The sparticle spectra for mAMSB have been calculated in [59–62]. With pure anomaly-mediation, (*i.e.* $m_0 = 0$) the gaugino masses are proportional to their beta functions:

$$M_i = \frac{\beta_{g_i}}{2g_i^2} m_{3/2} \tag{3.1}$$

where g_i are the gauge coupling constants with $i = 1, 2, 3$ indicating the gauge group, β_{g_i} are their corresponding renormalisation group beta functions,

$$\beta_{g_i} = \frac{d(g_i)^2}{d(\ln \mu)} , \tag{3.2}$$

and $m_{3/2}$ is the gravitino mass. AMSB therefore predicts that the gaugino masses are in the approximate ratios $M_1 : M_2 : M_3 \approx 3 : 1 : 7$ so that the wino (rather than the more conventional bino) is the lightest supersymmetric particle (LSP), and the gluino is nearly an order of magnitude heavier than the LSP.

The prediction in AMSB of a wino-like LSP has interesting phenomenological consequences. The most striking of these is that the lightest chargino is nearly mass-degenerate with the lightest neutralino. Near-degenerate particles are not unusual in SUSY phenomenology, but with AMSB one of these particles is the LSP. Since R-parity is assumed to be conserved (unlike *e.g.* [63,64]) the $\tilde{\chi}_1^+$ may only decay into the $\tilde{\chi}_1^0$ so the small mass difference,

$$\Delta M_{\tilde{\chi}_1} \equiv m(\tilde{\chi}_1^+) - m(\tilde{\chi}_1^0) , \tag{3.3}$$

means that the lightest chargino may have a lifetime long enough to be detected at collider experiments.

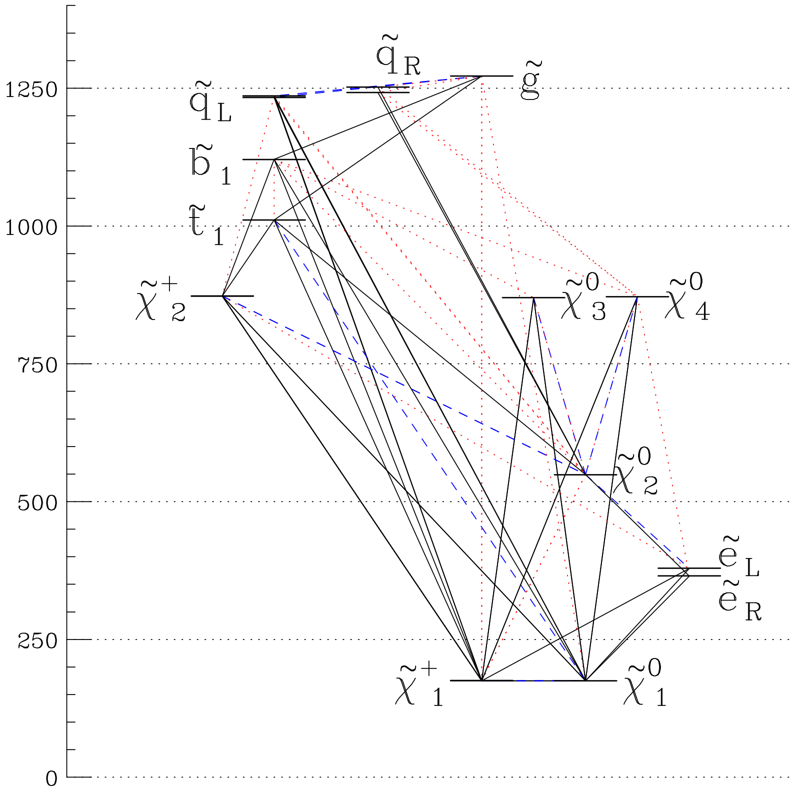

Figure 3.1: Part of the sparticle spectrum at the Snowmass point **SPS 9** which has $m_0 = 450$ GeV, $m_{3/2} = 60$ TeV and $\tan\beta = 10$, $\mu > 0$. Solid black lines indicate branching ratios (BRs) greater than 10%, dashed blue lines show BRs in the range 1% → 10%, while red dotted lines show BRs in the range 0.1 → 1%. The sparticles are displaced horizontally for clarity.

3.2 Benchmark points

A set of benchmark points and 'slopes' or model lines was suggested for study at Snowmass [65]. Of the eleven points, only one (**SPS 9**) applies to mAMSB. That point has the parameters: $m_0 = 450$ GeV, $m_{3/2} = 60$ TeV, $\tan\beta = 10$, with $\mu > 0$, and lies on the model line "slope" $m_0 = 0.0075 \times m_{3/2}$, where $m_{3/2}$ can vary. Part of the sparticle spectrum for **SPS 9** is shown in fig. 3.1. The lightest sparticles — the $\tilde{\chi}^+_1$ and $\tilde{\chi}^0_1$ — have masses about 170 GeV while squark and gluino masses are about 1.25 TeV, so one would expect copious sparticle production at the LHC.

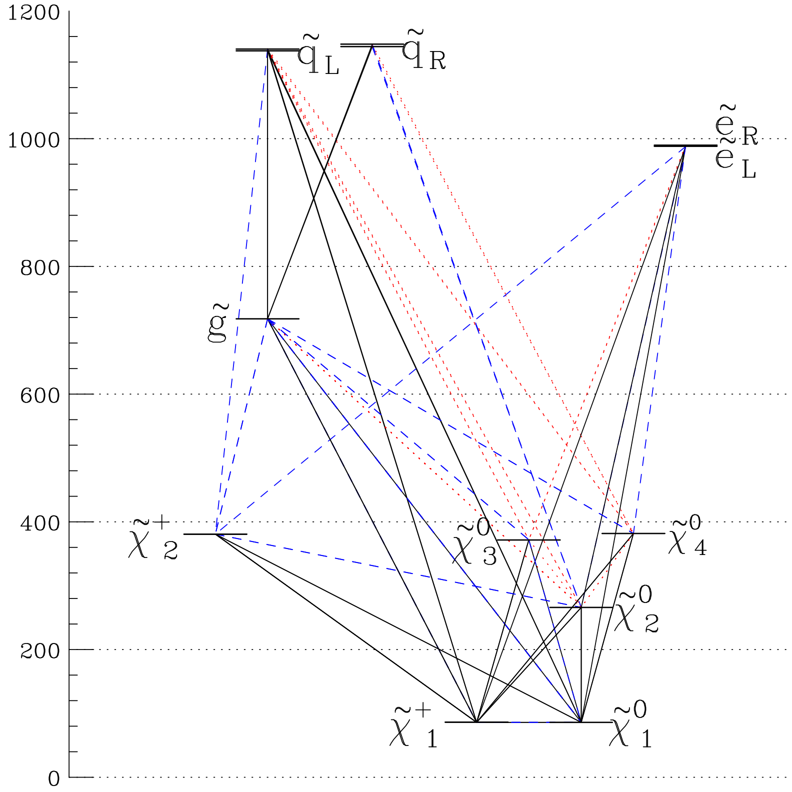

Figure 3.2: Part of the sparticle spectrum at the Point d'Aix: $m_0 =$ 1000 GeV, $m_{3/2} = 30$ TeV, $\tan\beta = 30$, $\mu > 0$. Branching ratios as for fig. 3.1. The sparticles are displaced horizontally for clarity.

The wino-like character of the lightest chargino and neutralino increases the relative cross-section to non-coloured sparticles as compared to *e.g.* minimal supergravity (mSUGRA) models. Indeed the `HERWIG-6.3` [66–68] Monte-Carlo event generator gives the inclusive SUSY cross-section as 3.9 pb, of which only about 0.5 pb is to squarks and gluinos. The chain $\tilde{q} \to \tilde{\chi}^0_2 \to \tilde{l} \to \tilde{\chi}^0_1$ is available[a], and has a large branching ratio, so good information about the squark, slepton, and at least two neutralino masses could be extracted from kinematic edges in the ll, lq and llq invariant-mass distributions [30, 69, 70].

The $\tilde{e}_R$ and $\tilde{e}_L$ masses are approximately equal (fig. 3.1) because in mAMSB the

---

[a] Note that in this chapter SM particles are omitted from decays when this can be done without ambiguity.

slepton masses are principally determined by m_0. A more detailed analysis would be required to determine if the $\tilde{e}_R$ and $\tilde{e}_L$ masses could be separately measured from two nearby edges in the ll invariant mass distribution, as was noted in [70] for a similar point. The decay of the right-sleptons to the wino-like LSP is suppressed, but not sufficiently to produce a measurable displaced vertex from slepton decay ($\tau \sim 10^{-16}$ s). In fact even if the bino-like component of the LSP becomes *extremely* small, the decay $\tilde{e}_R \to \tilde{\tau}_1 \to \tilde{\chi}_1^0$ will remain unsupressed. This is particularly true at high $\tan\beta$ since the mixing between the left- and right-handed staus increases with the tau Yukawa coupling.

Because the gluino has a similar mass to the heavier squarks at **SPS 9** it decays primarily to $\tilde{t}_1$ and $\tilde{b}_1$, meaning that gluino production will lead to large numbers of b-quarks. This is not a general (or unique) feature of mAMSB, and while vertex tagging of jets could help distinguish this particular point from the SM it is not used in this analysis.

Another set of benchmarks, the 'Points d'Aix' [71] chooses the mAMSB point $m_0 =$ 1000 GeV, $m_{3/2} = 30$ TeV also with $\mu > 0$, and with the higher value $\tan\beta$ =30. With a $\tilde{\chi}_1^+$ mass of 85 GeV, this point violates the limits from the LEP search [72] for $e^+e^- \to \tilde{\chi}_1^+\tilde{\chi}_1^-\gamma$, which places a lower limit on the $\tilde{\chi}_1^+$ mass of about 92 GeV for almost all values of the mass difference $\Delta M_{\tilde{\chi}_1}$.

The mAMSB Point d'Aix, despite being ruled out, still has a number of features which are of qualitative interest (fig. 3.2). The light gluino means that the decays $\tilde{g} \to \tilde{t}t$ and $\tilde{b}b$ are no longer kinematically allowed. This means that the major source of b quarks is from $\tilde{\chi}_{2,3,4}^0 \to \tilde{\chi}_1^0 h$ followed by $h \to b\bar{b}$, so fewer heavy quarks are produced than for the Snowmass point. The heavy sleptons can no longer participate in the various chains $\tilde{q} \to \tilde{\chi}_x^0 \to \tilde{l} \to \tilde{\chi}_y^0$ so slepton mass measurements would be extremely difficult at a hadron collider. There will, however, be large

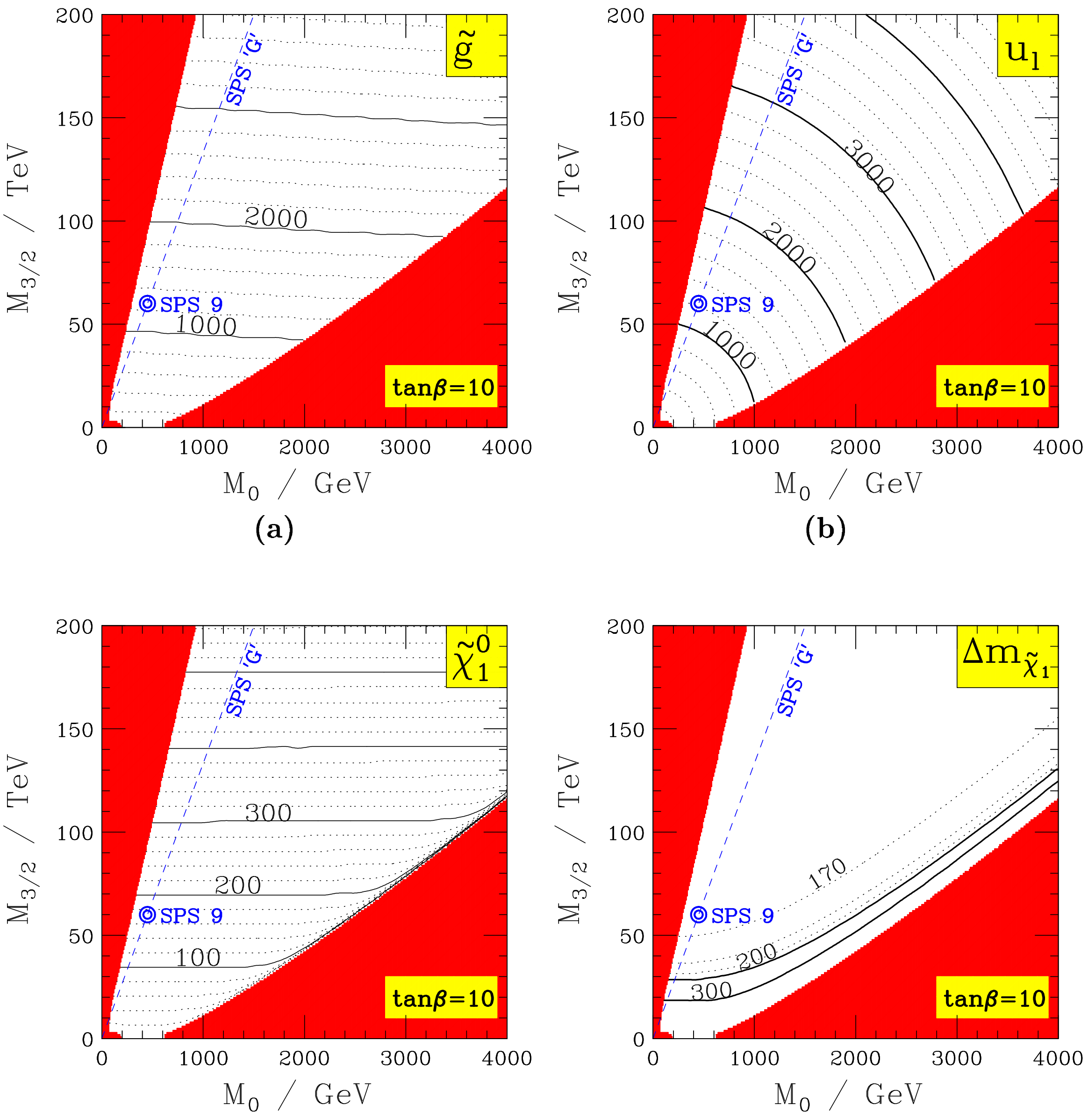

(a) **(b)** **(c)** **(d)**

Figure 3.3: The contours show the **(a)** gluino, **(b)** up left squark, and **(c)** lightest neutralino mass in GeV, and **(d)** the $\Delta m = \tilde{\chi}_1^+ - \tilde{\chi}_1^0$ mass difference in MeV as a function of m_0 and $m_{3/2}$. The other parameters are: $\tan\beta = 10$ and $\mu > 0$. The Snowmass point ($m_0 = 450$ GeV, $m_{3/2} = 60$ TeV) is marked as a pair of concentric circles, through which passes the Snowmass slope "model line G" (dashed line). The solid red regions are excluded because of lack of electroweak symmetry breaking (bottom right), charge- or colour-breaking minima, or non-$\tilde{\chi}_1^0$ LSP (left). Δm is greatest where μ is small, which occurs near to the region where electroweak symmetry is unbroken.

numbers of events in which $\tilde{\chi}_1^{\pm}$s are produced, either directly or from $\tilde{g} \rightarrow \tilde{\chi}_1^{\pm} q\bar{q}$, so a signature based on the near-degeneracy of the $\tilde{\chi}_1^{+}$ and $\tilde{\chi}_1^{0}$ is robust.

3.3 LHC reach for mAMSB

While some of the phenomenological features are particular to AMSB, one might expect to be able to distinguish AMSB from the SM using the same types of cuts – based on leptons, jets and missing transverse momentum – that are applied in mSUGRA analyses.

The sensitivity of the LHC to mAMSB has been demonstrated [70] for one point ($m_0 = 200$ GeV, $m_{3/2} = 35$ TeV, $\tan\beta = 3$, $\mu > 0$) with relatively light sparticles, where the sparticle spectrum was investigated in detail. In [73–75], the signatures for AMSB at a future linear e^+e^- or $e^-\gamma$ collider were investigated. In [76] the reach of the LHC was investigated using a simple generic detector simulation for 10 fb^{-1} of integrated luminosity. The production of charged and neutral winos via vector boson fusion was studied for AMSB in [77]. In that paper the LHC's reach was investigated for a signature consisting of two jets widely separated in pseudorapidity in association with missing transverse momentum.

In this section the aim is to determine the reach of the LHC with a realistic detector simulator, using optimised but generic SUSY cuts and for 100 fb^{-1} of integrated luminosity.

3.3.1 Event simulation

The mAMSB spectra were generated using `ISAJET-7.63` [81,82] on a grid 100 GeV × 5 TeV in the (m_0, $m_{3/2}$) plane. The mass difference, $\Delta M_{\tilde{\chi}_1}$ calculated by `ISAJET` was

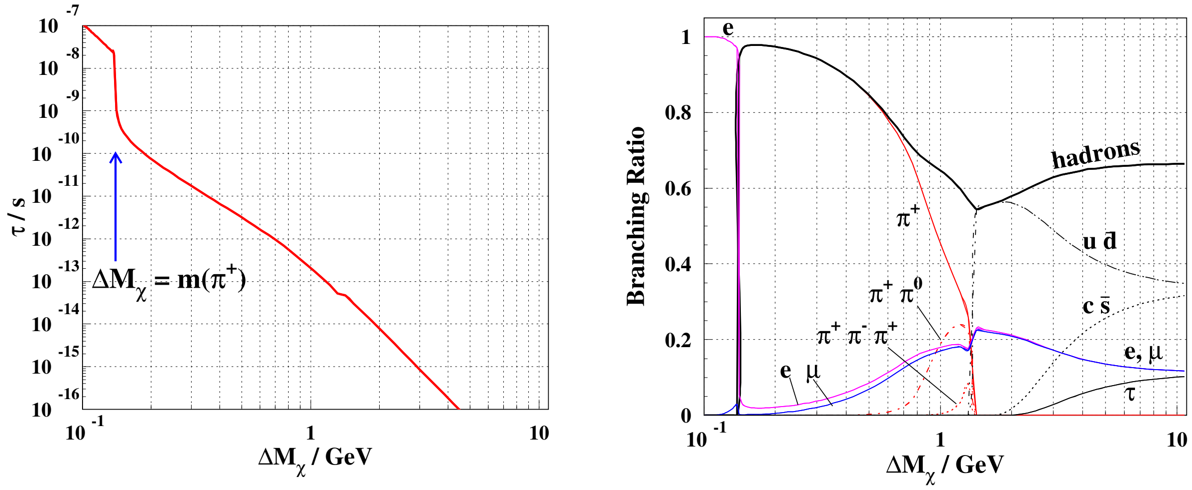

(a) **(b)**

Figure 3.4: The **(a)** lifetime and **(b)** branching ratios of the lightest chargino as a function of the mass difference $\Delta M_\chi = M(\tilde{\chi}_1^+) - M(\tilde{\chi}_1^0)$. The rapid decrease in the lifetime occurs at $\Delta M_\chi = m_{\pi^+}$ where the single pion mode becomes available. The discontinuity at $\Delta M_\chi = 1.4$ GeV comes from the switch in the calculation from hadronic to partonic decay widths. The leptonic channels implicitly include the corresponding neutrino. The branching ratio to $\pi^+\pi^0\pi^0$ was assumed to be equal to $\pi^+\pi^-\pi^+$. After [78–80].

used to recompute the $\tilde{\chi}_1^+$ lifetime and branching ratios using the results of [78,79]. In all cases the ratio of the Higgs vacuum expectation values ($\tan\beta$) was set equal to 10 and the sign of μ was positive. The mass of the top quark (important for electroweak symmetry breaking) was taken to be 175 GeV throughout. The dependence of some of the key sparticle masses on the input values of m_0 and $m_{3/2}$ is shown in fig. 3.3.

In the $\tilde{\chi}_1^\pm \to \tilde{\chi}_1^0$ decays, `ISAJET` does not include masses for the leptons, and does not contain multi-pion decay modes. Since the mass difference $\Delta M_{\tilde{\chi}_1}$ can be of the order of the mass of the muon, the lepton mass effects can be important in AMSB. To improve accuracy, the chargino decay modes calculated in [78, 79] were implemented with pion form factors from [80] and massive leptons. The resulting chargino lifetime and branching ratios are shown in fig. 3.4.

`HERWIG-6.3` was used to produce 200 fb^{-1} of unweighted inclusive supersymmetry events for each point (with a minimum of 5×10^4, and up to a maximum of 5×10^5 events).[b] This was then scaled to give the expected number of events for $\int \mathcal{L} =$ 100 fb^{-1}, which corresponds to the first year of 'high luminosity' (10^{34} cm^{-2}s^{-1}) running of the LHC. Background samples were generated with `HERWIG` for the production of $W^\pm$+jets, Z^0+jets, $t\bar{t}$, and QCD $2 \to 2$ (excluding $t\bar{t}$). For the $W^\pm$+jets sample, the cross-sections were multiplied by the factor:

$$1.6 \times \left[\frac{m_W^2 + (p_t^{\text{thr}})^2}{m_W^2} \right]^{2(N_{\text{jet}}-1)} , \tag{3.4}$$

where N_{jet} is the number of jets, and p_t^{thr} is the jet transverse energy threshold which was set to 10 GeV. This correction brings the `HERWIG` cross-section into better agreement with tree-level matrix element calculations [85]. A total of over 20 million background events were generated in logarithmic intervals in the `HERWIG` parameters `PTMIN` and `PTMAX` from 0 to 7000 GeV. The background cross-sections are shown before and after preselection cuts in fig. 3.5.

The events were passed through the ATLAS fast detector simulator, `ATLFAST-2.50` [86], which gives a parameterised detector response based on `GEANT3` Monte-Carlo simulations [87]. Jets were found using the `ATLFAST` cone algorithm with a cone size $\Delta R = 0.4$, and a minimum p_T of 10 GeV. The loss in resolution from pile-up was simulated. Calorimeter cells with E_T deposits below 1 GeV were not included in the $\not{p}_T$ calculation in order to more accurately model the expected resolution. Otherwise the default `ATLFAST` parameters were applied. The parameterised tracking simulation used is described in appendix C.

---

[b] No significant differences were found on comparing with `HERWIG-6.4` [83] which includes spin correlations as described in [84].

3.3.2 Optimisation of cuts

Cuts were applied to leptons (electrons and muons only), jets, and missing transverse momentum in a similar manner to those used in [30, 76, 88–90]. The variables to which cuts were applied were:

(1) $\not{p}_T$, missing transverse momentum;

(2) $p_{T(J1)}$, p_T of the hardest jet;

(3) $p_{T(J2)}$, p_T of the next-to-hardest jet;

(4) $\sum p_T$, scalar sum of the p_T of jets in the event;

(5) N_{jet}, number of jets in the event;

(6) S_{T}, transverse sphericity (circularity) of the event;

(7) $\Delta\phi_{(J1)}$, difference in azimuth between hardest jet and $\not{\mathbf{p}}_T$ vector;

(8) $p_{T(\ell 1)}$, p_T of hardest lepton (if any);

(9) $\Delta\phi_{(\ell 1)}$, difference in azimuth between hardest lepton (if any) and $\not{\mathbf{p}}_T$ vector;

(10) $M_T = \sqrt{2\, p_{T(\ell 1)}\, \not{E}_T\, (1 - \cos(\Delta\phi_{(\ell 1)}))}$, transverse mass of lepton and missing energy. Applied to single-lepton channel only to reduce SM leptonic $W^{\pm}$ background.

The preselection cuts which were applied to cut down the background, particularly at low p_T, are shown in the third column of table 3.1. The reduction in the background cross-section can be seen in fig. 3.5. Hard preselection cuts were not placed on isolated electrons or muons since it is foreseen that one jet with $p_T > 100$ GeV together with $\not{p}_T > 100$ GeV will be sufficient to provide the on-line trigger. Other trigger strategies which would improve the reach include:

- Allowing a hard ($\approx$ 20 GeV) isolated lepton as a trigger could improve the selection for points for relatively low m_0 in which the cascade decay $\tilde{q} \to \tilde{\chi}^0_x \to \tilde{l} \to \tilde{\chi}^0_y$ is available;
- Track vertex tagging which in ATLAS can be applied at the second trigger level could improve the selection for events containing heavy quarks;
- If all of the coloured sparticles are heavy then the dominant production of SUSY particles will be to the lightest gauginos. At leading order in perturbation theory, the production of $\tilde{\chi}^0_1$s and/or $\tilde{\chi}^\pm_1$s would be difficult to trigger on, but gaugino production in association with a high p_T jet or photon and $\not{p}_T$ might be observable [62, 91].

A fraction of the simulated gaugino production events contain high p_T jets from initial state parton showers. However the parton shower algorithm is based on the soft and co-linear approximations so this fraction will be smaller than that which would result from higher order matrix element calculations. The trigger requirements can therefore be considered conservative.

Different values of the cuts were applied to events with zero, one, two or three leptons (electrons and muons only) as reconstructed by `ATLFAST`, as well as to an inclusive lepton (‘ptmiss’) analysis. In the case of two-lepton events, different cuts were applied according to whether the leptons were of the same sign (SS) or opposite sign (OS).

For each of these analyses the cuts were optimised in the order listed in table 3.1, and allowed to take one of ten values shown. The significance of the signal was given by $S/\sqrt{B}$ where S and B are the number of signal and background events expected respectively for 100 fb^{-1}. For each variable, the cut was chosen to maximise the significance subject to the constraint that $S > 10$. The analysis was determined to

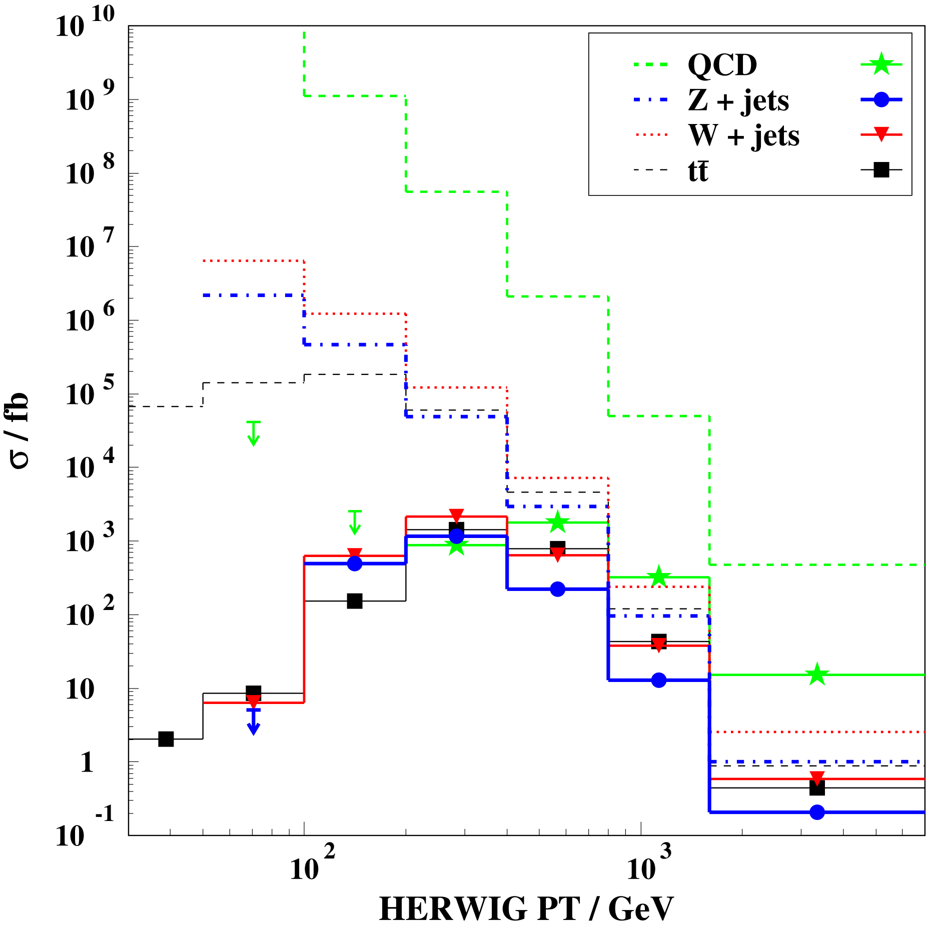

Figure 3.5: The cross-sections for the $t\bar{t}$, $W^{\pm}$ + Jets, and Z^0 + Jets and QCD (excluding $t\bar{t}$) backgrounds plotted as a function of the transverse momentum variable `PT`. This is the `HERWIG` internal variable which is compared to minimum and maximum requested values, `PTMIN` and `PTMAX`, and is of the same order of magnitude as the p_T of the hard process. The production cross-sections are denoted with dashed lines, while the cross-section to pass the preselection cuts are solid lines. Where no events passed the selection cuts (at low `PT`) arrows indicate 90% Poisson confidence limits on the selected cross-sections.

be successful if significance greater than five was achieved with at least ten events passing for any set of cuts.

This technique will not necessarily generate the global maximum in $S/\sqrt{B}$ since the cut variables are not totally independent, but it is sufficient for the purposes of a

	Variable		Allowed Values									
1	$\not{p}_T$	$>$	***200***	250	300	400	500	600	800	1000	1500	2000
2	$p_{T(J1)}$	$>$	***100***	150	200	300	400	600	800	1000	1500	2000
3	$p_{T(J2)}$	$>$	***100***	150	200	300	400	600	800	1000	1500	2000
4	$\sum p_T$	$>$	***200***	250	300	400	500	600	800	1000	1500	2000
5	$N_{\rm jet}$	$\geq$	***2***	3	4	5	6	7	8	9	10	11
6	$S_{\rm T}$	$>$	0	0.1	0.2	0.3	0.4	0.5	0.6	0.7	0.8	0.9
7	$\Delta\phi_{(J1)}$	$>$	0	0.3	0.6	0.9	1.2	1.5	1.8	2.1	2.4	2.7
8	$p_{T(\ell 1)}$	$>$	10	15	20	40	60	100	200	500	1000	2000
9	$\Delta\phi_{(\ell 1)}$	$>$	0	0.3	0.6	0.9	1.2	1.5	1.8	2.1	2.4	2.7
10	M_T	$>$	100	100	100	100	100	100	100	100	100	100

Table 3.1: Allowed values for each of the cuts described in the text. The preselection cuts (highlighted in ***bold italic***) are shown in the third column (applies to cuts 1 to 5 only). The units of the variables (1-4,8,10) are GeV.

large parameter-space scan, and it decreases the chances of over-fitting to a sparse background.

3.3.3 Results

The 5σ (and ≥ 10 event) discovery reaches for 100 fb^{-1} of integrated luminosity in fig. 3.6 and fig. 3.7 show that the LHC will be able to distinguish mAMSB from the SM over a large range of parameter space. As expected, the results are similar to previous generic R-parity conserving SUSY searches [30, 76, 88–90] with reach extending up to squark masses of about 2800 GeV, or to gluino masses of about 2100 GeV, whichever is the lower. The discovery reach is similar to, but greater than that found in [77] for wino production via vector boson fusion.

In general the best reach is obtained in the single-lepton and the inclusive channel. The same-sign dilepton signal is competitive at low m_0, when $m_{\tilde{\ell}} < m_{\tilde{\chi}_2^0}$ – a region

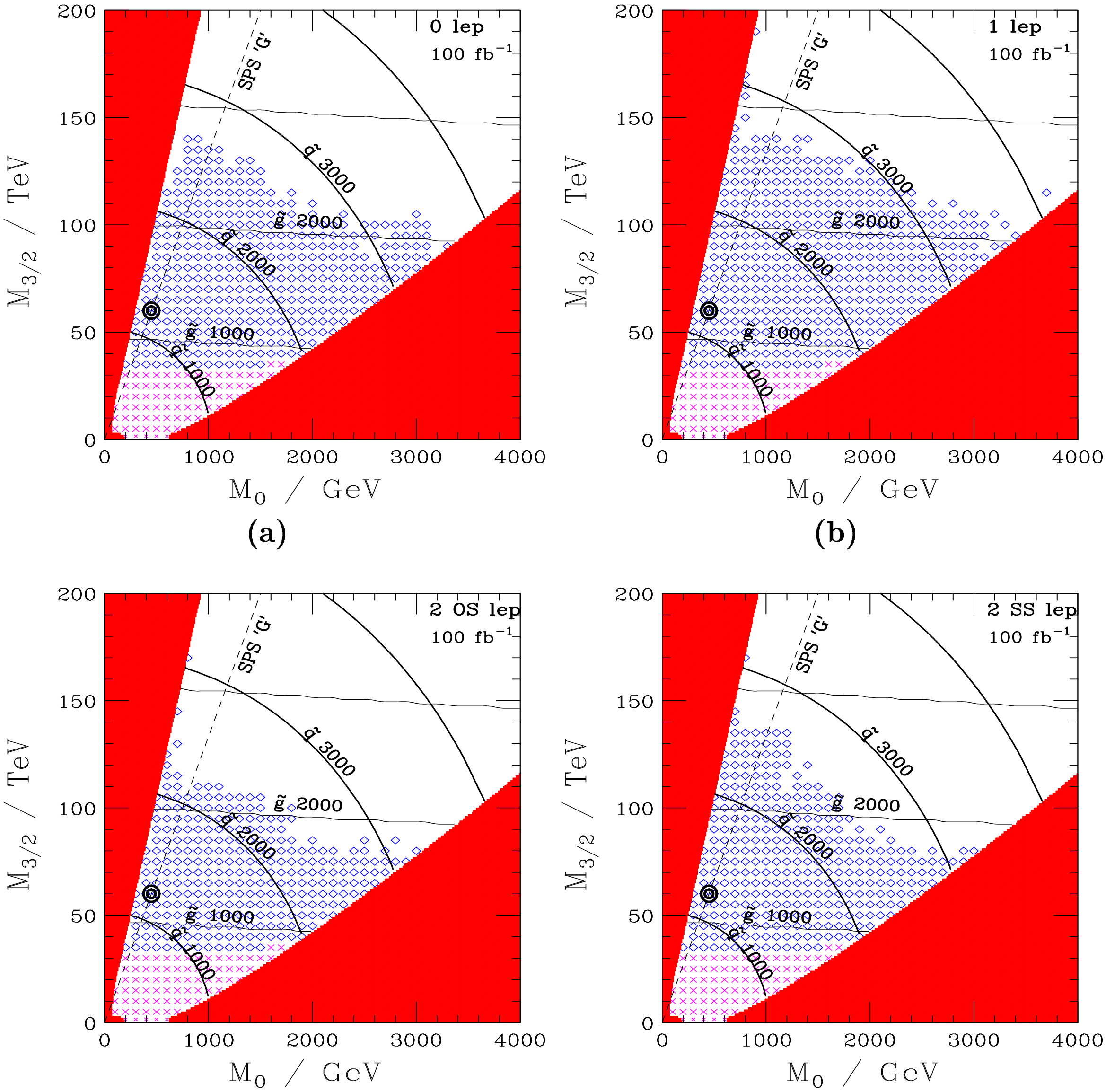

(a) **(b)**

(c) **(d)**

Figure 3.6: The 5 σ (and ≥ 10 event) discovery region for mAMSB in the m_0–$m_{3/2}$ plane, is shown by the light blue diamonds, for the **(a)** no lepton, **(b)** single lepton, **(c)** two opposite-sign leptons, and **(d)** two same-sign leptons channels. The other parameters are $\tan\beta = 10$ and $\mu > 0$ in all cases. The solid red regions are excluded because of lack of electroweak symmetry breaking (bottom right), charge- or colour-breaking minima, or non-$\tilde{\chi}_1^0$ LSP (left). The low $m_{3/2}$ region excluded by the LEP limit [72] on the chargino mass is indicated by purple crosses. The Snowmass mAMSB point **SPS 9** at m_0 = 450 GeV, $m_{3/2}$ = 60 TeV is marked with a pair of concentric circles, through which passes the Snowmass slope 'model line G' (dashed line). Contours of $\tilde{u}_L$ and $\tilde{g}$ iso-mass are shown as solid lines.

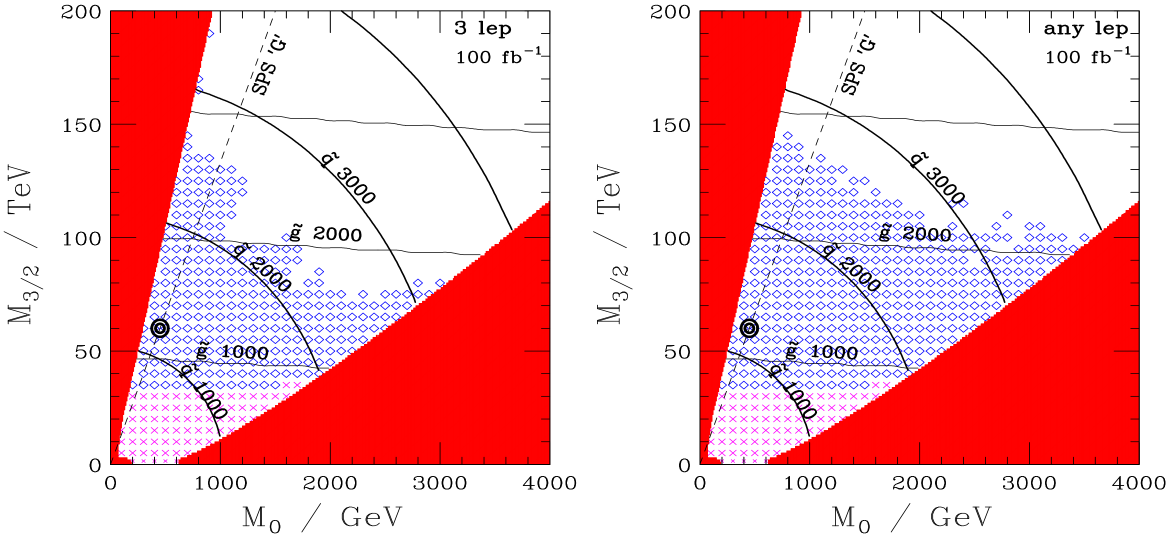

(a) **(b)**

Figure 3.7: As fig. 3.6 but for the **(a)** the three lepton channel and **(b)** the inclusive ('missing pt') channel.

Analysis	$\not{p}_T$	$p_{T(J1)}$	$p_{T(J2)}$	$\sum p_T$	N_{jet}	S_{T}	$\Delta\phi_{(J1)}$	$p_{T(\ell 1)}$	$\Delta\phi_{(\ell 1)}$
ptmiss	600	100	200	1000	9	0.2	0.3	N/A	N/A
0 Lep	800	150	200	1000	10	0.1	0	N/A	N/A
1 Lep	500	200	200	200	10	0.6	0	10	0
2 Lep OS	800	100	150	200	9	0.7	0	10	0
2 Lep SS	500	100	600	200	2	0.1	0	10	0
3 Lep	400	400	200	200	9	0	0	10	0

Table 3.2: The value of the cuts which maximised the significance $(S/\sqrt{B})$ for each of the analyses at the Snowmass mAMSB Point **SPS 9** for $\int \mathcal{L} = 100$ fb^{-1}. The M_T cut applied only to the single lepton channel and was kept at 100 GeV.

which includes the model line **SPS G** – but this sensitivity decreases as m_0 and $m_{\tilde{\ell}}$ increase. Points with large m_0 have a spectrum qualitatively similar to that in fig. 3.2, with heavy squarks and sleptons. Such points can still produce leptons, mostly from heavy chargino or neutralino decays. Another source of leptons is from gluino decays to Higgsinos along with a quark and anti-quark from the third

	SPS 9			**Point d'Aix**		
Analysis	S	B	$S/\sqrt{B}$	S	B	$S/\sqrt{B}$
ptmiss	3300	151	270	2650	0.25	5200
0 Lep	950	21	206	7800	4.46	3700
1 Lep	151	0.00005	21000	930	0.00005	10^5
2 Lep OS	15	0.00005	2100	62	0.00005	8800
2 Lep SS	13	0.0005	1900	67	0.0048	970
3 Lep	206	0.0001	20400	19	0.00010	1900

Table 3.3: The expected number of signal (S), and background (B) events and the significance ($S/\sqrt{B}$) for each of the analyses, at the Snowmass mAMSB Point **SPS 9** and the Point d'Aix, for integrated luminosity of 100 fb^{-1}. For all six analyses and for both points the backgrounds are dominated by high p_T vector boson production in association with jets. See main text for comments on expected number of background events.

generation, followed by leptonic t or b decay.

Along the Snowmass model line 'G' ($m_0 = 0.0075 \times m_{3/2}$) the LHC will be able to measure discrepancies from the Standard Model up to m_0=1050 GeV, $m_{3/2}$=140 TeV, at which point the gluino mass is 2.76 TeV and $m_{\tilde{u}_L}$ = 2.70 TeV. The Snowmass point **SPS 9** lies well within the discovery region for all of the six different analyses. The optimised cuts and the resultant significance are shown in table 3.2 and 3.3. The expected number of background events is very small in some of the channels where the background origantes from samples with high p_T in the hard scatter, which have very low weights. The background contribution from low-p_T hard scatters is small in these simulations. However it should be noted that there will be an additional source of background because non-linearities in the calorimeter response can generate apparently large missing energy. The high significance ($S/\sqrt{(B)}$) implies that it will be possible to extract further information from the data, for example to determine sparticle masses.

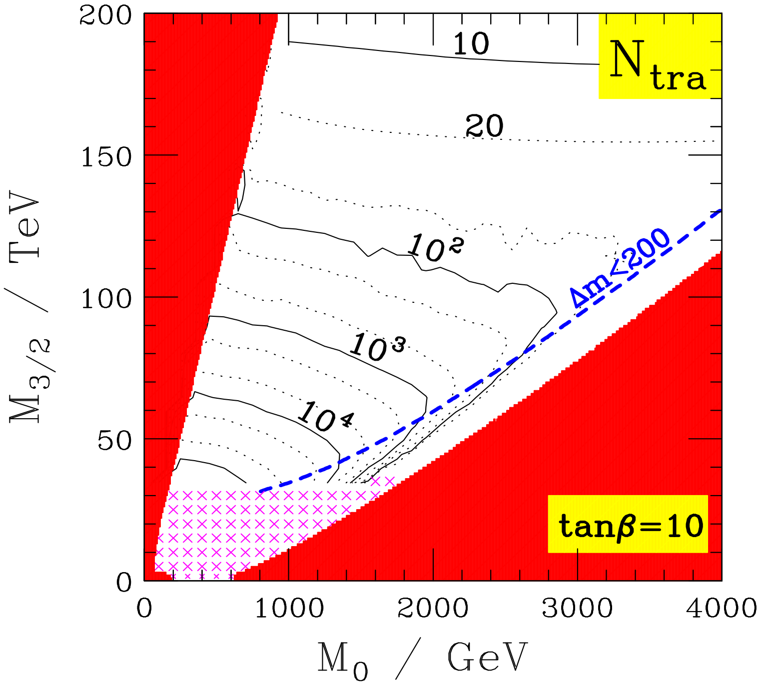

Figure 3.8: The number of $\tilde{\chi}_1^{\pm} \to \tilde{\chi}_1^0$ decays expected within the central region of the detector ($|\eta| < 2$) with transverse decay vertices between 100 mm and 800 mm from the interaction point for integrated luminosity of 100 fb^{-1}. The initial track from the chargino is required have $p_T > 10$ GeV. All events are required to have passed the preselection cuts (table 3.1) which ensure that the event will be triggered. The 10 event and 20 event contours have been smoothed for clarity. $\Delta M_{\tilde{\chi}_1}$ is less than 200 MeV above and to the left of the dashed blue line on the bottom right-hand side of the plot.

3.4 Distinguishing wino-like LSPs

Most of the mass-sum rules [61] for mAMSB involve terms like $m^2_{\tilde{d}_L} - m^2_{\tilde{u}_L}$ which would be extremely difficult to determine experimentally. The exception is the accidental near-degeneracy of the $\tilde{e}_L$ and $\tilde{e}_R$, which might be observable at some points, as was noted in sec. 3.2. However points with large m_0 have relatively heavy sleptons which would have a small production cross-section at a hadron collider. The wino-like LSP signature of AMSB, and the resultant near-degeneracy of the $\tilde{\chi}_1^+$ and $\tilde{\chi}_1^0$ will be the robust 'smoking gun' for anomaly mediation, and is applicable beyond the minimal model.

The LHC, like LEP [72], or the Tevatron [62,91] or a future linear e^+e^- collider [92] can use a variety of analyses in the search for long-lived charginos, each tailored to a different regime in $\Delta M_{\tilde{\chi}_1}$, according to the $\tilde{\chi}_1^+$ lifetime. The various regimes are ordered by decreasing $\tilde{\chi}_1^+$ lifetime below:

(1) $\Delta M_{\tilde{\chi}_1} < m_{\pi^+}$. If the pion decay mode is not available, the $\tilde{\chi}_1^+$ will be long lived ($c\tau \gtrsim 1$ m) and can leave a track through the muon chambers. Analysis of this type of signature was performed in [93] for a GMSB model with long-lived $\tilde{\tau}_1$ NLSP, and in [94] for an intermediate scale model with heavy stable leptons. The mass of the chargino can be measured using the muon detector as a time-of-flight system. Additional discrimination can be obtained by considering $\frac{dE}{dx}$ information from the transition radiation tracker. Higher-mass sparticles can then be reconstructed by forming the invariant mass of the stable particle with jets and leptons. Provided the $\tilde{\chi}_1^+$ lifetime, although long, is short enough that a reasonable number of $\tilde{\chi}_1^+$s decay within the inner detector, the mass difference $\Delta M_{\tilde{\chi}_1}$ could also be determined from that fraction using the techniques described below.

(2) $m_{\pi^+} < \Delta M_{\tilde{\chi}_1} \lesssim 200$ MeV. This is the regime in which high p_T chargino tracks often decay within the body of the inner tracker to soft pions or leptons along with large amounts of missing transverse momentum. The details of the detector resolution and track reconstruction algorithm are beyond the scope of this study, but isolated, high-p_T $\tilde{\chi}_1^+$ tracks which apparently disappear within the tracker at the point of the $\tilde{\chi}_1^+$ decay should provide a striking signature provided they occur in sufficient numbers.

Although $c\tau$ is only of the order of a few centimeters, the tracks are boosted and the lifetime describes an exponential distribution, so one would expect a reasonable proportion of $\tilde{\chi}_1^+$ tracks to reach transverse distances of 10 to 15 cm. The number of $\tilde{\chi}_1^+$s which would be produced at the LHC and decay within a fiducial volume in the active material of the ATLAS tracker is plotted in fig. 3.8 as a function of m_0 and $m_{3/2}$. Even though rather strict triggering requirements have been made, there are at least ten such events for 100 fb^{-1} over almost the entire plotted parameter-space provided $m_{3/2} \lesssim 185$ TeV.

One-prong chargino decays such as $\tilde{\chi}_1^+ \to \tilde{\chi}_1^0 \pi^+$ and $\tilde{\chi}_1^+ \to \tilde{\chi}_1^0 e^+ \nu_e$ will produce 'kinks' at the point where the charged SM particle is softly emitted. In some cases the SM particle will go undetected and the high p_T chargino track will seem to disappear. Such decays, producing track stubs, could also be detected with a dedicated off-line analysis. These signature should be essentially free of physics background, so 'detector' backgrounds will dominate. Since ATLAS should have three barrel pixel layers with $r < 122$ mm with noise occupancy of less than 10^{-5}, and average physics occupancy of the order of 10^{-4} the instrumental backgrounds should also be under control [36, 95]. Such a search could therefore achieve a large reach and would be sufficient to identify a near-degenerate LSP model.

(3) 200 MeV $\lesssim \Delta M_{\tilde{\chi}_1} \lesssim$ a few GeV. Chargino decays which occur before the first tracking layer can still be useful provided that the soft track from the SM particle can be found, using *e.g.* electron identification, track impact parameter, isolation from other tracks, and the direction of the $\not{p}_T$ 2-vector.

The maximum value of $\Delta M_{\tilde{\chi}_1}$ in minimal AMSB with $\tan\beta = 10$ is less than about 200 MeV except close to the region of no electroweak symmetry breaking. This leads to a decay distance $c\tau \gtrsim$ a few centimeters, and corresponds to category (2) above. However, other models such as 0-II string models [78, 79, 96] have wino-like $\tilde{\chi}_1^+$ and $\tilde{\chi}_1^0$ with $\Delta M_{\tilde{\chi}_1}$ typically of the order of a GeV. Such models fall into category (3), which is potentially the most difficult at a hadron collider because the short-lived $\tilde{\chi}_1^+$s will not be directly observable, and their softly emitted SM daughters suffer from a large background from other low-momentum tracks. In sec. 3.4.1 a range of model points are defined which allow this regime of shorter lifetimes to be studied. The modelling of the background from the proton remnant interactions is describted in sec. 3.4.2. Some of the methods which can enable the LHC to probe this region are explored in sec. 3.4.3 and 3.4.4.

3.4.1 Definition of points

The tree-level neutralino mass matrix is:

$$\begin{pmatrix} M_1 & 0 & -m_Z c_\beta s_W & m_Z s_\beta s_W \\ 0 & M_2 & m_Z c_\beta c_W & -m_Z s_\beta c_W \\ -m_Z c_\beta s_W & m_Z c_\beta c_W & 0 & -\mu \\ m_Z s_\beta s_W & m_Z s_\beta c_W & -\mu & 0 \\ & & & \end{pmatrix} \tag{3.5}$$

and the tree-level chargino mass matrix is:

$$\begin{pmatrix} M_2 & \sqrt{2} m_W s_\beta \\ \sqrt{2} m_W c_\beta & \mu \end{pmatrix} , \tag{3.6}$$

where $s_W \equiv \sin\theta_W$, $c_W \equiv \cos\theta_W$, $s_\beta \equiv \sin\beta$, $c_\beta \equiv \cos\beta$ and the conventions of [97] are used. The mass difference $\Delta M_{\tilde{\chi}_1} \equiv m_{\tilde{\chi}_1^+} - m_{\tilde{\chi}_1^+}$ is highly suppressed at tree-level, so the leading 1-loop correction can be important. It takes the form [98]:

$$\Delta M_{\tilde{\chi}_1}{}^{(1-\text{loop})} = \frac{\alpha_2 M_2}{4\pi} \left[F\left(\frac{m_W}{M_2}\right) - c_W^2 F\left(\frac{m_Z}{M_2}\right) + 5 s_W^2 \right] , \tag{3.7}$$

where $F(a) \equiv \int_0^1 dx(2+2x)\log[x^2+(1-x)a^2]$, and is also included in `ISAJET`.

One would like to investigate the collider phenomenology of long-lived charginos with various lifetimes. From eq. 3.5 and eq. 3.6, the leading tree-level mass difference term [98] $\Delta M_{\tilde{\chi}_1} \propto 1/\mu^2$. In order to explore different regimes in $\Delta M_{\tilde{\chi}_1}$, new points based on **SPS 9** and another minimal anomaly-mediated point with $m_0 = 500$ GeV, $m_{3/2} = 36$ TeV, $\mu > 0$ and $\tan\beta = 10$ are defined. The value of the μ parameter at the electroweak scale is then adjusted to the values shown in table 3.4. Point **A** has been chosen to have light sparticles, and hence a large cross-section.

In order to maintain consistent electroweak symmetry breaking when decreasing μ, the Higgs soft mass parameters, $m^2_{H_u}$ and $m^2_{H_d}$, must allowed to vary, as can be seen from tree-level equation,

$$\mu^2 = \frac{m^2_{H_u} - m^2_{H_d}\tan^2\beta}{\tan^2\beta - 1} - \frac{1}{2}m^2_Z\ . \tag{3.8}$$

The points with adjusted μ are then no longer in the minimal anomaly-mediated scenario, since $m^2_{H_u}$ and $m^2_{H_d}$ are not those which would be predicted from the mAMSB parameters m_0 and $m_{3/2}$. Decreasing μ has the side-effect of decreasing the masses of the Higgsinos, and can change the phenomenology somewhat – for example by opening chains such as $\tilde{q} \to \tilde{\chi}_2^+ q \to \tilde{\chi}_1^+ q Z^0$. When followed by leptonic Z^0 decay these chains could, in principle, be used to further constrain the dynamics. However the only requirement made in this analysis is that the decay $\tilde{q} \to \tilde{\chi}_1^+ q$ occurs, producing highly boosted $\tilde{\chi}_1^\pm$ pairs in association with jets.

3.4.2 The underlying event

In this section it is demonstrated that the low-p_T tracks from the charged SM daughters of $\tilde{\chi}_1^+$ decays can be identified and used to constrain $\Delta M_{\tilde{\chi}_1}$. To do so one must

Point	μ	$m_{\tilde{\chi}_1^+}$ (GeV)	$\Delta M_{\tilde{\chi}_1}$ (MeV)	$c\tau$ (mm)	$\tilde{\chi}_1^+ \to \tilde{\chi}_1^0 e^+ \nu_e$	$\tilde{\chi}_1^+ \to \tilde{\chi}_1^0 \mu^+ \nu_\mu$
SPS 9	864	171	164	56	2.0 %	0.2 %
SPS-300	300	165	886	0.11	17.0 %	15.9 %
SPS-250	250	159	1798	0.004	21.9 %	21.5 %
A	533	107	181	34	2.0 %	0.3 %
A-250	250	101	766	0.20	15.4 %	13.9 %
A-200	200	97	1603	0.007	22.5 %	22.2 %

Table 3.4: The mass of the lightest chargino, its mass difference with the LSP, decay length and leptonic branching ratios for six points. **SPS 9** is the Snowmass mAMSB point, from which **SPS-300** and **SPS-250** are made by adjusting μ at the electroweak scale to produce different $\Delta M_{\tilde{\chi}_1}$. Point **A** is the mAMSB point with $m_0 = 500$ GeV, $m_{3/2} = 36$ TeV, $\mu > 0$ and $\tan\beta = 10$, from which μ is adjusted at the electroweak scale to produce **A-250** and **A-200**.

distinguish these tracks from the large number of other low-p_T tracks from the particles generated in the proton remnant interactions, and from any pile-up events. To avoid having to deal with the contamination from multiple pile-up, in this section the initial three years of ‘low luminosity’ (10^{33} cm^{-2}s^{-1}) running of the LHC is simulated, which is expected to provide 30 fb^{-1} of integrated luminosity with an average of one inelastic collision per bunch-crossing. The loss of resolution from pile-up is therefore not simulated in this section.

Since we are looking for low p_T particles, we should take particular care when considering the backgrounds from the proton remnant interactions, known as the *underlying event*. The `HERWIG` soft underlying event model is based on the UA5 collaboration [100] $p\bar{p}$ Monte-Carlo. It gives a fairly accurate description of track multiplicity and of the p_T distribution in the range $0.4 < p_T < 1$ GeV. However it underestimates the number of tracks with $p_T > 1$ GeV (fig. 3.9) in minimum-bias events, because it does not model the semi-hard physics of multiple parton interactions.

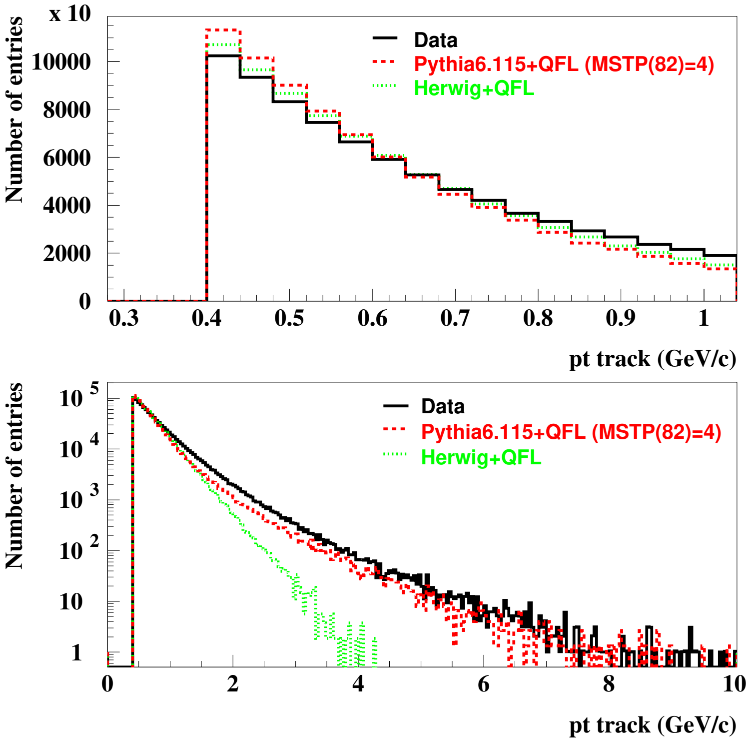

Figure 3.9: Transverse momentum distribution of charged tracks in minimum bias events at $\sqrt{s} = 1800$ GeV from the CDF experiment at the Tevatron [99].

Of course semi-soft tracks are also produced from QCD emissions from partons associated with the hard scatter. Measurements of the distribution of charged particle tracks were made at CDF in events with high energy jets [99]. Four samples were considered with transverse energy of the leading jet greater than 20, 50, 70 and 100 GeV. Comparisons were made of the number of charged-particle tracks, and their p_T distribution in two cones of radius 0.7, perpendicular to the leading jet in ϕ and at the same pseudorapidity. In these events `HERWIG` shows very good agreement with the p_T distributions across the whole energy range (fig. 3.10), and slightly *over-estimates* the charged track multiplicities [99]. This much better agreement comes from the contribution of particles softly emitted from the 'hard' process in the `HERWIG` model [101].

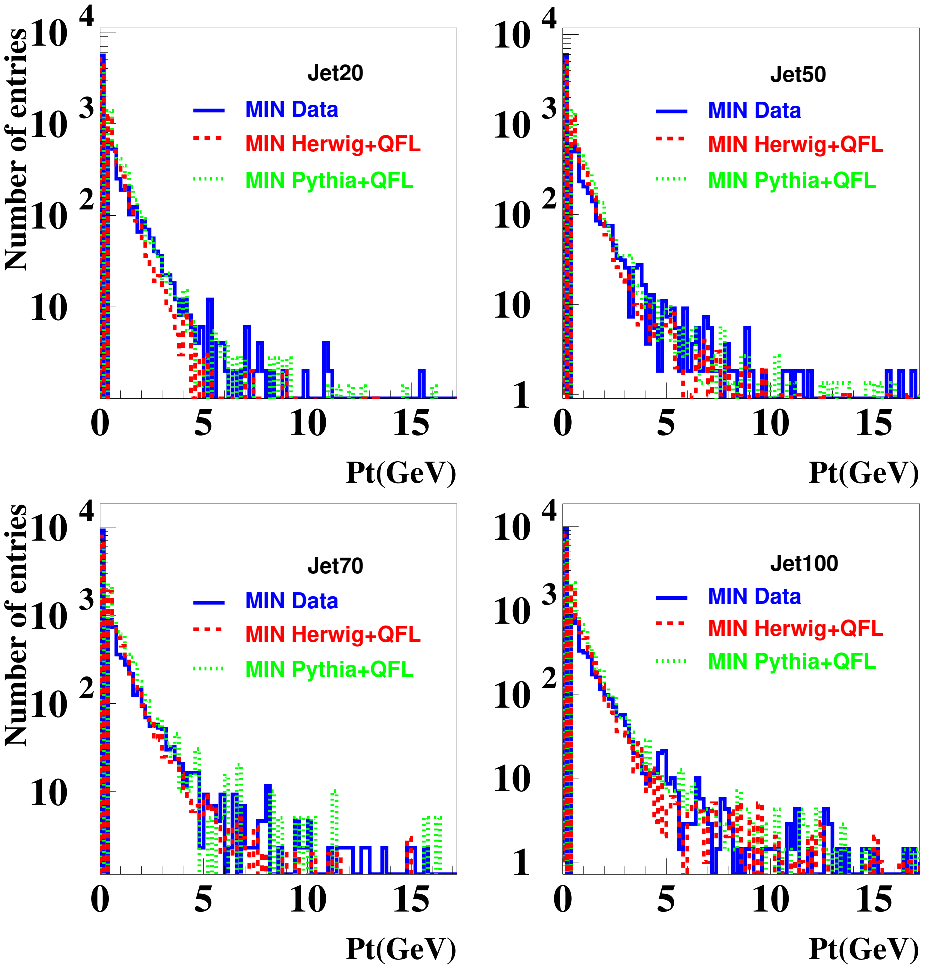

Figure 3.10: Transverse momentum distribution of charged tracks in jet events at $\sqrt{s} = 1800$ GeV. The tracks lie in a cone of radius 0.7, perpendicular to the leading jet in ϕ, and with the same pseudorapdity as that jet. Of the two possible cones, the one with the smaller scalar sum of track transverse momenta was chosen. The four plots show the results for leading jet transverse energy greater than 20, 50, 70, or 10 GeV. From the CDF experiment at the Tevatron [99].

To ensure that the analysis was insensitive to contamination from such tracks, a sample of 5000 inclusive QCD events with `PTMIN` = 4.5 GeV was generated. These are henceforth referred to as 'minimum bias events' because they simulate (better than the default `HERWIG` soft minimum bias option) the expected minimum bias

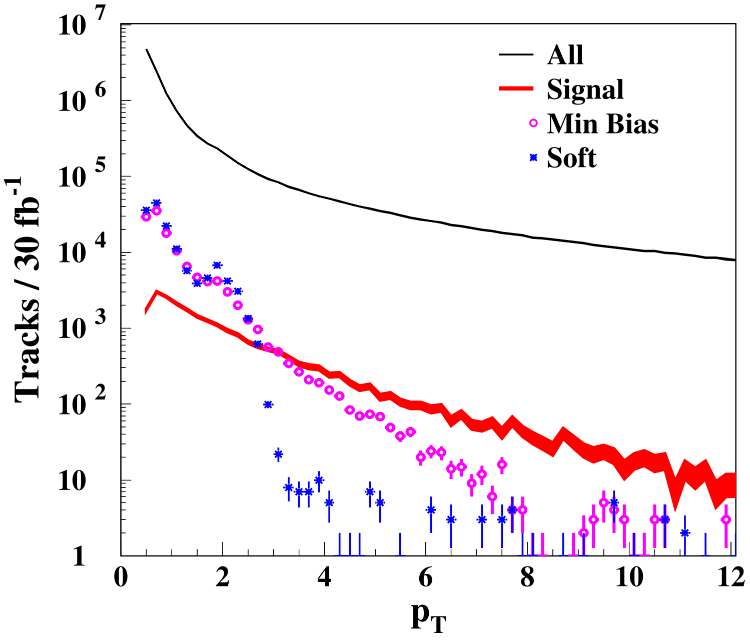

Figure 3.11: The transverse momentum distribution of reconstructed charged tracks after detector smearing for the point **SPS-250** (defined in table 3.4) after selecting events with $\not{p}_T > 200$ GeV. The thin black line shows all tracks; the distribution for particles originated from $\tilde{\chi}_1^{\pm}$ decays (the signal) is highlighted by the thick red line, where the thickness shows the statistical uncertainty; those from the `HERWIG` soft underlying event and from the additional minimum bias event are denoted by asterisks and circles respectively.

distribution of tracks, including a tail at higher p_T due to the onset of hard scattering. The particles from this minimum bias event were added to the SUSY event *in addition to* `HERWIG`'s usual underlying event, offering a conservative estimate of the background.

3.4.3 Event and track selection

An initial selection requiring a high p_T jet and large missing transverse momentum was made to trigger the event, reduce the SM background, and select those SUSY events in which the neutralino was highly boosted. In this section the short-lifetime

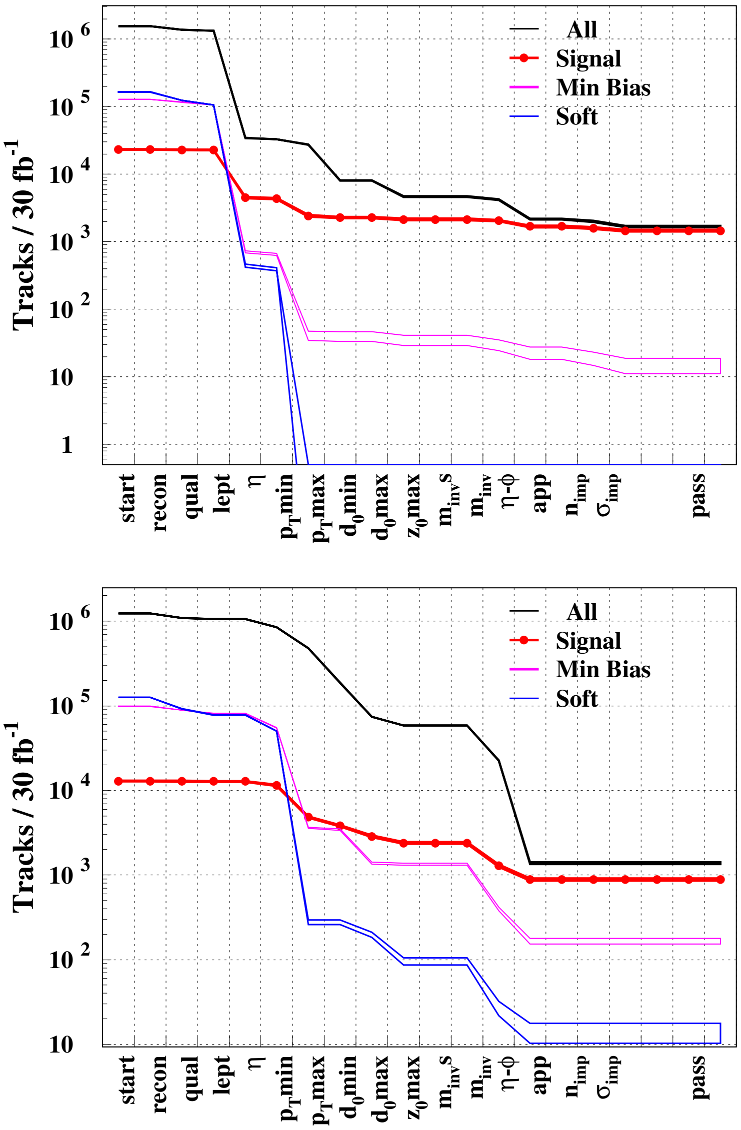

Figure 3.12: The number of tracks surviving subsequent cuts, after a preselection cut $\not{p}_T > 200$ GeV for the point **(a) SPS-250**, and **(b) SPS-250** (as defined in table 3.4). The signal tracks (from $\tilde{\chi}_1^{\pm}$ decays) are also plotted separately, as are tracks from the `HERWIG` soft underlying event and from the additional minimum bias QCD event. Not all cuts are used in any particular analysis.

regime ($c\tau < 1$ mm) is being studied, in which the boost will almost certainly *not* be sufficient to allow the chargino to live long enough to decay in the body of the detector. However a boosted chargino means that even particles which are very

	Points	**SPS-300 , A-250**	**SPS-250, A-200**
Event:	$\not{p}_T^{\mathrm{min}}$	500	500
	$p_{T(J1)}^{\mathrm{min}}$	400	400
	S_T^{min}	0.05	0.05
Track:	p_T^{min}	2.0	2.0
	p_T^{max}	5	10
	d_0^{min}	0.03	0
	d_0^{max}	0.3	0.1
	$\lvert\eta\rvert^{\mathrm{max}}$	1.5	2
	$\Delta R_{ij}^{\mathrm{min}}$	0.45	0.2
	M_{ij}^{min}	0.9	0.4
	R_{imp}	0.4	0.4
	σ_{imp}	3.0	3.0
	Particle	any	$\ell \in e, \mu$

Table 3.5: The cuts applied to events and to tracks for the different points in table 3.4. The missing transverse momentum ($\not{p}_T$), leading jet transverse momentum ($p_{T(J1)}$), and transverse sphericity (S_T) cuts were applied to the whole event, while the other cuts were applied track by track. The track transverse momentum was required to lie in the range $p_T^{\mathrm{min}} \to p_T^{\mathrm{max}}$; its transverse impact parameter in the range $d_0^{\mathrm{min}} \to d_0^{\mathrm{max}}$; and the absolute value of its pseudorapidity was required to be less than $|\eta|^{\mathrm{max}}$. The other cuts are described in the text. Energy, momentum and mass units are GeV; the impact parameter, d_0, is measured in mm.

softly emitted in the chargino rest frame will have a transverse momentum

$$p_{Tx} \sim \frac{p_{T\tilde{\chi}_1^0}}{m_{\tilde{\chi}_1^0}} \times m_x \tag{3.9}$$

as measured in the detector, where x is the charged SM daughter particle and $p_{T\tilde{\chi}_1^0}$ is of the order of the missing transverse momentum. This extra p_T assists the

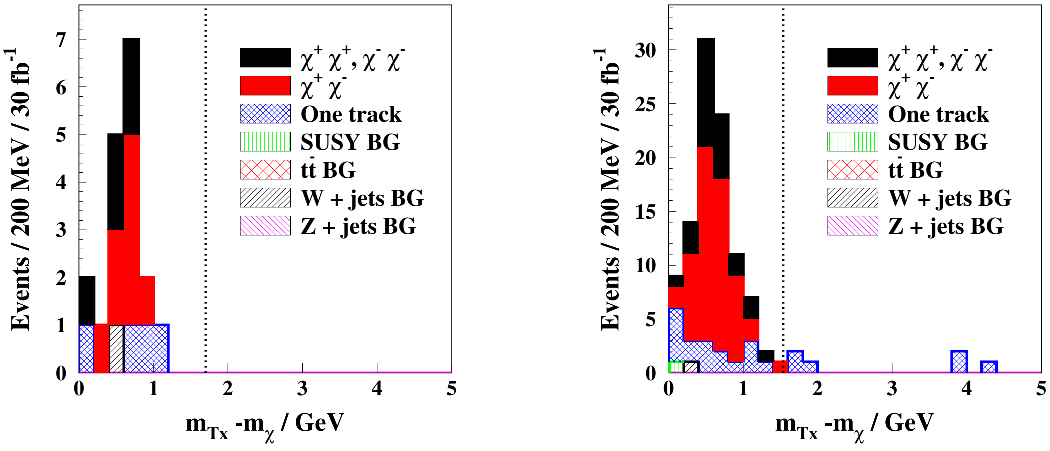

(a) (b)

Figure 3.13: The $m_{T4} - m_{\tilde{\chi}_1^0}$ distribution for the points **(a) SPS-250**, and **(b) A-200** (defined in table 3.4). These two points have similar values of $\Delta M_{\tilde{\chi}_1}$, and the same cuts were applied to both. Only events in which exactly two leptons passed the selection cuts are plotted. The signal tracks are those from events where both charged tracks come from $\tilde{\chi}_1^+$ or $\tilde{\chi}_1^-$ decays. Events where only one of the two tracks is from the product of a $\tilde{\chi}_1^\pm$ decay lead to a combinatorical background, and are plotted separately (labelled 'one track'). The vertical dotted line indicates $\Delta M_{\tilde{\chi}_1} = m_{\tilde{\chi}_1^+} - m_{\tilde{\chi}_1^0}$.

reconstruction of the SM daughters of charginos and helps distinguish them from even softer particles coming from the underlying event (fig. 3.11).

The tracks from SM daughters of chargino decays have other properties which can help in their identification. For larger $\Delta M_{\tilde{\chi}_1}$ the $\tilde{\chi}_1^+$ branching ratio to each of muon or electron and associated neutrino can be up to nearly twenty percent (fig. 3.4b). In the ATLAS experiment electrons and muons will be distinguished from other tracks by transition radiation and by penetration respectively (see appendix C).

Much of the background is associated with heavy-quark decay and can be removed by applying isolation cuts (table 3.5) which require that for any track, i, to be a candidate:

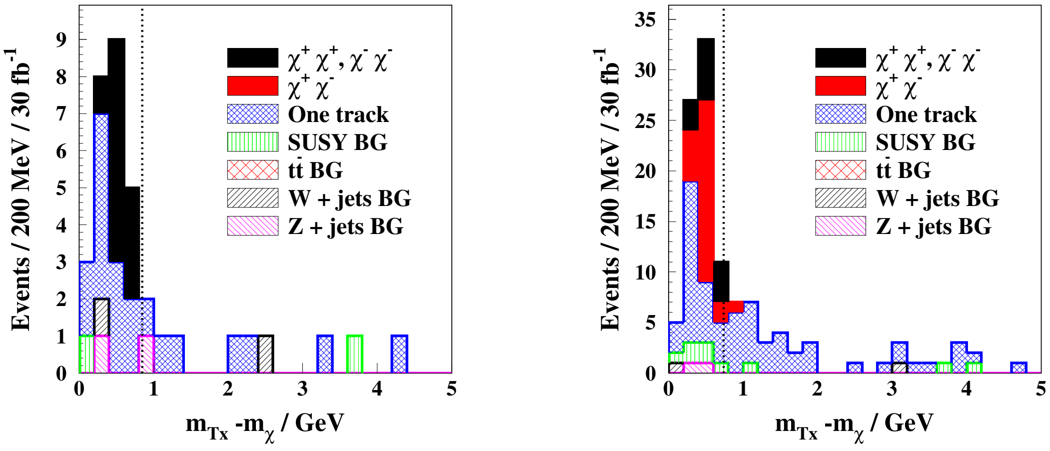

(a) **(b)**

Figure 3.14: The $m_{T2} - m_{\tilde{\chi}_1^0}$ distribution for **(a)** the point **SPS-300**, and **(b)** the point **A-250**. These two points have similar values of $\Delta M_{\tilde{\chi}_1}$, and the same cuts were applied to both. Only events in which exactly two particles (of any type) passed the selection cuts are plotted. The peak is closer than in fig. 3.13 to the upper kinematic limit at $m_{T2} - m_{\tilde{\chi}_1^0} = \Delta M_{\tilde{\chi}_1}$ (dotted line) since there are only two missing particles – the two neutralinos.

- no other track is found with $\Delta R_{ij} = \sqrt{(\Delta\eta_{ij})^2 + (\Delta\phi_{ij})^2}$ less than some value $\Delta R_{ij}^{\text{min}}$;
- the invariant mass of the track with another track, j, is greater than M_{ij}^{min} for all j, where it is assumed that $m_i = m_j = m_{\pi^+}$;
- no other track with $R_{ij} < R_{\text{imp}}$ has $d_0^{(j)}/\sigma(d_0^{(j)}) > 3$, where $d_0^{(j)}$ is the transverse impact parameter, and $\sigma(d_0^{(j)})$ is its uncertainty;
- $\sum_j \left[d_0^{(j)}/\sigma(d_0^{(j)})\right] < \sigma_{\text{imp}}$ where the sum is over all $j \neq i$ with $R_{ij} < R_{\text{imp}}$.

For the two points with $\Delta M_{\tilde{\chi}_1} \approx 1.7$ GeV, isolated leptons were selected. As $\Delta M_{\tilde{\chi}_1}$ decreases, the leptonic branching ratios decrease (see fig. 3.4b) and the detector's ability to distinguish the lower p_T leptons from hadrons is diminished (see appendix C). For this reason, at the two points with $\Delta M_{\tilde{\chi}_1} \approx 800$ MeV events were selected in which two tracks of *any* type satisfying the cuts in the third column of table 3.5. Most of these tracks will be pions because of the large branching ratio to $\pi^{\pm}$ or $\pi^{\pm}\pi^{0}$.

3.4.4 Results

Those events in which precisely two tracks satisfied the track cuts listed in table 3.5 were selected. For **SPS-250** the most effective cuts are those on the p_T of the track, and on selecting leptons ('lept'), while further cuts on the transverse impact parameter (d_0) and isolation ($\eta - \phi$) improve the selection (fig. 3.12a). For point **SPS-300** which has $\Delta M_{\tilde{\chi}_1} = 886$ MeV, the momentum, impact-parameter and isolation cuts are the most important (fig. 3.12b).

The m_{TX} variable was employed, because (as described in appendix D) it remains sensitive to $\Delta M_{\tilde{\chi}_1}$ even when there are uncertainties in the neutralino mass or the missing transverse momentum, providing an important handle on wino-LSP physics at hadron colliders. It was assumed that both the squark mass scale, $m_{\tilde{q}}$, and the $\tilde{\chi}_1^0$ mass have been previously determined from the measurement of other kinematic edges as described in [30,69,70,90], and so distributions of $m_{TX} - m_{\tilde{\chi}_1^0}$ were plotted, which have the property[c]:

$$0 < (m_{TX} - m_{\tilde{\chi}_1^0}) \leq (m_{\tilde{\chi}_1^+} - m_{\tilde{\chi}_1^0}) \equiv \Delta M_{\tilde{\chi}_1}. \qquad (3.10)$$

Distributions of $m_{T4} - m_{\tilde{\chi}_1^0}$ were plotted for the four points with $\Delta M_{\tilde{\chi}_1} < 1$ GeV as shown in figs. 3.13 and 3.14. For all four, the narrow peaks indicate that $\Delta M_{\tilde{\chi}_1}$ is

---

[c] The inequalities are strictly only valid for signal events measured with a 'perfect' detector and when $m_{\tilde{\chi}_1^0}$ is known. The (small) sensitivity of m_{TX} to uncertainties in these quantities is discussed in appendix D.3.

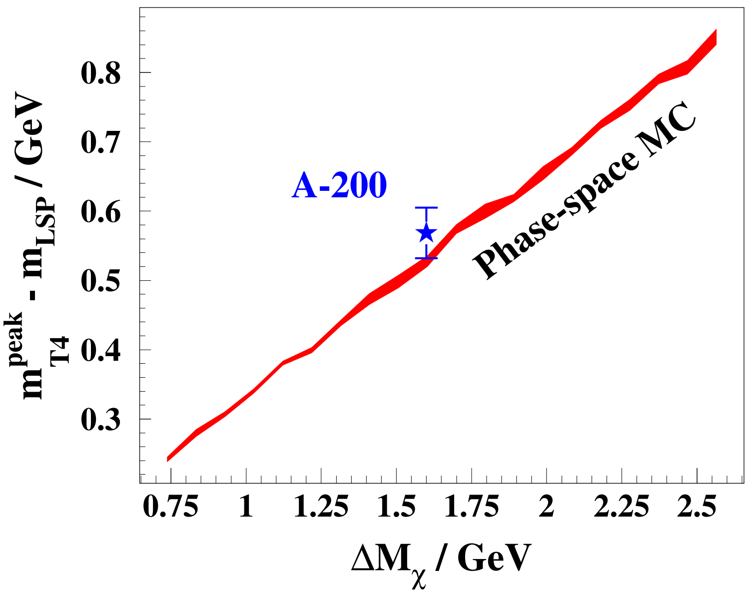

Figure 3.15: The diagonal line shows how the $m_{T4} - m_{\tilde{\chi}_1^0}$ peak value depends on $\Delta M_{\tilde{\chi}_1}$. The thickness of the line indicates the uncertainty in the peak position from a gaussian fit to the distribution combined in quadrature with a 10% uncertainty in the LSP mass and a 10 % uncertainty in the squark mass scale. The peak of the $m_{T4} - m_{\tilde{\chi}_1^0}$ distribution for the point **A-200** is marked with a star at its input value of $\Delta M_{\tilde{\chi}_1}$; the error bar shows its uncertainty.

of the order of 1 GeV. This confirms the wino-like nature of the LSP, providing the ‘smoking gun’ signature for anomaly mediation.

Each m_{TX} distribution depends principally on $\Delta M_{\tilde{\chi}_1}$, on the neutralino mass and the momentum distribution of the charginos. The latter depends largely on $m_{\tilde{q}}$ so if both $m_{\tilde{q}}$ and the lightest neutralino mass were already measured, then $\Delta M_{\tilde{\chi}_1}$ can be measured by fitting to each $m_{TX} - m_{\tilde{\chi}_1^0}$ distribution.

To demonstrate that m_{T4} can indeed make a quantitative measurement of $\Delta M_{\tilde{\chi}_1}$, a phase-space Monte-Carlo program was used to generate very simple ‘events’ in

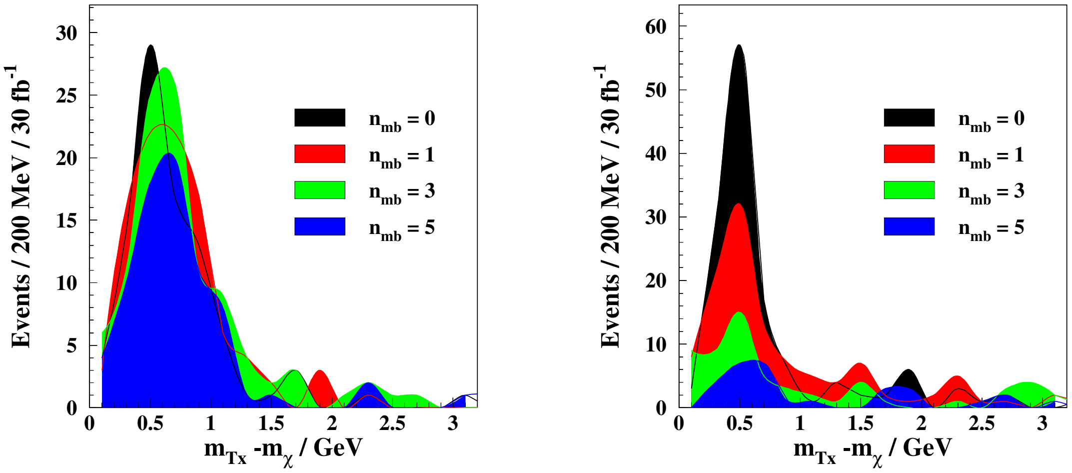

(a) **(b)**

Figure 3.16: The effect on the signal of adding n_{mb} additional minimum bias events on top of the `HERWIG` soft underlying event for points **(a)** **A-200** and **(b)** **A-250**.

which pairs of squarks decayed via the chain $\tilde{q} \to \tilde{\chi}_1^+ \; q \to \tilde{\chi}_1^0 \; e \; \nu_e \; q$. $m_{T4} - m_{\tilde{\chi}_1^0}$ distributions were produced for those events in which $\not{p}_T > 500$ GeV, and the peak determined from a gaussian fit. The correlation between the fitted peak positions and the input values of $\Delta M_{\tilde{\chi}_1}$ is shown in fig. 3.15. The peak of the $m_{T4} - m_{\tilde{\chi}_1^0}$ distribution for point **A-200** (fig. 3.13b), was likewise determined from a gaussian fit. As can be seen from fig. 3.15 the mass difference $\Delta M_{\tilde{\chi}_1}$ can be measured at that point with a statistical uncertainty of approximately 150 MeV (10%).

As was mentioned in sec. 3.4.2, the underlying-event model used can be considered conservative. We have added an additional 'minimum-bias' event on top of the usual `HERWIG` 'soft underlying event' – increasing the background above a model which already provides an slight overestimate of the charged particle backgrounds in jet events at the Tevatron. However is is instructive to consider the sensitivity of the signal distributions to the underlying event activity.

The effect of adding further minimum bias events is small for the point **A-200** (fig. 3.16a) because the lepton selection can still reduce the background. The analysis at the point **A-200** (fig. 3.16b) shows more sensitivity since here leptons are not selected, and the cut on the p_T of the track is much more important. The signal becomes indistinguishable when $n_{mb} \approx 3$ – *i.e.* when the background track multiplicity is about four times that in the `HERWIG` model. This loss in signal does not cast doubt on the analysis at this particular point since the backgrounds are not expected to be so large. However it indicates that the analysis will not suit points with smaller $\Delta M_{\tilde{\chi}_1}$, in which the chargino decays will produce softer pions which will be extremely difficult to distinguish.

Provided charginos are produced in sufficient numbers, their near-degeneracy with the LSP can be therefore be determined at the LHC

- for $\Delta M_{\tilde{\chi}_1} \lesssim 200$ MeV by the identifying track kinks and stubs in chargino tracks in the inner detector
- and for $\Delta M_{\tilde{\chi}_1} \gtrsim 700$ MeV by identifying the low-momentum pions from chargino decays.

3.5 Other constraints

3.5.1 Cosmological relic density

If R-Parity is conserved then the lightest supersymmetric particle can be a good candidate for the cold (non-relativistic) dark matter hypothesised by astrophysicists and cosmologists. The cold dark matter contribution to critical density of the

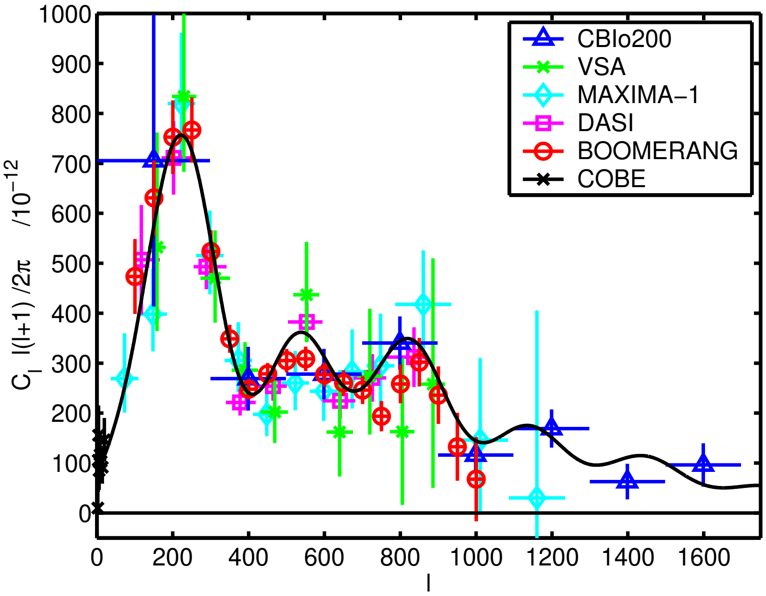

Figure 3.17: Cosmic microwave background anisotropy power-band data, with fit. From [102].

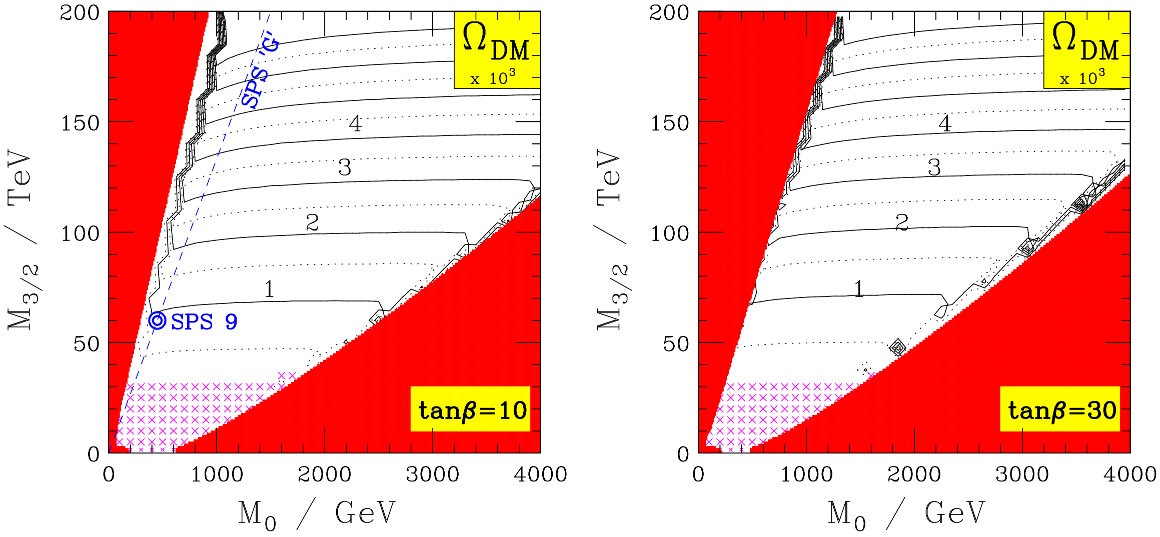

(a) **(b)**

Figure 3.18: The relic density of the lightest neutralino, $\Omega_{\rm CDM}h^2$ with $\mu > 0$; **(a)** for $\tan\beta = 10$ and **(b)** for $\tan\beta = 30$. The meaning of the symbols is explained in fig. 3.6. The astrophysical limits on $\Omega_{\rm CDM}h^2$ are discussed in the text. The contours are in units of 10^{-3}.

$\tilde{\chi}_1^0\tilde{\chi}_1^0 \to W^+W^-$	8 %	$\tilde{\chi}_1^+\tilde{\chi}_1^0 \to$ fermion pair	40 %
$\tilde{\chi}_1^+\tilde{\chi}_1^0 \to W^+ + Z^0/h/A$	11 %	$\tilde{\chi}_1^+\tilde{\chi}_1^+ \to W^+W^+$	8 %
$\tilde{\chi}_1^+\tilde{\chi}_1^- \to$ fermion pair	15 %	$\tilde{\chi}_1^+\tilde{\chi}_1^- \to$ boson pair	12 %

Table 3.6: The main cosmological relic annihilation channels for the Snowmass point **SPS 9**.

universe provided by the LSP is given by:

$$\omega_{\mathrm{CDM}} \equiv \Omega_{\mathrm{CDM}} h^2 = \frac{m_{\tilde{\chi}_1^0} n_{\tilde{\chi}_1^0}}{\rho_{\mathrm{crit}}/h^2} \tag{3.11}$$

where $\rho_{\mathrm{crit}} = 3H^2/8\pi G$ is the critical density, $n_{\tilde{\chi}_1^0}$ is the number density of LSPs, and $H = h \times 100$ km s^{-1} Mpc^{-1} is the Hubble constant.

Astronomical estimates from measurements of the acoustic power spectrum of the cosmic microwave background anisotropy [102–106], (fig. 3.17) suggest that $\omega_{\mathrm{CDM}} = 0.106 \pm 0.010$. Further constraints from the 2dF Galactic Redshift Survey [107] lead to $\omega_{\mathrm{CDM}} = 0.1151 \pm 0.0091$, assuming a flat universe ($\Sigma_i \Omega_{\mathrm{i}} = 1$).

In AMSB the wino-like $\tilde{\chi}_1^0$ and $\tilde{\chi}_1^+$ undergo rapid annihilation though reactions such as $\tilde{\chi}_1^0\ \tilde{\chi}_1^0 \to W^+\ W^-$ and $\tilde{\chi}_1^0\ \tilde{\chi}_1^+ \to q\ q'$. The relic density of cold dark matter was calculated for AMSB using the program `micrOmegas` [108], which includes the annihilation channels listed in table 3.6. The results, in fig. 3.18, show that the value of ω_{CDM} is small throughout the region, and about a factor of two less than was estimated in [46]:

$$\omega_{\mathrm{CDM}}^{\mathrm{no-coanh}} \approx 5 \times 10^{-4} \times \left(\frac{m_{\tilde{\chi}_1^0}}{100\ \mathrm{GeV}}\right) , \tag{3.12}$$

which neglected the co-annihilation channels.

(a) **(b)**

Figure 3.19: Feynman diagrams for two of the main SUSY contributions to the positive muon anomalous magnetic moment.

Thus in AMSB the LSP does not give any problems with relic overabundance, but suffers the opposite problem – that sparticles in thermal equilibrium in the early universe will not produce sufficient neutralino dark matter. It has been suggested in [109] that decays of cosmological moduli – which are low mass particles predicted by string theory when supersymmetry is broken – could have produced winos with sufficient abundance to be of astrophysical interest.

3.5.2 Muon $g - 2$

It is well know that the gyromagnetic moment of the muon, g_μ can sensitive to sparticle interactions through loop corrections [110–114], such as those shown in fig. 3.19. The recent BNL measurements [115,116] dominate the world experimental average of the positive muon anomalous moment,

$$a_\mu^{\mathrm{BNL}} = (g_\mu - 2)/2 = 11\ 659\ 203(8) \times 10^{-10}\ . \tag{3.13}$$

Standard Model calculations of a_μ have been reviewed in [117,118]. Recent calculations [119,120], which include a correction to the sign of the pion pole part of the

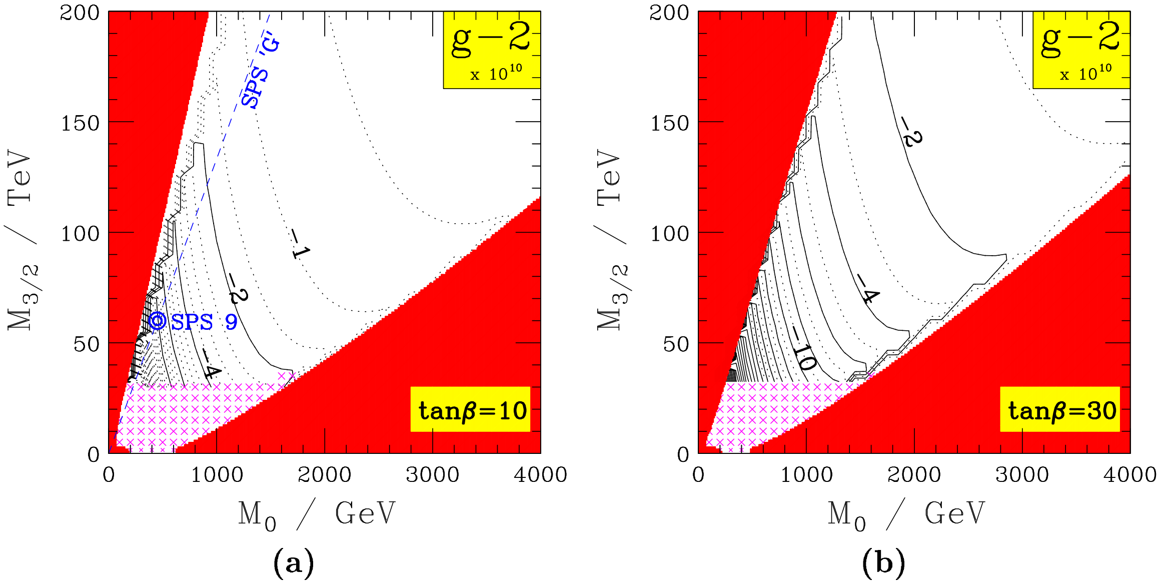

(a) **(b)**

Figure 3.20: The SUSY contribution to the anomalous magnetic moment of the muon, (in units of 10^{-10}) with $\mu > 0$; **(a)** for $\tan\beta = 10$ and **(b)** for $\tan\beta = 30$. The meaning of the symbols is explained in fig. 3.6.

hadronic light-by-light contribution [121–125], were combined in [116] to give:

$$11\ 659\ 177(7) \times 10^{-10} \quad \leq \quad a_\mu^{\rm SM} \quad \leq \quad 11\ 659\ 186(8) \times 10^{-10}\ . \tag{3.14}$$

The SUSY contribution is typically dominated by loops involving charginos and neutralinos [117, 126, 127], and is proportional to $\tan\beta$ in the high $\tan\beta$ limit. The AMSB contribution to a_μ ($a_\mu^{\rm AMSB}$) has been calculated in [60,127]. In fig. 3.20 $a_\mu^{\rm AMSB}$ is plotted for $\tan\beta = 10$ and 30, where again program `micrOmegas` has been used[d]. The AMSB contribution is small compared to both the experimental and theoretical uncertainties, except at small m_0, $m_{3/2}$.

---

[d] Note that `ISASUSY` produces AMSB points with negative M_1 and M_2 so the sign correlation between μ and $a_\mu^{\rm SUSY}$ is opposite to that in [127].

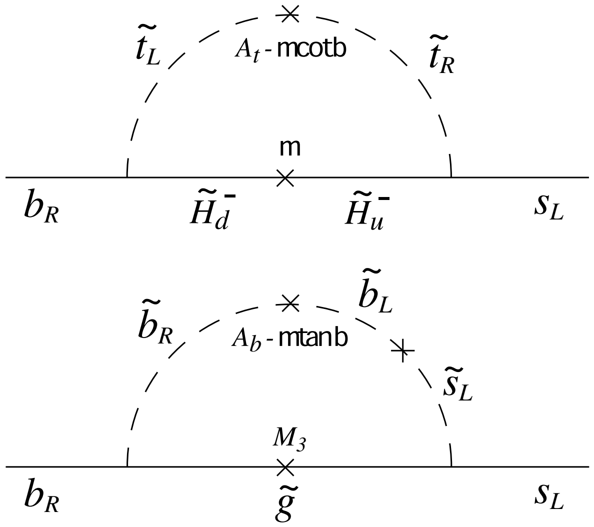

Figure 3.21: Feynman digrams for the leading contributions to $b \to s\gamma$ from chargino- and gluino-mediated processes for large $\tan\beta$. The photon, which may couple to any charged internal propagator is omitted. From [60].

3.5.3 $B \to X_s\gamma$

The inclusive radiative decay $B \to X_s\gamma$, (where X_s is a final state containing a strange quark) is sensitive to sparticle properties through radiative corrections involving charged Higgs, chargino and $\tilde{t}$ loops, such as those shown in fig. 3.21 (see for example [128–130]). This is a flavour-changing transition which in the SM is mediated by the W boson at one loop.

Experimental measurements of the branching ratio from the CLEO [131], BELLE [132] and BaBar [133] collaborations give:

$$\begin{aligned}
\mathcal{B}(B \to X_s\gamma)^{\mathrm{CLEO}} &= 3.21 \pm 0.43 \pm 0.27^{+0.18}_{-0.10} \times 10^{-4} \\
\mathcal{B}(B \to X_s\gamma)^{\mathrm{BELLE}} &= 3.39 \pm 0.53 \pm 0.42^{+0.51}_{-0.55} \times 10^{-4} , \\
\mathcal{B}(B \to X_s\gamma)^{\mathrm{BaBar}} &= 3.88 \pm 0.36 \pm 0.37^{+0.43}_{-0.23} \times 10^{-4} ,
\end{aligned} \tag{3.15}$$

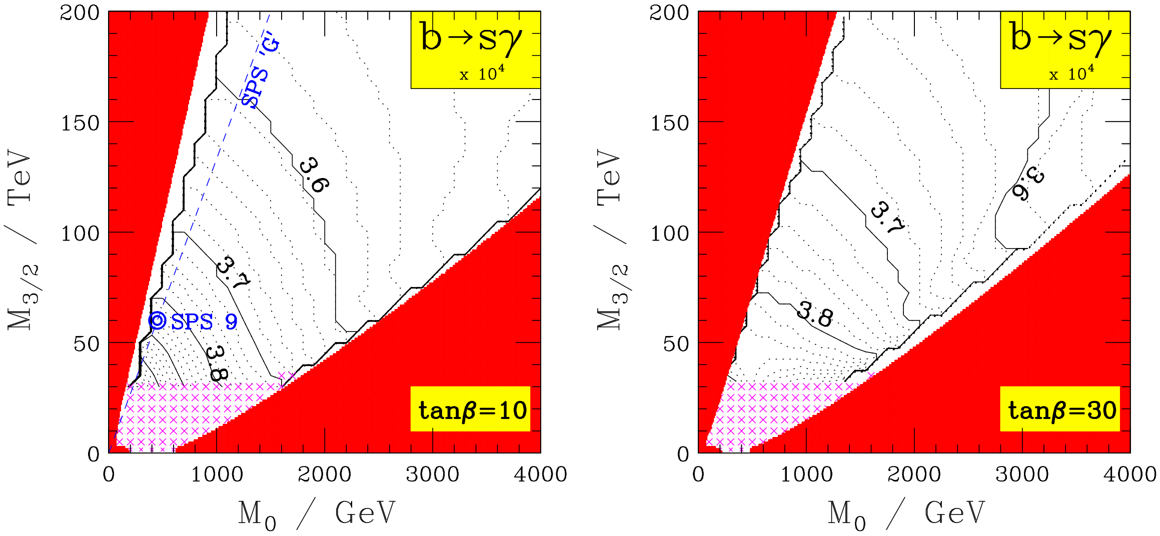

(a) **(b)**

Figure 3.22: The branching ratio $\mathcal{B}(B \to X_s\gamma)$ with $\mu > 0$; **(a)** for $\tan\beta = 10$ and **(b)** for $\tan\beta = 30$. The contours are in units of 10^{-4}. The meaning of the symbols is explained in fig. 3.6.

where the errors are statistical, systematic, and from theory respectively. Renormalisation scale uncertainties [134] lead to a 10% ($\pm 0.3 \times 10^{-4}$) uncertainty in the SM prediction. The mAMSB contributions were calculated using `micrOmegas` and the total prediction for $\mathcal{B}(B \to X_s\gamma)$ is plotted in fig. 3.22. The combined experimental and theoretical uncertainty does not constrain the mAMSB parameter space at better than 2σ for either of $\tan\beta = 10, 30$.

The overall effect of the $B \to X_s\gamma$ and to a greater extent the $g_\mu - 2$ constraint is to disfavour the low m_0, $m_{3/2}$ region especially when $\tan\beta$ is large.

3.6 Conclusions

If anomaly mediated supersymmetry is present at the 1 to 2 TeV scale, the LHC will observe excesses in various multi-lepton + $\not{p}_T$ channels. Using generic supersymmetry search procedures, and a realistic detector simulation, the ability of the experiments at the LHC to discover AMSB scenarios has been investigated. By selecting events with very large missing transverse momentum and identifying tracks from chargino decays, the wino-like nature of the LSP can be determined, and $m_{\tilde{\chi}_1^+} - m_{\tilde{\chi}_1^0}$ can be measured over a large range in parameter space. Careful study of the tracks left by $\tilde{\chi}_1^{\pm}$s and their decay products can give clear evidence for this class of models even in cases where the chargino is shorter-lived than predicted in minimal AMSB.

Chapter 4

Discovering baryon-violating RPV supersymmetry

4.1 Introduction

If R-parity is violated, then the lightest supersymmetric particle (LSP) can decay and the usual SUSY signature – missing transverse momentum – disappears. The difference in experimental signatures between R-parity violating (RPV) and R-parity conserving (RPC) SUSY models at the LHC depends on the strength of the RPV coupling. When the RPV couplings are small compared to the MSSM gauge couplings, the dominant effect is that the LSP can decay into SM particles.

In this analysis the trilinear coupling λ'' is assumed to dominate. This is the most difficult case at a hadronic collider, because the LSP decay mode $\tilde{\chi}_1^0 \rightarrow qqq$ generates large numbers of jets. The detection of SUSY with dominant λ and λ' RPV couplings has been investigated in [135].

If the RPV couplings and MSSM gauge couplings are of the same order of magnitude, RPV production processes and RPV decays of particles heavier than the LSP become important. There are various ways to detect large (~ 1) couplings at colliders. For a large λ''_{ijk} coupling the branching fractions of RPC and RPV decays of a squark can be of the same order of magnitude (fig. 4.1b), and SUSY particles can be produced singly, as was investigated in [136, 137]. A review of the various search strategies employed at the Tevatron can be found in [138].

If the RPV couplings are very small ($\ll 10^{-5}$) then the LSP is stable on the scale of the detector, and the usual R-parity conserving missing energy signature is recovered, while if $\lambda'' \sim 10^{-5}$ many of the LSPs will decay with observable lifetimes within the detector, producing a striking signature from non-pointing jets. The lifetime of the LSP ($\tilde{\chi}_1^0$) as a function of the strength of the RPV coupling λ''_{cds} is shown in fig. 4.1a.

In the intermediate regime, $10^{-4} \lesssim \lambda'' \lesssim 0.1$, the LSP decays promptly within the detector, but the production and decay of the other sparticles is essentially unchanged. As each event will usually contain two $\tilde{\chi}_1^0$s there will be at least six jets in the final state. Such a scenario has been considered to be rather difficult to detect at the LHC.

In our analysis, initially λ''_{cds} is the only RPV coupling set to a non-zero value. This gives rise to the LSP decay mode $\tilde{\chi}_1^0 \to cds$, which is the most challenging case experimentally, since there are no leptons or b-quarks among the $\tilde{\chi}_1^0$ decay products which can be used as tags for signal events. Unlike many other RPV couplings, λ''_{cds} is not currently constrained by experiment [139]. The possiblity of distinguishing a non-zero λ''_{cds} from the other λ'' couplings is investigated in sec. 4.7.

The RPV coupling was added to a mSUGRA model with five GUT-scale parameters:

- a universal scalar mass, $m_0 = 100$ GeV;
- a universal gaugino mass, $m_{1/2} = 300$ GeV;
- trilinear $H\tilde{f}\tilde{f}$ soft SUSY breaking terms, $A_0 = 300$ GeV;

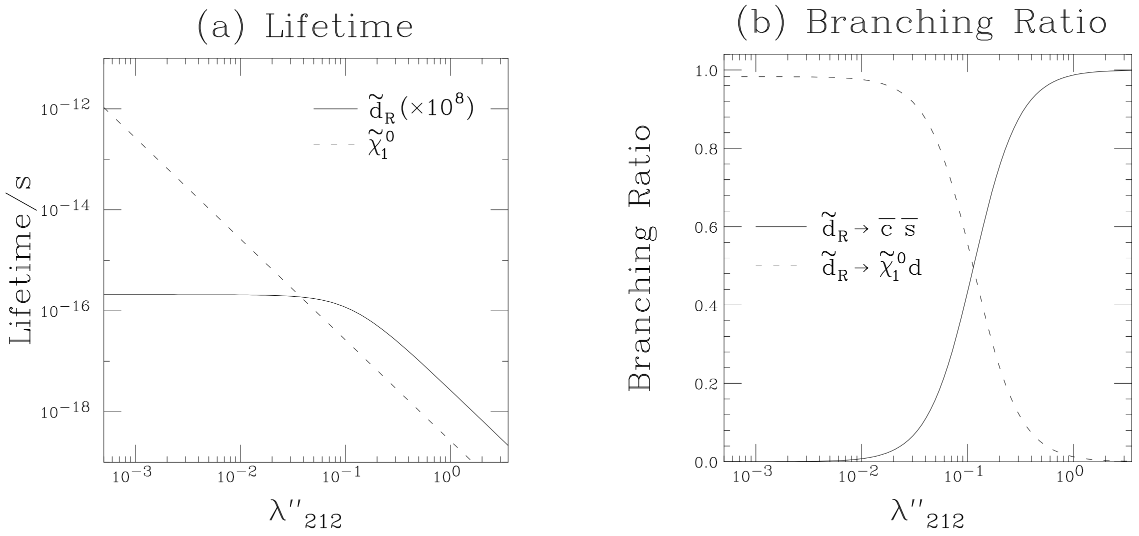

Figure 4.1: **(a)** Lifetimes of the $\tilde{d}_R$ and $\tilde{\chi}_1^0$ and **(b)** branching ratio of RPC (dashed) and RPV (solid) decays of the $\tilde{d}_R$, plotted against λ''_{cds} at the mSUGRA point $m_0 = 100$ GeV, $m_{1/2} = 300$ GeV, $A_0 = 300$ GeV, $\tan\beta = 10$ and sgn μ +. Plot by Peter Richardson.

- the ratio of the vacuum expectation values of the two Higgs doublets, $\tan\beta = 10$;
- and the sign of the SUSY Higgsino mass parameter, $\mu > 0$.

It should be noted that RPV coupling has been provided at the weak scale, and is not used in the evolution from the GUT scale, as was done in [140].

Five sets of parameter values have been extensively studied in the R-Parity (R_P) conserving MSSM. The parameters chosen here correspond to mSUGRA Point 5, with one modification: the value of $\tan\beta$ has been increased from 2.1 to 10 in order to keep the predicted Higgs mass near the current experimental limit. The masses of some key particles in this model are given in table 4.1. Searches in the mSUGRA Point 5 scenario have been well studied in the case of a stable $\tilde{\chi}_1^0$ [30]. At this mSUGRA point, the $\tilde{\chi}_1^0$ is the LSP as must be the case for the analysis to be valid, even though cosmological constraints which require the LSP to be neutral only apply

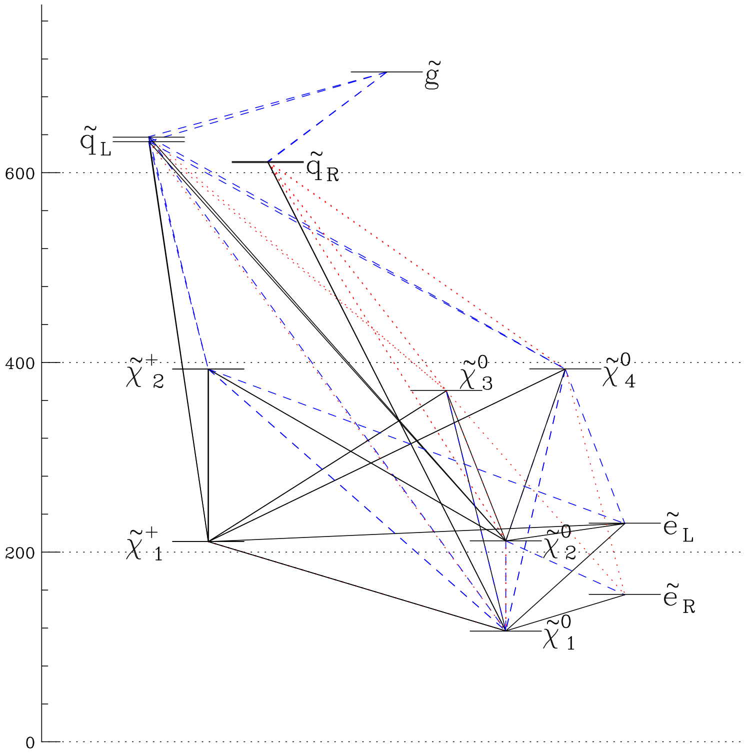

Figure 4.2: Part of the sparticle spectrum at the RPV mSUGRA point under investigation. Solid black lines indicate branching ratios (BR's) greater than 10%, dashed blue lines show BR's in the range 1% → 10%, while red dotted lines show BR's in the range 0.1 → 1%. The sparticles are displaced horizontally for clarity.

$\tilde{\chi}^0_1$	$\tilde{\chi}^0_2$	$\tilde{g}$	$\tilde{u}_R$	$\tilde{u}_L$	$\tilde{d}_R$	$\tilde{d}_L$	$\tilde{l}_R$	$\tilde{l}_L$	h^0
116.7	211.9	706.3	611.7	632.6	610.6	637.5	155.3	230.5	112.7

Table 4.1: Masses of selected particles (GeV) for the model investigated.

if it is stable.

The case of $\lambda''_{cds} = 0.005$ is considered first. This coupling strength gives rise to decay chains essentially identical to those in an RPC model, except for the decay of the $\tilde{\chi}^0_1$ inside the beam pipe, with a lifetime of 1.0×10^{-14} s.

The effect of varying the RPV coupling will be discussed in sec. 4.6. For RPV couplings of order 10^{-6} or smaller [135], the LSP has a sufficiently long lifetime to decay outside of the detector. If the LSP is charged, heavily ionizing low velocity tracks would be seen in the detector, providing a clear signature. This analysis addresses the case of a neutral LSP, the lightest neutralino ($\tilde{\chi}_1^0$), which has negligible interactions with the detector. For small RPV couplings, the experimental signature is then identical to that of an RPC model. However, if RPV couplings are above 10^{-4} [135], the LSP usually decays in the beam pipe and the missing energy signature, seen in RPC models, is not present.

The methods discussed in this chapter are an extension of work started by Lee Drage, and presented in Chapter 5 of his thesis [141].

4.2 Analysis Strategy

In this chapter, `HERWIG-6.1` [66] is used as the event generator[a], and the official ATLAS simulation program `ATLFAST-2.50` [86] is used to simulate the performance of the ATLAS detector. Jets are defined with the cone algorithm with a radius of 0.4, and with a minimum transverse energy of 10 GeV. Since each $\tilde{\chi}_1^0$ decays to three quarks, and in general the decay chain produces the $\tilde{\chi}_1^0$ in association with at least one other quark (typically from squark decay), the mean jet multiplicity (N_{jet}) in the signal events is high.

The principal difficulty in measuring the $\tilde{\chi}_1^0$ mass is the identification of the correct jets from the $\tilde{\chi}_1^0$ decay. Nearly all right-squarks decay via $\tilde{q}_R \rightarrow \tilde{\chi}_1^0 q \rightarrow qqqq$ and one might therefore expect $N_{\text{jet}} = 8$ for $\tilde{q}_R \tilde{q}_R$ production. Gluon radiation by quarks, however, raises this to an average of 9.2 jets, in spite of the fact that the three jets

---

[a] The simulation of RPV events in `HERWIG` is discussed in [142].

from harder $\tilde{\chi}_1^0$s are spatially close together and some merging of jets occurs. In $\tilde{q}_L\tilde{q}_L$ events $N_{\text{jet}} = 10.7$. The increase with respect to the right-handed states is due to the difference in couplings to charginos and neutralinos. Gluinos mostly decay into a squark and a quark and $\tilde{g}\tilde{g}$ events have a higher value of $N_{\text{jet}} = 12.8$. A simple algorithm is used to calculate the jet energies, summing the energy within a cone of size 0.4 about the jet axis in the $\eta - \phi$ plane, and at least 8 jets with $E_T > 25$ GeV are required in signal events.

The analysis proceeds in the following steps:

- Cuts are applied to reduce the SM background. These cuts rely on the presence of lepton pairs in the signal events. Such lepton pairs are produced from the decay chain $\tilde{\chi}_2^0 \to \tilde{l}_R\, l \to ll\tilde{\chi}_1^0$ in most SUSY models. An analysis based on looking for events with two such $\tilde{\chi}_2^0$ decays was proposed in [143] but the rate for events with four leptons is much lower than for events with only one $\tilde{\chi}_2^0$ decay of this type.

- In each signal event, cuts are made on the jet transverse momentum (p_T) in order to preferentially select jets from neutralino decays.

- All possible combinations of three of the selected jets are inspected, and their invariant mass, m_{jjj}, calculated. Events are retained if two combinations are compatible with the same candidate $\tilde{\chi}_1^0$ mass.

- One of these three-jet $\tilde{\chi}_1^0$ candidates is combined with an opposite sign, same flavour (OSSF) lepton pair. The invariant mass of this system, $m_{jjj\ell\ell}$, is a $\tilde{\chi}_2^0$ candidate. A clear peak at the $\tilde{\chi}_1^0$, $\tilde{\chi}_2^0$ masses in the m_{jjj}, $m_{jjj\ell\ell}$ plane is then observed.

- The $\tilde{l}_R$ and the $\tilde{q}_L$ masses are reconstructed using 3-jet combinations in the 2-dimensional ($\tilde{\chi}_1^0$, $\tilde{\chi}_2^0$) mass peak.

4.3 Standard Model Background

The SM background for this model was considered in [30, 141]. It is shown in [144] that the inclusive SUSY signal can be separated from the SM background by requiring that each event contains:

- at least 8 jets with $E_T > 25$ GeV;
- at least one jet with $E_T > 100$ GeV;
- transverse sphericity> 0.2, transverse thrust< 0.9;
- $m_{T,\text{cent}} > 1$ TeV, where $m_{T,\text{cent}} = \sum p_T^{\text{jet}} + \sum p_T^{\text{lepton}}$, where the sum includes central jets and leptons (i.e. with pseudorapidity $|\eta| < 2$);
- at least two leptons (e or μ) with $p_T > 15$ GeV and $|\eta| < 2.5$.

With these cuts, the signal to background ratio is greater than 10 in parton-shower Monte-Carlo simulations [144]. However current Monte-Carlo event generators are not capable of reliably simulating eight jet plus two lepton production with correct QCD matrix elements. For this reason, the SM background has not been explicitly simulated in this study. Instead, we used a sample of events containing eight jets and two leptons distributed according to phase space, and ensure that the analysis is not affected by this background.

In SUSY events, lepton pairs are created in the decay $\tilde{\chi}_2^0 \to \tilde{l}_R l \to ll\tilde{\chi}_1^0$. The leptons are therefore required to be OSSF. The invariant-mass distribution of the lepton pairs created in this decay has a kinematic edge [30, 69] which is given by:

$$m_{\ell\ell}^{max} = \sqrt{\frac{[m^2(\tilde{\chi}_2^0) - m^2(\tilde{l}_R)] \times [m^2(\tilde{l}_R) - m^2(\tilde{\chi}_1^0)]}{m^2(\tilde{l}_R)}}, \tag{4.1}$$

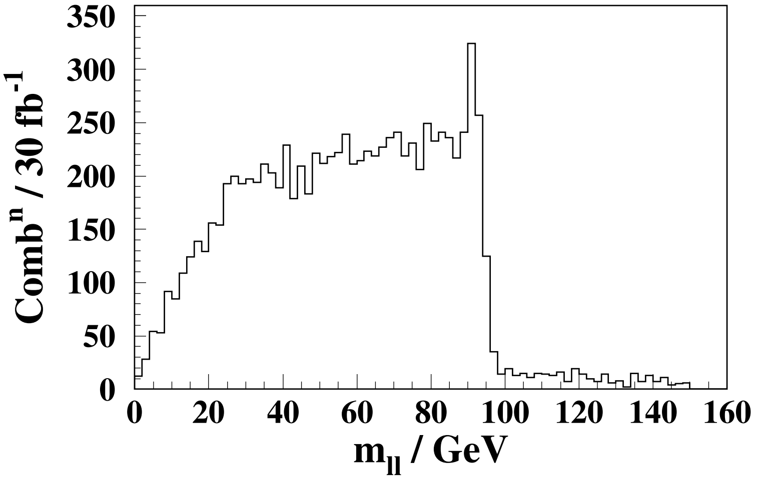

Figure 4.3: The dilepton invariant mass for events with an OSSF electron or muon pair, after the SM cuts have been applied. The kinematic limit for the decay chain shown in fig. 4.4 is at 95.1 GeV. Events are excluded if there is no jet combination which passes the jet cuts described in sec. 4.4. For the mSUGRA point chosen it happens that the kinematic edge lies just above the peak at $m(\mathrm{Z}^0)$ from the decay $\mathrm{Z}^0 \to \ell\ell$.

and is simulated after experimental resolution in fig. 4.3.

With the particular parameter set chosen this edge is calculated as 95.1 GeV. Accordingly, events are required to have a lepton pair with an invariant mass below this value. The corresponding edge can be easily measured for other parameter sets.

4.4 Detection of the $\tilde{\chi}_1^0$ and $\tilde{\chi}_2^0$

Many different decay chains can contribute to the SUSY signal selected by the cuts. One important example, $\tilde{q}_L \to \tilde{\chi}_2^0 q \to \tilde{l}_R \ell q \to \tilde{\chi}_1^0 \ell\ell q \to qqq\ell\ell q$, is shown in fig. 4.4.

When λ''_{cds} is small, there are nearly always two $\tilde{\chi}_1^0$s produced in an event and one can therefore search for two sets of three jets with similar invariant mass. An upper

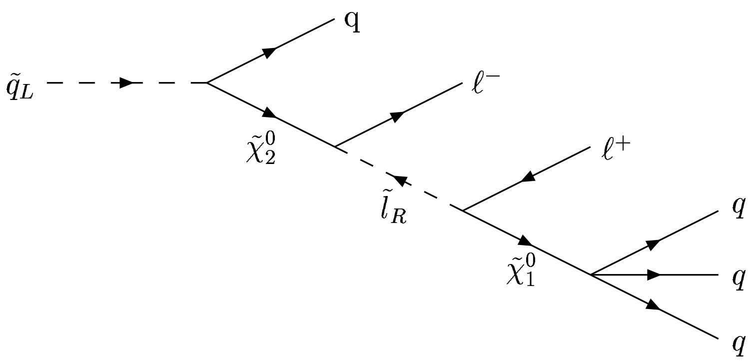

Figure 4.4: One of the decay chains of the $\tilde{q}_L$ contributing to the signal.

limit on the invariant mass difference of $\delta m_{jjj} = |m_{jjj}^{(a)} - m_{jjj}^{(b)}| < 20$ GeV is used in this analysis, where a and b label the two $\tilde{\chi}_1^0$ LSP candidates.

In order to limit the combinatorial background, the search for the $\tilde{\chi}_1^0$ signal is initially restricted to events with $8 \leq N_{\rm jet} \leq 10$, with the following cuts on the allowed range of jet transverse momenta in GeV:

- $100 < p_T^{(a1)}$; $17.5 < p_T^{(a2)} < 300$; $15.0 < p_T^{(a3)} < 150$;
- $17.5 < p_T^{(b1)} < 300$; $17.5 < p_T^{(b2)} < 150$; $15.0 < p_T^{(b3)} < 75$,

where $a1$ denotes the highest p_T jet from neutralino candidate a, and so on.

Candidate sets of jets from the $\tilde{\chi}_1^0$ decay can also be identified by their separation in the $\eta - \phi$ plane. For both $\tilde{\chi}_1^0$s, cuts are made on the distance between the hardest and next hardest jets (ΔR_{12}) and between the combined momentum vector of the two hardest quarks and the softest quark (ΔR_{12-3}), where $\Delta R = \sqrt{(\Delta\phi)^2 + (\Delta\eta)^2}$. The following cuts are chosen based on simulations:

- $\Delta R_{12}^{(a)} < 1.3$; $\Delta R_{12-3}^{(a)} < 1.3$;
- $\Delta R_{12}^{(b)} < 2.0$.

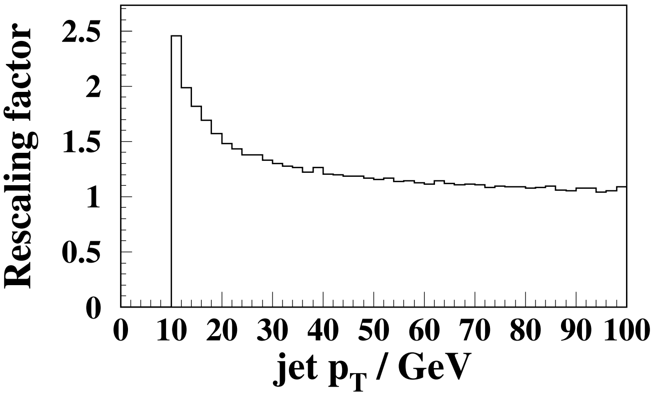

Figure 4.5: The rescaling factor applied to the observed jet energy as a function of jet p_T.

Since the SUSY cross section is dominated by production of squarks and gluinos, about 95% of events have two hard jets with $E_T^{(h1)} > 200$ GeV and $E_T^{(h2)} > 100$ GeV from the squark decays. It is required that two jets in an event satisfy these cuts. Those jets are not then used to construct $\tilde{\chi}_1^0$ candidates, decreasing the background from wrong combinations.

For each combination of jets passing the kinematic cuts, the jet energies are rescaled according to their p_T, to allow for energy lost out of the jet cones. The rescaling function, shown in fig. 4.5, is the ratio p_T^{jet}/p_T^u used in `ATLFAST`.

The reconstructed masses of the $\tilde{\chi}_1^0$ candidates are shown in fig. 4.6a. If N_{comb} combinations of jets from one event pass the cuts, the masses from each combination are plotted with weight $1/N_{\mathrm{comb}}$, so that the total weight for any one event is unity. If there are more than five combinations which pass the cuts in any one event then that event is omitted. In events with more than one combination passing the cuts,

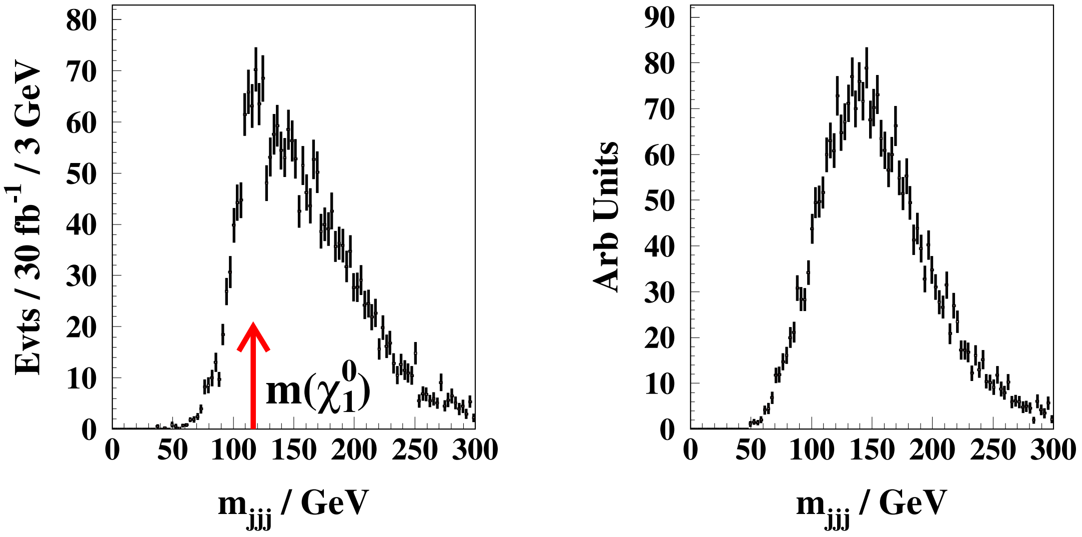

(a) (b)

Figure 4.6: **(a)** The invariant mass of three-jet combinations passing the cuts described in the text. The mass peak from the decay $\tilde{\chi}_1^0 \to qqq$ can be seen above the background from wrong combinations of jets. The input $\tilde{\chi}_1^0$ mass is indicated by the arrow. **(b)** A phase-space sample shows a peak in much the same region.

two combinations of jets often differ only in the choice of jets for one of the two $\tilde{\chi}_1^0$s. In such cases, the repeated mass combination is included only once.

Up until this point the method is based closely on that of Drage [141]. In particular, the cuts to reduce the SM background, and the jet cuts, are as presented in his thesis. However the method of Drage now encounters serious problems.

There is a broad combinatorial background beneath the $\tilde{\chi}_1^0$ mass peak in Figure 4.6a, the shape of which is defined by the kinematic cuts and is reproduced by the phase-space sample, as shown in fig. 4.6b. Drage attempts to remove the combinatorical background by subtracting from the m_{jjj} distribution a 'background' sample consisting of combinations in which the two $\tilde{\chi}_1^0$ candidates had masses differing by

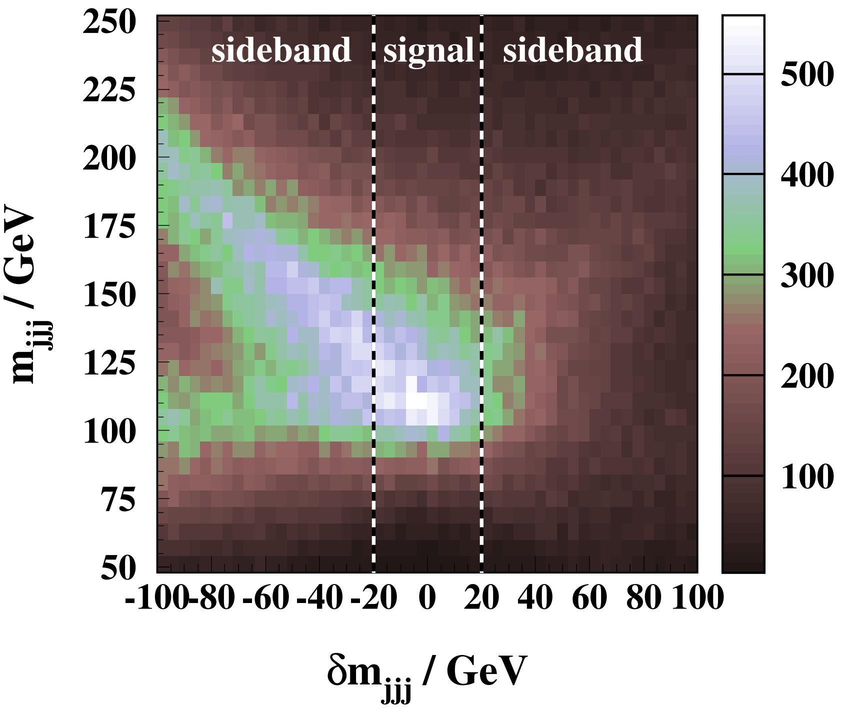

Figure 4.7: The colour gives the density of the reconstructed neutralino candidates as a function of their reconstructed masses (m_{jjj}) and of the mass difference $\delta m_{jjj} = m^{(a)}_{jjj} - m^{(b)}_{jjj}$ between the two candidates. The true neutralino peak is the dense region at (0, 117). Normalising the 'sidebands' to the 'signal' at large and small m_{jjj} and subtracting them will create an artificial peak in m_{jjj} because the sidebands are depleted at intermediate m_{jjj}.

$20 < \delta m_{jjj} < 100$ GeV. The sidebands were normalised at the edges of the m_{jjj} distribution.

Drage found that after background subtraction, the sample still contained features which he was unable to explain. He was nevertheless able to find a peak in the subtracted jjj mass plot, around which he selected combinations in order to reconstruct the higher mass sparticles.

The problem with the background-subtraction method of Drage is that the peak it produces is also found in a phase-space sample, *i.e.* in the absence of any neutralino decays. This occurs because events in which the neutralino candidates have very different masses will tend to contribute more at the edges of the m_{jjj} distribution, as can be seen in fig. 4.7. This means that even after sideband subtraction, a peak will remain near the center of the distribution, even in the absence of any signal. The creation of a false peak is most undesirable, so background-subtraction method of Drage is not used in this analysis.

In this analysis, instead of subtracting the background, the extra information from the lepton pair is used to dilute it. The $\tilde{\chi}_2^0$ is reconstructed using the decay chain $\tilde{\chi}_2^0 \to \tilde{l}_R\, l \to ll\tilde{\chi}_1^0$ by forming the total invariant mass of the OSSF dilepton pair and one of the 3-jet candidates, choosing the $\tilde{\chi}_1^0$ candidate which is nearest in $\eta - \phi$ to either lepton. The branching ratios of the next-to-lighest neutralino are in table 4.2.

$\mathcal{B}(\tilde{\chi}_2^0 \to X)$	
$\tilde{\chi}_1^0\ Z^0$	3.6%
$\tilde{\chi}_1^0\ \tilde{e}_R^\pm\ e^\mp$	11.1%
$\tilde{\chi}_1^0\ \tilde{\mu}_R^\pm\ \mu^\mp$	11.1%
$\tilde{\chi}_1^0\ \tilde{\tau}_1^\pm\ \tau^\mp$	73.6 %

Table 4.2: $\tilde{\chi}_2^0$ branching ratios at the point described in the text.

A clear peak in the ($\tilde{\chi}_1^0$, $\tilde{\chi}_2^0$) mass plane is visible in fig. 4.8a. Fig. 4.9 shows slices through the peak along the axes $m^\pm = (m_{jjj\ell\ell} \pm m_{jjj})/\sqrt{2}$. The peak is present in the central slices, while the sidebands show similar shapes to the background under the peak. It is clear that this peak is not determined by the kinematic cuts, as it is absent in the phase-space sample (fig. 4.8b). In addition it is found that the position of the peak accurately follows the input masses, when the lightest two neutralino masses are varied from {116.7, 211.9} to {137.8, 252.6} GeV.

The data in the rectangle shown in fig. 4.8 were fitted with a 2-d gaussian. Since

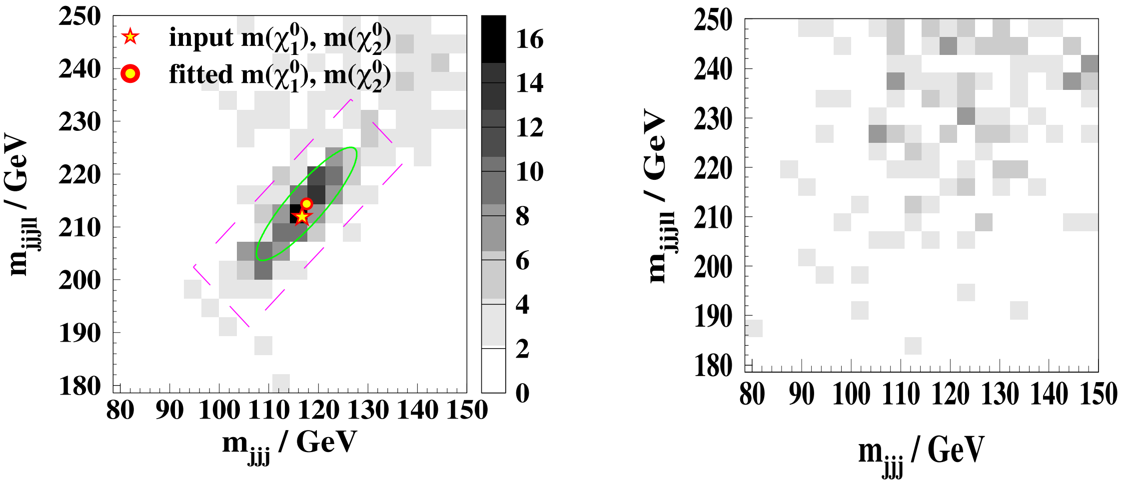

(a) (b)

Figure 4.8: **(a)** The $\tilde{\chi}_1^0$ (m_{jjj}) and $\tilde{\chi}_2^0$ ($m_{jjj\ell\ell}$) candidates. The number of jet combinations passing the cuts per 30 fb^{-1} is given by the key. The circle and the ellipse show the peak and standard deviation of a 2-d gaussian fitted to the data contained in the dashed box. The star shows the input masses. **(b)** The corresponding (m_{jjj}, $m_{jjj\ell\ell}$) invariant mass combinations from the phase-space sample show no such peak.

m_{jjj} and $m_{jjj\ell\ell}$ are highly correlated, the peak was fitted in the rotated (m^+, m^-) coordinate system in which the correlations are smaller. The mass difference relies on lepton rather than jet momenta, so the width in the m^- direction ($\approx$ 4 GeV) is smaller than in the m^+ direction ($\approx$ 15 GeV). The standard error on the peak was 5.4 GeV in m^- and 1.8 GeV in m^+. This corresponds to a 4 GeV uncertainty in each of the neutralino masses.

The fitted masses for the lightest two neutralinos were $\{118.9, 215.5\}$ GeV, which are slightly high when compared to the input values of $\{116.7, 211.9\}$ GeV. This is due to several effects, including overlap between the jets, and the contribution of energy from the underlying event in the jet cones. Indeed it is expected that the simple rescaling factor will overcompensate for energy losses from jet cones, since

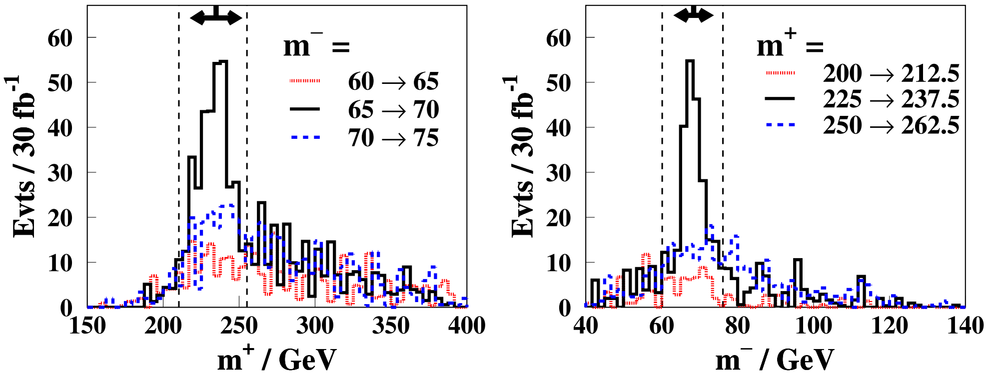

Figure 4.9: Slices taken through fig. 4.8a in the rotated (m^+, m^-) coordinate directions. The 2-dimensonal fit was performed on the data contained in the region between the dotted lines. The dotted and dashed lines are from the side-bands. The fitted peak and width of the gaussian are shown by the thick line and double arrow at the top of each plot.

the three jets from the $\tilde{\chi}_1^0$ decay are close in $\eta - \phi$, so energy losses from one cone can end up in one of the other two.

A fuller investigation of these effects is beyond the scope of this study, requiring as it does a full investigation of the calorimeter calibration procedure for multi-jet events. It is estimated that in the actual experiment, the uncertainty in the absolute jet energy scale will be of the order of 1% for jets with $p_T > 50$ GeV [30]. For lower energy jets an uncertainty of 2-3% is more likely. With real data, therefore, it may be possible to reduce the systematic uncertainty on the $\tilde{\chi}_1^0$ mass to 3 GeV.

4.5 Detection of the $\tilde{l}_R$ and $\tilde{q}_L$

For the measurement of the slepton mass, having fitted the $\tilde{\chi}_1^0$ and $\tilde{\chi}_2^0$ masses, combinations are selected within $1 \times \sigma$ of the peak. These combinations, with two

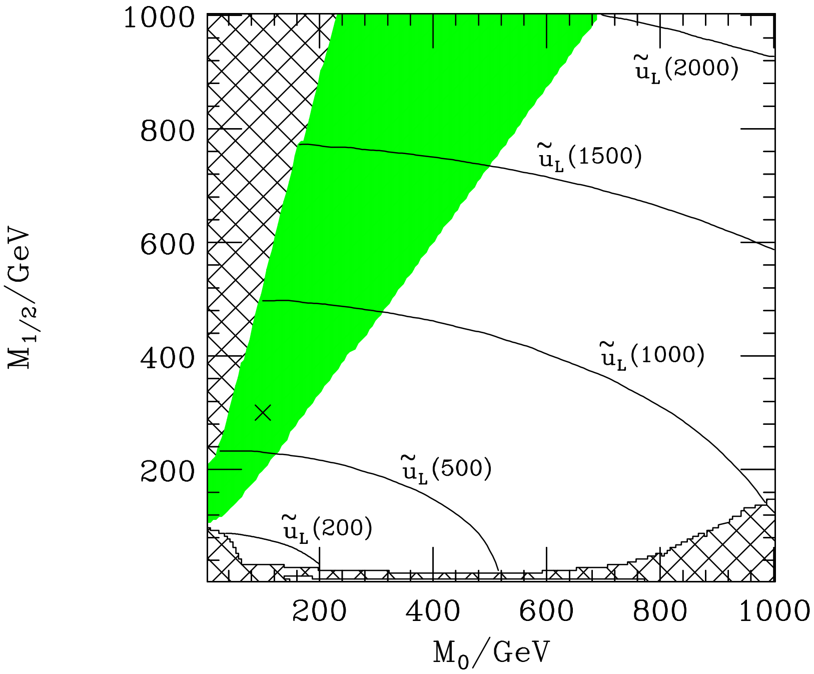

Figure 4.10: The region of mSUGRA parameter space over which the decay $\tilde{\chi}_2^0 \to \tilde{l}_R\ell \to \tilde{\chi}_1^0\ell\ell$ occurs is shaded. M_0 is the universal scalar mass, and $M_{1/2}$ is the universal gaugino mass at the GUT scale. The lower hatched region is excluded by lack of electroweak symmetry breaking or have charge- or colour-breaking minima, whereas in the upper hatched region the $\tilde{\chi}_1^0$ is not the LSP and this analysis does not apply. The contours show the mass of the $\tilde{u}_L$ squark. The × marker shows the chosen point. The other parameters are: $\tan\beta = 10$, $A_0 = 300$ GeV and $\mu > 0$. Plot by Peter Richardson.

OSSF leptons preferentially select the decay chain $\tilde{\chi}_2^0 \to \tilde{l}_R l \to ll\tilde{\chi}_1^0$. This decay is only available when the slepton is lighter than the $\tilde{\chi}_2^0$. The region of mSUGRA parameter space in which $m(\tilde{\chi}_2^0) > m(\tilde{l}_R)$ is shown in fig. 4.10. Beyond this region the $\tilde{\chi}_2^0$ can decay to the $\tilde{\chi}_1^0$ through Z^0 emission, or if $m_{\tilde{\chi}_2^0} \lesssim m_{\tilde{\chi}_1^0} + m_{Z^0}$ in a three-body decay, both of which are also sources of OSSF lepton pairs. In any of these cases one may obtain the lighest two neutralinos from jjj and $jjj\ell\ell$ invariant mass combinations. However it is only in the shaded region of fig. 4.10 where the $jjj\ell$ mass combination may correspond to the slepton mass.

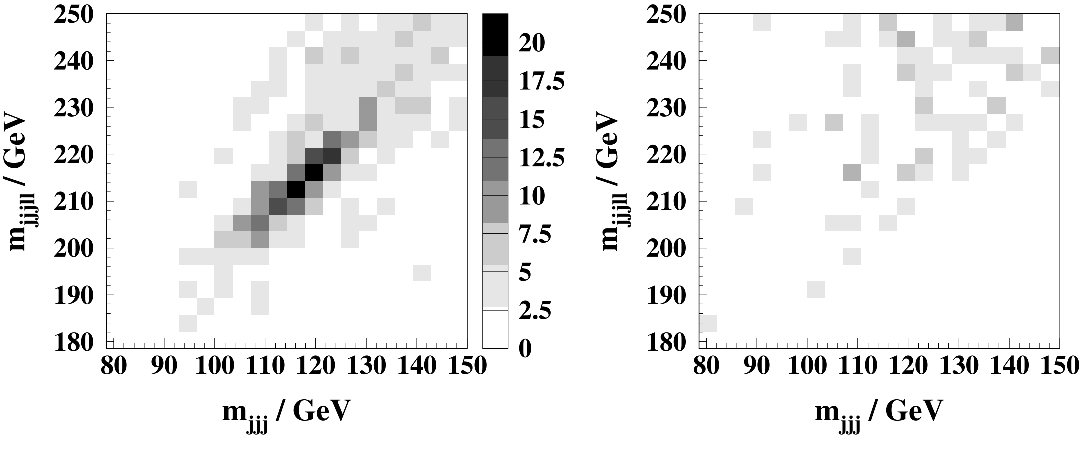

(a) (b)

Figure 4.11: Reconstructed masses of the $\tilde{\chi}_1^0$ and $\tilde{\chi}_2^0$ **(a)**, and phase-space sample **(b)** similar to fig. 4.8 but with $8 \leq N_{\text{jet}} \leq 11$.

The dilepton invariant mass distribution (fig. 4.3) for the point investigated shows only a very small peak at the Z^0 mass, but a clear kinematic edge, indicating that the slepton decay chain $\tilde{\chi}_2^0 \to \tilde{l}_R l \to ll\tilde{\chi}_1^0$ dominates. This is expected at this point, since the $m(\tilde{\chi}_2^0) - m(\tilde{\chi}_1^0)$ mass difference of 95.2 GeV means that there is little phase space available for the decay $\tilde{\chi}_2^0 \to \mathrm{Z}^0\tilde{\chi}_1^0$. If the masses and couplings for this decay were significant, then one would exclude events with dilepton invariant mass near $m(\mathrm{Z}^0)$ from the $\tilde{l}_R$ measurement. Both chains may have been preceded by $\tilde{q}_L \to \tilde{\chi}_2^0 q$, so both can be used for the $\tilde{q}_L$ mass measurement.

Recall that the initial sample of $\tilde{\chi}_1^0$ candidates was restricted to events with $8 \leq N_{\text{jet}} \leq 10$ in order to reduce the combinatoric background. However, choosing combinations from under the $(\tilde{\chi}_1^0, \tilde{\chi}_2^0)$ mass peak removes much of the background, so in this section the jet multiplicity cut is therefore relaxed to $8 \leq N_{\text{jet}} \leq 11$ in order to increase the available statistics (see fig. 4.11). The invariant mass of the three-jet neutralino candidates is adjusted to the best-fit mass of the $\tilde{\chi}_1^0$ by rescaling

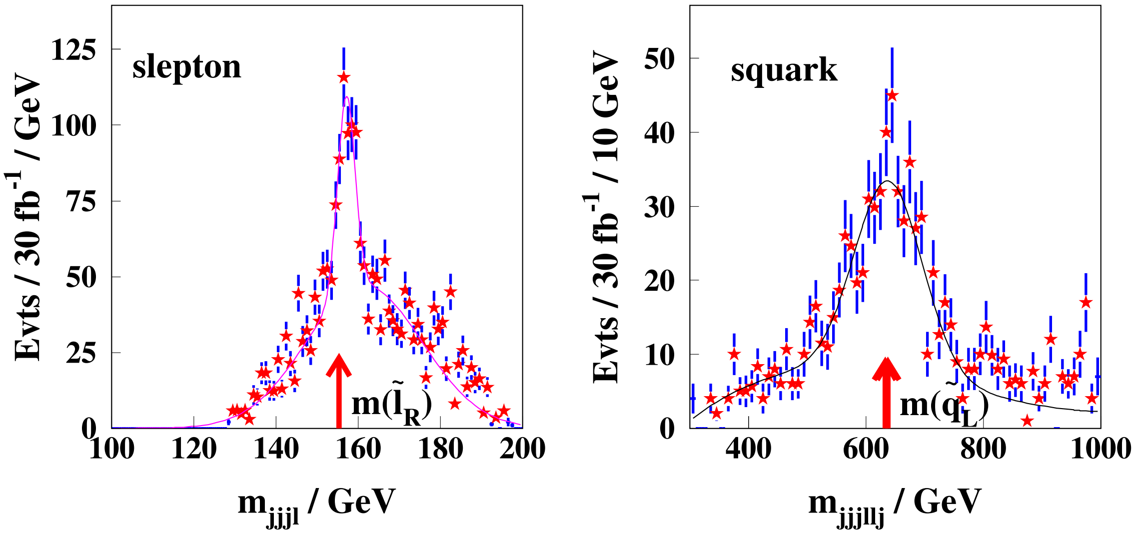

(a) (b)

Figure 4.12: The masses of **(a)** $\tilde{l}_R$ and **(b)** $\tilde{q}_L$ candidates. Only combinations from under the $(\tilde{\chi}_1^0,\tilde{\chi}_2^0)$ mass peak, and satisfying the cuts described in the text are plotted. Each jjj invariant mass has been rescaled to the fitted $\tilde{\chi}_1^0$ mass. The total contribution from each event has been rescaled to unity for each event in which at least one combination passes the cuts. The $\tilde{l}_R$ and $\tilde{q}_L$ masses are indicated by the arrows. The fitted functions are described in the text.

the $\tilde{\chi}_1^0$ jet momenta by the same factor.

The $\tilde{l}_R$ mass is found by combining the $\tilde{\chi}_1^0$ candidate closest to a lepton in $\eta-\phi$ with that lepton. The resulting invariant mass distribution, $m_{jjj\ell}$, is shown in fig. 4.12a. The sharp peak was fitted with a gaussian, with another gaussian for the background. This gave $m(\tilde{l}_R) = 157.1 \pm 0.2$ GeV, which is slightly high when compared to the input value of 155.3 GeV for the same reasons as were discussed in sec. 4.4.

The experimental electron and muon momentum scale uncertainties are expected to be small fractions of 1% [30], so the systematic error in the slepton mass measurement will be dominated by the same (3 GeV) jet scale uncertainty as $m(\tilde{\chi}_1^0)$. The statistical error in rescaling the 3-jet invariant mass to the fitted $m(\tilde{\chi}_1^0)$ peak introduces another 3 GeV systematic error into the $\tilde{l}_R$ and $\tilde{q}_R$ masses. The overall systematic error in $m(\tilde{l}_R)$ is therefore $3 \oplus 3 = 4.2$ GeV.

The hardest two jets in the event are assumed to have come from squark or gluino decay, and so are not used in making three-jet combinations for neutralino candidates. The $\tilde{q}_L$ mass is found by combining each $\tilde{\chi}_2^0$ candidate with the harder of these two leading jets. To reduce the background, combinations are selected within $2 \times \sigma$ of the m($\tilde{l}_R$) peak. This allows the relaxation of the cut around the ($\tilde{\chi}_1^0$,$\tilde{\chi}_2^0$) peak from 1 to $2 \times \sigma$. The resultant invariant mass distribution, $m_{jjj\ell\ell j}$, is shown in fig. 4.12b. A peak is visible near the $\tilde{u}_L$ and $\tilde{d}_L$ masses of 633 GeV and 638 GeV respectively, but the resolution is not sufficient to separate the states.

The background was modelled by finding the invariant-mass distribution of the $\tilde{\chi}_2^0$ candidates with the hardest jet from other $\tilde{q}_L$ candidate events. A gaussian fit to the signal with this background shape gave $m(\tilde{q}_L) = 638 \pm 4$ GeV. The uncertainty in modelling the background was estimated by fitting the distribution with other, simpler background shapes. These decrease the position of the peak to 634 GeV (for a resonance-shaped background) and to 632 GeV (for a linear background). This shows a systematic uncertainty in the $\tilde{q}_L$ mass of about 5 GeV. The hard jet used in the calculation of $m(\tilde{q}_L)$, has $p_T > 100$ GeV introducing an uncertainty in the mass scale of 1% [30], or 6 GeV. Carrying forward a 3 GeV uncertainty in the jjj invariant mass scale and 3 GeV from the $\tilde{\chi}_1^0$ fit, the total systematic error in the squark mass is 9 GeV.

At this mSUGRA point the dominant decay mode of the $\tilde{q}_R$ is $\tilde{q}_R \to \tilde{\chi}_1^0 q$. One might therefore try to reconstruct the $\tilde{q}_R$ mass by combining the $\tilde{\chi}_1^0$ candidate not used in the $\tilde{q}_L$ reconstruction with the second hard jet. However while the cuts which were applied to reduce the SM background, *i.e.* requiring the presence of two leptons, mean that almost all the signal events contain a $\tilde{q}_L$, they do not necessarily contain a right squark. Only a third of the signal events actually contain a $\tilde{q}_R$. Most of the SUSY events at this mSUGRA point come from gluino production which will either be rejected due to the large number of jets or contain additional hard jets from the gluino decay, and hence have a large combinatoric background for the $\tilde{q}_R$ reconstruction. In an attempt to reduce this background it is possible to use cuts on the $\tilde{\chi}_2^0$ and $\tilde{l}_R$ masses from $\tilde{q}_L$ decay on the other side of the event such that there is only one $\tilde{q}_R$ candidate. However this reduces the available statistics so that a signal cannot be observed. This combination of factors makes it impossible to reconstruct the $\tilde{q}_R$ mass at this mSUGRA point with the luminosity simulated.

4.6 Other values of λ''_{cds}

The method outlined above is relatively insensitive to the size of the coupling λ''_{cds}. However as the RPV coupling λ''_{cds} is decreased the lifetime of the $\tilde{\chi}_1^0$ increases as shown in fig. 4.1a. The method will start to fail when $\tilde{\chi}_1^0$s predominately decay beyond the first tracking layer of the detector. Special reconstruction could, in principle, increase this by about an order of magnitude, at which point the decays would occur outside of the tracking volume. The maximum value of λ'' for which the analysis is valid can therefore be found by excluding events when one or other of the $\tilde{\chi}_1^0$s has travelled more than 100 mm (1000 mm) from the interaction point in the transverse direction.

As can be seen in fig. 4.13 statistics become limiting for λ''_{cds} less than about 10^{-5}, when $c\tau \approx 800$ mm. With smaller couplings the RPV decay of the $\tilde{\chi}_1^0$ effectively switches off, and a RPC analysis based on a missing transverse energy + lepton(s) signature, such as [30, 69], is effective.

If λ''_{cds} is larger than 0.1, an initial $\tilde{q}_R$ often decays immediately into 2 jets and then

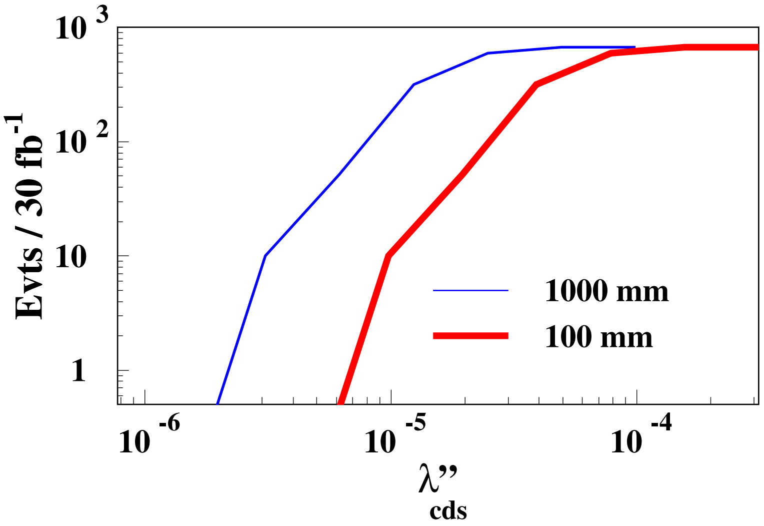

Figure 4.13: The number of events in which both $\tilde{\chi}_1^0$s have transverse decay lengths less than 100 mm (thick line), or less than 1000 mm (thin line), as a function of the RPV coupling. Events which do not have two 3-jet combinations within $1 \times \sigma$ of the ($\tilde{\chi}_1^0$,$\tilde{\chi}_2^0$) peak found for $\lambda''_{cds} = 0.005$ are excluded.

only one 3 jet invariant mass combination will necessarily be close to the neutralino mass.

The size of the RPV coupling can be determined from the $\tilde{\chi}_1^0$ lifetime, as shown in fig. 4.1a. The lifetime is, in principle, measurable for a wide range of couplings, by using vertexing information. However the need for detector-level Monte-Carlo simulation makes the measurement of λ''_{cds} beyond the scope of this study.

4.7 Extracting the Flavour Structure

If RPV couplings are observed, it is probable that they come from an underlying theory which also determines the fermion mass spectrum. This idea has been explored [145–148] in the context of gauged $U(1)_X$ models of flavour. In such models, the hierarchy of the low-energy Yukawa couplings is generated from selection rules in interactions involving an approximate symmetry. Such models also predict a hierarchical pattern of RPV couplings from the same symmetry from which the fermion mass spectrum is derived. Thus the determination of the flavour structure of an RPV coupling could be a vital clue in the search for the origin of flavour.

In this section the flavour content of the quark jets from $\tilde{\chi}_1^0$ decays is investigated. The aim is to identify which λ''_{ijk} coupling is dominant in the neutralino decay. The index i is the generation number of an up-type quark, and j and k correspond to down-type quarks. The coupling is antisymmetric in j and k, so there are nine possible non-zero elements.

Three of the couplings, λ''_{tjk}, produce very different signatures because they allow the $\tilde{\chi}_1^0$ to decay via the top quark. If the neutralino is lighter (heavier) than the top quark then the decay is propagator (phase-space) suppressed. For the mSUGRA point investigated (which is described in sec. 4.1) the branching ratio through the top coupling is a factor of 4.2×10^6 smaller than through a non-top coupling of the same size.

For a top mode to dominate the decay, a λ'' coupling to top would need to be a factor of at least 2000 greater than any of the non-top couplings. In that case the lightest neutralino would typically be long-lived (fig. 4.14) and for $\lambda''_{tjk} \lesssim 10^{-2}$ nearly all $\tilde{\chi}_1^0$ s would decay outside the detector. Determination of these couplings could then only be achieved by searching for the rare decay of $\tilde{\chi}_1^0$s in the active volume, while sparticle mass measurements could be made in the same way as for the R_P conserving case [30].

The other six couplings are investigated – λ''_{uds}, λ''_{udb}, λ''_{usb}, λ''_{cds}, λ''_{cdb} and λ''_{csb} – assuming that one is significantly larger than the others. Since the branching ratio

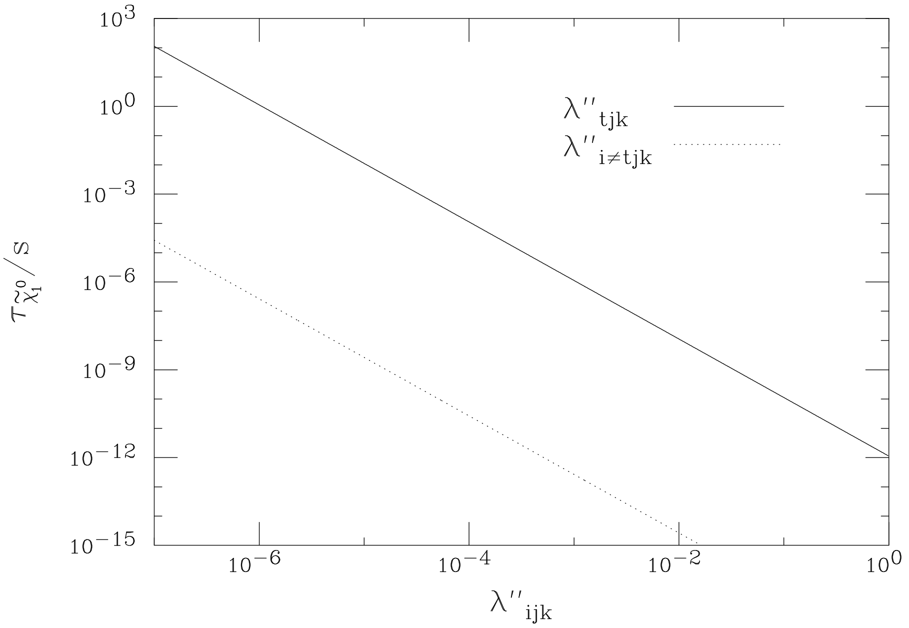

Figure 4.14: The lifetime of the $\tilde{\chi}^0_1$ at the mSUGRA point described in the text, with one of λ''_{ijk} non-zero. The solid line shows the lifetime for a dominant top quark coupling, which leads to the decay $\tilde{\chi}^0_1 \to \mathrm{qq't^*} \to \mathrm{qq'bW^*} \to \mathrm{qq'bff'}$, where q and q′ are quarks other than top and f and f′ are Standard Model fermions. The dashed line shows the lifetime for couplings to quarks other than the top. The calculation approximates the final state particles as massless, so that the lines for λ''_{tjk} are the same for all j, k, as are those for λ''_{ijk} for all $i \neq \mathrm{t}, j, k$. Plot by P. Richardson [2].

is proportional to the square of the coupling, it is sufficient for this analysis that all the subdominant couplings are 4.5 times smaller than the dominant coupling. Then just 5% of all $\tilde{\chi}^0_1$s will decay though the subdominant channel, and 90% of events, each with two $\tilde{\chi}^0_1$s, will contain only dominant-coupling decays.

4.7.1 Vertex Tagging

The lifetimes of hadrons containing *b*- and *c*-quarks give rise to displaced vertices which can be reconstructed from charged tracks in the inner detector. In general the lifetimes of charmed hadrons are shorter than for hadrons containing a *b*-quark,

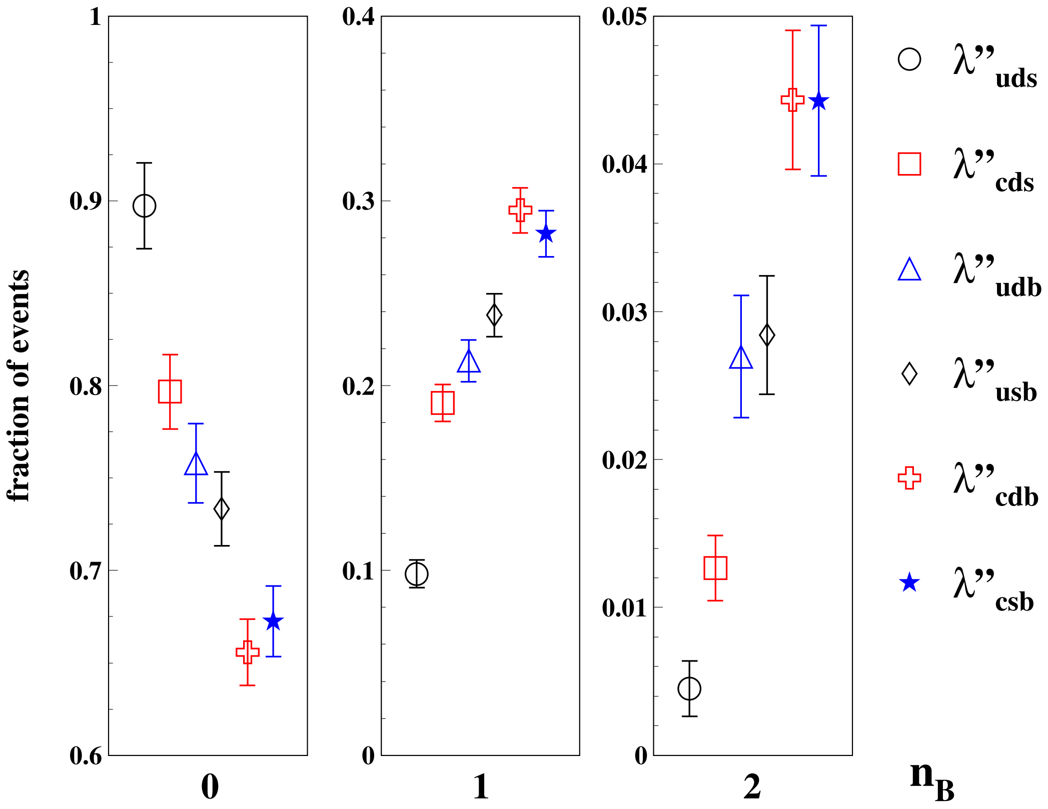

Figure 4.15: The fraction of signal events with 0, 1, and 2 vertex tags, for different types of RPV coupling λ''. The statistical errors are those expected for an integrated luminosity of 30 fb^{-1}. Points are horizontally displaced to allow them to be distinguished by eye.

for example $c\tau_{D^0} = 124\ \mu$m compared to $c\tau_{B^0} = 468\ \mu$m. This allows statistical separation of c-quark jets from b-quark jets, and of c- and b-jets from light quark (u, d, s) and gluon jets. Strange hadrons have longer lifetimes with $c\tau$ of the order of tens of centimeters. Since they decay to a small number of particles it is difficult to reconstruct a secondary vertex, and so strange hadrons cannot be tagged within jets in the LHC environment.

The vertex tagging performance of the ATLAS Inner Detector was simulated in [30]. In that study a likelihood ratio method was applied to the transverse impact

b-tagging efficiency	Rejection factor	
ϵ_b	u, d, s and g jets (r_j)	c-jets (r_c)
0.33	1400	22.9

Table 4.3: b-tagging efficiencies and mis-tagging rejection factors from a full simulation of the ATLAS inner detector [30]. $1/r_c$ is the probability of tagging a c-jet, while $1/r_j$ is the probability of tagging a u, d, s or gluon jet, averaged over p_T, η and ϕ. The typical reconstructed jet p_T scale is 50 GeV.

parameter (d_0) of the tracks within the jet cone. The resultant b-tagging efficiency and the rejection rates for c- and other jets were parameterised as functions of the transverse momentum and pseudorapidity of the reconstructed jet and were implemented in ATLFAST. The rejection factors, averaged over all directions and transverse momenta, are summarised in table 4.3. In order to select a higher purity sample, a rather low b-tagging efficiency (33%), was tolerated.

The proportions of events with 0, 1 and 2 tagged jets are shown in fig. 4.15, for the six different λ'' couplings. As expected, the vertex tagging rate is greatest when the $\tilde{\chi}_1^0$ decay products include both c and b quarks, and smallest for couplings which produce light-quark daughters. As d- and s-jets cannot be distinguished in this analysis, there is no discrimination between $\lambda''_{i\mathrm{db}}$ and $\lambda''_{i\mathrm{sb}}$ (for i=u,c).

In these simulations, in which $\lambda'' = 5 \times 10^{-3}$, the $\tilde{\chi}_1^0$ lifetime of 10^{-14} seconds corresponds to a typical decay length $c\tau$ of 3 μm. This is short in comparison with typical b- and c-jet vertex displacements so it should not severely affect vertex reconstruction. However the lifetime is inversely proportional to the square of the coupling strength. When $c\tau$ becomes bigger than about 3 cm (for $\lambda'' \lesssim 5 \times 10^{-5}$) special vertex reconstruction would be required. Vertex tagging becomes almost impossible when neutralinos travel more than about 30 cm in the transverse direction

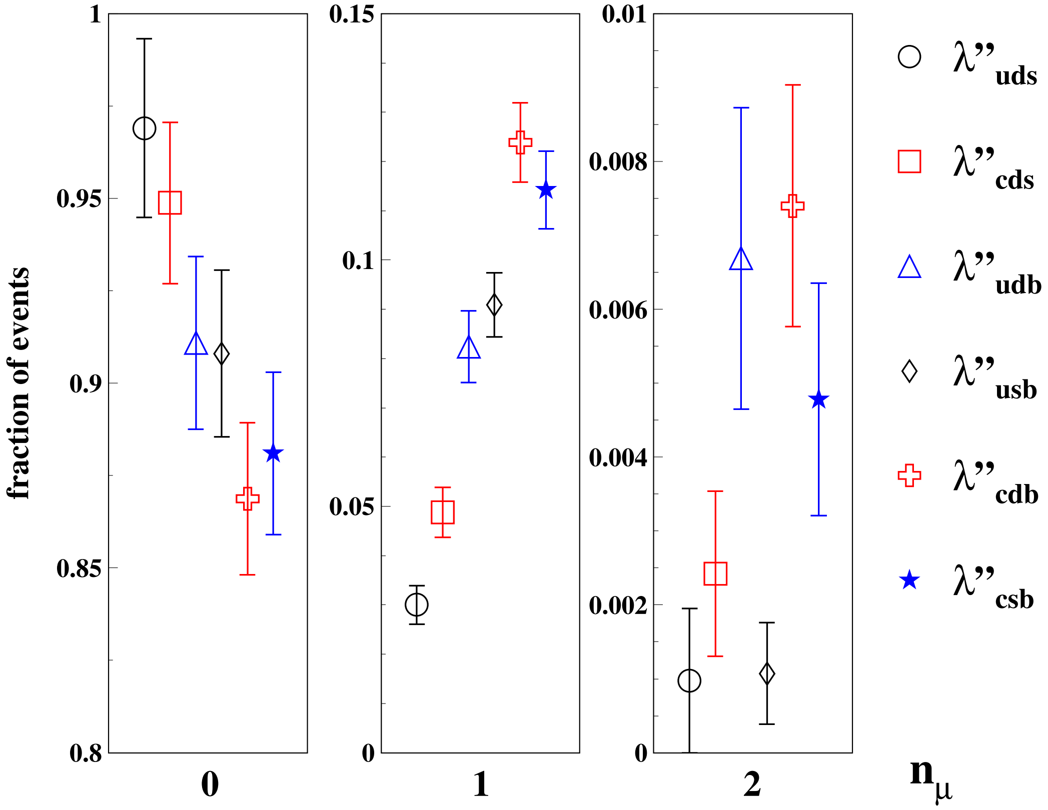

Figure 4.16: The fraction of signal events with 0, 1 and 2 muons that lie within $\sqrt{\Delta\eta^2 + \Delta\phi^2} \leq 0.4$ of the signal jets, for different types of RPV coupling, λ''. The statistical errors are those expected for an integrated luminosity of 30 fb^{-1}. Points are horizontally displaced to allow them to be distinguished by eye.

since their daughters will produce hits only in the outermost silicon layers.

4.7.2 Flavour Discrimination from Muons

The weak decay of hadrons containing heavy quarks can produce muons, which will generally lie within the associated quark jet. The muons will pass though the calorimeter and so can be measured by the muon detector even if they lie inside the jet cone. The frequency with which these "non-isolated" muons occur in signal events can be used as an additional discriminator between quark flavours.

The number of non-isolated muons per event in the six signal jets is plotted in fig. 4.7.2. Since bottom mesons produce more muons [$\mathcal{B}(B^0 \to \mu^+ \nu_\mu \mathrm{X}) = 10\%$] than charmed mesons [$\mathcal{B}(D^0 \to \mu^+ \nu_\mu \mathrm{X}) = 7\%$] [149], the number of muons in signal jets is used to statistically separate b- from c-jets.

4.7.3 Statistical Significance

The confidence with which one can identify the dominant coupling was explored for all pairs of couplings for both the vertex tagging and muon rates (fig. 4.7.1 and fig. 4.7.2 respectively). The variable,

$$\chi^2 = \sum_i \frac{(x_i - y_i)^2}{\sigma_x^2 + \sigma_y^2}$$

was calculated, where x_i and y_i are the fractions of events with i muons (or vertex tags) for the test pair of couplings and the σ^2s are their variances assuming Poisson-distributed numbers of events. Bins where one or other distribution contained fewer than five events were excluded.

The calculated χ^2 values for both the muon and vertex-tagging plots are shown in table 4.7.3. If one uses only the muon information then all couplings are distinguishable at 90% except for the ambiguity between d- and s-jets. In general the vertexing rate gives better discrimination, but would be difficult for a long-lived $\tilde{\chi}_1^0$ for the reasons discussed in sec. 4.7.1. Combining the results from both analyses gives separation at better than 3.5 σ in all cases, again with the exception that it is not possible to distinguish down from strange quarks.

If the branching ratios of the neutralino through two or more couplings were comparable, then as the information in the distributions is rather degenerate, definitive identification of the couplings becomes difficult. However the method could then be used to constrain the possible values of the couplings.

Distinguishing		Vertexing		Muons		Combined
λ''_{ijk} from	λ''_{lmn}	χ^2/d.f.	P/%	χ^2/d.f.	P/%	discrimination/σ
uds	udb	59.1/1	-	28.7/1	-	9.4
	usb	73.0/1	-	31.7/1	-	10.2
	cds	30.5/1	-	4.0/1	4	5.9
	cdb	106.9/1	-	47.2/1	-	12.4
	csb	113.4/1	-	49.2/1	-	12.8
udb	usb	1.6/2	44	0.4/1	54	1.4
	cds	10.3/2	1	13.0/1	-	4.8
	cdb	18.3/2	-	6.8/2	3	5.0
	csb	16.3/2	-	5.1/2	8	4.6
usb	cds	17.5/2	-	17.2/1	-	5.9
	cdb	12.1/2	-	5.1/1	2	4.2
	csb	9.9/2	1	3.1/1	8	3.6
cds	cdb	56.1/2	-	37.4/1	-	9.7
	csb	55.8/2	-	35.3/1	-	9.5
cdb	csb	0.6/2	72	1.3/2	51	1.4

Table 4.4: Chi-squared function, and number of degrees of freedom (d.f.) for the difference in distributions for pairs of RPV couplings (λ'') for an integrated luminosity of 30 fb^{-1}. The contributions from vertexing and muon counting are shown separately. The probability (P) in the tail of the chi-squared distribution is given when P $\geq$ 1%. The number of degrees of freedom is one less than the number of histogram bins in which both couplings contain at least five events.

4.8 Conclusion

The usual ubiquitous signature for the R_P conserving MSSM is missing transverse energy. This signature disappears once R_P violating couplings are added, unless they are extremely small and the lifetime of a neutralino LSP is such that it decays outside the detector.

The case where the neutralino LSP is unstable and decays to 3 jets, was examined, which corresponds to the RPV coupling λ'', the trilinear RPV coupling giving the hardest case in which to detect and measure sparticles.

By analysing the decay chain, $\tilde{q}_L \to \tilde{\chi}_2^0 q \to \tilde{l}_R \ell q \to \tilde{\chi}_1^0 \ell\ell q$, it has been shown that the $\tilde{\chi}_1^0$, $\tilde{\chi}_2^0$ and $\tilde{q}_L$ be detected and their masses measured, and that the mass of the $\tilde{l}_R$ can also be obtained in much of parameter space. The sparticle production and decays in this signal are all R_P conserving apart from the $\tilde{\chi}_1^0$ decay into three jets.

Although a point near mSUGRA point 5 has been used to derive the soft SUSY breaking parameters, the method should in principle work for other more general SUSY breaking parameter sets in which the decay chain in fig. 4.4 exists. When some of the sparticles involved in the decay chain become much heavier than 1 TeV, the analysis will become statistics limited.

If baryon-number violating couplings to quarks other than top are $\gtrsim 5 \times 10^{-5}$ then $\tilde{\chi}_1^0$s will typically decay within the tracking volume of an LHC detector. For these couplings, simulations show that displaced secondary vertices and muons from heavy quark decays allow statistical separation of b- from c-quark jets, and b- and c-jets from light-quark jets. A dominant RPV coupling can then be identified at better than 3.5 σ, except for an ambiguity caused by the inability to distinguish strange from down quarks.

It has therefore been demonstrated that if the MSSM breaks baryon number, not only can the LHC detect and measure the masses of sparticles [1], but it can even distinguish the flavour structure of the RPV coupling.

Part III

Beam tests of ATLAS silicon modules

Chapter 5

Silicon Detectors and the ATLAS Semiconductor Tracker

> *Shine inward, Irradiate, there plant eyes that I may see and tell*
> *Of things invisible to mortal sight*

The supersymmetry search analyses described in chapter 3 and chapter 4, make use all of the various ATLAS detector subsystems. One of these components, the SCT, a silicon microstrip detector, is particularly important in tracking, particle charge sign determination, and vertex tagging.

A preliminary description of the SCT has been given in sec. 2.4.2. This chapter provides a more detailed description of the components, providing a background for the beam test analysis presented in chapter 6.

5.1 Semiconductor Detectors

All of the particle physics experiments at the LHC will use semiconductor detectors. They provide a fast, accurate and efficient method of detecting the passage of charged particles.

The basic principle is that charged particles pass through a semiconductor which has been depleted of charge carriers by reverse-biasing a p-n junction. The energy deposited by the particle (typically a few keV per μm) creates electron–hole pairs which are swept away by the same electric field which provides the bias. The resulting charge is collected on the implant strips, either directly or by capacitive AC coupling to a metalisation layer.

A pedagogical introduction to the physics of semiconductor devices can be found in, for example [150]. Briefly, symmetry under translation of the crystal lattice leads to allowed energy bands for electrons. In some materials, such as silicon, the lower energy levels (valence band) are filled up, leaving an energy gap of about an electron-volt to a higher 'conductance' band. Thermal excitation of electrons across this gap creates two types of electrical charge carrier – the electron itself, and the positively charged 'hole' caused by its absence from the valence band. These charge carriers allow macroscopic currents to flow, so the materials are known as semiconductors.

The addition of impurities to an intrinsic semiconductor has a profound effect on its electrical properties. The material may be doped in one of two ways. Adding group V atoms like phosphorus to the crystal lattice leaves an unbonded electron which will fill a state near the bottom of the conduction band. These atoms are therefore called donors, and the semiconductor is said to be n-type. By contrast adding group III impurities, such as aluminium, creates a site in which a valence electron can be captured. These sites, known as acceptors, create a surplus of holes at the top of the valence band, creating a p-type material.

When a p-type and n-type region adjoin, electrons flow across from the n-type to the p-type material until the electrochemical potential is equalised. This creates a region on either side in which charge carriers are almost totally absent. The width,

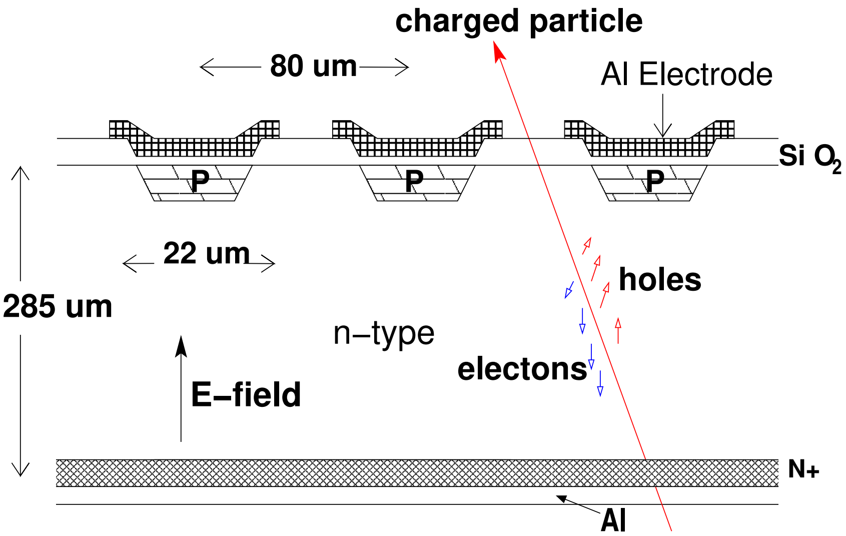

Figure 5.1: A schematic cross-section through a p-on-n silicon microstrip detector. The dimensions are those of an ATLAS barrel SCT sensor. The protective passivisation layer is not shown.

W, of the depleted region can be estimated by solving Poisson's equation,

$$\frac{d^2V}{dx^2} = \frac{\rho}{\epsilon_0 \epsilon_{\mathrm{Si}}}, \tag{5.1}$$

where ρ is the charge density, V is the electrical potential, ϵ_0 is the permittivity of free space, and ϵ_{Si} is the relative permittivity of silicon. Since the band gap energy is usually much greater than $k_B T$ it is reasonable to assume that there is total depletion of charge carriers up until an abrupt boundary. Integrating eq. 5.1 twice one finds that the width of this depletion region is

$$W \approx \sqrt{\frac{2\epsilon_0 \epsilon_{\mathrm{Si}} V_{\mathrm{bias}}}{e N_{\mathrm{eff}}}}, \tag{5.2}$$

where $N_{\mathrm{eff}} = \rho/e$ is the effective dopant concentration.

5.1.1 Radiation Damage

The unprecedented levels of radiation expected at the LHC provide one of the major challenges for the SCT. The maximum dose expected after ten years of operation is equivalent to 1.4×10^{14} 1 MeV neutrons per square centimeter. Damage is primarily caused by the non-ionising interactions of high energy hadrons. Recoiling nuclei which remain displaced from their lattice sites can create stable defects such as interstitial atoms and vacancies.

The overall effect of irradiation of the bulk is to increase the effective number of acceptors so that the material becomes more p-type. During heavy irradiation of a lightly doped n-type material, N_{eff} will be reduced until the material undergoes type inversion and eventually becomes p-type. Irradiation therefore increases N_{eff} so that, by eq. 5.2, a higher bias voltage must be applied to fully deplete the detector. After type inversion, the module must be operated fully depleted, since the depletion region grows from the n^+ side of the detector.

Radiation-induced defects also create electron energy levels near the center of the band gap, which causes an enhancement in the reverse bias current, I_{det}. Statistical fluctuation in this 'leakage current', I_{det}, lead to shot noise $\propto \sqrt{I_{\text{det}}}$. Another problem with higher leakage currents is that they dump heat into the detectors. This could lead to potentially catastrophic problems, since higher temperatures will in their turn cause an increase in thermally-created majority charge carriers in the depleted region, which are themselves a source of leakage current. If uncontrolled this cycle can lead to thermal runaway which makes it impossible to apply sufficient bias to efficiently operate the detectors. Irradiation also creates defects which trap charge carriers, decreasing the observed signal.

The damage caused by irradiation is strongly dependent on the temperature of the silicon. Soon after irradiation the detector exhibits thermally-activated annealing as the effective number of donors is reduced. However on a longer time-scale interactions between radiation-generated defects leads to a detrimental effect known as 'reverse annealing'. Both processes are very temperature-dependant, having time constants, $\tau \propto \exp(-k_B T)$. Reverse annealing can be efficiently suppressed by keeping the detectors at low temperature (<0 C). For this reason, as well as to reduce the leakage current, the ATLAS SCT will be operated at -7 C. A network of thin-walled Cu/Ni tubes will contain C_3F_8 which will provide evaporative cooling.

Irradiation also causes changes to the SiO_2 passivisation layer. This surface damage is caused by ionising irradiation, and is important in AC coupled devices which have a SiO_2 layer in the metal oxide semiconductor (MOS) read-out capacitor. The electric field across the capacitor preferentially sweeps away electrons, leaving a net positive charge, which induces a surface layer of electrons in the bulk. That charge can then affect the shape of the electric field around the strips, potentially leading to high-field breakdown.

The dominant pre-amplifier load is the interstrip capacitance, which increases with irradiation, due to trapped charges at the Si/SiO_2 boundary. The resultant increase in capacitiance increases the front-end noise meaning that irradiated sensors generally have a lower signal to noise ratio even when fully depleted. A recent review of the effects of radiation damage in silicon detectors can be found in reference [151].

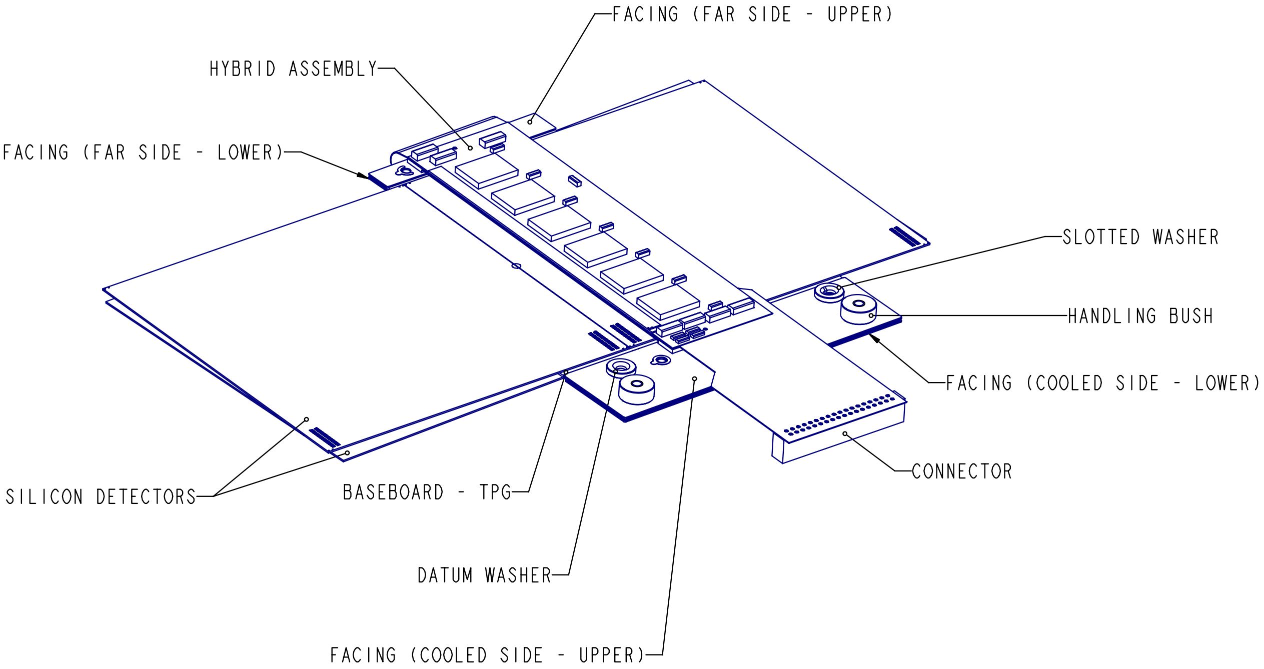

Figure 5.2: Diagram of a SCT barrel module. Adapted from [152].

5.2 The ATLAS SCT

5.2.1 Detectors

For the ATLAS SCT, the sensors are manufactured from n-type silicon with p^+ implants. There are 768 active strips on each, with a strip pitch of 80 μm pitch in the barrel. For the wedge-shaped forward detectors, the pitch varies from 50 to 90 μm.

The sensors are single-sided, and are mounted back-to-back at a 40 mrad stereo angle between the strips to provide a two-dimensional readout. The active surface of the sensors is 62×61.6 mm with a thickness of 285 μm. The effective strip length is doubled by daisy-chaining pairs of detectors together with wire bonds, leaving a narrow inactive region between the detectors. The four sensors required for each module are glued onto a stiff, high thermal conductivity graphite (TPG) baseboard with BeO facings on both surfaces. The technical description of the ATLAS SCT detectors can be found in [153].

5.2.2 Readout

Electronic readout is provided by the `ABCD` [154–156] application-specific integrated circuit (ASIC). Each chip serves 128 silicon detector strips, so six chips are required on both the top and the bottom of the module. These chips are mounted on a wrap-around electronics hybrid which thermally decouples the ASICs from the detectors.

The ASICs have been manufactured using the radiation-hard DMILL process [157, 158], which allows them to contain both a bipolar analogue and a complimentary metal oxide semiconductor (CMOS) binary part (see fig. 5.3). The signal from the strips is initially processed in the front-end analogue section of the chip which contains a low-noise preamplifier, integrator, and shaper. The integrated signal is then compared with a threshold potential set by an internal digital-to-analogue converter (DAC), producing a binary hit or miss. This threshold can calibrated against an injected input charge (in fC), supplied via 100 fF capacitors. In order to compensate for channel-to-channel variation in the discriminator offset, each channel is provided with a four-bit ‘Trim-DAC’.

The digital hit information is then pipelined in a 132-bit deep first-in-first-out buffer (FIFO), pending the arrival of a level-1 trigger accept. If the bit pattern corresponding to such a trigger is received, the data is again buffered, compressed, and sent to an optical link for transmission to the off-detector electronics.

The final output is a bit-pattern corresponding to hit information at the 40 MHz

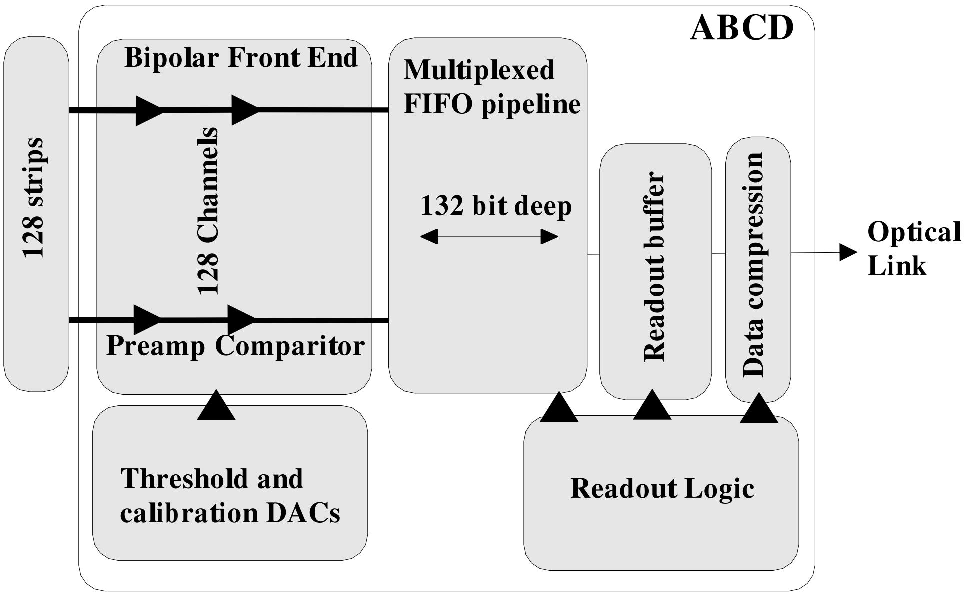

Figure 5.3: Simplified block diagram of the SCT readout architecture.

clock/bunch-crossing frequency.

5.3 Performance

For track reconstruction the important performance parameters are the efficiency with which particles are detected, the occupancy due to noise hits, and the spatial resolution. The specifications in [35] state that detection efficiency should be greater than 99%, with noise occupancy less than 5×10^{-4}. Both efficiency and noise occupancy decrease when the threshold is increased, so these numbers should be found at the operating threshold, near 1 fC.

The spatial resolution for a one-strip cluster on any single detector will be $\sigma_1 = 80\ \mu\text{m}/\sqrt{12}$. This leads to RMS resolutions in $r\phi$ and z of:

$$\sigma_{r\phi} = \frac{\sigma_1}{\sqrt{2}\cos\alpha/2} \approx \frac{\sigma_1}{\sqrt{2}}, \tag{5.3}$$

and

$$\sigma_z = \frac{\sigma_1}{\sqrt{2}\sin\alpha/2} \approx \frac{\sqrt{2}\sigma_1}{\alpha}, \tag{5.4}$$

where α is the 40 mrad stereo angle. Thus the resolution for any particular module can be expected to be better than 16.3 μm in $r\phi$, and 815 μm in z. when multi-strip clusters are also included.

Chapter 6

SCT module beam tests

6.1 Introduction

Once the inner detector has been installed at the heart of ATLAS it will be extremely difficult to access. Replacing any central component will entail a huge logistical operation, during a specially extended shut-down. Components must therefore perform well in a very challenging environment, and to continue to do so for many years.

During the development and production of ATLAS, a huge variety of tests have been made to to evaluate detector properties, to compare and make choices between different technologies, and to ensure the quality of those components destined for the final detector. These have involved detailed investigations of electrical, magnetic, mechanical and thermal properties, as well as checks of radiation hardness, and large-scale system tests.

Many of the module properties which will be most important for ATLAS physics reconstruction can be well tested by firing high energy particles with known properties at modules, and testing their response. It is these beam tests of ATLAS SCT modules that form the subject of this chapter.

This work was carried out in collaboration with many other members of the ATLAS experiment. For a list of those involved the reader is refered to the author-lists of

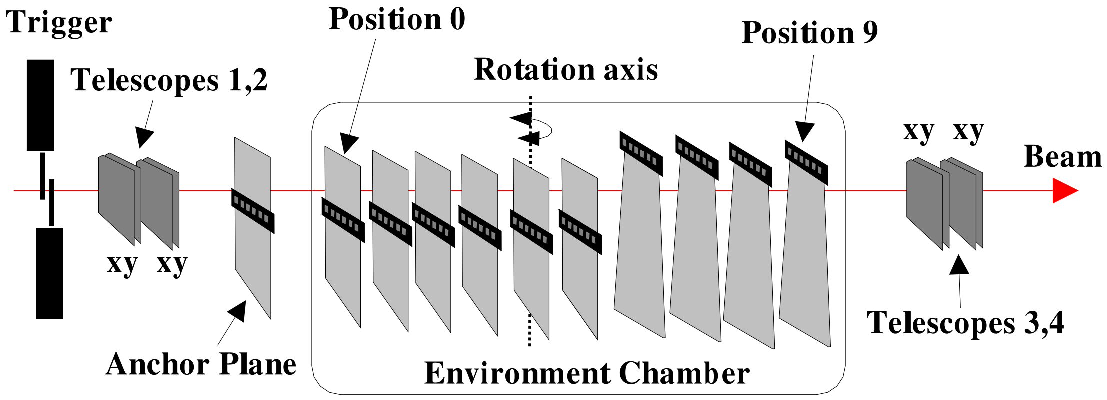

Figure 6.1: Diagrammatic representation of the testbeam setup. The devices under test were contained within the environment chamber and could be rotated together about the vertical axis.

references [5–7].

6.2 The beam test environment

A series of beam tests were carried out on a sample of irradited and non-irradiated SCT modules at CERN's 450 GeV super proton synchrotron (SPS). Protons incident on a fixed target in the CERN North Area were used to generate a highly collimated 180 GeV π^+ beam with a small fraction of muons from pion decay. The beam width was approximately 2 cm full-width at half maximum, with about 100k particles per 3.2 second spill.

The modules under test were mounted in individual aluminium boxes which had perspex windows to reduce the material in the beam. The module boxes were chilled with a water/glycerol heat exchanger, and fed with cold dry nitrogen gas to prevent condensation. A mechanical screw gauge allowed them to be rotated about a vertical axis so that the incident angle of the incoming beam relative to the detector plane could be varied. The entire apparatus was mounted on a stable trolley to allow its insertion into a large, uniform-field 1.56 T dipole magnet.

The tracking telescope consisted of four silicon microstrip modules, each of which contained two detectors with strips orientated perpendicular to the beam, thus giving both an x and a y measurement. The telescope detectors had a 50 μm pitch and were read-out by Viking analogue chips [159]. This arrangement provides an interpolated track position at the position of an SCT module with resolution generally better than 10 μm. The read-out was triggered by the coincidence of a pair of scintillators several meters upstream of the devices under test. Chip power and detector bias were supplied by SCTLV and SCTHV modules respectively [160].

6.2.1 Devices Under Test

Six barrel SCT modules and three endcap modules were present during the August 2001 beam tests (see fig. 6.1). My investigations concentrate on the barrel modules. Two of these had previously been irradiated at the CERN PS T7 facility [161] to a fluence of 3×10^{14} protons per square centimeter. This is the standard SCT irradiation fluence and corresponds to the maximum fluence expected for any SCT module after ten years of LHC operation with an additional safety margin. The bulk damage caused in silicon is equivalent to a neutron fluence of about 2×10^{14} per cm^2.

Each module under test was read-out with `ABCD3TA` ASICs (see sec. 5.2.2), via an electrical support card. Electrical signal and power cables approximately 20 m long ran to a barrack for data acquisition (DAQ), and detector monitoring and control. Clock and control was provided by CLOAK modules [162], slow controls by the SLOG [163] and readout through the MUSTARD [164]. The control software

Slot	ID	Name	Type	Irrad.	T/C	Plane
0	0	0029	Barrel		-6	$\langle 111 \rangle$
1	1	0018	Barrel		-7	$\langle 111 \rangle$
2	2	0020	Barrel	*	-5	$\langle 100 \rangle$
3	3	0037	Barrel	*	-4	$\langle 100 \rangle$
4	4	0035	Barrel		-1	$\langle 100 \rangle$
5	5	0036	Barrel		-7	$\langle 100 \rangle$
6	6	K4_218	Endcap outer	*	4	$\langle 111 \rangle$
7	7	K4_229	Endcap inner		25	$\langle 111 \rangle$
8	8	K4_200	Endcap outer		11	$\langle 111 \rangle$

Table 6.1: Modules in the August 2001 SCT beam test. The slot is the physical position of the module in the environment chamber, and increases in the downstream direction. 'ID' is the DAQ identifier. An asterisk indicates that the module has been irradiated as described in the text. T indicates the typical running temperature at a point on the hybrid. The ASIC temperatures are typically 6-7 C higher. The forward hybrid (with an early version of the cooling conection) shows a higher hybrid temperature than on the barrel modules. All modules had ABCT3TA ASICs [154]. The last column shows the crystal plane orientation of the sensors.

was TBDAQ [165], a modified version of the SCTDAQ [166] module test software, running under ROOT [167].

Thermistors and PT1000 devices were installed at various points within some of the module boxes so that the temperature on the hybrids could be monitored. This was especially important in the irradiated modules to prevent both reverse-annealing and thermal run-away.

6.2.2 Calibration

The modules were calibrated *in situ* using the charge-injection method discussed in sec. 5.2.2. However there remain a number of uncertainties in the absolute charge scale. One such uncertainty is caused by capacitance variations in the charge-injection circuit which is used for threshold calibration. Variations between different batches of chips can be accounted for by cross-calibration measurements made on test structures on the silicon wafers. For the barrel modules in this testbeam, this correction means that the recalibrated charge,

$$Q_{\mathrm{th}}^{\mathrm{calib}} = 1.13 \times Q_{\mathrm{th}}^{\mathrm{nominal}}. \tag{6.1}$$

However it should be noted that other variations, such as those between different chips of the same batch, are not corrected by this procedure.

6.3 Analysis Overview

The ATLAS SCT modules have binary readout electronics, so the beam test generally involves scans of approximately 8 hours, during which the threshold is automatically adjusted in 16 steps from 0.7 to 6.0 fC, with smaller (0.1 fC) steps around the 1 fC point at which the modules are expected to operate. At each threshold approximately 15k events were recorded, most of which contained a single particle track. The trajectories of the track(s) were determined from the telescope modules, and then projected onto the devices under test.

6.3.1 Track-finding and alignment

The relative alignment of the telescopes, and between the telescopes and the modules under test was calculated by members of the Valencia testbeam group [168] by minimising the sum of the squares of the residuals (a residual is the difference between the expected and the true hit positions).

For barrel modules a four-parameter fit was made, with parameters: d_0 (the shortest distance from the center of the beam to the left-most active strip on that plane), z_0 (the position of the module parallel to the beam – primarily determined by beam divergence), ϕ (the rotation angle about the beam axis), and η (the rotation angle about an axis parallel to the strips). Thse parameters chosen are sufficiently general to account for the beam bending in a magnetic field.

Initially one upstream and one downstream telescope module were used to define the track, and the relative position of the other two telescope modules calculated. Next tracks were found using all four telescope modules, and the relative positions of the modules under test were calculated. The starting values for the minimisation were taken from a physical (mm-scale) survey. The values of the alignment parameters were recalculated after any beam-area intervention, beam steering, or magnetic field adjustment.

6.3.2 DST production

The raw data were initially processed into files known as data summary tapes (DSTs). These files contained all of the raw hit information, as well as higher-level objects, such as tracks and run conditions. Hits on consecutive strips were combined into *clusters*. For normal incidence the majority of clusters consisted of a single hit, about 7% were two-hit with a very small fraction number of three- or more hit clusters.

6.3.3 Efficiency algorithm

For a particular run, the module, environment and alignment information relevant to that run were found. Then for each event in that run, and for each side (or *link*) of each module the efficiency analysis algorithm followed the following steps:

(1) Events were ignored where they have been flagged as having a possible error during DST production, for example in a small number of events where a DAQ readout error meant that the analogue telescope data were not correctly synchronised with those from the binary modules. Noise events (see sec. 6.4.4) are not used for the efficiency calculation.

(2) Events in which exactly one track had been found by the telescope were considered. Track quality cuts were applied, requiring a track to have gradients $\frac{dx}{dz}$ and $\frac{dy}{dz}$ less than 0.5 mrad relative to the average beam direction, and requiring clusters associated with that track on all four of the telescope modules.

(3) The projected position of the track on the plane under investigation was found. The event is rejected if the projected position on the plane under test is within 120 μm of a bad strip (defined below), or if there was no cluster on the reference module (also known as the *anchor plane*) within 100 μm of the track's projected position.

(4) Hits on bad strips (defined below) were ignored. For all other clusters, the perpendicular distance between the projected track position and the strip position is calculated; this is the residual.

Module	0029	0018	0020*	0037*	0035	0036
# bad	4	0	5	5	1	4

Table 6.2: The number of noisy, unbonded, or unresponsive channels for each module, from a total of 1536.

(5) If the minimum residual was less than 150 μm then the plane records a hit, otherwise it records a miss.

The efficiency with which particles are detected is then given by $\varepsilon = n_{\text{hit}}/n_{\text{tot}}$, where $n_{\text{tot}} = n_{\text{hit}} + n_{\text{miss}}$. The error in the efficiency was estimated using binomial statistics *i.e.* $(\Delta\varepsilon)^2 = \varepsilon(1-\varepsilon)/n_{\text{tot}}$.

Steps 3 and 4 make reference to 'bad strips', which includes unbonded, and strips with occupancy greater than three times, or less than their neighbours. These were either masked in the on-line DAQ software, or later in the offline analysis. The numbers of bad channels per 1536-channel module are shown in table 6.2 and are in all cases less than 0.4%.

The efficiency varies according to the phase in the clock cycle in which the particle is received. In this (asynchronous) test beam pions arrived at a random point in the clock cycle. A time-to-digital converter (TDC) was used to record the time from the last clock edge to the scintillator trigger. Since the `ABCD` chip was usually set in the mode in which it reads out three consecutive time bins, the efficiency could be plotted as a function of TDC over a 75 ns period. A 10 ns window was found for each module by eye for the final efficiency calculation. The window for module 0018 was from 23 to 33 ns, as shown in fig. 6.2.

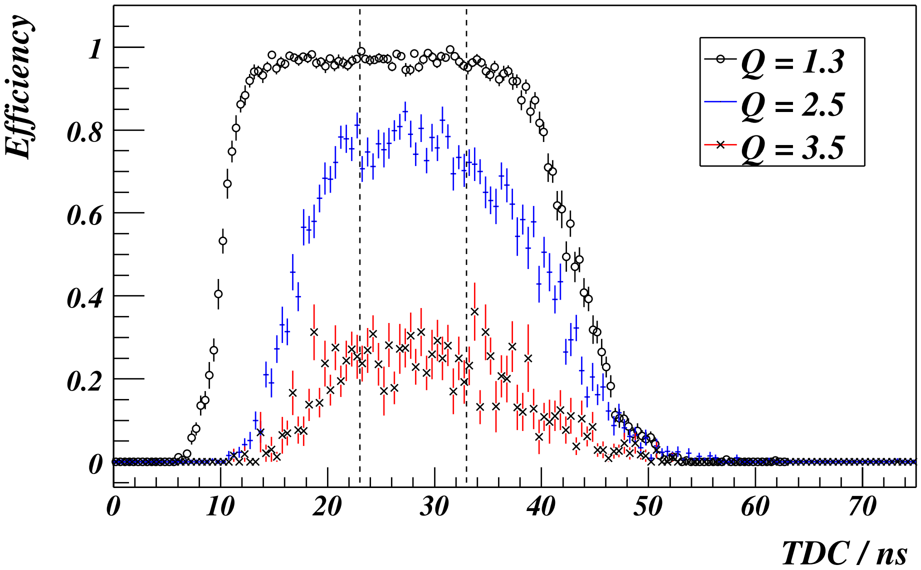

Figure 6.2: Efficiency as a function of TDC for module 0018, with nominal thresholds of 1.3, 2.5 and 3.5 fC, for normal incidence in the absence of a magnetic field, and with a 200 V bias. The time window $23.0 < t/\mathrm{ns} < 33$ used was for the final efficiency calculation. The value on the x axis is the TDC count converted into nanoseconds. Clusters in the second (third) time bin have had 25 (50) ns subtracted from the TDC, as described in the text.

During the beam tests the bias voltage was supplied by high tension power supplies. The radiation-damaged modules had leakage currents typically in the range 1.1 to 1.5 mA at at temperature of about -12 C. This current passes through a 11.2 kΩ bias resistor, resulting in voltage drop of about 15 V on the hybrid. The bias voltages are quoted in this chapter are the those on the detectors *i.e.* after the effect of the biasing resistor has been accounted for. For unirradiated modules, which typically have leakage currents less than a microamp, the potential difference across the detectors was very close to that supplied.

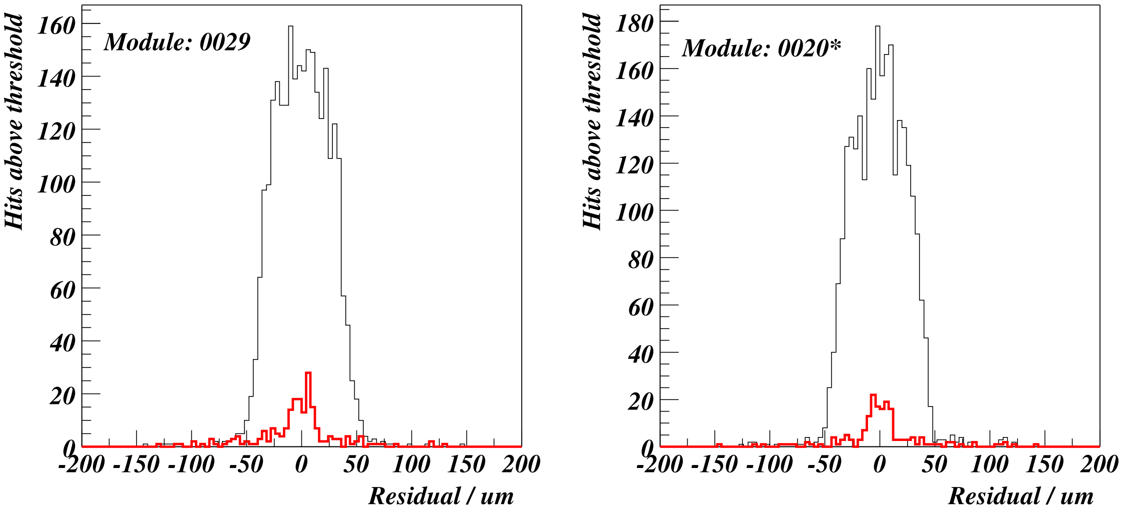

(a) (b)

Figure 6.3: Residual distributions for module **(a)** 0029 and **(b)** 0020* (the asterisk indicates that the module has been irradiated). The thin (black) line shows all clusters, while the thick (red) line shows only those clusters in which there were multiple adjacent strips hit. The detector bias was 250 V for 0029 and 435 V for 0020*. The data were taken at normal incidence with no magnetic field at a nominal threshold of 1.0 fC.

6.4 Results

6.4.1 Residuals

The difference between the projected track position and the nearest cluster position in the direction perpendicular to the strips is called the residual. The position of the cluster is simpler than in analogue-readout systems, being simply the average of the positions of the neighbouring hits which define that cluster. Residual distributions for one unirradiated and one irradiated module are shown in fig. 6.3. As can be seen, the fraction of clusters in which charge-sharing has provoked hits on two or more channels is rather small – about 7% at normal incidence – so the resolution is dominated by the single-hit clusters.

The width of a Gaussian fit to the residual distribution was found to lie in the range 22.6 to 24.6 μm.[a] Since the intrinsic resolution of the telescope modules leads to a $\lesssim 10$ μm uncertainty in the projected track position, these widths are consistent with the expected resolution for a single plane of $80/\sqrt{12} = 23.1$ μm. This agreement demonstrates that the module alignment is giving an accurate projection of the track onto the module.

6.4.2 Module Efficiency

The amount of charge deposited by a minimally ionising particle (MIP) is a stochastic process, with a probability density function described by a Landau distribution [169],

$$L(\phi) = \frac{1}{2\pi i} \int_{\epsilon - i\infty}^{\epsilon + i\infty} \exp\left[\phi s + s \ln s\right] ds \tag{6.2}$$

where $\phi = (x, x_{peak})/x_{wid}$, x_{peak} is the most probable charge deposited, and x_{wid} is the width parameter. Since the binary electronics give us only information at a particular threshold, the basic unit for most of the analysis was a threshold scan. Plots of efficiency against threshold (known as 'S-curves' because of their shape) would have the shape of an integrated Landau distribution if the charge collection was perfect. The charge losses and various noise sources can be roughly modeled as Gaussian so the collected charged is more accurately described by an 'improved Landau' distribution – a Landau convoluted with a gaussian distribution of width σ_g:

$$L^{\text{imp}}(\phi, \sigma_g) = \int_{-\infty}^{+\infty} L(\phi') G(\phi - \phi', \sigma_g) d\phi' \ , \tag{6.3}$$

---

[a] Except for the one of the planes (link 1) of module 0026 where the shape of the residual distribution indicated a probable wire bonding error.

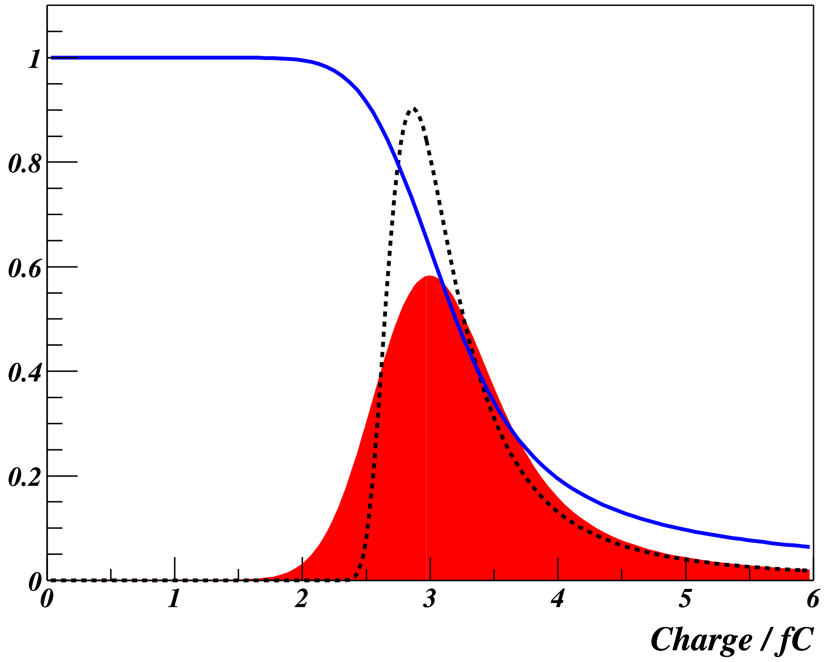

Figure 6.4: Example of a Landau distribution (dashed black line), improved Landau distribution (filled red curve), and the corresponding S-curve (solid blue line). The peak of the Landau, x_{peak} = 2.9 fC, and its width parameter, x_{wid} = 0.17 fC. The width of the gaussian, σ_g =0.2 fC.

where $G(\bar{x}, \sigma)$ is a Gaussian distribution with mean $\bar{x}$ and width σ. The function used to fit the S-curves was the integral of the improved Landau distribution:

$$S(\phi, \sigma_g) = \int_{\phi}^{\infty} L^{\text{imp}}(\phi', \sigma_g) d\phi' \ , \tag{6.4}$$

as shown in fig. 6.4. The width of the gaussian was allowed to vary during the fit; typical values were about 0.2 fC (which is consistent with the R.M.S. noise which can be found in table 6.3 on page 152). The threshold at 50% efficiency gives the median charge collected.

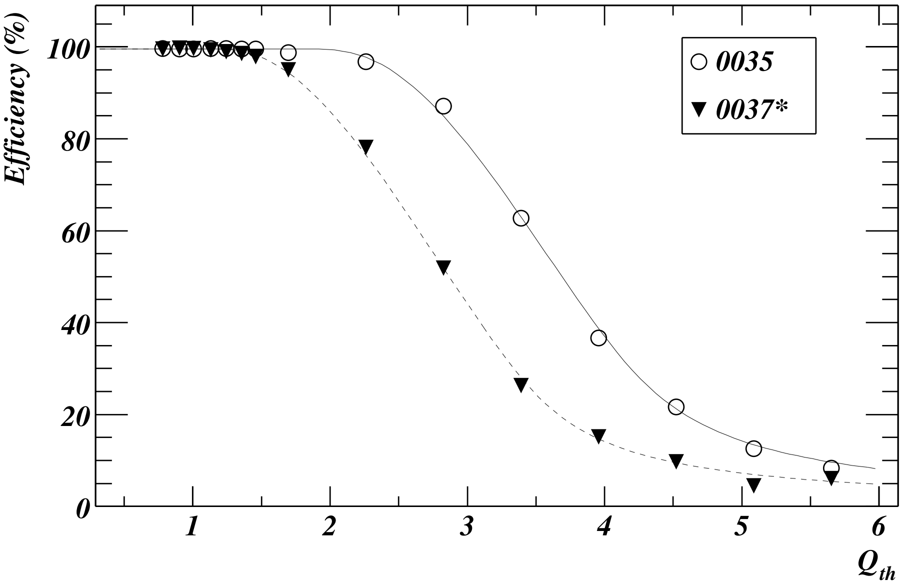

Figure 6.5: 'S-curve' for module 0035 with detector bias of 200 V (circles), and for the irradiated module 0037* with detector bias of 385 V (triangles). Data taken at normal incidence and with no applied magnetic field. The thresholds have been calibrated using eq. 6.1. The fit function is an improved Landau distribution.

6.4.3 Charge collection as a function of bias

The median charge collected on the strips depends on the bias voltage applied. For unirradiated detectors the charge deposited is proportional to the width of the depletion region *i.e.* $\propto V_{\mathrm{bias}}^{\frac{1}{2}}$ neglecting the built-in voltage of the junction. The deposited charge saturates when the detector is fully depleted, but the collected charge can increase slowly with bias due to reduced diffusion and recombination.

For irradiated modules which have undergone type-inversion the depletion region grows from the back plane. If the module is not fully depleted this region does not reach the p-strips and a large proportion of the generated holes are lost through recombination in the intervening bulk. A small proportion of the charge can still diffuse through the undepleted region, but an irradiated p-on-n detector must be

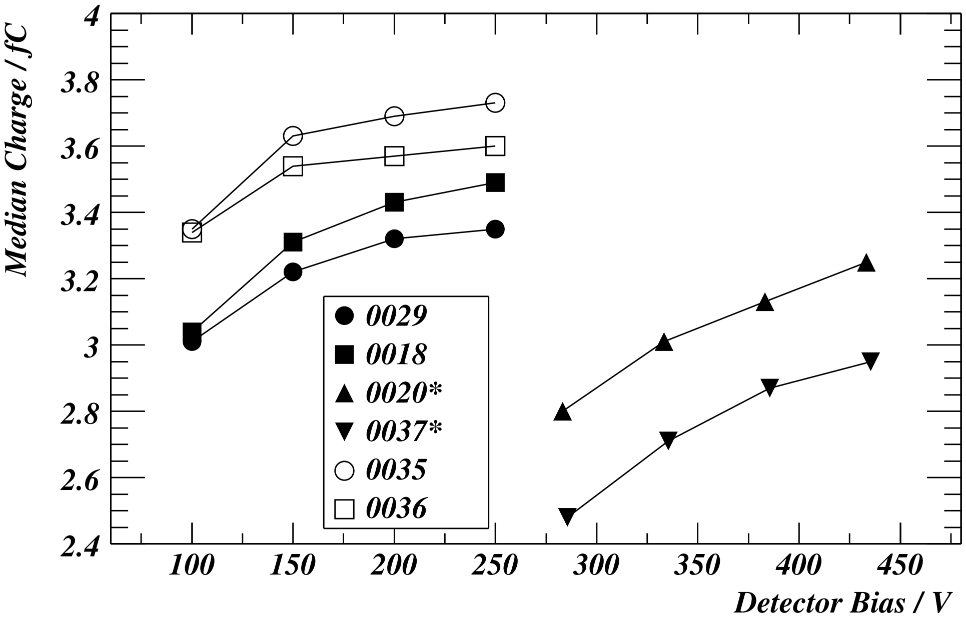

Figure 6.6: Median charge collected as a function of detector bias for the six barrel modules under test. Data taken at normal incidence and in the absence of an applied magnetic field. The median charges were calculated from calibrated thresholds, as given by eq. 6.1.

fully depleted if reasonable charge collection is to be achieved.

The most probable charge deposited (the peak of the Landau distribution) is 22,500 electrons for 285 μm of silicon [149][b], which corresponds to a charge of 3.6 fC. However the Landau distribution has a large upper tail from particles which lose a large amount of energy. This means that the median charge is significantly larger than the most probable value. From fits to the integrated Landau distributions (such as those shown in fig. 6.5) it was found that the median charge was consistently 0.40 ± 0.02 fC greater than the peak. Thus full charge collection should lead to a median charge of about 4 fC.

---

[b] This number includes a 285/300 correction factor for the thickness of the detectors, and a 8% correction for the relativisitic increase of a 180 GeV pion relative to a MIP.

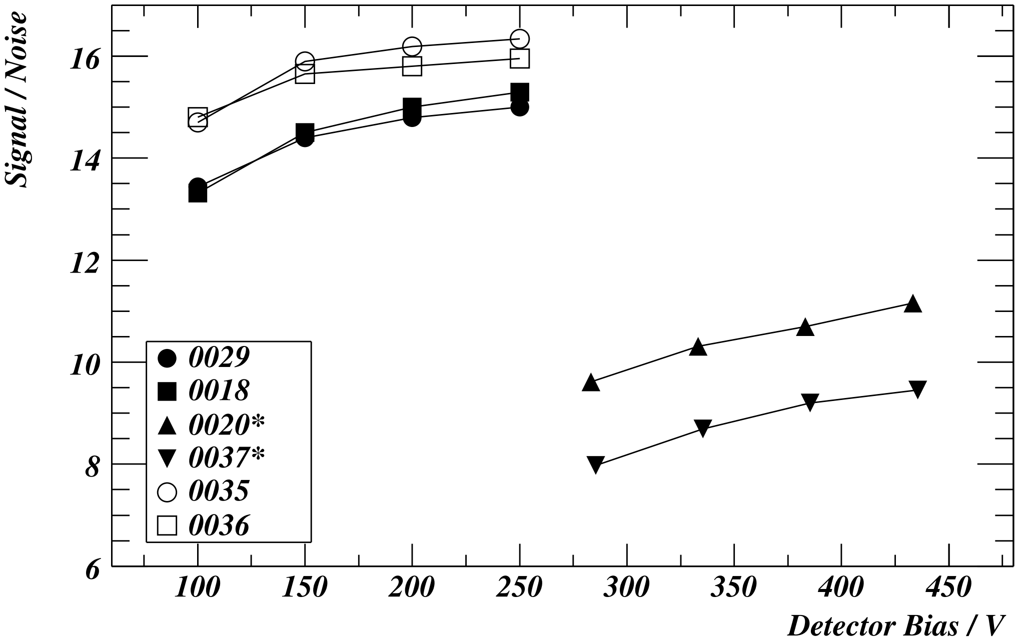

Figure 6.7: The ratio of the median charge collected to the noise. The median charge was measured under the same conditions as in fig. 6.6. The measurement of the noise is described in the text.

The median charge collected is plotted as a function of detector bias in fig. 6.6. The corresponding numbers are also given in table 6.3. The trend of increasing median charge with bias is clear for both the irradiated and the unirradiated modules. The signal from the unirradiated modules is starting to saturate between 150 and 200 V, somewhat above full depletion, which occurs at $V_{\text{bias}} \approx 80$ V for these detectors.

The difference in the saturation charge between the pairs of unirradiated modules {0029, 0018} and {0035, 0036} is more surprising. At first it might be reasonable to assume that the pairs have a systematic shift in the threshold calibration capacitors. However in sec. 6.4.5 it is shown that the signal-to-noise ratio, in which the calibration has been factored out shows a similar disparity. Differences due to timing (TDC) cuts are discounted in sec. 6.4.6. A previous beam test of ATLAS SCT modules [5] showed no significant difference between the charge collected by

Module		**0029**	**0018**	**0020***	**0037***	**0035**	**0036**
Noise / fC		0.223	0.229	0.292	0.312	0.228	0.225
100 V	S	3.01	3.04	-	-	3.35	3.34
	S/N	13.4	13.3	-	-	14.7	14.8
150 V	S	3.22	3.31	-	-	3.63	3.54
	S/N	14.4	14.5	-	-	15.9	15.6
200 V	S	3.32	3.43	-	-	3.69	3.57
	S/N	14.8	15.0	-	-	16.2	15.8
250 V	S	3.35	3.49	-	-	3.73	3.60
	S/N	15.0	15.2	-	-	16.3	16.0
285 V	S	-	-	2.80	2.48	-	-
	S/N	-	-	9.6	8.0	-	-
335 V	S	-	-	3.01	2.71	-	-
	S/N	-	-	10.3	8.7	-	-
385 V	S	-	-	3.13	2.87	-	-
	S/N	-	-	10.7	9.3	-	-
435 V	S	-	-	3.25	2.95	-	-
	S/N	-	-	11.2	9.5	-	-

Table 6.3: Median charge collected, S, in fC; and median signal to R.M.S. noise ratio, S/N, as a function of detector bias (left column). Note that both the median charge and the noise charge have been calibrated using eq. 6.1.

$\langle 100 \rangle$ and $\langle 111 \rangle$ orientated sensors, either irradiated or unirradiated. It is however notable that the two modules in each pair were controlled by the same low-voltage power supply.

In any case, none of the modules collect the full 4.08 fC even at high bias. This may be explained somewhat by hole recombination but is primarily due to sub-threshold charge sharing with neighbouring strips. Charge sharing is larger for irradiated modules, since they have a larger interstrip capacitance.

There are also other reasons why the irradiated modules collect a smaller charge. Radiation-induced point defects can trap the charge carriers (holes). Also, with longer collection times but fast shaping electronics, irradiated modules lose charge through ballistic deficit.[c] The shape of the curves in fig. 6.6b for 0020* and 0037* are typical – the collected charge continuing to increase up to 435 V. The systematic shift of 0037* relative to 0020* is not understood.

6.4.4 Noise occupancy

A module can still register a small number of hits even in the absence of ionising particles. This will occur if a charge fluctuation at the comparitor exceeds the binary threshold. These *noise hits* will interfere with track reconstruction unless they are very sparse, and at a higher level could saturate the optical readout electronics. The quantity which is important is the *noise occupancy* – the number of noise hits per track per event. The ATLAS specification is for noise occupancy in the SCT of less than 5×10^{-4}, both before and after irradiation.

Before discussing the noise occupancy measurements made at the testbeam it is important to make some preliminary comments about the H8 environment. It is not possible to achieve during beam test the degree of electrical hygiene enjoyed at, for example, the SCT system test, where various shielding and grounding schemes have been investigated. In particular there may be significant noise pickup in both the power cables and the (electrical) signal cables supplying the modules. Since it can be sensitive to external noise sources the testbeam is not the place to make definitive noise measurements. However beam tests are the only way in which the efficiency can be accurately determined, and it is important that a noise occupancy measurement is made under the same experimental conditions.

To avoid complications from multiple tracks, the events from which the noise mea-

---

[c] These losses are explored further in sec. 6.4.6.

surements were calculated were triggered during those phases of the super proton synchrotron (SPS) cycle in which the beam was not being extracted. These events were flagged as *noise events* and were excluded from efficiency calculations.

Hits on bad channels (see table 6.2) were ignored, but all other hits contributed to the noise occupancy, which is shown as the lower set of points in fig. 6.8. Typical noise values are a few $\times 10^{-6}$ for the unirradiated modules at 1 fC threshold – well within specifications. Module 0020* shows typical noise occupancy for an irradiated module, of a few $\times 10^{-4}$ at 1 fC, dropping below 10^{-4} at about 1.1 fC, at which threshold the efficiency is still well above 99%.

The appearance of a seemingly higher noise occupancy on the other irradiated module, 0037, disagreed other with measurements made in the laboratory, and *in situ* noise measurements (described in sec. 6.4.5) where 0037 and 0020 were found to have very similar noise. The excess in the beam test was found to have been caused by a very small number of events in which very many channels registering hits. This common mode noise is almost certainly an artifact caused by noise pickup in the testbeam setup, and does *not* reflect the true module performance, and indeed was not observed in the October 2001 beam test of the same module.

6.4.5 Signal to noise ratio

As well as the noise occupancy, the absolute value of the noise can be determined by the internal calibration circuit of the ABCD chip, using a set of standard algorithms. To measure the noise, first the amplitude response curve is found by injecting charge from the calibration DAC and varying the threshold. Once the amplification factor is known, the input noise is calculated from the statistical variations in the output signal[d].

The signal to noise ratio (S/N), defined here to be the median charge collected divided by the R.M.S. input noise is shown in fig. 6.7 (and in table 6.3). The noise measurements were made *in situ* to reduce systematic uncertainties from the calibration and threshold DACs, which are temperature dependent at the level of about 0.1% per C. The hybrid temperatures during these noise measurements were about 5 C those in the last column of table 6.1.

The noise charge for the two irradiated modules was found to be rather similar – 0.291 fC (1820 electrons) for 0020* and 0.312 fC (1950 electrons) for 0037*, after calibraton (eq. 6.1). This supports the statement in sec. 6.4.4 that the apparently higher noise occupancy of 0037* was an artifact caused by common mode noise injection.

Signal to noise is typically 14 to 15 for unirradiated, and 10 to 11 for irradiated modules. Note that in calculating the ratio S/N, any differences between the calibration capacitors have been canceled out. The fact that there are significant variations in S/N between different modules implies that the observed variations in the collected charge cannot be due systematic differences in their calibration circuits alone.

6.4.6 Pulse-Shape Analysis

It is informative to use our data to reconstruct the preamplifier output pulse. The output pulse depends both on the pulse-shape received at the input and point spread function of the preamplifier circuit in the analogue part of the `ABCD` chip.

The potential at the discriminator will be the time convolution of the received charge at the chip front-end, and the preamplifier–shaper time response. The detector

---

[d] Alternatively the noise can be found from noise occupancy.

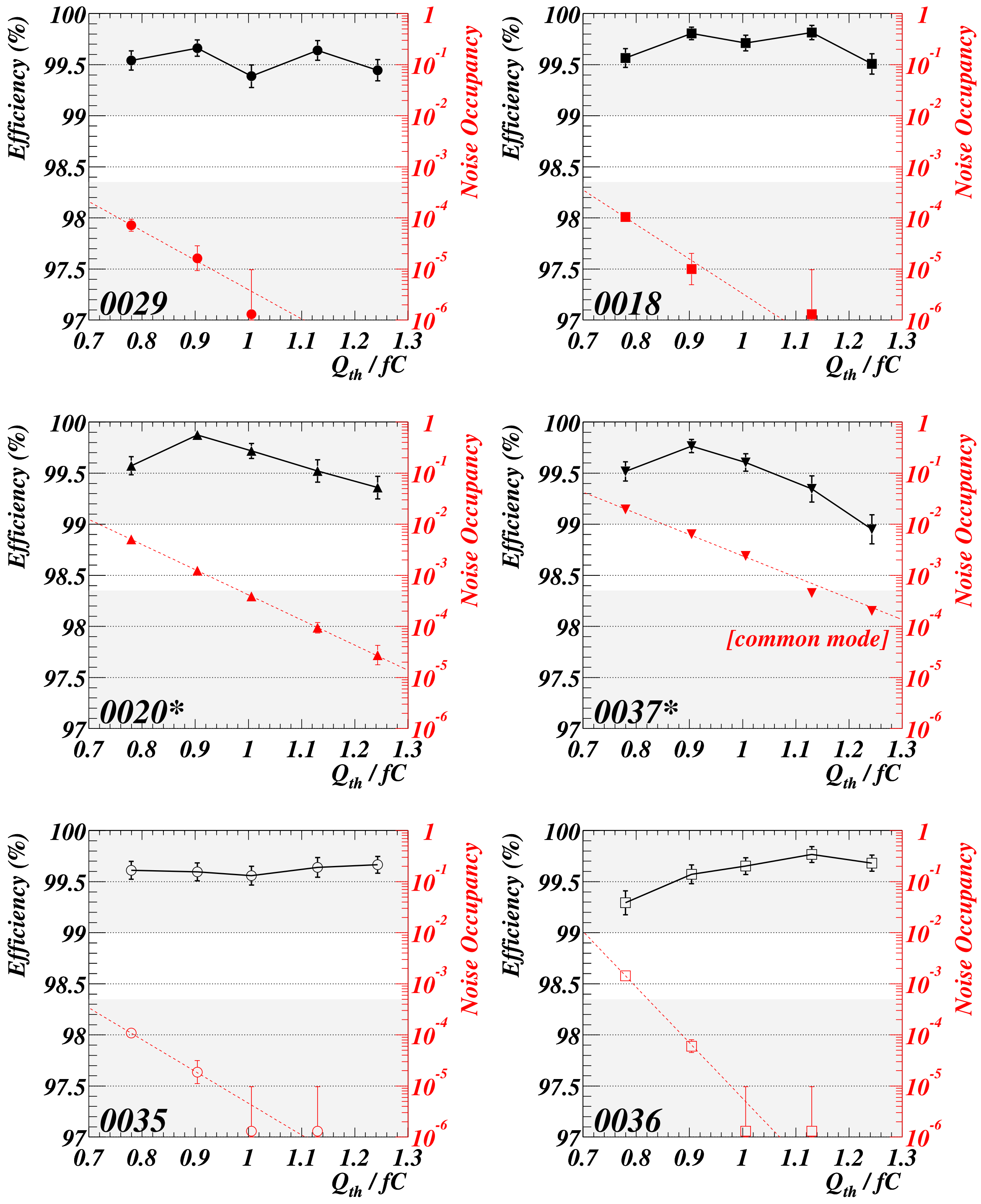

Figure 6.8: Efficiency (black, left axis) and noise occupancy (red, right axis) near the working threshold point for the six barrel modules. Data taken at normal incidence with no applied magnetic field with detector bias of 385 V for the irradiated modules 0020* and 0037*, and 200 V for the unirradiated modules. The thresholds have been calibrated according to eq. 6.1. *See text for explanation of 0037* common mode noise.*

charge collection time is about 10 nanoseconds for an unirradiated detector – much less than the amplifier shaping time of several tens of nanoseconds, so the charge collected can be approximated as a delta function. The extent to which this approximation can be justified is discussed later.

With a short collection time, by varying the arrival time and the threshold the preamplifier–shaper transfer function is recovered. While the threshold scan was conducted in steps, the time-scan was enforced during these asynchronous tests. The beam particles arrived at the detector with a flat probability density function hence with random phases relative to the 25 ns clock on the readout chips.

The response of the preamplifier–shaper circuit of the `ABCD` chips to a delta pulse is given by [170]:

$$h(t) = [\alpha_2 t^2 + \alpha_1 t + \alpha_0] \exp(-\xi t) - \beta \exp(-\zeta t) \tag{6.5}$$

where t is the time in nanoseconds, $\alpha_2 = 5.26 \times 10^{-4}$ ns^{-2}, $\alpha_1 = 5.54 \times 10^{-4}$ ns^{-1}, $\alpha_0 = 5.83 \times 10^{-3}$, $\xi = 0.1$ ns^{-1}, $\beta = 5.83 \times 10^{-3}$, and $\zeta = 5 \times 10^{-3}$ ns^{-1}. The input delta pulse is assumed to come at t=0. In order to describe the experimental data three fit parameters are needed: the amplitude of the pulse, the start time of the pulse and the amplifier peaking time. The amplifier response function then becomes:

$$R(t) = A \cdot H\left(19.1 \frac{t-d}{\tau_p}\right) \tag{6.6}$$

where A is the amplitude), d the delay, and τ_p peaking time of the electronics.

There are various methods in which this pulse reconstruction can be done. In this analysis the 50% points of the rise and fall in the efficiency versus time plot (fig. 6.2) are found for a particular threshold, Q_{thr}. These points give the times after the particle arrival at which the median charge is equal to Q_{thr}. By varying this thresh-

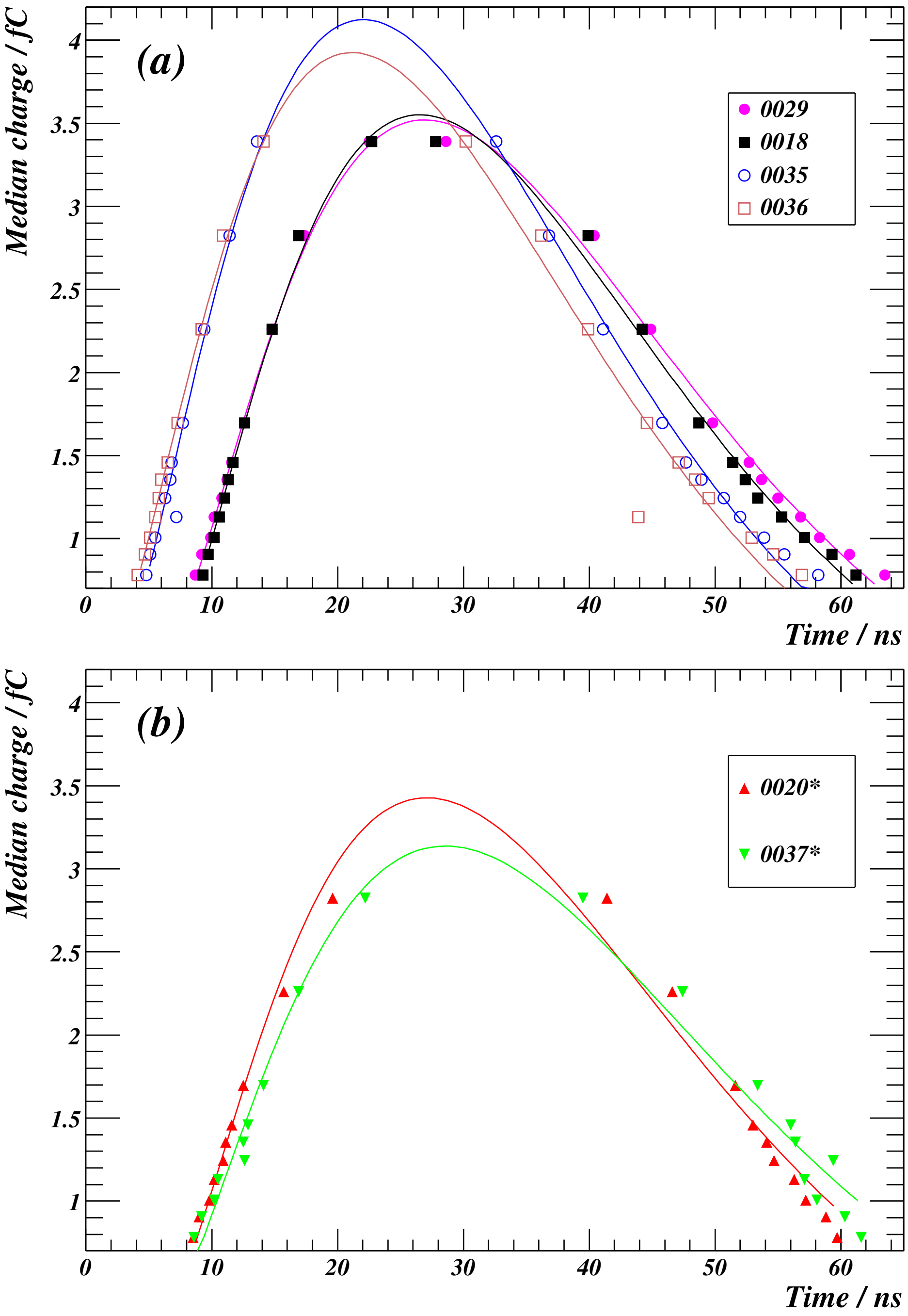

Figure 6.9: Pulse shapes calculated from the 50% points of the efficiency–time graphs for particles at normal incidence and with no applied magnetic field, for **(a)** the non-irradiated and **(b)** the irradiated modules. The detector bias was 435 V for the irradiated and 250 V for the non-irradiated modules.

Module	Link	τ_p	Error	Delay	Error
0029	0	23.1	0.8	3.9	1.4
	1	21.9	0.7	4.6	0.7
0018	0	22.3	0.5	4.4	0.8
	1	21.8	0.5	4.8	0.7
0020*	0	23.0	1.1	4.1	0.9
	1	23.6	1.5	4.6	1.2
0037*	0	25.2	1.7	3.3	1.4
	1	25.3	1.0	3.9	1.0
0035	0	22.0	1.6	0.3	1.3
	1	20.7	1.1	-0.2	0.8
0036	0	21.8	1.2	-0.4	0.8
	1	21.1	1.2	-1.4	0.9

Table 6.4: Peaking times and delays (with their associated statistical errors) from the fitted pulse shapes in fig. 6.9.

old, and plotting the 50%-efficiency times, the output pulse shape is reconstructed (fig. 6.9). The points were fitted with the three-parameter preamplifier–shaper function eq. 6.6. The fit parameters (table 6.4) show a small increase in the fitted peaking time (τ_p) for the irradiated modules.

In general the unirradiated modules (fig. 6.9a) show a good agreement between the measured and fitted shapes. The greater height of the peak for 0035 and 0036 relative to 0018 and 0029 is in agreement with the plot showing median charge collected as a function of bias (fig. 6.6), and shows that modifying TDC cuts will not change the conclusion that there is a systematic difference between these pairs. The displacement offset along the time axis is an artifact caused by slightly different signal-cable lengths serving the modules.

The data are a little flatter in the peak region compared to the fits, or equivalently a little broader in time. This is because the input pulse, which in reality is a few nanoseconds wide, has been approximated by a delta function in time. This

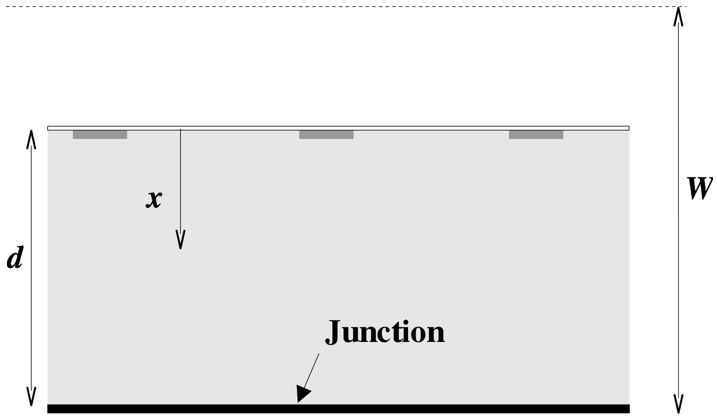

Figure 6.10: Dimensions for the 1-dimensional charge-collection model described in the text. W is the width that the depletion region would have in a semi-infinite junction.

broadening is greater for the irradiated modules (fig. 6.9b) for which the charge collection time will be longer.

The charge collection time can be investigated using a simple 1-dimensional model in which diffusion, recombination and charge trapping are neglected (fig. 6.10). If the detector is over-depleted, then the Maxwell equation for the electric field,

$$\frac{dE_x}{dx} = \frac{eN_{\text{eff}}}{\epsilon_0 \epsilon_{\text{Si}}} \ , \tag{6.7}$$

can be solved with the boundary condition:

$$\int_0^d E_x(x)\ dx \ = \ -V_{\text{bias}} \ . \tag{6.8}$$

For an irradiated detector which has undergone type inversion the depletion region grows from the back-plane, and so the electric field must be given by:

$$E_x = \frac{eN_{\text{eff}}}{\epsilon_0 \epsilon_{\text{Si}}}(x + \Delta) \ , \tag{6.9}$$

where $\Delta = \frac{W^2-d^2}{2d}$, d is the physical width of the detector, and W ($> d$) is is the width that the depletion region would have in a semi-infinite junction at that bias,

$$W = \sqrt{\frac{2\epsilon_0\epsilon_{\mathrm{Si}}V_{\mathrm{bias}}}{eN_{\mathrm{eff}}}} \ . \tag{6.10}$$

Note that as in sec. 5.2 a sharp edge to the depletion region is assumed. The time, t, for a charge at depth x to reach the strips is then given by:

$$t(x) = \tau_\mu \ln\left(x/\Delta + 1\right) \ , \tag{6.11}$$

where $\tau_\mu = \epsilon_0\epsilon_{\mathrm{Si}}/(\mu e N_{\mathrm{eff}})$ and μ is the hole mobility. Thus the total time during which charge is collected is:

$$t(d) = \tau_\mu \ln\left(\frac{W^2+d^2}{W^2-d^2}\right) \ . \tag{6.12}$$

This time structure leads to an asymmetric signal which is larger at later times. Of course this model is very simplified. For example it does not include the trapping, recombination or diffusion in the bulk, or capacitive coupling or diffusion into the oxide at the surface. However the asymmetric charge pulse could explain the distortion from the expected ABCD response curve in fig. 6.9b. The convolution of an increasing input pulse function with the ABCD response function (eq. 6.5) will skew the peak of the output curves to higher values at later times. One must however be careful in assigning changes in the output pulse shape to the detectors alone. The resistors and capacitors in the ASICs have also undergone irradiation, so the constants in eq. 6.5 may also have changed.

One might expect that the effect of reducing the bias voltage such that $W \to d$ would be that the collection time will become large. This has indeed been observed (see [7]), however the increase in the collection time is rather slower than would be predicted by eq. 6.12. This may be because of inadequacies in the model, which does not take into account capacitive coupling to holes at short distances from the top of of the detector, charge diffusion or the trapping of free carriers at radiation-induced defects. A description of a more realistic 2-dimensional numerical model can be found in [171].

6.4.7 Magnetic field and non-normal incident tracks

The effect of applying a 1.56 T magnetic field directed along the direction of the strips has been studied in [7], as has the effect of varying the incident angle of the particle from the normal. At an incident angle of 15° an increase in charge sharing was observed, with the proportion of multi-hit clusters up to about 30%, leading to an improvement in spatial resolution of about 2 μm. Sub-threshold charge sharing led to a ≈ 0.4 fC loss in median charge collected, which did not cause a significant loss in efficiency at $Q_{\mathrm{th}} = 1$ fC. The application of the magnetic field was found to be equivalent to a shift in the angle of the incident particle by the 'Lorentz angle', $\Theta_L = \mu^H B \approx 2-3°$, where μ^H is the Hall mobility.

6.4.8 Edge measurements

In the ATLAS SCT there will be a small overlap between neighbouring modules. This will allow their relative alignment to be calculated from tracks which pass through the edge of both modules. It is therefore important that the detectors remain efficient at their edges, and that the residuals are not significantly distorted by edge effects (the efficiency loss in the gap between the detectors is examined in sec. 6.4.9). The numbering convention used in this section (shown in fig. 6.11) is

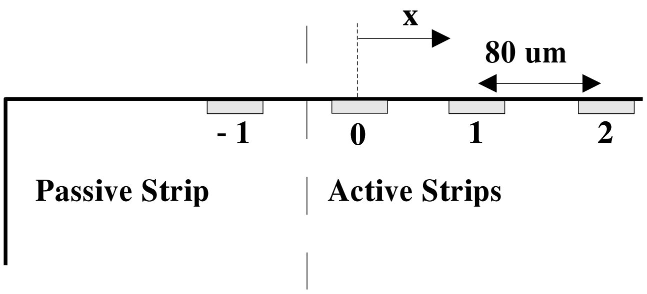

Figure 6.11: Diagram demonstrating the numbering convention for strips (not to scale).

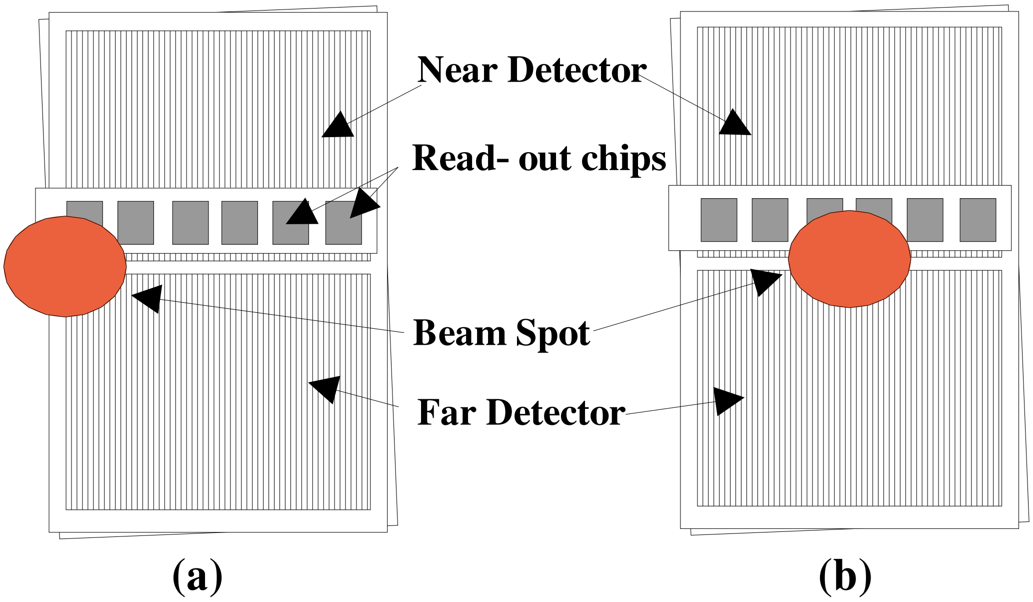

Figure 6.12: The beam edge **(a)** and gap **(b)** positions.

$\{0, 1, 2, 3, \ldots\}$ for the active strips, starting from the edge of the link which is nearest the center of the beam. The very edge strip is not connected to the readout ASICs. This passive strip is assigned the number -1.

To investigate the behaviour of the modules near their edges, during the period 10th to 13th August 2001 some of the barrel modules were offset so that the beam passed through the corners of the detectors (as in fig. 6.12a), or through the gap bewteen the detectors (fig. 6.12b).

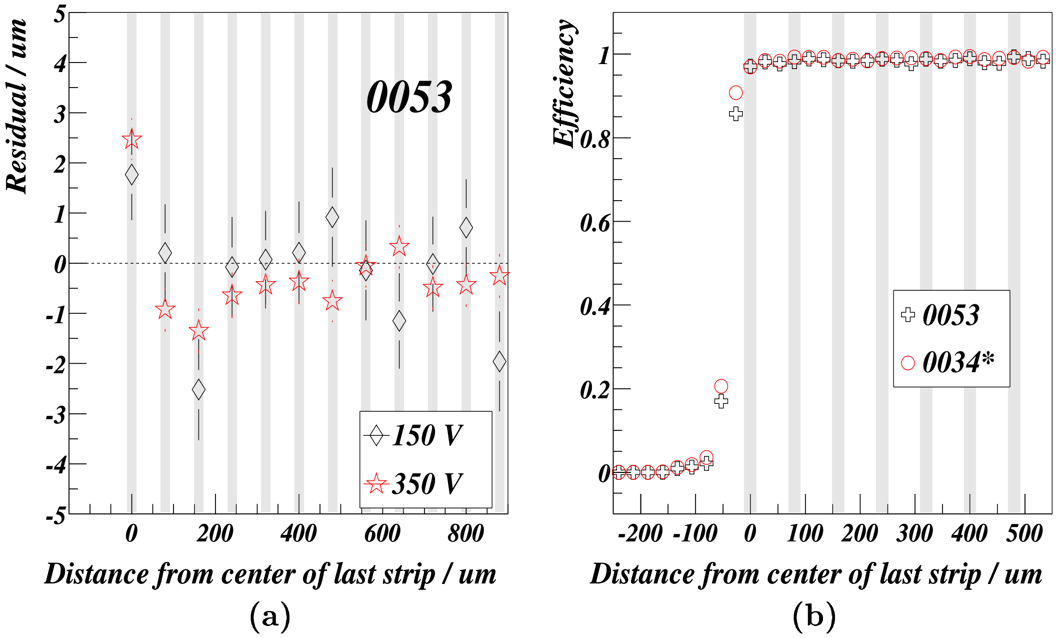

Figure 6.13: (a) Residuals and (b) efficiency at the edge of the detector. as a function of the projected distance of the track from the center of the final read-out strip. A positive residual means that the average hit position is towards the center of the module relative to the projected track position. Grey lines indicate active strips. Data taken at normal incidence in the absence of an applied magnetic field. $V_{\text{bias}} = 460$ V on 0034*. Both links have been added together to increase the statistics.

The edge measurements were repeated with higher statistics in the beam test of July 2002 with the unirradiated barrel modules 0053 and 0056, and the irradiated modules 0007 and 0034. The low-statistics results from August 2001 were presented in [7], and are not repeated here.

Fig. 6.13a shows the residuals as a function of the projected perpendicular position of the track from the center of the first active strip. No significant deviation from zero is observed for the tracks centered on the second strip or beyond. No significant difference was observed when the bias is varied, as was also found for the irradiated modules.

Those tracks in the bin with projected postions $-40 < x < 40$ μm show a ≈ 2 μm

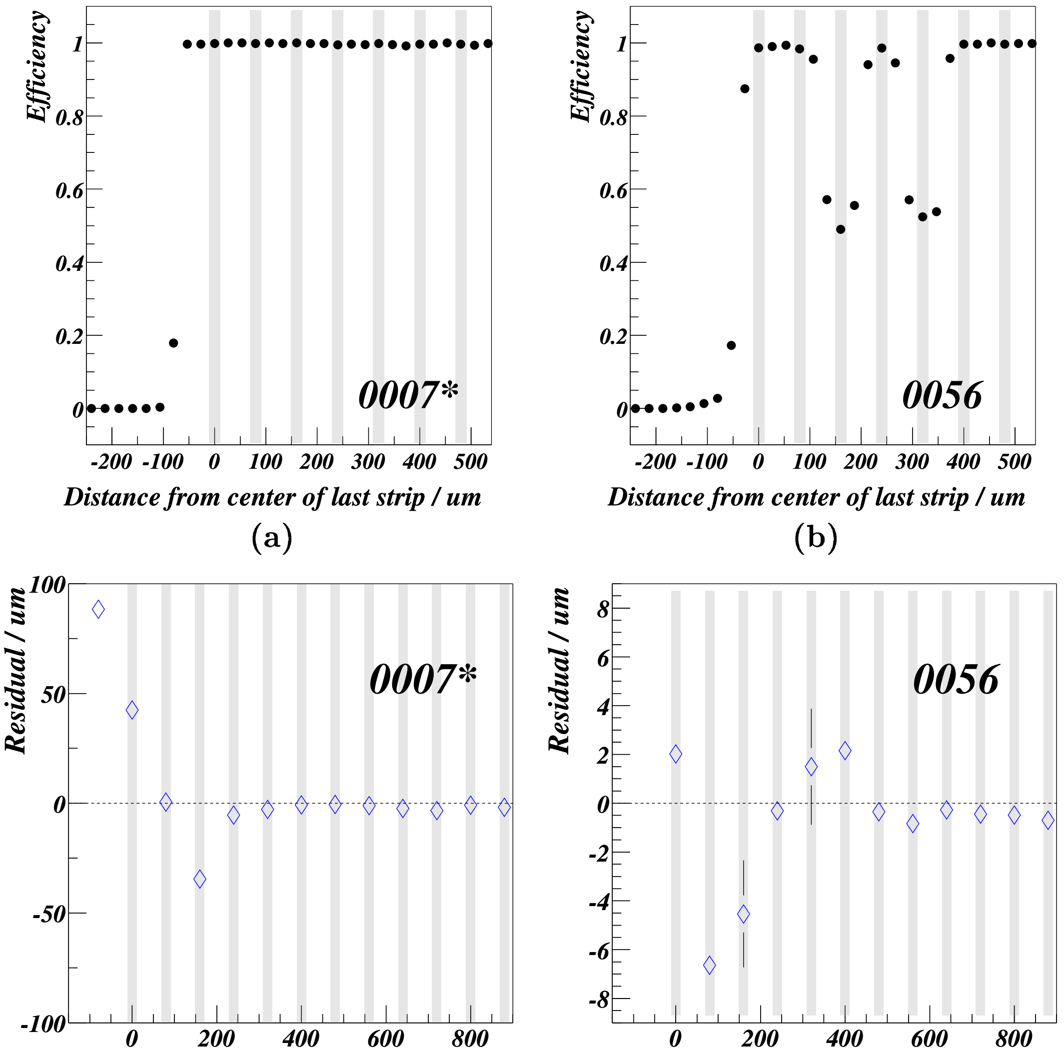

(a) (b) (c) (d)

Figure 6.14: Systematic effects at the edge of the detector caused by noisy and unbonded channels. $V_{\text{bias}} = 460$ V on 0007 and 300 V on 0056. Data taken at normal incidence, in the absence of an applied magnetic field. Data is plotted for link '1' only.

average shift towards the center of the module. Such a shift is to be expected, since the charge deposited by these particles can only be detected if it is shared in the direction of #1. From plots like fig. 6.3 it is found that about 7% of clusters have more than one hit. We would therefore expect to find a systematic shift in the residuals for the last active strip of about $7\%/2 \times 40 = 1.4$ μm, where the factor of one half comes from half of the charge being shared in each direction.

The fall-off in efficiency near the edge of the detector is shown in fig. 6.13b. It can be seen that the module remains fully efficient to the center of the last read-out strip, beyond which the efficiency drops rapidly to almost zero over a distance about 40 μm. This is what one might expect, since beyond this point, the majority of the charge will fall in the inactive region.

Some of the effects of bad strips are shown in fig. 6.14. Module 0007* had an extremely noisy strip which was not masked (#1). This channel recorded a hit in almost every event, causing a 40 μm shift in the residuals for the neighbouring (#0 and #2) strips (fig. 6.14c), and artificially forcing full efficiency out to $x = -40$ (fig. 6.14a).

Noisy strips are usually removed either by hardware or software masking. The effect of removing strips can be seen in fig. 6.14b and 6.14d. On this detector, channels #2 and #4 showed a very small occupancy – behaviour consistent with having been left unbonded. The dips in efficiency near the dead strips are obvious. Just as importantly, the residuals of the neighbouring strips are shifted by several microns because of charge-sharing asymmetry.

The very first point in fig. 6.14c ($-120 < x < -40$) shows a large (≈ 90 μm) residual which originates from a different source. This is the residual for the tracks incident near the passive strip. Tracks in this region will not be detected unless they share charge into the neighbouring active strip, so must necessarily give rise to large residuals ($> 40\mu$m). Similar features are observed in fig. 6.13a and fig. 6.14d at about +60 μm if the y-axes are extended. In the case of module 0007* the noisy strip (#1) has had the effect of further exacerbating this effect.

To obtain an accurate alignment from the strips near the edge of the detectors one must not be biased by loss of charge shared to a bad (noisy, dead or unbonded) strip, or off the edge of the module. For normal incidence the cluster size is almost never greater than two strips, and so two-strip clusters can be assumed to have lost no charge. Single-hit clusters next to bad strips or on the last active channel may have had significant loss of shared charge, and so must be ignored to aviod introducing a bias.

If the incident angle of the particle is *a priori* unknown, then the cluster size may be large. In such a situation the only way to be confident that charge was not lost is to ensure that clusters are terminated by good strips on both sides.

6.4.9 Gap measurements

Each plane of a module consists of pairs of 62 mm long strips wire-bonded together to obtain an effective 124 mm strip length. The module is obviously not expected to be efficient in the gap between the two detectors. The width of the “dead area” was investigated for the modules with the beam in the corner position (fig. 6.12a). Efficiency was measured as a function of the projected position of the track in the direction parallel to the strips.

The efficiency drop in the inactive region is shown for module 0029 in fig. 6.16. The size of the region, found by fitting a step function, smeared with a gaussian to each edge. The full width at half maximum of the fitted gap was found for each side of three modules, using the five-parameter fitting function:

$$\varepsilon = \varepsilon_0 \cdot f\left(\frac{y_{near} - y}{\delta_{near}}\right) \cdot f\left(\frac{y - y_{far}}{\delta_{far}}\right) \quad , \tag{6.13}$$

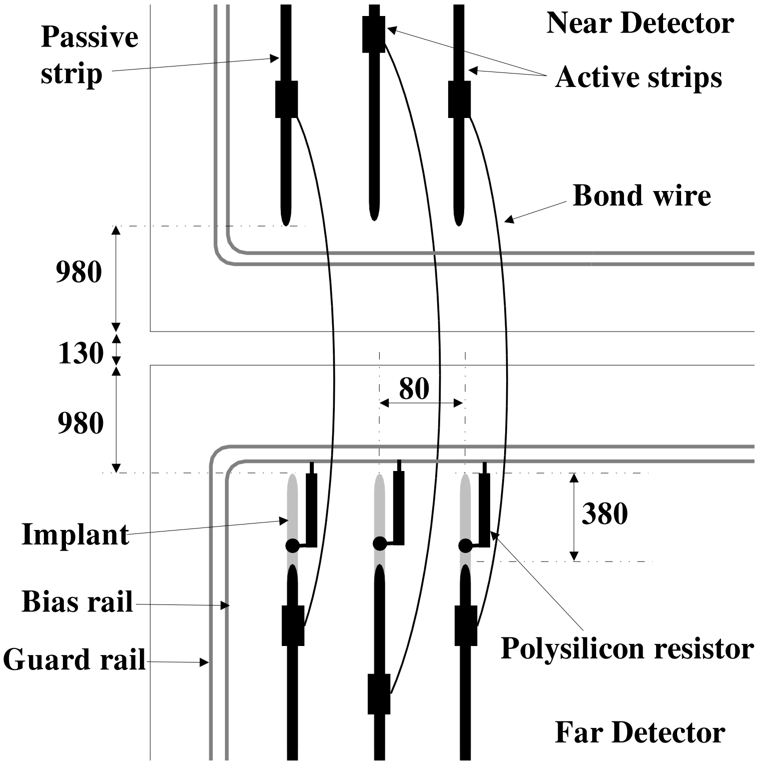

Figure 6.15: Diagram of the corners of the two detectors, showing the dimensions of the gap between them (not to scale). The inactive area consists of the physical gap between the cut ends of the detectors plus the distance between the end of the strip implant and the cut end of each detector. The polysilicon bias resistors actually directly overlie the p-implant, but have been offset for clarity. All distances are in μm.

where

$$f(x) = \frac{1}{2}\left[1 + \tanh(x)\right] \ . \tag{6.14}$$

The size of the gap was found to lie in the range 2038 to 2082 μm, with a weighted mean of 2057 μm (fig. 6.17). The expected dimensions of the dead area around the gap are shown in fig. 6.15. The total inactive distance is expected to be $130 + 2 \times 980 = 2090$ μm. Note that the detectors are precision-placed to within a few microns of the values shown in fig. 6.15. There is a suggestion of a slight decrease in the effective size of the gap for the irradiated module 0020* (χ^2/n.d.f. = 10.9/5, P=0.053).

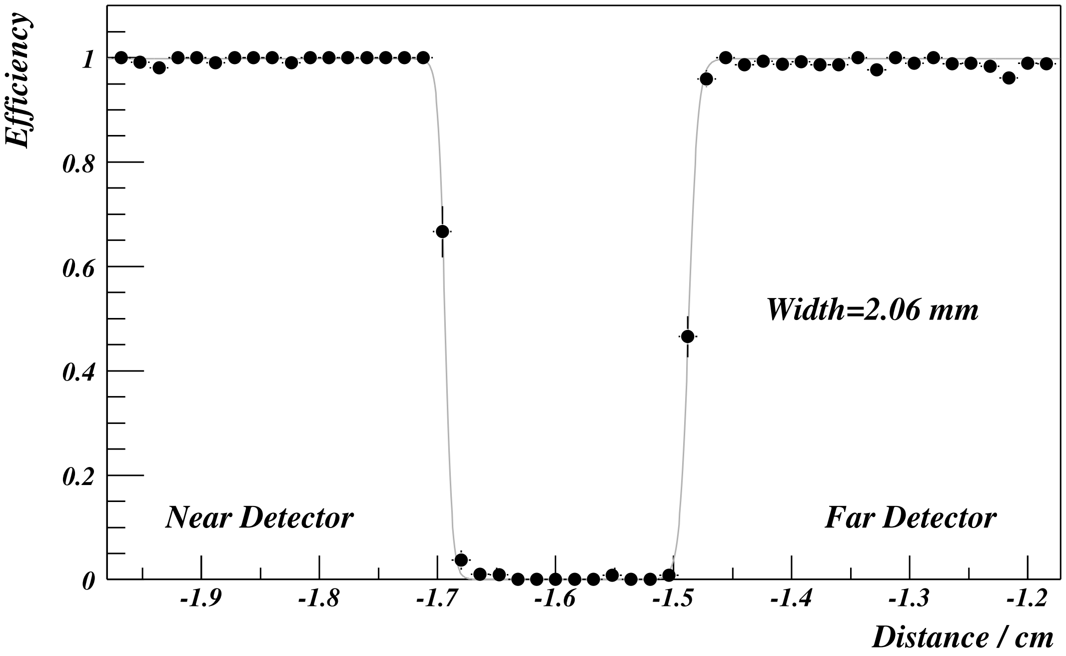

Figure 6.16: The efficiency of module 0029 as a function of distance parallel to the strips, with a zero-point defined by the tracking telescope. The central inefficient region corresponds to the inactive area of the module, between detectors. The fitted function is given by eq. 6.13. Data taken at 1.0 fC nominal threshold, with no magnetic field, with an applied bias of 200 V. Link '0' only.

The average loss in efficiency for normally incident particles at $\eta = 0$ will therefore be about 2 mm/124 mm = 1.6% for a single plane. The effect on a whole module can be calculated from the geometry (see fig. 6.18). The 40 mrad stereo angle means that the gap between detectors on one side of the module will be partially covered by those on the the opposite side. There will remain four triangular regions each of size $\frac{1}{2}(61.44/2)^2 \cdot \sin(0.04) = 19\ \mathrm{mm}^2$ in which one can expect a hit on only one detector - corresponding to 1% of the total area. The fractional area left uncovered by any of the module's four detectors is a further 1.1%.

There is no metalisation over the end of the strip on the far detector because of the presence of a polysilicon biasing resistor. To investigate whether this might cause a

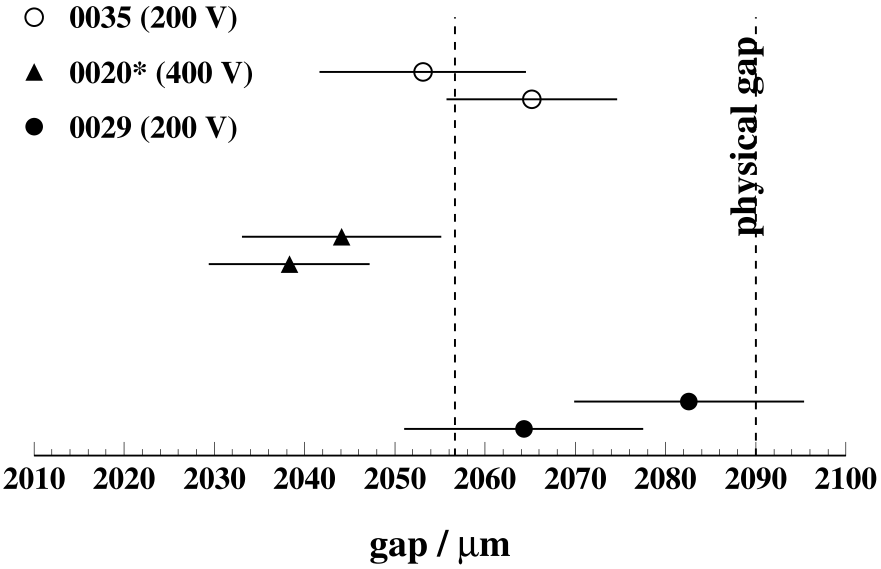

Figure 6.17: Fitted full width at half-maximum of the gap region for both sides of each of three modules. The values are offset vertically for clarity, the lower of each pair being link '0'. Data taken with no magnetic field, and at normal incidence.

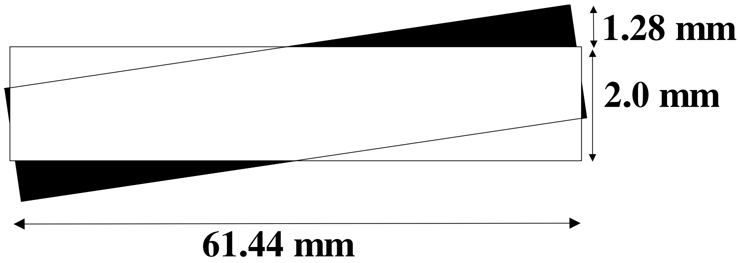

Figure 6.18: The geometry of the overlap region. Each rectangle represents the gap between the planes on one side of a module. The stereo angle between the planes is 40 mrad.

decrease in efficiency near the end of the strips, the asymmetry in the sharpness of the rise- and fall-rates was measured. No significant asymmetry was observed at the 90% confidence level, either in the irradiated or the unirradiated modules (fig. 6.19).

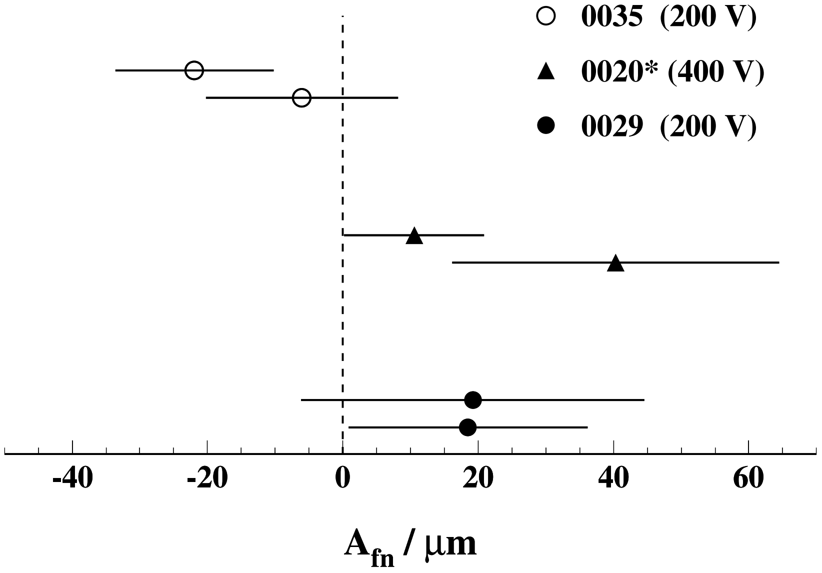

Figure 6.19: Asymmetry between the rate of loss in efficiency at the near and the far detector edges. $A_{fn} = \delta_{far} - \delta_{near}$, where δ_{far} and δ_{near} are defined in eq. 6.13.

6.5 Conclusions

Data from the August 2001 and part of the July 2002 ATLAS SCT beam test have been analysed. My analysis focuses on the six barrel modules present in the August 2001 test, two of which had been irradiated to a fluence greater than that expected during 10 years of LHC operation. These modules demonstrated that the ATLAS SCT production modules can be expected to operate within specification, with strip efficiency of $> 99\%$ for noise occupancy $< 5 \times 10^{-4}$, even after irradiation.

Measurements of the median charge collected and the associated signal to noise ratios showed systematic variations between modules which could not be explained by known calibration or timing differences.

The inefficient region between pairs of daisy-linked detectors was found to be about 30 μm smaller than the physical gap between the ends of the implants for both irradiated and unirradiated modules.

Precision measurements were made at the edge of the detectors on two irradiated and two unirradiated barrel modules during July 2002. These show no significant drop in efficiency except for a few percent lost on the final active strip. Asymmetric charge sharing causes a shift in the residual of a few microns on the last strip, and indeed in any strip immediately next to a masked channel. However the shift in the residuals due to extremely noisy strips which remain unmasked can be much larger. No other significant distortion of the residuals was found at the 1 μm level.

Chapter 7

Conclusions

While the standard model of particle physics has been immensely successful, there are strong reasons for expecting that there should be new physics at the TeV scale. Supersymmetry is arguably the least unbelievable solution, and is certainly favoured by many in the theoretical community. However the physics of fundamental particles is *science* and so our theoretical models must be subject to experimental test.

When, in a few years time, the LHC starts taking data, direct experimental tests of TeV-scale supersymmetry will become possible.

I have emphasised in this thesis the need to examine a representative set of supersymmetry models so that the opportunity to discover new particles is not wasted. To this end I have presented experimental analyses based on Monte-Carlo simulation which can tease out two of the most experimentally difficult signatures for supersymmetry.

In the case of baryon-violating supersymmetry I show that, using leptons from cascade decays, the large jet multiplicity of the final state can be disentangled, allowing the mass reconstruction of squark, slepton, and two neutralino states. Furthermore, by examining the fraction of jets which contain secondary vertices and non-isolated muons, insight can be gained into the flavor structure of the R-parity violating coupling.

For anomaly-mediated supersymmetry, where the $\tilde{\chi}_1^+$ and $\tilde{\chi}_1^0$ are almost mass-degenerate, I demonstrate that by using isolation cuts and particle identification, the low-momentum particles from $\tilde{\chi}_1^+$ decays *can* be detected at the LHC in events with large missing transverse momentum. What is more, provided sufficient SUSY particles are produced, the mass difference between the $\tilde{\chi}_1^+$ and the $\tilde{\chi}_1^0$ can be measured with an uncertainty of about 10%.

In the final chapters I present an investigation into the performance of one of the ATLAS sub-detectors which will be vital for the above analyses. Beam tests of ATLAS semiconductor tracker barrel modules demonstrate that these modules can be expected to perform to specification even after exposure to radiation equivalent to ten years of LHC running.

Appendix A

Abbreviations

AMSB	anomaly mediated supersymmetry breaking
ASIC	application-specific integrated circuit
CERN	the European particle physics laboratory
CMOS	complimentary metal oxide semiconductor
CMS	compact muon solenoid experiment
CSC	cathode strip chamber
DAC	digital-to-analogue converter
DAQ	data acquisition
ECAL	electromagnetic calorimeter
EM	electromagnetic
eV	electron volt $\approx 1.602 \times 10^{-19}$ joules
FCAL	forward calorimeter
FIFO	first-in-first-out buffer
GMSB	gauge-mediated supersymmetry breaking
GUT	grand unified theory
HCAL	hadronic calorimeter
ID	inner detector
LAr	liquid argon
LEP	large electron positron collider
LHC	large hadron collider
LSP	lightest supersymmetric particle
MDT	monitored drift tube
MIP	minimally ionising particle
MOS	metal oxide semiconductor
MSSM	minimal supersymmetric standard model
mSUGRA	minimal supergravity
NLSP	next-to-lightest supersymmetric particle
OSSF	opposite sign, same flavour

p_T	transverse momentum
QCD	quantum chromodynamics
QED	quantum electrodynamics
RGE	renormalisation group equation
RPC	R-parity conserving
RPC	resistive plate chamber
RPV	R-parity violating
SCT	semiconductor tracker
SM	standard model
SPS	super proton synchrotron (or Snowmass points and slopes)
SUSY	supersymmetry
TDC	time-to-digital converter
TGC	thin gap chamber
TRT	transition radiation tracker
VEV	vacuum expectation value

Appendix B

The Higgs mechanism

The usual QED lagrangian density is written in terms of a vector field, A_μ, and a Dirac spinor field, ψ

$$\mathcal{L}_{\mathrm{QED}} = \bar{\psi}(i\gamma^\mu \partial_\mu - m)\psi + e\bar{\psi}\gamma^\mu A_\mu \psi - \frac{1}{4}F_{\mu\nu}F^{\mu\nu} \tag{B.1}$$

where the Dirac matrices γ_μ satisfy the anticommutation relations $\gamma^\mu\gamma^\nu + \gamma^\nu\gamma^\mu = 2g^{\mu\nu}$, with $g^{\mu\nu}$ the metric tensor, and $F_{\mu\nu} = \partial_\mu A_\nu - \partial_\nu A_\mu$.

Eq. B.1 can be derived from the Dirac equation $(i\gamma^\mu \partial_\mu - m)\psi = 0$ by insisting that it be invariant under a local $U(1)$ gauge transformation:

$$\psi \to e^{-i\alpha}\psi, \qquad A_\mu \to A_\mu + \frac{1}{e}\partial_\mu \alpha \tag{B.2}$$

Adding a term $\mathcal{L}_{\mathrm{m}} = -\frac{1}{2}m_A^2 A_\mu A^\mu$ which is not invariant under eq. B.2 would destroy the gauge symmetry so a vector boson mass cannot be added “by hand”.

The Higgs method, by which vector boson masses *can* be introduced without breaking the gauge invariance is illustrated below, following closely the arguements of [9].

Considering the langrangian density of two real, scalar fields, φ, and a vector field, A_μ,

$$\mathcal{L}_{\mathrm{H}} = -\frac{1}{2}D_\mu\varphi_1 D^\mu\varphi_1 - \frac{1}{2}D_\mu\varphi_2 D^\mu\varphi_2 - V(\varphi_1^2 + \varphi_2^2) - \frac{1}{4}F_{\mu\nu}F^{\mu\nu}, \tag{B.3}$$

where the gauge covariant derivatives are given by:

$$\begin{aligned} D_\mu\varphi_1 &\equiv \partial_\mu\varphi_1 - eA_\mu\varphi_2, \\ D_\mu\varphi_2 &\equiv \partial_\mu\varphi_2 + eA_\mu\varphi_1 \end{aligned}$$

and where e is a dimensionless constant, $\mathcal{L}_{\rm H}$ is invariant under the local gauge transformation:

$$\varphi_1 \to \varphi_1 e^{i\alpha}, \qquad \varphi_2 \to \varphi_2 e^{i\alpha}, \qquad A_\mu \to A_\mu + \frac{1}{e}\partial_\mu\alpha$$

For spontaneous symmetry breaking the potential V should have a local minimum at $V'(\varphi_0^2) = 0$ with $V''(\varphi_0^2) > 0$ for some $\varphi \neq 0$.

Treating A^μ, $\Delta\varphi_1$ and $\Delta\varphi_2$ as small quantities, and expanding about the minimum with the gauge fixed such that $\varphi_1 = 0, \varphi_2 = \varphi_0$, gives the equations of motion

$$\partial^\mu\{\partial_\mu(\Delta\varphi_1) - e\varphi_0 A_\mu\} = 0 \tag{B.4}$$

$$\{\partial_\mu\partial^\mu - 4\varphi_0^2 V''(\varphi_0^2)\}(\Delta\varphi_2) = 0 \tag{B.5}$$

$$\partial_\nu F^{\mu\nu} = e\varphi_0\{\partial^\mu(\Delta\varphi_1) - e\varphi_0 A^\mu\} \tag{B.6}$$

The Euler-Lagrange equation obtained from $\Delta\varphi_2$ leads to eq. B.5 which describes a scalar whose quanta have mass $m_h^{bare} = 2\varphi^0\sqrt{V''(\varphi_0^2)}$. Here a prime ($'$) indicates a derivative of V with respect to the square of the field so

$$V''(\varphi_0) \equiv \left.\frac{d^2V}{d(\varphi^2)^2}\right|_{\varphi=\varphi_0} = (2\varphi_0)^{-2}\left.\frac{d^2V}{d\varphi^2}\right|_{\varphi=\varphi_0} \tag{B.7}$$

The corresponding equations for $\Delta\varphi_1$ and A^μ produce eq. B.4 and eq. B.6 respec-

Figure B.1: Broken-symmetry diagrams which lead to a mass for the gauge field. The dashes represent interactions with the non-zero field VEV $\langle\varphi_2\rangle$; dots represent the φ_1 propagator; and waves correspond to the A_μ propagator. After [10].

tively which can be transformed using the new variables

$$B_\mu \equiv A_\mu - \frac{1}{e\varphi_0}\partial_\mu(\Delta\varphi_1), \quad \text{and} \quad C_{\mu\nu} \equiv \partial_\mu B_\nu - \partial_\nu B_\mu = F_{\mu\nu}$$

into

$$\partial_\mu B^\mu = 0, \qquad \partial_\nu C^{\mu\nu} + e^2\varphi_0^2 B^\mu = 0$$

This is the equation for a vector boson with a bare mass $e\varphi_0$.

This effective mass will only appear when the vector field is coupled to “rotations” in the degenerate vacuum state, as in eq. B.3, and where the potential V takes a non-zero vacuum expectation value (VEV). The diagrams which lead to the mass for the gauge field are shown in fig. B.1.

It is important to note that while the guage symmetry is spontaneously broken in the vacuum state, in the limit $T \to \infty$, when the masses become negligable, the symmetry is restored.

Appendix B The Higgs mechanism

Appendix C

Simulation of particle tracks

Part of the `ATLFAST` [86] software provides fast parameterised simulation of the ATLAS inner detector performance. In particular it calculates the expected track reconstruction efficiency, and smears the five track helix parameters and according to particle type. The parameterisation used was based on `GEANT3` Monte-Carlo simulations [87] using a Kalman-filter algorithm for track reconstruction [172]. A parameterisation from a large statistics Monte-Carlo sample [173], was used for the hadronic track smearing in chapter 3. The probability density function is the sum of a narrow gaussian which corresponds to the experimental resolution, and a wide gaussian which simulates the effect of multiple scattering.

C.1 Low p_T electron identification

In ATLAS the transition radiation tracker allows the identification of low-energy electrons because they emit more transition radiation than more massive particles with the same momentum. The issue of particle misidentification is not dealt with in the standard version of `ATLFAST`, and so has been implemented independently in our analysis.

Test beam performance was compared to Monte-Carlo simulations in [174] using a combined discriminator which considered both the number of high threshold clusters

p_T	0.5	1	2	5	10	≥ 20
ϵ_π	0.01	0.003	0.005	0.007	0.008	0.012

Table C.1: Pion misidentification efficiency at $|\eta| = 0.3$ as a function of transverse momentum for an electron identification efficiency of 90%. Interpolations were made linearly in p_T and logarithmically in ϵ_π. Particles with $p_T < 0.5$ GeV are assumed not to be reconstructed into tracks.

$\lvert\eta\rvert$	≤ 0.2	0.3	0.65	0.8	1.15	1.4	1.9	2.15	≥ 2.4
p_T 2 GeV	1.2	1.0	0.88	1.	0.6	0.4	0.028	0.88	2
p_T 20 GeV	1.1	1.0	1.	2.0	1.4	0.78	0.22	1.4	2.3

Table C.2: η dependent correction factor applied to ϵ_π, the hadron misidentification efficiency, for two different values of transverse momentum. Interpolations were made logarithmically in ϵ_π and linearly in p_T and η. Tracks beyond $|\eta| = 2.5$ are not reconstructed.

and the time for which the charge deposited exceeded a lower threshold. In that paper the pion misidentification probability was calculated as a function of transverse momentum at $\eta = 0.3$ for an electron efficiency of 90% (table C.1). For our simulation these efficiencies were extrapolated to other values of η by comparison with the `GEANT3` simulations performed in [30]. The p_T and η dependent correction factors are shown in table C.2.

C.2 Low p_T muon identification

High energy muons are easily identified because of their high penetration. Identification efficiency is drastically reduced when muons have an insufficient transverse momentum to extend their track helix into the dedicated muon detectors. The applied identification efficiencies for muons were based on [30] and are shown in table C.3.

p_T	≤ 2	3	4	5	6	8	≥ 10
Efficiency	0	0.34	0.66	0.89	0.95	0.96	0.98

Table C.3: Applied muon identification efficiency as a function of transverse momentum. Efficiencies were interpolated linearly in ϵ_μ and p_T.

Appendix D

The variable m_{T2} and its generalisation

The Cambridge m_{T2} variable, proposed in [175], can be used in analyses such as [69], where particles are pair-produced at hadronic colliders, and decay semi-invisibly, as is the case in R-parity conserving SUSY. This variable is used in symmetrical, two-body decays of supersymmetric particles, where the LSP is unobserved, and so must be inferred from missing energy.

D.1 The properties of m_{T2}

For events in which the decay of a heavy object produces an unseen particle, such as

$$\tilde{\chi}_1^+ \to \tilde{\chi}_1^0 \pi^+ \tag{D.1}$$

one can write the Lorentz invariant

$$m^2_{\tilde{\chi}_1^+} = m^2_\pi + m^2_{\tilde{\chi}_1^0} + 2\Big[E_T^\pi E_T^{\tilde{\chi}_1^0} \cosh(\Delta\eta) - \mathbf{p}_T^\pi \cdot \mathbf{p}_T^{\tilde{\chi}_1^0}\Big] \tag{D.2}$$

where $\mathbf{p}_T^{\pi}$ and $\mathbf{p}_T^{\tilde{\chi}_1^0}$ indicate pion and neutralino 2-vectors in the transverse plane, and the transverse energies are defined by

$$E_T^{\pi} = \sqrt{(\mathbf{p}_T^{\pi})^2 + m_{\pi}^2} \qquad \text{and} \qquad E_T^{\tilde{\chi}_1^0} = \sqrt{(\mathbf{p}_T^{\tilde{\chi}_1^0})^2 + m_{\tilde{\chi}_1^0}^2}\ . \tag{D.3}$$

Also

$$\eta = \frac{1}{2}\log\left[\frac{E+p_z}{E-p_z}\right] \tag{D.4}$$

is the true rapidity, so that

$$\tanh\eta = p_z/E\ , \qquad \sinh\eta = p_z/E_T\ , \qquad \cosh\eta = E/E_T. \tag{D.5}$$

In a hadron collider, only the transverse components of a missing particle's momentum can be inferred, so it is useful to define the transverse mass,

$$m_T^2(\mathbf{p}_T^{\pi}, \mathbf{p}_T^{\tilde{\chi}_1^0}) \equiv m_{\pi^+}^2 + m_{\tilde{\chi}_1^0}^2 + 2(E_T^{\pi}E_T^{\tilde{\chi}_1^0} - \mathbf{p}_T^{\pi}\cdot\mathbf{p}_T^{\tilde{\chi}_1^0}) \tag{D.6}$$

which, because $\cosh(x) \geq 1$, is less than or equal to the mass of the lightest chargino, with equality only when the rapidity difference between the neutralino and the pion, $\Delta\eta_{\tilde{\chi}_1^0\pi}$ is zero. All other $\Delta\eta$ lead to $m_T < m_{\tilde{\chi}_1^+}$, so if we knew the neutralino momentum we could use m_T to give an event by event lower bound on the lightest chargino mass. m_T was used in this way by CDF [176] and D0 [177] in the measurement of the $W^{\pm}$ mass.

In R-parity conserving SUSY events there are expected to be two unseen LSPs.[a] Since only the *sum* of the missing transverse momentum of the two neutralinos is

---

[a] Though there may also be other unseen particles – see appendix D.2.

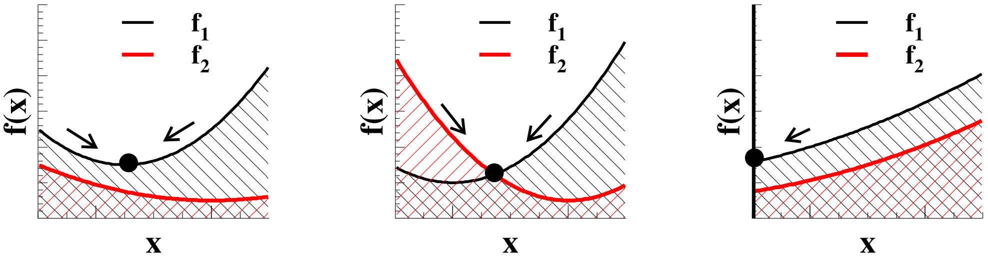

(a) (b) (c)

Figure D.1: A diagram demonstrating that the minimisation over some parameter of the maximum of two well-behaved functions may occur either at **(a)** a minimum value of one of them, or **(b)** when they are equal, or **(c)** at the boundary of the domain.

known, the variable

$$m_{T2}^2 \equiv \min_{\not{q}_T^{(1)}+\not{q}_T^{(2)}=\not{p}_T} \left[\max\left\{m_T^2(\mathbf{p}_T^{\pi^{(1)}}, \not{q}_T^{(1)}),\ m_T^2(\mathbf{p}_T^{\pi^{(2)}}, \not{q}_T^{(2)})\right\}\right] \tag{D.7}$$

is a lower bound on the transverse mass m_T for events where two decays of the type eq. D.1 occur. In eq. D.7 we have been forced to minimise over all consistent neutralino 2-momenta. Note that $\not{q}_T^{(i)}$ is the hypothesised momentum of the ith neutralino which need not be equal to its true momentum.

To find the range of values m_{T2} may take we first let $f_1 = m_T^2(\mathbf{p}_T^{\pi^{(1)}}, \not{q}_T^{(1)})$, and $f_2 = m_T^2(\mathbf{p}_T^{\pi^{(2)}}, \not{q}_T^{(2)})$. We then note that the minimum over a parameter x of the maximum of $f_1(x)$ and $f_2(x)$ can occur at a local minimum, $f'_{1(2)}(x^*) = 0$, provided $f_{1(2)}(x^*) > f_{2(1)}(x^*)$, as shown in fig. D.1a. Alternatively the minimum can occur when the functions cross one another when $f_1 = f_2$ (fig. D.1b) or at a boundary (fig. D.1c). The parameter x corresponds to the fraction of the missing momentum (in one of the transverse directions) which is assigned to each half of the event. Since $f_1, f_2 \to \infty$ as $x \to \pm\infty$ fig. D.1c is not relevant to our minimisation problem.

To see that case (a) cannot occur, consider the unconstrained minimisation over $\not{q}_T$, of $m_T^2(\mathbf{p}_T^\pi,\ \not{\mathbf{q}}_T)$. Using the relationship

$$\frac{\partial \not{E}_T}{\partial \not{q}_k} = \frac{\not{q}_k}{\not{E}_T} \ , \tag{D.8}$$

where $\not{E}_T^2 = \not{\mathbf{q}}_T^2 + m_{\tilde{\chi}_1^0}^2$, it is straightforward to show that,

$$\frac{\partial m_T^2}{\partial \not{q}_k} = 2\left(E_T^\pi \frac{\not{q}_k}{\not{E}_T} - p_k^\pi\right) \qquad k = 1, 2 \ . \tag{D.9}$$

This means that at the minimum

$$\mathbf{v}_T^\pi = \not{\mathbf{u}}_T \ , \tag{D.10}$$

where we introduce the notation $\mathbf{v}_T \equiv \mathbf{p}_T/E_T$, $\not{\mathbf{u}}_T \equiv \not{\mathbf{q}}_T/\not{E}_T$. where $\mathbf{p}_T$ and $\mathbf{v}_T$ represent the true transverse momentum and velocity of a particle, while $\not{\mathbf{q}}_T$ and $\not{\mathbf{u}}_T$ are assigned by the minimisation.

Using the basis (t, x, y) with the metric diag(1,-1,-1), one can write

$$m_T^2 = (E_T^{\text{tot}}, \mathbf{p}_T^{\text{tot}}) \cdot (E_T^{\text{tot}}, \mathbf{p}_T^{\text{tot}}) \ , \tag{D.11}$$

where $E_T^{\text{tot}} = E_T^\pi + \not{E}_T$ and $\mathbf{p}_T^{\text{tot}} = \mathbf{p}_T^\pi + \not{\mathbf{q}}_T$. This 1+2 dimensional Lorentz invariant can be evaluated in any frame boosted from the lab in the transverse plane. eq. D.10 has told us that at the unconstrained minimum the transverse velocities $\mathbf{v}_T^\pi$ and $\not{\mathbf{u}}_T$ are equal; a statement necessarily true in all transverse frames, including the special one in which both the transverse velocities (and associated momenta) are zero. Evaluating eq. D.11 in this frame, we find that the unconstrained minimum of eq. D.11 then becomes $(m_\pi + m_{\tilde{\chi}_1^0},\ 0,\ 0) \cdot (m_\pi + m_{\tilde{\chi}_1^0},\ 0,\ 0)$, and we recover the expected result

$$m_T^{\text{min}} = m_\pi + m_{\tilde{\chi}_1^0} \ . \tag{D.12}$$

We therefore conclude that the function m_T^2 has only one stationary value and it is the global minimum, and is common to both sides of the event provided the same type of particles are emitted. Thus when f_1 is minimum it cannot be greater than f_2, and so the minimisation in eq. D.7 forces $f_1 = f_2$. This could of course occur when *both* f_1 and f_2 are at their global minima, in which case m_{T2} takes its minimum value:

$$m_{T2}{}^{\min} = m_\pi + m_{\tilde\chi_1^0} \; . \tag{D.13}$$

To summarise, m_{T2} is the minimum of $m_T^{(1)}$ subject to the two constraints $m_T^{(1)} = m_T^{(2)}$, and $\not{\mathbf{p}}_T^{(1)} + \not{\mathbf{p}}_T^{(2)} = \not{\mathbf{p}}_T$. The condition for the minimisation can be calculated by Lagrange multiplier methods, the result of which is that the velocity vectors $\not{\mathbf{u}}_T^{(1,2)}$ of the *assigned* neutralino momenta $\not{\mathbf{q}}_T^{(1,2)}$ must satisfy

$$\left(\not{\mathbf{u}}_T^{(1)} - \mathbf{v}_T^{\pi^{(1)}}\right) \;\propto\; \left(\not{\mathbf{u}}_T^{(2)} - \mathbf{v}_T^{\pi^{(2)}}\right) \; . \tag{D.14}$$

To find the maximum of m_{T2} over many events we note that for each event the minimisation will select hypothesised momenta satisfying eq. D.14. We now note events can occur in which the *true* transverse velocities of the neutralinos were exactly those which were assigned by the minimisation, *i.e.* they can satisfy

$$\mathbf{v}_T^{\tilde\chi_1^0(1)} = \not{\mathbf{u}}_T^{(1)}, \qquad \mathbf{v}_T^{\tilde\chi_1^0(2)} = \not{\mathbf{u}}_T^{(2)} \; . \tag{D.15}$$

These events will have both hypothesised transverse masses equal not only to each other but also to true transverse masses which would have been calculated if the neutralino momenta had been known:

$$m_T^{(i)}\left(\mathbf{p}_T^{\pi^{(i)}}, \not{\mathbf{p}}_T^{\tilde\chi_1^0(i)}\right) = m_T^{(i)}\left(\mathbf{p}_T^{\pi^{(i)}}, \not{\mathbf{q}}_T^{(i)}\right) \tag{D.16}$$

If events occur where, in addition to the transverse components of the neutralino momenta satisfying eq. D.15, the rapidity differences satisfy $\eta_{\tilde{\chi}_1^0(1)} = \eta_{\pi(1)}$ and $\eta_{\tilde{\chi}_1^0(2)} = \eta_{\pi(2)}$, then by eq. D.2 m_{T2} will equal the true mass of the chargino. Combining this with eq. D.13 and recalling that m_{T2} cannot be greater than the chargino mass by construction, we can see that the event-by event distribution of m_{T2} can span the range

$$m_{\tilde{\chi}_1^0} + m_\pi \;\leq\; m_{T2} \;\leq\; m_{\tilde{\chi}_1^+} \tag{D.17}$$

showing that m_{T2} is sensitive to the $m_{\tilde{\chi}_1^+} - m_{\tilde{\chi}_1^0} \equiv \Delta M_{\tilde{\chi}_1}$ mass difference.

The variable is equally applicable to two same-sign $\tilde{\chi}_1^+$ decays so m_{T2} signal events can be defined as those having two $\tilde{\chi}_1^\pm \to \tilde{\chi}_1^0\ \pi^\pm$ decays with any combination of charges.

D.2 Generalisations of m_{T2}

In our analysis we also wish to make use of the leptonic decays $\tilde{\chi}_1^+ \to \tilde{\chi}_1^0\ \ell\ \nu_\ell$ where $\ell \in e, \mu$. We therefore generalise m_{T2} to cases where more than two particles go undetected.

Consider events in which a chargino is produced and then decays to $\tilde{\chi}_1^0\ e\ \nu_e$. If we expand the Lorentz invariant

$$(m_{\tilde{\chi}_1^+})^2 = (p_{\tilde{\chi}_1^0} + p_e + p_\nu)^2 \tag{D.18}$$

we obtain three mass-squared terms for each of the decay particles and three cross-terms. The cross-terms can each be written in the form

$$p_a \cdot p_b = E_T^{(a)} E_T^{(b)} \cosh(\Delta\eta_{ab}) - \mathbf{p}_T^{(a)} \cdot \mathbf{p}_T^{(b)}\ . \tag{D.19}$$

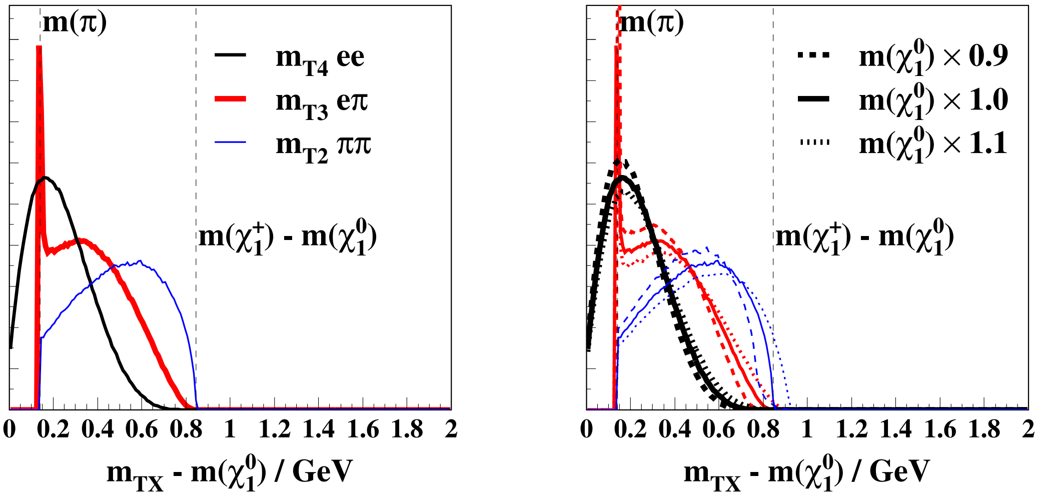

(a) (b)

Figure D.2: **(a)** Simulations of $m_{TX} - m_{\tilde{\chi}_1^0}$ for $X = 2, 3, 4$ using a simple phase-space Monte-Carlo generator program for a pair of decays $\tilde{q} \to \tilde{\chi}_1^+ q$ followed by $\tilde{\chi}_1^+ \to \tilde{\chi}_1^0\ \pi$ or $\tilde{\chi}_1^+ \to \tilde{\chi}_1^0\ e\ \nu_e$. As the number of invisible particles increases the proportion of events near the upper limit decreases. The peak in $m_{T3} - m_{\tilde{\chi}_1^0}$ near the pion mass is explained in the text. **(b)** The distortion of $m_{TX} - m_{\tilde{\chi}_1^0}$ when the LSP mass is varied by ± 10%, showing that $M_{TX} - m_{\tilde{\chi}_1^0}$ remains sensitive to the mass difference $\Delta M_{\tilde{\chi}_1} = m_{\tilde{\chi}_1^+} - m_{\tilde{\chi}_1^0}$. In this simulation $\Delta M_{\tilde{\chi}_1} = 0.845$ GeV, $m_{\tilde{\chi}_1^0} = 161.6$ GeV, and the electron and neutrino mass were neglected. The normalisation is arbitrary.

If the neutralino and neutrino transverse momenta were individually known we could evaluate the transverse mass,

$$m_T^2 = m_{\tilde{\chi}_1^0}^2 + m_e^2 + 2\left[(E_T^e E_T^\chi - \mathbf{p}_T^e \cdot \mathbf{p}_T^\chi) + (E_T^\nu E_T^\chi - \mathbf{p}_T^\nu \cdot \mathbf{p}_T^\chi) + (E_T^e E_T^\nu - \mathbf{p}_T^e \cdot \mathbf{p}_T^\nu)\right], \quad \text{(D.20)}$$

where the neutrino mass is assumed to be negligible. m_T will be equal to the $\tilde{\chi}_1^+$ mass in events where $\Delta\eta_{ab} = 0$ for all pairs of e, ν_e, and $\tilde{\chi}_1^0$.

In events with two leptonic chargino decays a variable like m_{T2} can be defined as in eq. D.7 but using the three-particle definition of m_T from eq. D.20 and with the modified constraint,

$$\mathbf{q}_T^{\nu(1)} + \mathbf{q}_T^{\chi(1)} + \mathbf{q}_T^{\nu(2)} + \mathbf{q}_T^{\chi(2)} = \not{\mathbf{p}}_T \; , \tag{D.21}$$

where the labels (1) and (2) indicate which chargino the particles were emitted from. We call this variable m_{T4} (or indeed m_{TX} where X is the number of undetected particles).

The conditions for the minimisation required to calculate m_{T4} can be calculated just as for m_{T2}. The Euler-Lagrange equations involving

$$\frac{\partial (m_T^{(i)})^2}{\partial \mathbf{q}_T^{\nu(i)}} \quad \text{and} \quad \frac{\partial (m_T^{(i)})^2}{\partial \mathbf{q}_T^{\tilde{\chi}_1^0(i)}} \tag{D.22}$$

show that the minimisation will select the invisible particles' momenta such that $\mathbf{u}_T^{\tilde{\chi}_1^0(i)} = \mathbf{u}_T^{\nu(i)}$. The other E-L equations reproduce eq. D.14 but with electrons replacing pions.

This means that when calculating m_{T4} one can replace the missing particles from each chargino decay with a pseudo-particle with mass equal to the sum of the masses of those invisible particles and proceed as for m_{T2}. In the case of leptonic chargino decay the mass of the neutrino can be safely neglected in comparison to that of the $\tilde{\chi}_1^0$, and the constraint $\mathbf{u}_T^{\chi(i)} = \mathbf{u}_T^{\nu(i)}$ is equivalent to $\mathbf{q}_T^{\nu(i)} = (0,0)$.

The generalisation to m_{TX} for other values of X is straightforward. The distribution of m_{T3} is shown in fig. D.2a for events in which one chargino decays to $\tilde{\chi}_1^0, e, \nu$ and another to $\tilde{\chi}_1^0, \pi^+$. Unlike m_{T2} and m_{T4} it has a sharp peak at $m_{T3} = m_{\tilde{\chi}_1^0} + m_\pi$. This occurs because the visible particles on each side of the event are different and so the unconstrained minimum of the values of m_T on each side of the event are not equal as they are in the case of m_{T2} and m_{T4}:

$$\min_{\not{\mathbf{q}}_{\mathbf{T}}^{(\mathbf{1})}} \left(m_T^{(1)}(\mathbf{p}_T^{\pi}, \not{\mathbf{q}}_T^{(1)}) \right) \;=\; m_\pi + m_{\tilde{\chi}_1^0} \quad \neq \quad m_e + m_{\tilde{\chi}_1^0} \;=\; \min_{\not{\mathbf{q}}_{\mathbf{T}}^{(\mathbf{2})}} \left(m_T^{(2)}(\mathbf{p}_T^{e}, \not{\mathbf{q}}_T^{(2)}) \right) \tag{D.23}$$

Some of the events can then fall into the category shown in fig. D.1a, producing a peak of events with $m_T = m_{\tilde{\chi}_1^0} + m_\pi$.

The distribution over events of m_{T4} will have fewer entries near the upper kinematic limit ($m_{T4} = m_{\tilde{\chi}_1^+}$) because when more particles go undetected an event at that limit must satisfy a larger number of constraints. For fully leptonic chargino decay, there are six constraints of the type $\Delta\eta = 0$, two $\mathbf{p}_T^{\nu(i)} = 0$ and finally the modified constraint from eq. D.14. This effect can be seen in fig. D.2a for events where a total of two, three and four invisible particles are produced.

A further generalisation which we do not require here might be relevant in cases where more than one *visible* particle is emitted from each mother. For such decays, one would sum the full 4-momenta of the visible particles from each decay as well as summing the masses of the invisible particles from each side of the event and proceed as for m_{T2}.

D.3 Uncertainties in $\not{p}_T$ and $m_{\tilde{\chi}_1^0}$

The sensitivity of m_{TX} to the estimated mass of the neutralino is shown in fig. D.2b, where 10% (16 GeV) errors in $m_{\tilde{\chi}_1^0}$ result in similar *fractional* errors in $\Delta M_{\tilde{\chi}_1}$ *i.e.* of a few tens of MeV. m_{TX} shows similar insensitivity to measurement uncertainties in the missing transverse momentum vector. This behaviour can be (at least partially) understood from the non-relativistic limit of m_{T2}, when the proportionality in eq. D.14 becomes an equality and

$$m_{T2}{}^2 - (m_\pi + m_{\tilde{\chi}_1^0})^2 = \frac{1}{4 m_\pi m_{\tilde{\chi}_1^0}} \left(m_\pi \not{\mathbf{p}}_T - m_{\tilde{\chi}_1^0} \mathbf{p}_T^{\pi_1} - m_{\tilde{\chi}_1^0} \mathbf{p}_T^{\pi_2} \right)^2 + \mathcal{O}\left((\mathbf{v}_T \cdot \mathbf{v}_T)^2 \right) \ . \tag{D.24}$$

One can see that in eq. D.24 m_π multiplies the missing momentum, while $m_{\tilde{\chi}_1^0}$ multiplies the pion transverse momenta.

Bibliography

[1] B. C. Allanach et al., Measuring supersymmetric particle masses at the LHC in scenarios with baryon-number R-parity violating couplings, *JHEP* **03**, 048 (2001), `hep-ph/0102173`.

[2] B. C. Allanach, A. J. Barr, M. A. Parker, P. Richardson, and B. R. Webber, Extracting the flavour structure of a baryon-number R-parity violating coupling at the LHC, *JHEP* **09**, 021 (2001), `hep-ph/0106304`.

[3] A. J. Barr, B. C. Allanach, C. G. Lester, M. A. Parker, and P. Richardson, Discovering anomaly-mediated supersymmetry at the LHC, (2002), Submitted to *JHEP*, `hep-ph/0208214`.

[4] A. J. Barr, C. G. Lester, and P. Stevens, in progress.

[5] A. Barr et al., Beamtests of prototype ATLAS SCT modules at CERN H8 in June and August 2000, (2001), ATLAS note, `ATL-INDET-2002-005`, `http://weblib.cern.ch/`.

[6] A. J. Barr et al., Beamtests of prototype ATLAS SCT modules at CERN H8 in 2000, `CERN-2001-005, CERN-LHCC-2001-034`.

[7] A. J. Barr et al., Beamtests of ATLAS SCT modules in August and October 2001, ATLAS internal note, `ATL-COM-INDET-2002-017`.

[8] Millennium madness, physics problems for the next millennium, 2000, presented at the Strings 2000 conference.

[9] P. W. Higgs, Broken symmetries and the masses of gauge bosons, *Phys. Rev. Lett.* **13**, 508 (1964).

[10] F. Englert and R. Brout, Broken symmetry and the mass of gauge vector mesons, *Phys. Rev. Lett.* **13**, 321 (1964).

[11] Y. Fukuda et al., Evidence for oscillation of atmospheric neutrinos, *Phys. Rev. Lett.* **81**, 1562–1567 (1998), `hep-ex/9807003`.

[12] S. Fukuda et al., Constraints on neutrino oscillations using 1258 days of Super-Kamiokande solar neutrino data, *Phys. Rev. Lett.* **86**, 5656–5660 (2001), `hep-ex/0103033`.

[13] Q. R. Ahmad et al., Measurement of the charged of current interactions produced by B-8 solar neutrinos at the Sudbury Neutrino Observatory, *Phys. Rev. Lett.* **87**, 071301 (2001), `nucl-ex/0106015`.

[14] M. Hirsch, M. A. Diaz, W. Porod, J. C. Romao, and J. W. F. Valle, Neutrino masses and mixings from supersymmetry with bilinear R-parity violation: A theory for solar and atmospheric neutrino oscillations, *Phys. Rev.* **D62**, 113008 (2000), `hep-ph/0004115`.

[15] Search for the standard model Higgs boson at LEP, (2001), `hep-ex/0107029`.

[16] D. Abbaneo et al., A combination of preliminary electroweak measurements and constraints on the standard model, (2001), `hep-ex/0112021`.

[17] C. Lee, B.W. Quigg and H.B. Thacker, Strength of weak interactions at very high energies and the higgs boson mass, *Phys. Rev. Lett.* , 883–885 (1977).

[18] S. Ferrara, editor, *Supersymmetry*, World scientific, 1987.

[19] S. Weinberg, *Supersymmetry*, volume 3 of *The quantum theory of fields*, Cambridge Univ. Pr., 2000.

[20] Stephen P. Martin, A supersymmetry primer, (1997), `hep-ph/9709356`.

[21] Joseph Polchinski, Introduction to supersymmetry, Presented at 13th Annual SLAC Summer Inst. on Particle Physics, Stanford, CA, Jul 29 - Aug 9, 1985.

[22] Manuel Drees, An introduction to supersymmetry, (1996), `hep-ph/9611409`.

[23] Jonathan A. Bagger, Weak-scale supersymmetry: theory and practice, (1996), `hep-ph/9604232`.

[24] Michael Dine, Supersymmetry phenomenology (with a broad brush), (1996), `hep-ph/9612389`.

[25] S. Coleman and J. Mandula, All possible symmetries of the S matrix, *Phys. Rev.* **159**, 1251 (1967).

[26] Rudolf Haag, Jan T. Lopuszanski, and Martin Sohnius, All possible generators of supersymmetries of the S matrix, *Nucl. Phys.* **B88**, 257 (1975).

[27] Keith R. Dienes, String theory and the path to unification: A review of recent developments, *Phys. Rept.* **287**, 447–525 (1997), `hep-th/9602045`.

[28] G. 't Hooft, Symmetry breaking through Bell-Jackiw anomalies, *Phys. Rev. Lett.* **37**, 8–11 (1976).

[29] M. Shiozawa et al., Search for proton decay via $p \to e^+\pi^0$ in a large water Cherenkov detector, *Phys. Rev. Lett.* **81**, 3319–3323 (1998), `hep-ex/9806014`.

[30] *ATLAS Detector and Physics Peformance TDR*, CERN, 1999, `CERN/LHCC/99-14, CERN/LHCC/99-15`.

[31] *TESLA TDR, Part III: Physics at an e^+e^- Linear Collider*, DESY, 2001.

[32] Savas Dimopoulos and Howard Georgi, Softly broken supersymmetry and SU(5), *Nucl. Phys.* **B193**, 150 (1981).

[33] Savas Dimopoulos and David W. Sutter, The supersymmetric flavor problem, *Nucl. Phys.* **B452**, 496–512 (1995), `hep-ph/9504415`.

[34] C. G. Lester, *Model Independant sparticle mass measurements at ATLAS*, PhD thesis, Cambridge University, 2001.

[35] *ATLAS Inner Detector TDR*, CERN, 1997, `CERN/LHCC/97-16` and `CERN/LHCC/97-17`.

[36] *ATLAS Pixel Detector TDR*, CERN, 1998, `CERN/LHCC 98-13`.

[37] D. Barberis, ATLAS inner detector developments, *Nucl. Instrum. Meth.* **A446**, 331–337 (2000).

[38] *ATLAS Calorimeter Performance TDR*, CERN, 1996, `CERN/LHCC 96-40`.

[39] *ATLAS Liquid Argon Calorimeter TDR*, CERN, 1996, `CERN/LHCC 96-41`.

[40] S. Akhmadalev et al., Results from a new combined test of an electromagnetic liquid argon calorimeter with a hadronic scintillating- tile calorimeter, *Nucl. Instrum. Meth.* **A449**, 461–477 (2000).

[41] *ATLAS Tile Calorimeter TDR*, CERN, 1996, `CERN/LHCC 96-42`.

[42] *ATLAS Muon Spectrometer TDR*, CERN, 1997, `CERN/LHCC 97-22`.

[43] W.J. Sterling, presented at the Workshop on Theory of LHC Processes, CERN February 1998.

[44] *ATLAS trigger performance status report*, 1998, `CERN/LHCC 98-15`.

[45] Lisa Randall and Raman Sundrum, Out of this world supersymmetry breaking, *Nucl. Phys.* **B557**, 79–118 (1999), `hep-th/9810155`.

[46] Gian F. Giudice, Markus A. Luty, Hitoshi Murayama, and Riccardo Rattazzi, Gaugino mass without singlets, *JHEP* **12**, 027 (1998), `hep-ph/9810442`.

[47] Alex Pomarol and Riccardo Rattazzi, Sparticle masses from the superconformal anomaly, *JHEP* **05**, 013 (1999), `hep-ph/9903448`.

[48] Z. Chacko, Markus A. Luty, Ivan Maksymyk, and Eduardo Ponton, Realistic anomaly-mediated supersymmetry breaking, *JHEP* **04**, 001 (2000), `hep-ph/9905390`.

[49] Emanuel Katz, Yael Shadmi, and Yuri Shirman, Heavy thresholds, slepton masses and the mu term in anomaly mediated supersymmetry breaking, *JHEP* **08**, 015 (1999), `hep-ph/9906296`.

[50] Marcela Carena, Katri Huitu, and Tatsuo Kobayashi, RG-invariant sum rule in a generalization of anomaly mediated SUSY breaking models, *Nucl. Phys.* **B592**, 164–182 (2001), `hep-ph/0003187`.

[51] I. Jack and D. R. T. Jones, Fayet-Iliopoulos D-terms and anomaly mediated supersymmetry breaking, *Phys. Lett.* **B482**, 167–173 (2000), `hep-ph/0003081`.

[52] Nima Arkani-Hamed, David E. Kaplan, Hitoshi Murayama, and Yasunori Nomura, Viable ultraviolet-insensitive supersymmetry breaking, *JHEP* **02**, 041 (2001), `hep-ph/0012103`.

[53] Z. Chacko, Markus A. Luty, Eduardo Ponton, Yael Shadmi, and Yuri Shirman, The GUT scale and superpartner masses from anomaly mediated supersymmetry breaking, *Phys. Rev.* **D64**, 055009 (2001), `hep-ph/0006047`.

[54] David Elazzar Kaplan and Graham D. Kribs, Gaugino-assisted anomaly mediation, *JHEP* **09**, 048 (2000), `hep-ph/0009195`.

[55] Ann E. Nelson and Neal J. Weiner, Gauge/anomaly syzygy and generalized brane world models of supersymmetry breaking, *Phys. Rev. Lett.* **88**, 231802 (2002), `hep-ph/0112210`.

[56] Markus Luty and Raman Sundrum, Anomaly mediated supersymmetry breaking in four dimensions, naturally, (2001), `hep-th/0111231`.

[57] Roni Harnik, Hitoshi Murayama, and Aaron Pierce, Purely four-dimensional viable anomaly mediation, (2002), `hep-ph/0204122`.

[58] I. Jack, D. R. T. Jones, and R. Wild, Fayet-Iliopoulos D-terms, neutrino masses and anomaly mediated supersymmetry breaking, *Phys. Lett.* **B535**, 193–200 (2002), `hep-ph/0202101`.

[59] Tony Gherghetta, Gian F. Giudice, and James D. Wells, Phenomenological consequences of supersymmetry with anomaly-induced masses, *Nucl. Phys.* **B559**, 27–47 (1999), `hep-ph/9904378`.

[60] Jonathan L. Feng and Takeo Moroi, Supernatural supersymmetry: Phenomenological implications of anomaly-mediated supersymmetry breaking, *Phys. Rev.* **D61**, 095004 (2000), `hep-ph/9907319`.

[61] K. Huitu, J. Laamanen, and P. N. Pandita, Sparticle spectrum and constraints in anomaly mediated supersymmetry breaking models, *Phys. Rev.* **D65**, 115003 (2002), `hep-ph/0203186`.

[62] Jonathan L. Feng, Takeo Moroi, Lisa Randall, Matthew Strassler, and Shufang Su, Discovering supersymmetry at the Tevatron in Wino LSP scenarios, *Phys. Rev. Lett.* **83**, 1731–1734 (1999), `hep-ph/9904250`.

[63] B. C. Allanach and A. Dedes, R-parity violating anomaly mediated supersymmetry breaking, *JHEP* **06**, 017 (2000), `hep-ph/0003222`.

[64] F. De Campos, M. A. Diaz, Oscar J. P. Eboli, M. B. Magro, and P. G. Mercadante, Anomaly mediated supersymmetry breaking without R-parity, *Nucl. Phys.* **B623**, 47–72 (2002), `hep-ph/0110049`.

[65] B. C. Allanach et al., The Snowmass points and slopes: Benchmarks for SUSY searches, (2002), `hep-ph/0202233`.

[66] G. Corcella et al., HERWIG 6: An event generator for hadron emission reactions with interfering gluons (including supersymmetric processes), *JHEP* **01**, 010 (2001), `hep-ph/0011363`.

[67] Stefano Moretti, Kosuke Odagiri, Peter Richardson, Michael H. Seymour, and Bryan R. Webber, Implementation of supersymmetric processes in the HERWIG event generator, *JHEP* **04**, 028 (2002), `hep-ph/0204123`.

[68] G. Corcella et al., Herwig 6.3 release note, (2001), `hep-ph/0107071`.

[69] B. C. Allanach, C. G. Lester, M. A. Parker, and B. R. Webber, Measuring sparticle masses in non-universal string inspired models at the LHC, *JHEP* **09**, 004 (2000), `hep-ph/0007009`.

[70] Frank E. Paige and James Wells, Anomaly mediated SUSY breaking at the LHC, (1999), `hep-ph/0001249`.

[71] A Djouadi et al., Les Points d'Aix, 2001, Euro GDR SUSY workshop.

[72] A. Heister et al., Search for charginos nearly mass degenerate with the lightest neutralino in e^+e^- collisions at centre-of-mass energies up to 209-GeV, *Phys. Lett.* **B533**, 223–236 (2002), `hep-ex/0203020`.

[73] Dilip Kumar Ghosh, Anirban Kundu, Probir Roy, and Sourov Roy, Characteristic Wino signals in a linear collider from anomaly mediated supersymmetry breaking, *Phys. Rev.* **D64**, 115001 (2001), `hep-ph/0104217`.

[74] Dilip Kumar Ghosh, Probir Roy, and Sourov Roy, Linear collider signal of a Wino LSP in anomaly-mediated scenarios, *JHEP* **08**, 031 (2000), `hep-ph/0004127`.

[75] Debajyoti Choudhury, Dilip Kumar Ghosh, and Sourov Roy, Signals of anomaly mediated supersymmetry breaking in an $e^-\gamma$ collider, (2002), `hep-ph/0208240`.

[76] Howard Baer, J. K. Mizukoshi, and Xerxes Tata, Reach of the CERN LHC for the minimal anomaly-mediated SUSY breaking model, *Phys. Lett.* **B488**, 367–372 (2000), `hep-ph/0007073`.

[77] Anindya Datta, Partha Konar, and Biswarup Mukhopadhyaya, Invisible charginos and neutralinos from gauge boson fusion: A way to explore anomaly mediation?, *Phys. Rev. Lett.* **88**, 181802 (2002), `hep-ph/0111012`.

[78] C. H. Chen, M. Drees, and J. F. Gunion, A non-standard string/SUSY scenario and its phenomenological implications, *Phys. Rev.* **D55**, 330–347 (1997), `hep-ph/9607421`.

[79] C. H. Chen, M. Drees, and J. F. Gunion, Addendum/erratum for 'Searching for invisible and almost invisible particles at e^+e^- colliders' and 'A non-standard string/SUSY scenario and its phenomenological implications', (1999), `hep-ph/9902309`.

[80] Johann H. Kuhn and A. Santamaria, Tau decays to pions, *Z. Phys.* **C48**, 445–452 (1990).

[81] Frank E. Paige, Serban D. Protopopescu, Howard Baer, and Xerxes Tata, ISAJET 7.40: A Monte Carlo event generator for pp, $\bar{p}p$, and e^+ e^- reactions, (1998), `hep-ph/9810440`.

[82] Howard Baer, Frank E. Paige, Serban D. Protopopescu, and Xerxes Tata, Simulating supersymmetry with ISAJET 7.0 / ISASUSY 1.0, (1993), `hep-ph/9305342`.

[83] G. Corcella et al., Herwig 6.4 release note, (2001), `hep-ph/0201201`.

[84] Peter Richardson, Spin correlations in Monte Carlo simulations, *JHEP* **11**, 029 (2001), `hep-ph/0110108`.

[85] W. T. Giele, T. Matsuura, M. H. Seymour, and B. R. Webber, W boson plus multijets at hadron colliders: Herwig parton showers versus exact matrix elements, Contribution to Proc. of 1990 Summer Study on High Energy Physics: Research Directions for the Decade, Snowmass, CO, Jun 25 - Jul 13, 1990.

[86] E. Richter-Was, D. Froidevaux, and L. Poggioli, Atlfast 2.0: A fast simulation package for ATLAS, (1998), ATLAS internal note, `ATL-PHYS-98-131`.

[87] E.J. Buis et al., Update of inner detector performance parameterisations, (1998), ATLAS note, `ATL-INDET-98-215`.

[88] S. Abdullin et al., Discovery potential for supersymmetry in CMS, *J. Phys.* **G28**, 469 (2002), `hep-ph/9806366`.

[89] S. I. Bityukov and N. V. Krasnikov, The LHC (CMS) discovery potential for models with effective supersymmetry and nonuniversal gaugino masses, (2001), `hep-ph/0102179`.

[90] D. R. Tovey, Inclusive SUSY searches and measurements at ATLAS, (2002), ATLAS Scientific Note, `SN-ATLAS-2002-020`.

[91] John F. Gunion and Stephen Mrenna, A study of SUSY signatures at the Tevatron in models with near mass degeneracy of the lightest chargino and neutralino, *Phys. Rev.* **D62**, 015002 (2000), `hep-ph/9906270`.

[92] John F. Gunion and Stephen Mrenna, Probing models with near degeneracy of the chargino and LSP at a linear e^+e^- collider, *Phys. Rev.* **D64**, 075002 (2001), `hep-ph/0103167`.

[93] S. Ambrosanio, B. Mele, S. Petrarca, G. Polesello, and A. Rimoldi, Measuring the SUSY breaking scale at the LHC in the slepton LSP scenario of GMSB models, *JHEP* **01**, 014 (2001), `hep-ph/0010081`.

[94] B. C. Allanach, C. M. Harris, M. A. Parker, P. Richardson, and B. R. Webber, Detecting exotic heavy leptons at the large hadron collider, *JHEP* **08**, 051 (2001), `hep-ph/0108097`.

[95] Kevin Einsweiler, Private communication.

[96] A. Brignole, Luis E. Ibanez, and C. Munoz, Soft supersymmetry-breaking terms from supergravity and superstring models, (1997), `hep-ph/9707209`.

[97] Howard E. Haber and Gordon L. Kane, The search for supersymmetry: Probing physics beyond the Standard Model, *Phys. Rept.* **117**, 75 (1985).

[98] Hsin-Chia Cheng, Bogdan A. Dobrescu, and Konstantin T. Matchev, Generic and chiral extensions of the supersymmetric Standard Model, *Nucl. Phys.* **B543**, 47–72 (1999), `hep-ph/9811316`.

[99] Valeria Tano, *A study of QCD processes at low momentum transfer in hadron-hadron collisions*, PhD thesis, RWTH Aachen, 2001.

[100] G. J. Alner et al., The UA5 high-energy $\bar{p}p$ simulation program, *Nucl. Phys.* **B291**, 445 (1987).

[101] R. Field, October 2002, Talk presented at the Fermilab ME/MC Tuning Workshop.

[102] S. Bridle A. Lewis, Cosmological parameters from CMB and other data: a Monte-Carlo approach, (2002), `astro-ph/0205436`.

[103] A. H. Jaffe et al., Cosmology from Maxima-1, Boomerang and COBE/DMR CMB observations, *Phys. Rev. Lett.* **86**, 3475–3479 (2001), `astro-ph/0007333`.

[104] C. Pryke et al., Cosmological parameter extraction from the first season of observations with DASI, *Astrophys. J.* **568**, 46–51 (2002), `astro-ph/0104490`.

[105] T. J. Pearson et al., The anisotropy of the microwave background to l = 3500: Mosaic observations with the Cosmic Background Imager, (2002), `astro-ph/0205388`.

[106] Jose Alberto Rubino-Martin et al., First results from the Very Small Array. IV: Cosmological parameter estimation, (2002), MNRAS submitted, `astro-ph/0205367`.

[107] W. J. Percival et al., Parameter constraints for flat cosmologies from CMB and 2dFGRS power spectra, (2002), MNRAS submitted, `astro-ph/0206256`.

[108] G. Belanger, F. Boudjema, A. Pukhov, and A. Semenov, MicrOMEGAs: A program for calculating the relic density in the MSSM, (2001), `hep-ph/0112278`.

[109] Takeo Moroi and Lisa Randall, Wino cold dark matter from anomaly-mediated SUSY breaking, *Nucl. Phys.* **B570**, 455–472 (2000), `hep-ph/9906527`.

[110] U. Chattopadhyay and Pran Nath, Probing supergravity grand unification in the brookhaven $g-2$ experiment, *Phys. Rev.* **D53**, 1648–1657 (1996), `hep-ph/9507386`.

[111] Stephen P. Martin and James D. Wells, Muon anomalous magnetic dipole moment in supersymmetric theories, *Phys. Rev.* **D64**, 035003 (2001), `hep-ph/0103067`.

[112] S. Baek, P. Ko, and J. H. Park, Muon anomalous magnetic moment from effective supersymmetry, *Eur. Phys. J.* **C24**, 613–618 (2002), `hep-ph/0203251`.

[113] Mark Byrne, Christopher Kolda, and Jason E. Lennon, Updated implications of the muon anomalous magnetic moment for supersymmetry, (2002), `hep-ph/0208067`.

[114] Motoi Endo and Takeo Moroi, Muon magnetic dipole moment and higgs mass in supersymmetric $SU(5)$ models, *Phys. Lett.* **B525**, 121–129 (2002), `hep-ph/0110383`.

[115] David W. Hertzog, The BNL muon anomalous magnetic moment measurement, (2002), `hep-ex/0202024`.

[116] G. W. Bennett, Measurement of the positive muon anomalous magnetic moment to 0.7 ppm, (2002), `hep-ex/0208001`.

[117] Andrzej Czarnecki and William J. Marciano, The muon anomalous magnetic moment: A harbinger for 'new physics', *Phys. Rev.* **D64**, 013014 (2001), `hep-ph/0102122`.

[118] F. J. Yndurain, Disagreement between standard model and experiment for muon g-2?, (2001), `hep-ph/0102312`.

[119] Stephan Narison, Muon and tau anomalies updated, *Phys. Lett.* **B513**, 53–70 (2001), `hep-ph/0103199`.

[120] J. F. de Troconiz and F. J. Yndurain, Precision determination of the muon $g_\mu - 2$ and $\bar{\alpha}_{QED}(M_Z^2)$, (2001), `hep-ph/0111258`.

[121] Marc Knecht and Andreas Nyffeler, Hadronic light-by-light corrections to the muon g-2: The pion-pole contribution, *Phys. Rev.* **D65**, 073034 (2002), `hep-ph/0111058`.

[122] M. Knecht, A. Nyffeler, M. Perrottet, and E. De Rafael, Hadronic light-by-light scattering contribution to the muon g-2: An effective field theory approach, *Phys. Rev. Lett.* **88**, 071802 (2002), `hep-ph/0111059`.

[123] Masashi Hayakawa and Toichiro Kinoshita, Comment on the sign of the pseudoscalar pole contribution to the muon g-2, (2001), `hep-ph/0112102`.

[124] Johan Bijnens, Elisabetta Pallante, and Joaquim Prades, Comment on the pion pole part of the light-by-light contribution to the muon g-2, *Nucl. Phys.* **B626**, 410–411 (2002), `hep-ph/0112255`.

[125] Ian Blokland, Andrzej Czarnecki, and Kirill Melnikov, Pion pole contribution to hadronic light-by-light scattering and muon anomalous magnetic moment, *Phys. Rev. Lett.* **88**, 071803 (2002), `hep-ph/0112117`.

[126] Jorge L. Lopez, D. V. Nanopoulos, and Xu Wang, Large $g_\mu - 2$ in $SU(5) \times U(1)$ supergravity models, *Phys. Rev.* **D49**, 366–372 (1994), `hep-ph/9308336`.

[127] Utpal Chattopadhyay, Dilip Kumar Ghosh, and Sourov Roy, Constraining anomaly mediated supersymmetry breaking framework via ongoing muon $g - 2$ experiment at brookhaven, *Phys. Rev.* **D62**, 115001 (2000), `hep-ph/0006049`.

[128] G. Degrassi, P. Gambino, and G. F. Giudice, $B \to X_s\gamma$ in supersymmetry: Large contributions beyond the leading order, *JHEP* **12**, 009 (2000), `hep-ph/0009337`.

[129] Marco Ciuchini, G. Degrassi, P. Gambino, and G. F. Giudice, Next-to-leading QCD corrections to $B \to X_s\gamma$: Standard Model and two-Higgs doublet model, *Nucl. Phys.* **B527**, 21–43 (1998), `hep-ph/9710335`.

[130] Paolo Gambino and Mikolaj Misiak, Quark mass effects in $\bar{B} \to X_s\gamma$, *Nucl. Phys.* **B611**, 338–366 (2001), `hep-ph/0104034`.

[131] S. Chen et al., Branching fraction and photon energy spectrum for $b \to s\ \gamma$, *Phys. Rev. Lett.* **87**, 251807 (2001), `hep-ex/0108032`.

[132] Yutaka Ushiroda, Radiative B meson decay, (2001), `hep-ex/0104045`.

[133] B. Aubert et al., Determination of the branching fraction for inclusive decays $B \to X_s\gamma$, (2002), `hep-ex/0207076`.

[134] Paolo Gambino and Ulrich Haisch, Complete electroweak matching for radiative B decays, *JHEP* **10**, 020 (2001), `hep-ph/0109058`.

[135] Adrian Mirea and Elemer Nagy, Study of the determination of the SUGRA parameters using the ATLAS detector in the case of L-violating R-parity breaking, (1999), `hep-ph/9904354`.

[136] P. Chiappetta et al., Single top production at the LHC as a probe of R-parity violation, *Phys. Rev.* **D61**, 115008 (2000), `hep-ph/9910483`.

[137] Edmond L. Berger, B. W. Harris, and Z. Sullivan, Single-top-squark production via R-parity-violating supersymmetric couplings in hadron collisions, *Phys. Rev. Lett.* **83**, 4472–4475 (1999), `hep-ph/9903549`.

[138] B. C. Allanach et al., Searching for R-parity violation at run-II of the Tevatron, (1999), `hep-ph/9906224`.

[139] B. C. Allanach, A. Dedes, and H. K. Dreiner, Bounds on R-parity violating couplings at the weak scale and at the GUT scale, *Phys. Rev.* **D60**, 075014 (1999), `hep-ph/9906209`.

[140] B. C. Allanach, A. Dedes, and H. K. Dreiner, 2-loop supersymmetric renormalisation group equations including R-parity violation and aspects of unification, *Phys. Rev.* **D60**, 056002 (1999), `hep-ph/9902251`.

[141] Lee Drage, *The Evaluation of Silicon Microstrip Detectors for the ATLAS Semiconductor Tracker and Supersymmetry Studies at the Large Hadron Collider*, PhD thesis, Cambridge University, 1999.

[142] Herbi Dreiner, Peter Richardson, and Michael H. Seymour, Parton-shower simulations of R-parity violating supersymmetric models, *JHEP* **04**, 008 (2000), `hep-ph/9912407`.

[143] P. Binetruy et al., Broken R-parity, (1991), In *Aachen 1990, Proceedings, Large Hadron Collider, vol. 2 666-675.* CERN Geneva 666-675, `CERN-90-10-B`.

[144] J Soderqvist, Consequences of baryonic R-parity violation for measurements of SUSY particles using the ATLAS detector, (1998), ATLAS note PHYS-98-122.

[145] John Ellis, Smaragda Lola, and Graham G. Ross, Hierarchies of R-violating interactions from family symmetries, *Nucl. Phys.* **B526**, 115 (1998), `hep-ph/9803308`.

[146] J. L. Chkareuli, I. G. Gogoladze, A. B. Kobakhidze, M. G. Green, and D. E. Hutchcroft, On SUSY inspired minimal lepton number violation, *Phys. Rev.* **D62**, 015014 (2000), `hep-ph/9908451`.

[147] G. K. Leontaris and J. Rizos, New fermion mass textures from anomalous $U(1)$ symmetries with baryon and lepton number conservation, *Nucl. Phys.* **B567**, 32 (2000), `hep-ph/9909206`.

[148] John Ellis, G. K. Leontaris, and J. Rizos, Implications of anomalous $U(1)$ symmetry in unified models: The flipped $SU(5) \times U(1)$ paradigm, *JHEP* **05**, 001 (2000), `hep-ph/0002263`.

[149] K. Hagiwara et al., Review of Particle Physics, *Physical Review D* **66** (2002), `http://pdg.lbl.gov`.

[150] S.M. Sze, *Physics of semiconductor devices*, John Wiley & Sons, 2nd edition, 1981.

[151] M. Bruzzi, Radiation damage in silicon detectors for high-energy physics experiments, *IEEE Trans. Nucl. Sci.* **48**, 960–971 (2001).

[152] A.Carter et al., SCT barrel module: Requirements and specifications, `SCT-BM-FDR`.

[153] Silicon detector PRR papers, (August 2000), `ATL-IS-MR-0001`, `http://edmsoraweb.cern.ch`.

[154] ABCD3T ASIC project specification, version 1.2.

[155] W. Dabrowski et al., Design and performance of the abcd chip for the binary readout of silicon strip detectors in the atlas semiconductor tracker, *IEEE Trans. Nucl. Sci.* **47**, 1843–1850 (2000).

[156] W. Dabrowski et al., Progress in development of the readout chip for the atlas semiconductor tracker, Prepared for 6th Workshop on Electronic for LHC Experiments, Cracow, Poland, 11-15 Sep 2000.

[157] M.F. Dentan et al., RD29 final status report : DMILL, a mixed analog-digital radiation hard technology for high energy physics electronics, (1998), `CERN-LHCC-98-037`.

[158] M. Dentan et al., DMILL (Durci Mixte sur Isolant Logico-Lineaire): A mixed analog-digital radiation hard technology for high energy physics electronics, *Nucl. Phys. Proc. Suppl.* **32**, 530–534 (1998).

[159] E. Chesi et al., Performance of Si pad sensors for a RICH detector, *Nucl. Instrum. Meth.* **A384**, 159–166 (1996).

[160] J. Bohm et al., SCT LV & HV Power Supply System Project, `http://www-hep2.fzu.cz/Atlas/WorkingGroups/Projects/MSGC.html`.

[161] ATLAS SCT PS-irradiations, `http://atlas-sct-irradiation.web.cern.ch/`.

[162] J. Lane J. Butterworth, D. Hayes and M. Postranecky, ATLAS SCT clock and control module, `http://www.hep.ucl.ac.uk/atlas/sct/cloac/Welcome.html`.

[163] M.Morrissey, SLOG slog command generator, `http://hepwww.rl.ac.uk/atlas-sct/mm/slog/`.

[164] M. Goodrick and M. Morrissey, Multichannel semiconductor tracker ABC(D) readout device, `http://hepwww.rl.ac.uk/Atlas-SCT/mm/mustard/MUSTARD.PS`.

[165] G. Moorhead, Testbeam extensions to SCTDAQ, `http://atlas.web.cern.ch/Atlas/GROUPS/INNER_DETECTOR/SCT/testbeam`.

[166] G. Moorhead L. Eklund, J. Hill and P. Phillips, Atlas SCT test DAQ online documentation, `http://sct-testdaq.home.cern.ch/sct-testdaq/sctdaq/sctdaq.html`.

[167] F. Rademakers R. Brun, ROOT – an object orientated data analysis framework, `http://root.cern.ch/`.

[168] J.E.Navarro, M.Vos; IFIC - University of Valencia/CSIC.

[169] L Landau, On the energy loss of fast particles by ionisation, *J. Phys. USSR* **8(4)**, 201 (1944).

[170] S.Gadomski and P.Reznicek, Measurement of amplifier pulse shapes in sct modules using a laser setup, (2000), `ATL-INDET-2001-010`.

[171] T. Akimoto et al., Beam study of irradiated ATLAS-SCT prototypes, *Nucl. Instrum. Meth.* **A485**, 67–72 (2002).

[172] I.Gavrilenko, Description of global pattern recognition program XKalman, (1997), ATLAS note, `ATL-INDET-97-165`.

[173] V. M. Ghete B. Epp and A. Nairz, A new hadronic-track parameterisation for fast simulation of the ATLAS inner detector, (2001), ATLAS note, `ATL-PHYS-2001-009`.

[174] T. Akesson et al., Particle identification using the time-over-threshold method in the ATLAS transition radiation tracker, (2001), ATLAS note, `ATL-INDET-2000-021`.

[175] C. G. Lester and D. J. Summers, Measuring masses of semi-invisibly decaying particles pair produced at hadron colliders, *Phys. Lett.* **B463**, 99–103 (1999), `hep-ph/9906349`.

[176] T. Affolder et al., Measurement of the W boson mass with the Collider Detector at Fermilab, *Phys. Rev.* **D64**, 052001 (2001), `hep-ex/0007044`.

[177] V. M. Abazov et al., Improved D0 W boson mass determination, (2001), FERMILAB-CONF-01-284-E, `hep-ex/0106018`.